Gravitational Wave Modelling and Analysis for Binary Neutron Star Inspirals

by

Natalie Williams

UNIVERSITY OF BIRMINGHAM

A thesis submitted to the University of Birmingham for the degree of Doctor of Philosophy

Astronomy and Space Research
School of Physics and Astronomy
College of Engineering and Physical Sciences
University of Birmingham

December 2024

"Her friend the stars dripping from the jewelled sky

When she was passing by

Would keep her calm "

- Belle and Sebastian, *For the Price of a Cup of Tea*

Abstract

The detection of gravitational waves has revolutionised our understanding of the universe by providing direct insights into some of its most extreme phenomena. In particular, observations of gravitational waves from binary neutron star inspirals provide a unique opportunity to probe ultra-dense matter by placing constraints on the still-unknown neutron star equation of state. This information is encoded within the tidal interactions between the neutron stars, which influence the merger dynamics, and imprint tidal information on the phase of the emitted gravitational waves. With dramatic increases in detector sensitivity anticipated, measurement accuracy will increase and currently undetectable features of the late inspiral and merger will be unveiled. To prepare for this, it is essential to: (i) quantify the tidal measurements that can be expected from future detectors (ii) develop accurate, efficient and flexible tidal waveform models and (iii) assess the impact of assumptions on the resulting measurements. These are the key aims of this thesis. Firstly, we investigate the prospects of measuring higher order resonant tides with third generation detectors. Secondly, we develop a tidal waveform model for binary neutron star systems which provides efficiency whilst making minimal assumptions on nuclear matter. Finally we assess the validity of approximate equation of state independent relations within gravitational wave analysis in the context of exotic matter.

Acknowledgments

Throughout the course of my PhD, I have undergone a great amount of professional and personal growth, and I would like to thank those who accompanied me in this portion of my life.

Firstly I would like to thank my supervisor Dr. Patricia Schmidt for her support, guidance, and the knowledge she has imparted on me over these past 4 years. Also, I would like to thank Dr. Geraint Pratten for coming to the rescue whenever confusion took over. Thank you to my viva examiners Dr. Michalis Agathos and Dr Clément Bonnerot for a pleasent viva, and for supplying thoughtful comments.

Next I thank the fellow students of G26 and G27 with whom I shared highs and lows as we navigated PhD life, one pub club to another. To Daria and Evan, we started in COVID together, thank you for seeing it though with me. To Alice for letting me close the blinds when the Sun was too strong, but mostly for listening to my rants, muddling through gravitational wave physics, and being a constant friend. To Penny for always being supportive, encouraging me to believe in myself and always being a close friend to call. Especially to Lucy, forever my big sister in gravitational waves - may we be bad influences on each other forever.

To Sophie and Sophie, for making my years in undergrad lectures so enjoyable I stuck around.

To Martin, thank you for making me laugh. To Ruth, thank you for always being my best friend - I hope to someday be as good as the person you see in me. To Stuart,

for going from a nemesis to a close friend. To Mum, always a phone call away for unconditional support. And particularly to Dad whom I have called upon countless times for his professional insight but also his personal advice and comfort. To Dunoon, for always being a safe refuge only one Calmac journey away. Thank you to Toad for seeing me start this journey, and Banjo for seeing me finish it.

This thesis was written on the narrowboat *'Fosse'* whilst travelling the canal and waterways system of the UK. Chapter 1 was written during a prolonged breakdown at High Offley on the Shropshire Union canal, Ch. 2 was written on the Llangollen canal, Ch. 3 on the Bridgewater canal, Ch. 4 on the Peak Forest canal, Ch. 5 on the Trent and Mersey canal and Ch. 6 on the Oxford canal. So I want to dedicate a line of thanks for the ducklings, countryside pubs, River Canal Rescue (6 times), chippies, and countless hours of distraction playing the fiddle. And finally thank you to Roo, my travel and life companion. Your unwavering love, support, and patience has kept me steady throughout this PhD. No matter where we find ourselves, you always make our lives more vibrant and fulfilling. From Glasgow to Birmingham and beyond.

Contents

List of Figures

List of Tables

Acronyms

BBH Binary Black Hole

BNS Binary Neutron Stars

BH Black Hole

CBC Compact Binary Coalescence

CE Cosmic Explorer

EFE Einstein Field Equations

EOB Effective-One-Body

EOS Equation of State

ET Einstein Telescope

GR General Relativity

GSF Gravitational Self Force

GW Gravitational Wave

ISCO Innermost Stable Circular Orbit

KAGRA Kamioka Gravitational Wave Detector

LIGO Laser Interferometer Gravitational-Wave Observatory

LVK	LIGO-Virgo-KAGRA
MECO	Minimum Energy Circular Orbit
NS	Neutron Star
NR	Numerical Relativity
PN	Post-Newtonian
PSD	Power Spectral Density
QCD	Quantum Chromodynamics
SNR	Signal-to-noise ratio
SPA	Stationary Phase Approximation
TOV	Tolman–Oppenheimer–Volkoff
UR	Universal Relations
3G	Third Generation

Symbols Glossary

This glossary is provided for symbols that are repeatedly used to quickly refer to their meaning and definition

- $g_{\mu\nu}$: *Metric tensor*
- $G_{\mu\nu}$: *Einstein tensor* - Eq. (1.5)
- $T_{\mu\nu}$: *Stress-energy tensor*
- $\mathcal{Q}$: *Quadrupole moment*
- m_1, m_2: *Binary component masses* where $m_1 > m_2$
- $M = m_1 + m_2$: *Binary total mass*
- $q = m_1/m_2$: *Binary mass ratio*
- $\eta = q/(q+1)^2$: *Symmetric mass ratio*
- $\mu = m_1 m_2/M$: *Reduced mass ratio*
- $\mathcal{M}_c$: *Chirp mass* - Eq. (3.1)
- z: *Redshift*
- D_L: *Luminosity distance*
- $\alpha, \delta, \Psi, \iota$: *Right ascension, declination, polarisation angle, inclination* - Fig. 1.3

- t_c: *Time of coalescence*
- $h, h_+, h_\times$: *Gravitational wave strain, plus polarisation, cross polarisation* - Eq. (1.32), Fog. 1.1
- ${}_{-2}Y_{\ell m}$: *Spin -2 weighted spherical harmonic* - Eq. (1.36)
- P, ρ, ϵ - *Pressure, density, energy density*
- $\lambda_\ell, \sigma_\ell$: *Electric tidal deformability, magnetic tidal deformability* - Eqs. (2.6), (2.7)
- k_ℓ, j_ℓ: *Electric Love number, magnetic Love number* - Eqs. 2.8, 2.9
- $\Lambda_\ell, \Sigma_\ell$: *Dimensionless electric Love number, dimensionless magnetic Love number* - Eqs. (2.10), (2.11).
- Λ_s, Λ_a: *Symmetric and anti-symmetric tidal deformabilities* - Eqs. (2.15), (2.14)
- ω_ℓ, f_ℓ: *Oscillation mode frequency* $\omega_\ell = 2\pi f_\ell$
- $\mathcal{M}, \mathcal{MM}$: *Match , mismatch* - Eqs. (1.40), (1.42)

Chapter 1

Gravitational Waves

In this chapter we introduce those aspects of gravitational waves which are relevant to this thesis. In Sec. 1.1 we recap the key foundations of General Relativity and the consequence of gravitational waves. In Sec. 1.2 we explore the pertinent astrophysical sources of gravitational waves, and in Sec. 1.3 we give an overview of the detection of gravitational waves with current ground based interferometers. In Sec. 1.4 we introduce the waveform decompositions which are utilised throughout this work, and in Sec. 1.5 we outline methods for verifying waveform accuracy. Finally in Sec. 1.6 we detail the process of determining the source properties of a gravitational wave signal through parameter estimation.

This chapter is a summary of the field of gravitational waves and contains no original material.

1.1 General Relativity: An overview

General relativity (GR) [17] is often regarded as an infamously difficult topic in physics, and its reputation has put many undergraduates off taking it as a course.

In fact Eddington was once asked *"Professor Eddington, is it true that only three people in the world understand Einstein's Theory?"* to which he replied *"Who is the third?"*. However, since Eddington's time, there have been many textbooks written and various approaches to learning GR devised, leaving us with a plethora of literature on the subject [18–24]. Therefore, we will not be deriving GR from first principles here and unnecessarily adding to this library. Instead we point the reader towards these popular and well explained textbooks on GR. We will, however, provide an overview of those parts of GR that are pertinent to the contents of this thesis, namely the generation of gravitational waves (GWs) [25] where we will closely follow the derivation and conventions laid out in Ref. [18]. The aim of this section is not to provide full derivations, but point out important milestones along the path of derivation. Firstly we will refresh the reader on some notation and mathematical preliminaries in Sec. 1.1.1, before laying out the foundations and main findings of GR in Sec. 1.1.2, the following natural consequence of GWs in Sec. 1.1.3, and finally the generation of GWs at the source 1.1.4.

1.1.1 Preliminaries

Throughout this section we will use Einstein summation notation to denote contraction of tensors

$$A_\alpha B^\alpha = \sum_{\alpha=0}^{3} A_\alpha B^\alpha \tag{1.1}$$

for which Greek letters denote spacetime coordinates {0,1,2,3} and Latin letters denote spatial coordinates {1,2,3} within tensors and vectors. We use (-,+,+,+) sign convention for the metric signature.

Spacetime is described as a four dimensional differentiable manifold known as a

pseudo-Riemann manifold M, on which a symmetric tensor g acts as the metric, fully describing the curvature of the manifold and thus the structure of spacetime. The metric therefore allows us to obtain a distance, or line element, on the manifold

$$ds^2 = g_{\mu\nu} dx^\mu dx^\nu \tag{1.2}$$

The coefficients of the metric in the above above expression rely on the choice of coordinates, and with an appropriate choice the metric can always be described as locally flat. In the case of flat Minkowski spacetime the metric is given as

$$g_{\mu\nu} \equiv \eta_{\mu\nu} = \text{diag}(-1, 1, 1, 1) \tag{1.3}$$

as per our choice of sign convention.

Throughout this thesis we will use the geometric units $G = c = 1$, which can be converted to physical units with $M_\odot \approx 5 \times 10^{-6}$ s.

1.1.2 General Relativity

With the notation for describing spacetime established, we can briefly revisit the founding principles that ultimately lead to the Einstein field equations (EFEs). The goal here is to connect the curvature of spacetime with the matter it contains.

Galileo's famous experiment at the Leaning Tower of Pisa showed, in GR terminology,

"Freely falling particles move on timelike geodesics of spacetime".

Here, free-falling refers to particles unaffected by forces other than gravity, timelike implies possible causality between events (any path that allows for speed less than

the speed of light), and the geodesic is by definition the path on which free-falling particles move. Today this principle is known as the *Weak Equivalence Principle*, named so because it concerns the motion of objects under gravity alone. In Minkowski spacetime the geodesic is a straight line in an inertial frame. In another chosen frame though, this may no longer be true, though it will always follow its geodesic regardless. This is an important postulate in special relativity, and the goal is to extend this to the framework of GR. The general form of the Galilean principle, or *Einstein's equivalence principle* is then

> *"Any local physical experiment not involving gravity will have the same result if performed in a freely falling inertial frame as if it were preformed in the flat spacetime of special relativity".*

This is the guiding principle that governs GR. By postulating a law linking the gravitational field to the metric we can combine this with Einstein's equivalence principle to arrive at the EFEs. A sensible starting point for postulating a gravitational law is Newton's law of gravitation

$$\nabla^2\phi(r) = 4\pi G\rho(r) \tag{1.4}$$

for gravitational field ϕ and mass density ρ at radial distance r from a point source. Not only is this a starting point, but we should also expect any theory to reduce back to Eq. (1.4) in the limit of weak gravity. It would appear from Newton's Law that the source of the gravitational field is ρ, however this is not meaningful relativistically. Therefore we must choose another source of the gravitational field that reduces to ρ in weak gravity. This takes the form of the stress-energy tensor $T^{\alpha\beta}$, for which $T^{00} = \rho$ as required.

When applying Einstein's equivalence principle with this description of the source of the gravitational field and the requirement of the Newtonian limit, one can (eventually) reach the EFEs

$$G_{\mu\nu} \equiv \underbrace{R_{\mu\nu}}_{\substack{\text{Ricci}\\ \text{tensor}}} - \frac{1}{2}\underbrace{R}_{\substack{\text{Ricci}\\ \text{scalar}}} g_{\mu\nu} = 8\pi \underbrace{T_{\mu\nu}}_{\substack{\text{Stress-energy}\\ \text{tensor}}} . \tag{1.5}$$

Let us take a moment to dissect this fundamental result. Firstly concentrating on the left hand side, we have various contractions of the *Riemann curvature tensor* $R^{\mu}_{\ \alpha\beta\gamma}$ which encapsulates the curvature of spacetime

$$R^{\mu}_{\ \alpha\beta\gamma} = \Gamma^{\mu}_{\ \beta\sigma}\Gamma^{\sigma}_{\ \gamma\alpha} - \Gamma^{\mu}_{\ \gamma\sigma}\Gamma^{\sigma}_{\ \beta\alpha} + \partial_{\beta}\Gamma^{\mu}_{\ \gamma\alpha} - \partial_{\gamma}\Gamma^{\mu}_{\ \beta\alpha} , \tag{1.6}$$

with *Christoffel symbols*

$$\Gamma^{\alpha}_{\ \mu\nu} = \frac{1}{2} g^{\alpha\beta}(\partial_{\mu} g_{\nu\beta} + \partial_{\nu} g_{\mu\beta} - \partial_{\beta} g_{\mu\nu}) . \tag{1.7}$$

The contraction on the first and third indices of the Riemann curvature tensor $R^{\mu}_{\ \alpha\beta\gamma}$ gives the *Ricci tensor*

$$R_{\alpha\beta} = R^{\mu}_{\ \alpha\mu\beta} , \tag{1.8}$$

and further contraction of the Ricci tensor with the metric gives the *Ricci scalar*

$$R = g^{\alpha\beta} R_{\alpha\beta} . \tag{1.9}$$

The left hand side of Eq. (1.5) may seem complicated on first glance, but in reality as shown above it can be solely computed with the metric.

While the left hand side of Eq. (1.5) describes the curvature of space, the right hand

side encapsulates the matter within the stress-energy tensor $T_{\mu\nu}$. From this equivalence in (1.5) we can mathematically infer the statement made by John Wheeler

"Matter tells space how to curve, and space tells matter how to move." [26],

where the stress-energy tensor $T_{\mu\nu}$ is both the source and the consequence of the curvature of spacetime.

Highlighting that Eq. (1.5) is in 4 dimensional space, we see that it is not one equation, but 10 (due to symmetry) coupled equations which can be infamously difficult to solve. Therefore although EFEs allow coordinate freedom, it is advantageous to make wise choices when deciding upon coordinate systems, or risk creating a mathematical headache. We will next choose our coordinates wisely to show that GWs are a natural consequence of this relationship between spacetime curvature and matter.

1.1.3 Gravitational radiation

Fortunately, we reside in what is known as the weak field regime. This is one in which spacetime is 'nearly' flat, and hence why special relativity and Newtonian gravity are adequate approximations for everyday life. Therefore when considering the effects of GR, we can consider a metric that is 'nearly' Minkowski with a small perturbation $h_{\mu\nu}$

$$g_{\mu\nu} = \eta_{\mu\nu} + h_{\mu\nu} \tag{1.10}$$

where we quantify 'small' as $|h_{\mu\nu}| \ll 1$. This defines linearised gravity, as we will only retain terms linear in $h_{\mu\nu}$ through this approximation.

Before we place this metric into the EFEs, we are free to make our choice of coordinates, or gauge. We find that our problem simplifies considerably if we choose the

Lorenz gauge condition for which

$$\partial^{\mu}\bar{h}_{\mu\nu} = 0 \tag{1.11}$$

where $\bar{h}_{\mu\nu}$ is the trace reversed metric perturbation

$$\bar{h}_{\mu\nu} = h_{\mu\nu} - \frac{1}{2}\eta_{\mu\nu}h \tag{1.12}$$

for which h is the trace $h = h^{\mu}_{\ \mu}$. The trace reversed metric is so called because $\bar{h} = \bar{h}^{\mu}_{\ \mu} = -h$ and therefore the inverse is

$$h_{\mu\nu} = \bar{h}_{\mu\nu} - \frac{1}{2}\eta_{\mu\nu}\bar{h} \tag{1.13}$$

Substituting Eq. (1.10) with the Lorenz gauge (Eq. (1.11)) using properties (1.12) and (1.13), one may finally arrive at

$$\left(-\frac{\partial}{\partial t^2} + \nabla^2\right)\bar{h}_{\mu\nu} = -16\pi T_{\mu\nu}\ . \tag{1.14}$$

For now we are interested in the effect of GWs here at Earth, so we consider a distance far away from the source of the field. Therefore we can take $T_{\mu\nu} = 0$ to find that in a vacuum

$$\left(-\frac{\partial}{\partial t^2} + \nabla^2\right)\bar{h}_{\mu\nu} = 0\ . \tag{1.15}$$

This is immediately recognisable as a wave equation. Therefore we can show that a possible complex solution to (1.15) is

$$\bar{h}_{\mu\nu} = A_{\mu\nu}\exp(ik_{\alpha}x^{\alpha}). \tag{1.16}$$

We next impose another gauge condition (whilst staying in the Lorenz class of gauges) called the transverse-traceless gauge. This imposes $\bar{h} = 0$ which results in

$$\begin{aligned} \bar{h}_{\mu\nu} &= h_{\mu\nu} \ , & &\textbf{Traceless} \\ h_{0i} &= 0 \ . & &\textbf{Transverse} \end{aligned} \tag{1.17}$$

When combining the transverse-traceless gauge Eqs. (1.17) with the Lorenz gauge condition (1.11) we find

$$\begin{aligned} \partial^0 h_{00} &= 0 \ , \\ \partial^i h_{ij} &= 0 \ . \end{aligned} \tag{1.18}$$

This shows that $h_{\mu\nu}$ is purely spatial, and when assuming the wave propagates along the z axis only two independent elements are left within the GW

$$h_{\mu\nu} = \begin{pmatrix} 0 & 0 & 0 & 0 \\ 0 & h_{xx} & h_{xy} & 0 \\ 0 & h_{xy} & -h_{xx} & 0 \\ 0 & 0 & 0 & 0 \end{pmatrix} \ , \tag{1.19}$$

where $h_{xx} = -h_{yy} \equiv h_+$ and $h_{xy} = h_{yx} \equiv h_\times$ are the *plus polarisation* and *cross polarisation*, and form an orthogonal basis on which GWs affect spacetime. Physically, this indicates that the GWs affect the plane perpendicular to the direction of travel. Note here that Einstein's Equivalence Principle states that physics is the same in every coordinate system - thus the conclusion that GWs only have two polarisations is true

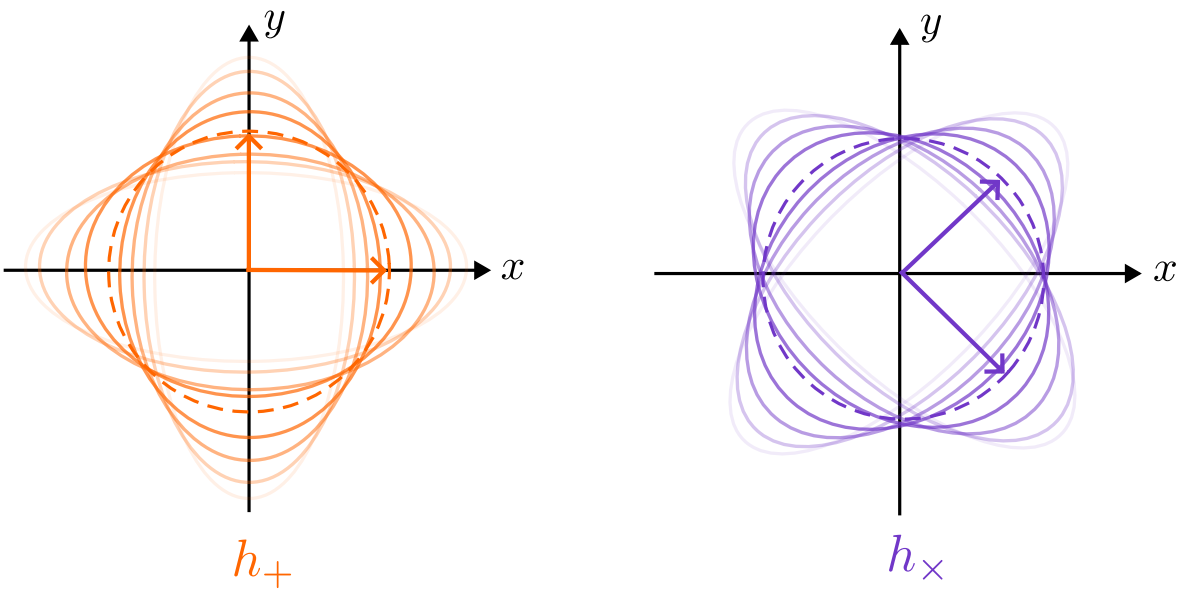

Figure 1.1: Visualisation to show the two GW polarisations h_+ (left) and $h_\times$ (right) on a ring of free particles (dashed lines). The motion of this ring is shown (concentric lines), alongside the direction of the basis vectors for each polarisation which we use in Fig. 1.3.

for any gauge choice. The transverse-traceless gauge merely paints this clearly and makes the mathematics less cumbersome.

These polarisations correspond to the fluctuation in spacetime and equivalently change proper distance between free particles. When considering a ring of free particles on the $x - y$ plane, the h_+ polarisation changes separation maximally along the lines of $x = 0$ and $y = 0$ lines, and the $h_\times$ polarisation on the lines of $x = y$ and $x = -y$. This is visualised in Fig. 1.1.

1.1.4 Generation of gravitational waves

When considering the effect of GWs at a distance far away from the source, we took $T_{\mu\nu} = 0$ in Eq. (1.14). However, we're also interested in the generation of GWs

from the source. When considering the general case $T_{\mu\nu} \neq 0$ one can arrive at

$$\bar{h}_{\mu\nu}(t, \vec{x}) = 4 \int d^3x' \frac{T_{\mu\nu}(t' = t - |\vec{x} - \vec{x}'|, \vec{x}')}{|\vec{x} - \vec{x}'|} \tag{1.20}$$

where $t = x^0$ and $\vec{x} = \{x^1, x^2, x^3\}$. In the limit of a weak source at large distance r, we can find the *Quadrupole formula*

$$h_{ij} = \frac{2}{r} \ddot{\mathcal{Q}}_{ij}(t - r) \tag{1.21}$$

where $\mathcal{Q}$ is the reduced quadrupole moment

$$\mathcal{Q}_{ij} \equiv \int \rho \left(x_i x_j - \frac{1}{3} r^2 \delta_{ij} \right) d^3x \tag{1.22}$$

Therefore GWs are produced by a time-varying mass quadrupole moment – in short, an accelerating mass. No lower order multipole solutions are allowed, as mass conservation forbids monopole radiation, and conservation of momentum forbids dipole radiation.

1.2 Astrophysical sources of gravitational waves

When considering accelerating masses as the source of GWs, there may seem to be an overwhelming amount of possibilities. However, we want to consider sources that stand a chance of being detectable. These fall into broad categories [27, 28]:

- *Compact Binary Coalescences* (CBCs): These form the population of binaries that have been detected to date [29] containing black holes (BHs) and neutron stars (NSs) in their various combinations: binary black hole (BBH) systems, binary neutron stars (BNS) systems and neutron star - black holes (NSBH) systems.

These are the sources this thesis is concerned with, specifically BNS systems.

- *Bursts*: This encompasses all transient GW sources such as core-collapse supernovae. Here the signal would appear as a momentary excess of power from the detector.

- *Continuous Waves*: These are GWs of fixed frequency, and in the context of current detectors corresponds to isolated spinning NSs. For a fully smooth and symmetrical spinning NS, there would be no GW emission expected due to a non changing mass quadrupole. However if there is a presence of 'mountains' or non-uniformity in the NS, there would indeed be GW emission. The lack of GW detection from continuous waves from known electromagnetic pulsars have placed an upper limit of these 'mountains' of $\lessapprox 1\,\mathrm{mm}$ [30, 31].

- *Stochastic Background*: A stochastic background of GWs is expected from both cosmological and astrophysical sources. Primordial GWs from the inflation period following the Big Bang are expected to leave a stochastic background of GWs with a frequency on the order of $1/\tau_{\mathrm{Hubble}}$ given Hubble time τ_{Hubble}. In addition, there is also a background of stellar binaries far from merger which has been recently detected through pulsar timing arrays NANOGrav [32, 33], EPTA[34] and CPTA [35].

1.2.1 Compact binary coalescences

Let us apply the quadrupole formula from Eq. (1.21) to a CBC of two compact objects of masses m_1, m_2 where $m_1 > m_2$. We work in source frame Cartesian coordinates $(x^S, y^S, z^S) \equiv (x, y, z)$ and confine the orbit to the $x^S - y^S$ plane. The binary has total mass $M = m_1 + m_2$, with components at separation R and distance r from the observer

in the simple setup shown in Fig. 1.2. We will follow a simple example here, assuming no *radiation reaction* (loss of energy due to GW emission) and a flat spacetime. In practice neither of these are true for a binary system, which will back-react on the spacetime and inspiral due to energy losses. However at large separations we can use these assumptions to gain a rough estimate of the magnitude of GWs from a binary system. As we consider the system as a whole, we will make use of the *binary reduced mass* $\mu = m_1 m_2/M$. From Eq. (1.22) it follows that:

$$\begin{aligned} \mathcal{Q}_{xx} &= \mu R^2 \left(\cos^2(\omega_{\rm orb}(t)) - \frac{1}{3} \right), \\ \mathcal{Q}_{yy} &= \mu R^2 \left(\sin^2(\omega_{\rm orb}(t)) - \frac{1}{3} \right), \\ \mathcal{Q}_{xy} = \mathcal{Q}_{yx} &= \mu R^2 \left(\sin(\omega_{\rm orb}(t)) \cos(\omega_{\rm orb}(t)) \right), \end{aligned} \tag{1.23}$$

then from the Quadrupole formula (Eq. (1.21))

$$\begin{aligned} h_{xx} = h_+ &= A \cos(2\omega_{\rm orb}(t-r)), \\ h_{xy} = h_\times &= A \sin(2\omega_{\rm orb}(t-r)), \end{aligned} \tag{1.24}$$

where

$$A = \frac{4\mu R^2 \omega_{\rm orb}^2}{r}. \tag{1.25}$$

This tells us that the GW frequency emitted is twice the orbital frequency $\omega_{\rm GW} = 2\omega_{\rm orb}$, and gives us a rough estimate of the amplitude we can expect of an inspiraling binary. Using GW170817 [36] as an example at a distance of 40Mpc and masses of around $1.4 M_\odot$, this corresponds to an amplitude (strain) of 10^{-21}. Notice that this is dimensionless by definition, we will next detail how this can be translated into a measurable quantity.

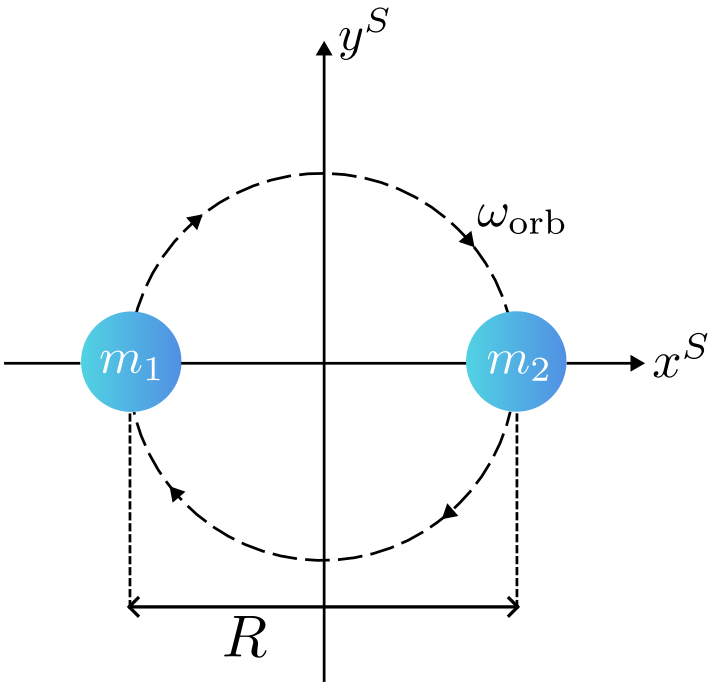

Figure 1.2: Setup of binary star system of masses m_1, m_2, separation R and orbital frequency ω_{orb} on the source frame $x^S - y^S$ plane.

1.3 Detection of gravitational waves

When Einstein theorised GWs, he did not anticipate that they would ever be detectable. However the discovery of the first GW observation GW150914 [37], proved that GWs are out there and detectable. This landmark event was made possible with the LIGO Livingston and Hanford detectors [38, 39], and since the detection of GW150914 there have been over 100 CBCs detected, whilst in conjunction the Virgo [40, 41] and KAGRA [42–44] detectors have joined the worldwide network of GW detectors in 2017 and 2021 respectively. Though these detectors all differ substantially in design, they are all based upon Michelson interferometers [45] with Fabry-Pérot cavities. Physically these detectors are comprised of two arms in an 'L' shape, each one several kms long. The differential change in proper length of the light path along

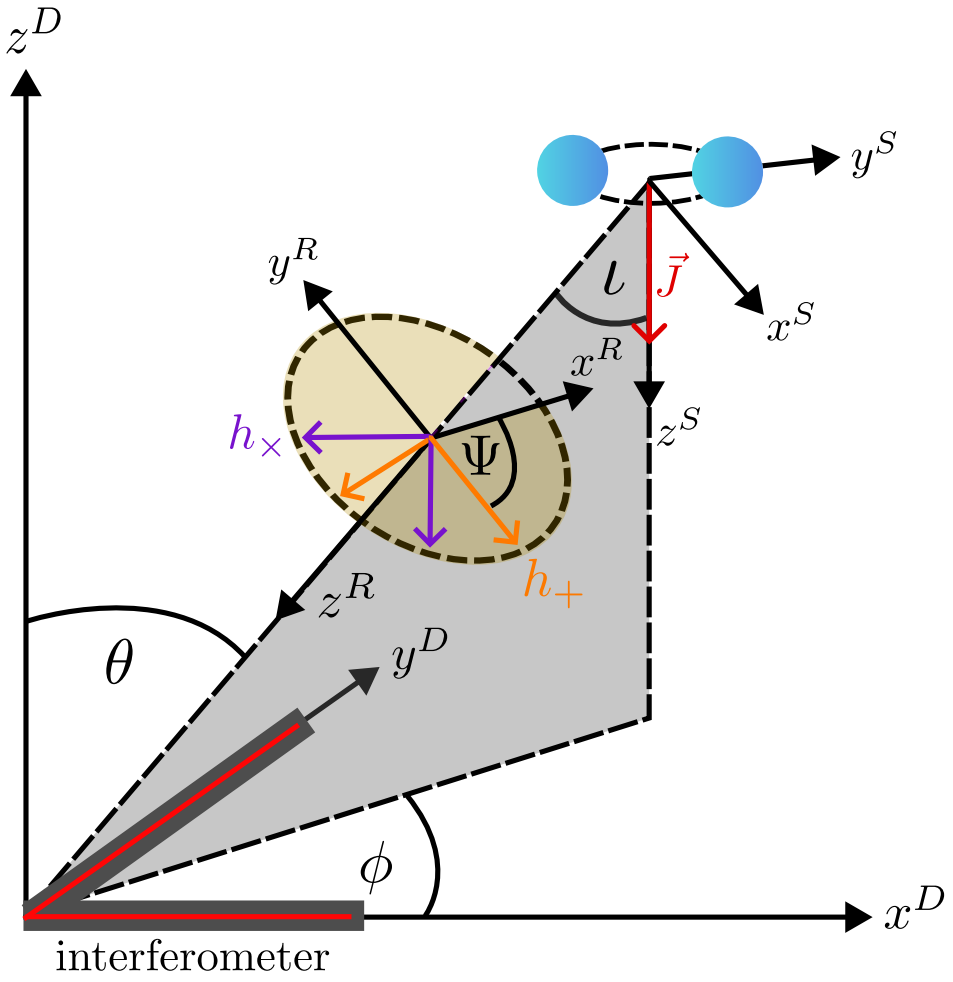

Figure 1.3: Schematic showing the relative orientation between the *detector frame* (x^D, y^D, z^D), *source frame* (x^S, y^S, z^S) and *radiation frame* (x^R, y^R, z^R). The detector frame is defined by the arms of the L shaped detector on the $x^D - y^D$ plane with the z^D axis along the zenith, with the GW source located at polar and azimuth angles (θ, ϕ). The source frame is defined by the orbital plane of binary on the $x^S - y^S$ plane, with the orbital angular momentum $\vec{J}$ directed along the z^S axis. The radiation frame is defined with the z^R axis along the line of sight between the source and the detector, and plane $x^R - y^R$ is defined as the $x^D - y^D$ plane after rotation (θ, ϕ). The remaining degree of freedom is the rotation around z^R which is defined by the polarisation angle Ψ: the angle between the basis vector which defines the h_+ GW polarisation axis and x^R. The inclination angle ι is the angle between $z^S \equiv \vec{J}$ and line of sight z^R.

these arms signals the presence of a GW. However, to quantify this fractional change in length, we must take into account the detector orientation with respect to the source. This is visualised in Fig. 1.3 with polar angles (θ, ϕ) and polarisation angle Ψ. This is mathematically taken into account through the *detector tensor* D^{ij}. The detector tensor can be decomposed into the plus and cross polarisations given bases $e^{+}_{ij}, e^{\times}_{ij}$ to give the *detector response* functions [28]

$$F_+ = D^{ij}e^{+}_{ij} = \frac{1}{2}(1+\cos^2\theta)\cos 2\phi\cos 2\Psi - \cos\theta\sin 2\phi\sin 2\Psi, \tag{1.26}$$

$$F_\times = D^{ij}e^{\times}_{ij} = \frac{1}{2}(1+\cos^2\theta)\cos 2\phi\sin 2\Psi + \cos\theta\sin 2\phi\cos 2\Psi, \tag{1.27}$$

which is combined with h_+ and $h_\times$ to give the strain at the detector h_D

$$h_D = F_+(\theta,\phi,\Psi)h_+ + F_\times(\theta,\phi,\Psi)h_\times. \tag{1.28}$$

In practice these polar angles are often translated into right ascension α and declination δ given the position of the detector. The change in proper length L if we consider a fractional change in the x direction is then

$$L + \delta L = \int_0^L \sqrt{g_{xx}}dx = \int_0^L \sqrt{1+h_{xx}}dx \approx L\left(1+\frac{h_+}{2}\right), \tag{1.29}$$

and thus $\delta L \approx Lh_+/2$, which if given $h_+ \sim \mathcal{O}(10^{-21})$ translates to $\delta L \sim \mathcal{O}(10^{-18})$m. With such small changes in arm length, it is a feat of engineering that a population of CBCs has been detected, especially when factoring in noise sources. The given data d at the detector can be written in terms of the GW signal h with source parameters $\vec{\theta}$ and noise n

$$d(\vec{\theta};t) = h(\vec{\theta};t) + n(t)\,. \tag{1.30}$$

It is not difficult to imagine the plethora of noise sources that these detectors battle on an everyday basis. Noise such as thermal and quantum noise is ever present, whereas seismic noise fluctuates as activity changes on various timescales [46]. Given these varying sources of noise, separating them out becomes much more feasible when considered in the frequency domain, as opposed to the time domain. This translates a noisy time domain data stream into a (one-sided) *power spectral density* (PSD) $S_n(f)$ when assuming the noise is Gaussian and stationary [47] through [48]

$$\langle \tilde{n_i}^*, \tilde{n_j} \rangle = \frac{T}{2} S_n(f) \delta_{ij} \tag{1.31}$$

where $\tilde{n}$ is the Fourier transform of n and $\tilde{n}^*$ is the complex conjugate of $\tilde{n}$, the indices denote frequency bins, the inner product is given by $\langle \cdot \rangle$, T is the time duration of the signal analysed and δ_{ij} is the Kronecker delta. The PSDs for current and future detectors are shown in Chapter 4 in Fig. 4.1. In the frequency domain, sources of noise can be identified and mitigated for with greater ease, though we point the reader to Ref [47] for a full discussion of noise sources and mitigation.

1.4 Waveform decomposition

The frequency domain complex strain $\tilde{h}$ can be given in terms of orthogonal polarisations $\tilde{h}_+, \tilde{h}_\times$ as a function of GW frequency $f \equiv f_{\rm GW}$, intrinsic parameters $\vec{\theta}$ (additionally including distance), and inclination ι (as in Fig. 1.3) and phase angle φ denoting the orientation of the binary with respect to an observer

$$\tilde{h}(f, \vec{\theta}, \iota, \varphi) = \tilde{h}_+(f, \vec{\theta}, \iota, \varphi) - i\tilde{h}_\times(f, \vec{\theta}, \iota, \varphi), \tag{1.32}$$

or equivalently as an amplitude A and phase ψ

$$\tilde{h}(f, \vec{\theta}, \iota, \varphi) = A(f, \vec{\theta}, \iota, \varphi) e^{-i\psi(f, \vec{\theta}, \iota, \varphi)} \,. \tag{1.33}$$

Note that the detector response is not included here, so this is not equivalent to the strain at the detector in Eq. (1.28), where sky location is taken into account. This choice means that we may keep our waveform detector agnostic, and then decompose into $h_+, h_\times$ and fold in the detector response to obtain the strain at the detector. The negative sign in Eq. (1.32) is a choice of convention corresponding to the sign used in the Fourier transform which maps the time domain strain to the frequency domain strain,

$$\tilde{h}(f, \vec{\theta}) = \int_{-\infty}^{\infty} h(t, \vec{\theta}) e^{2\pi i f t} dt \,. \tag{1.34}$$

Therefore though we choose to work here in the frequency domain, the following relations also hold in the time domain.

It is also common in waveform modelling to separate the radial and angular dependence. This results in a spin weighted multipolar decomposition

$$\tilde{h}(f, \vec{\theta}) = \sum_{\ell=2}^{\infty} \sum_{m=-\ell}^{\ell} \tilde{h}_{\ell m}(f, \vec{\theta}) {}_{-2}Y_{\ell m}(\iota, \varphi), \tag{1.35}$$

where ${}^{-2}Y_{lm}$ is the (ℓ, m) spherical harmonic [49, 50] of spin weight $s = -2$ given by

$${}_{-2}Y_{\ell m}(\iota, \varphi) = \sqrt{\frac{2\ell + 1}{4\pi}} d^{\ell}_{m,-2}(\iota) e^{im\varphi}, \tag{1.36}$$

where $d^{\ell}_{m,-2}$ denote the small-d Wigner matrices [51]

$$d^{\ell}_{m,-2}(\iota) = \sum_{\alpha=\max(0,m+2)}^{\min(\ell+m,\ell+2)} \frac{(-1)^{\alpha}[(\ell+m)!(\ell-m)!(\ell-2)!(\ell+2)!]^{1/2}}{(\ell+m-\alpha)!(\ell+2-\alpha)!\alpha!(\alpha-2-m)!} \times \left[\cos\frac{\iota}{2}\right]^{2\ell+m+2-2\alpha}\left[\sin\frac{\iota}{2}\right]^{2\alpha-2-m}. \quad (1.37)$$

The multipole modes can also be decomposed into a mode amplitude $A_{\ell m}$ and mode phase $\psi_{\ell m}$

$$\tilde{h}_{\ell m}(f,\vec{\theta}) = A_{\ell m}(f,\vec{\theta})e^{-i\psi_{\ell m}(f,\vec{\theta})}\,. \quad (1.38)$$

The dominant (ℓ, m) mode is the $(\ell = 2, m = 2)$ mode, subsequent modes are known as *higher order modes* which are particularly excited in systems which present asymmetry (i.e. in the presence of high mass ratio [52] or spin precession [53–58]). For aligned spin systems, GW emission is symmetric about the z-axis perpendicular to the orbial plane. This defines the direction of total orbital momentum or equivalently the orbital angular momentum. This means we can utilise the symmetry

$$\tilde{h}_{lm}(f,\vec{\theta}) = (-1)^{\ell}\tilde{h}^{*}_{l,-m}(f,\vec{\theta})\,. \quad (1.39)$$

1.5 Waveform Accuracy

When assessing the agreement between two waveforms h_1 and h_2, one can compute the match $\mathcal{M}$ defined as the time- and phase-optimised noise-weighted inner product between two waveforms given by

$$\mathcal{M}(h_1,h_2) = \max_{t_0,\phi_0}\frac{\langle h_1,h_2\rangle}{\sqrt{\langle h_1,h_1\rangle\langle h_2,h_2\rangle}}, \quad (1.40)$$

where we have maximised about time and phase shifts t_0, ϕ_0 between minimum over frequncy interval frequencies $[f_{\min}, f_{\max}]$, and utilise the *noise weighted inner product*

$$\langle h_1, h_2 \rangle = 4\,\mathrm{Re} \int_{f_{\min}}^{f_{\max}} \frac{\tilde{h}_1(f)\tilde{h}_2^*(f)}{S_n(f)} df. \tag{1.41}$$

The *mismatch* $\mathcal{MM}$ is then defined as

$$\mathcal{MM}(h_1, h_2) \equiv 1 - \mathcal{M}\,. \tag{1.42}$$

The mismatch is the quantity which we will use to quantify the agreement between waveform models, where we consider $\mathcal{MM}(h_1, h_2) < 10^{-3}$ as satisfactory agreement, which corresponds to a 0.1% disagreement. This disagreement can be attributed to the loss of *signal-to-noise ratio* (SNR) between the data d and template waveform h_i [47]

$$\rho = \sqrt{\langle d, h_i \rangle}\,. \tag{1.43}$$

1.6 Parameter estimation

So far we have discussed GW generation from a given source working forwards to the detector response. However, in practice, the objective is to work in reverse, using the detected signal to infer the parameters of the source. This is achieved through parameter estimation which uses Bayesian techniques [59, 60] to obtain the probability distribution for each parameter that defines the signal.

Bayes theorem [61] states that the posterior probability density function (PDF) of

a set of parameters $\vec{\theta}$ given the data d is

$$p(\vec{\theta}|d) = \frac{\mathcal{L}(d|\vec{\theta})\pi(\vec{\theta})}{\mathcal{Z}_d}, \tag{1.44}$$

where $\mathcal{L}(d|\vec{\theta})$ denotes the likelihood of a particular detector output given the input parameters, $\pi(\vec{\theta})$ our prior knowledge on the parameters (for example retstricting the parameters to physical values), and $\mathcal{Z}_d$ the evidence or marginalised likelihood which is defined as

$$\mathcal{Z}_d = \int \mathcal{L}(d|\vec{\theta})\pi(\vec{\theta})d\vec{\theta}, \tag{1.45}$$

and serves as a normalisation factor.

Assuming that the detector noise is stationary and Gaussian, the likelihood that the data is represented by model h given parameters $\vec{\theta}$ can be given as

$$\mathcal{L}(d|\vec{\theta}) \propto \exp\left(-\frac{1}{2}\langle d - h(\vec{\theta}), d - h(\vec{\theta})\rangle \right), \tag{1.46}$$

where we have used the noise weighted inner product Eq. (1.41). To obtain the posterior PDF of any single parameter θ_i, we may marginalise over all other parameters [59]

$$p(\theta_i|d) = \int \left(\prod_{j \neq i} d\theta_j \right) p(\vec{\theta}|d) = \frac{\int (\prod_{j \neq i} d\theta_j)\mathcal{L}(d|\vec{\theta})\pi(\theta_j)\pi(\theta_i)}{\int d\vec{\theta}\mathcal{L}(d|\vec{\theta})\pi(\vec{\theta})}. \tag{1.47}$$

The parameters included with $\vec{\theta}$ are both *extrinsic* parameters such as distance and sky location, and *intrinsic* properties of the source itself such as masses, spins and tidal parameters. Therefore this can be a high dimensional and computationally complex problem, where a typical BNS system can be described by an excess of 13 parameters. It is not possible to compute Eq. (1.44) to obtain a continuous probability distribution,

so instead we must sample points in the parameter space. The simplest solution would be to uniformly sample across the parameter space, however in 13 dimensions this is simply not feasible. Therefore parameter estimation usually employs some form of stochastic sampling, which navigates the parameter space efficiently by converging upon high likelihood points.

The most common sampling techniques used today are Markov-chain Monte Carlo (MCMC) sampling [62, 63] and nested sampling [64]. MCMC sampling uses a series of chains to "walk" around the parameter space, placing a criterion that the next position it travels to must be of a higher likelihood than its current position. This is useful for highly dimensional parameter spaces, however can struggle with multimodal likelihood distributions where chains can get "stuck" at a local maximum without converging on the global maximum.

Nested sampling instead samples from contours of constant likelihood, which corners off a section of the parameter space of high likelihood, and iteratively redraws these contours in a converging nested manner, zoning in on the global maximum. Nested sampling in general handles multimodal distributions better than MCMC, though can be computationally more expensive. Within this thesis we will exclusively use nested sampling with DYNESTY [65] as implemented in BILBY [66].

The DYNESTY [65] package uses dynamic nested sampling, which adjusts the number of samples (or *live points*) accordingly. This differs from regular nested sampling where the number of live points is constant. This allows DYNESTY to increase the density of live points in areas of high likelihood in a process called *adaptive refinement*.

The BILBY [66] package is a Bayesian inference library, primarily built for GW CBC parameter estimation. It collates all the code necessary to run parameter estimation on data in addition to mock injections. This includes generation of waveform models

(mostly through the LIGO Algorithms Library (LAL) [60]), functions to describe the likelihood and priors, samplers to run the inference, and post-processing to plot and analyse the posterior distributions.

Chapter 2

Neutron stars

In this chapter we will introduce neutron stars in the context of gravitational wave astronomy, the motivation for their study, and describe the effects that matter introduces into the gravitational wave signal.

In Sec. 2.1 we discuss the origin of neutron stars and the motivation for their study with gravitational waves. In Sec. 2.2 we introduce the neutron star equation of state and current experimental channels which are attempting to infer it. In Sec. 2.3 we discuss the matter effects that alter the GW signal, introducing adiabatic and dynamical tides. Finally in Sec. 2.4 we introduce universal relations and review a selection that we utilise within this thesis.

This chapter is a review of the current state of the field and contains no original contributions.

2.1 Introduction

The death of a star is as appropriately dramatic as the star is massive. Throughout the main sequence and red giant phase, the hydrostatic equilibrium of gravity and

radiation pressure from fusion supports the star as a stable object. However, all things must come to an end – including fusible materials in the stellar core. Once iron has been fused, its time is up, as no heavier elements can be created through stable fusion. With the radiation pressure from fusion gone, hydrostatic equilibrium fails and the star collapses inwards until another pressure halts it. For a less massive star such as our Sun ($M_{\text{progenitor}} \lessapprox 8M_{\odot}$), this will likely be electron degeneracy pressure, where the electrons from the atoms create outwards pressure on one another to support a white dwarf star. This results in the outer layers being gently released into the interstellar void. However, at higher masses ($M_{\text{progenitor}} \gtrapprox 8M_{\odot}$) the star does not go so quietly. Electron degeneracy pressure is not enough here, and the electrons and protons are forced together to form neutrons and create unstable nuclei. This pushes the neutrons out of their respective nuclei through the Pauli exclusion principle, resulting in a fluid of mostly neutrons. This contraction of the core leads to a bounce, sending a shockwave outwards and leading to a supernova - a devastating explosion that outshines all the stars in it's galaxy. The supernova blasts off the outer layers of the star, leaving behind the neutron dense core. It is then neutron degeneracy pressure which keeps this star stable: a neutron star (NS). This is a delicate line though, for if the progenitor star is even more massive ($M_{\text{progenitor}} \gtrapprox 20M_{\odot}$) there is no pressure that can save it, and it collapses into an infinitely dense singularity of no extended matter: a black hole (BH). As a result of this sequence of events, NSs contain the densest nuclear matter currently known in the universe: if the Sun was compacted into the density of a NS, it would fit comfortably inside the 11 circular bus route around Birmingham. At densities beyond nuclear saturation density $\rho_{\text{sat}} = 2.7{\times}10^{17}$ kg m^{-3}, and cold temperatures[1] [68–71], their conditions cannot be replicated

[1]NSs are cold relative to their Fermi temperature of 10^{11}K. This is seen as a reasonable assumption since NS cool quickly, 10^{8}K within a month of birth, and 10^{6}K within a million years [67].

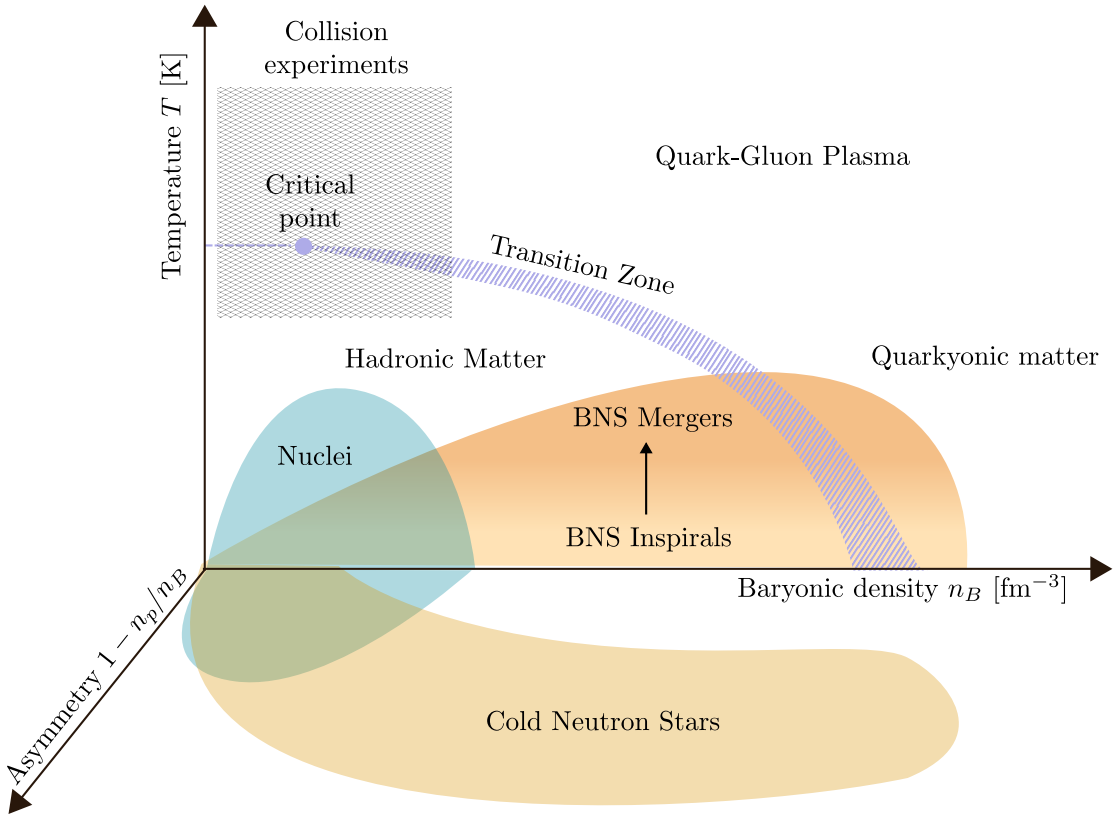

Figure 2.1: A simplified diagram of the QCD phase diagram as a function of temperature T, baryonic density n_B and matter asymmetry $1 - n_p/n_B$, where n_p is the proton density. Ordinary nuclei are shown (blue) alongside NS matter (yellow/orange), and phase transition zone (hatched purple), the critical point which separates the transition zone from a hard transition (purple dot), and high energy collision experiments (hatched black).

on Earth. Therefore NSs provide an ideal laboratory for ultra-dense nuclear physics. This is visualised in Fig. 2.1 with the quantum chromodynamic (QCD) phase diagram. The QCD phase diagram relates temperature, baryonic density and matter asymmetry. Hadronic matter is restricted to lower temperatures and baryonic densities, separated by a phase transition zone from quark-gluon plasma, and at extreme densities possibly quarkyonic matter. Collision experiments are shown at relatively low densities and high temperature, which include the Large Hadron Collider and heavy ion collision experiments [72–75]. In contrast, NSs occupy a lower temperature and extend to extreme baryonic densities. Therefore NSs occupy a unique and highly uncertain space in the QCD phase diagram. Observations of NSs have great potential to understand the behaviour of matter at extreme densities. This predicted range may even cross the transition zone, giving potential to exotic matter such as deconfined quarks [76, 77] and hyperons [78] within the NS core. Observations of BNS inspirals hold the additional potential to draw a path across the QCD phase diagram as they increase in temperature in the merger phase, possibly allowing observation of phase transitions [79]. Ultimately however, these theoretical models currently have extremely limited observational data.

Cold NSs were first observed in the form of pulsars in 1967 by Jocelyn Bell Burnell [80]. Pulsars are a sub-class of spinning NS which emit radio jets from their magnetic poles, and observationally result in extremely precise periodic pulses as the jet sweeps across the Earth. In 1974 the Hulse-Taylor pulsar-NS binary was discovered [81], which provided the first indirect evidence of GWs due to the shrinking orbit of the system. To date over 3000 pulsars have been detected, with observations not limited to radio waves, but also x-rays and gamma-rays. To glean nuclear information from NSs, we must connect microscopic properties to observational macroscopic quantities such as mass, radius and spin [70]. Pulsars inherently give a spin measurement,

as trivially from the pulses we can calculate the spin speed. Spin measurements give some information on the matter composition, as there will theoretically be a maximum break-up spin defined by the balance between gravity and the centrifugal force outwards given the composition. Beyond this break-up spin the NS cannot support itself and is ripped apart. To date, the highest spinning pulsar detected has a spin of 716 Hz [82], moving at nearly a quarter of the speed of light at the equator. Masses of pulsars are more difficult to obtain, as they require a pulsar in a binary from which redshift measurements can give upper limits on the mass. The maximum NS mass is a particularly useful quantity, as it is linked directly to the radiation pressure at the brink of stability before it collapses into a BH [83]. The largest NS mass measured from pulsars to date is $2.14 \pm^{0.20}_{0.18} M_\odot$ [1] to 95% confidence. Measuring the radius of NSs is the most challenging piece of the puzzle, and it is currently only the NICER experiment which has provided dependable electromagnetic constraints on (two) pulsars [3, 4, 84, 85].

These measurements may give upper limits on the properties of nuclear matter of cold NSs, however they are far from precise, and the inner composition of NSs is still largely unknown. However, these prospects have changed with the detection of GWs from BNS mergers. GWs hold the unique ability to constrain mass, spin and tidal information which can lead to a constraint on the currently unknown NS equation of state (EOS) [86]. In addition, GWs expose a new frontier of multimessenger astronomy since the kilonova and subsequent afterglow from the merger can be observed in several electromagnetic bands. This culminated in the landmark event GW170817 [5, 87], where constrains were made on the properties of the NSs alongside the gamma ray burst GRB170817A [88–90] and the resulting afterglow [91–96]. Aside from tidal measurements, as an electromagnetically observed event, GW170817 was able to give an independent constraint on the Hubble constant [97–102] and revealed BNS mergers

as the dominant source of r-process elements [103–106]. We point the readers towards Refs. [107–109] for detailed discussions on BNS merger electromagnetic counterparts. Over the coming decades, a rise in the rate of BNS detections is predicted [110]. With detectors increasing in sensitivity and models increasing in accuracy and efficiency, our understanding of the nuclear matter within NSs will expand. This thesis aims to contribute to these improvements, both assessing potentials with future detectors, and furthering GW BNS modelling.

2.2 The neutron star equation of state

The interior of NSs is approximated as a fluid, comprised of many fluid elements. The properties of NSs are characterised by the EOS. The NS EOS is barotropic, relating the pressure P to the density ρ (or equivalently energy density ϵ) of the NS, $P \equiv P(\rho)$. Strictly, the EOS should also include the temperature T, and matter asymmetry Y_e. However, when considering the cold matter of NSs, the entropy is assumed to be practically zero, and matter symmetry is dictated by chemical equilibrium. To translate the thermodynamic properties described by the EOS to macroscopic mass and radius we must describe the NS in GR. Considering the EFEs (Eq. (1.5)), we need two ingredients: a metric $g_{\mu\nu}$, and a stress energy tensor $T_{\mu\nu}$. The metric for a static, spherically symmetric body at radial coordinate r is given by [20]

$$ds^2 = -e^{\nu(r)}dt^2 + e^{\lambda(r)}dr^2 + r^2(d\theta^2 + \sin^2\theta\, d\phi^2) \tag{2.1}$$

The stress energy tensor of a perfect fluid is given by

$$T_{\mu\nu} = (\epsilon + P)u_\mu u_\nu + P g_{\mu\nu} \tag{2.2}$$

where u is the 4-velocity of the fluid. In the rest frame this is simply $T_{\mu\nu} = \text{diag}(\epsilon, P, P, P)$. A perfect fluid assumes no shear stress, viscosity, magnetic field, anisotropic pressure or heat conduction. Considering old NSs which have cooled to cold matter, these assumptions can be considered, which is not the case for young NSs [111]. Substituting these into the EFEs and requiring energy momentum conservation $\nabla_\nu T^{\mu\nu} = 0$, results in the relativistic equations of hydrostatic equilibrium, otherwise known as the Tolman–Oppenheimer–Volkoff [112] (TOV) equations

$$\frac{dP}{dr} = -\frac{1}{r^2}\frac{(\rho + P)(m(r) + 4\pi r^3 P)}{1 - \frac{2m(r)}{r}}\,, \tag{2.3}$$

$$\frac{dm}{dr} = 4\pi r^2 \epsilon(r)\,, \tag{2.4}$$

where $m(r)$ is the total mass contained inside radius r, and ϵ is the energy density.

The TOV equation allows us to translate a given EOS into a mass - radius relationship. A selection of EOS alongside their mass radius relationship is shown in Fig. 6.1. The density is synonymous with the depth within the NS, where the inner crust and core is shown. The EOSs generally align with one another at lower densities within the crust, however they diverge at the higher densities within the core. This corresponds to the highest uncertainties which lie in the EOS within the core. While these divergences may appear small, they have dramatic effects on the macroscopic makeup of the NS, as demonstrated by the corresponding mass radius curves. EOSs that tend towards lower radii are labelled *soft* EOS, and physically translate to higher compactness and lower tidal deformation. In contrast, EOSs that tend towards higher radii are labelled *stiff* EOS, and physically translate to lower compactness and higher tidal deformation.

EOS models are diverse in their matter composition, encompassing hadronic matter [113–117], hyperonic matter [118, 119], quark matter [120], exotic matter (such as

boson condensates [121–123] and dark matter [124–126]), and hybrid models which separate hadronic and quark matter with a phase transition [127]. For a more comprehensive review of EOS matter composition, we point the reader towards Ref. [69]. Many of these models are highly complex, with a large number of parameters. Therefore it is also common to use phenomenological EOS models, which have much fewer parameters and although may give less information on the microscopic physics, provides a stepping stone between complex models and achievable observational constraints. One widely used category of parameterised model is the *piecewise polytrope* [16] EOS, which divides the EOS above a density ρ_0 into density intervals $\rho_0 < \rho_1 < \rho_2 < ...$ each described by parameters K_i, Γ_i in a polytropic equation such that

$$P(\rho) = K_i \rho^{\Gamma_i}, \qquad \rho_{i-1} \leq \rho \leq \rho_i \tag{2.5}$$

where continuity must be ensured across the density range considered. Therefore for an EOS with 3 density intervals, only 6 parameters are required, which can be systematically varied to cover a wide range of matter compositions. Therefore piecewise polytropes can phenomenologically model more complex tabulated EOS, as well as covering more sparse parts of the parameter space.

Current constraints on the NS EOS come from various channels, which can be combined as shown in Fig. 2.3. A few notable examples are:

1. Radio and X-ray observations

   (a) *Pulsar radio timing measurements:* Radio pulsars as we have mentioned, may give NS mass estimates, however do not well constrain the radius and can thus provide limited EOS information. This is shown in Fig. 2.3 with two particularly massive pulsars [1, 2], which give an upper limit on the NS

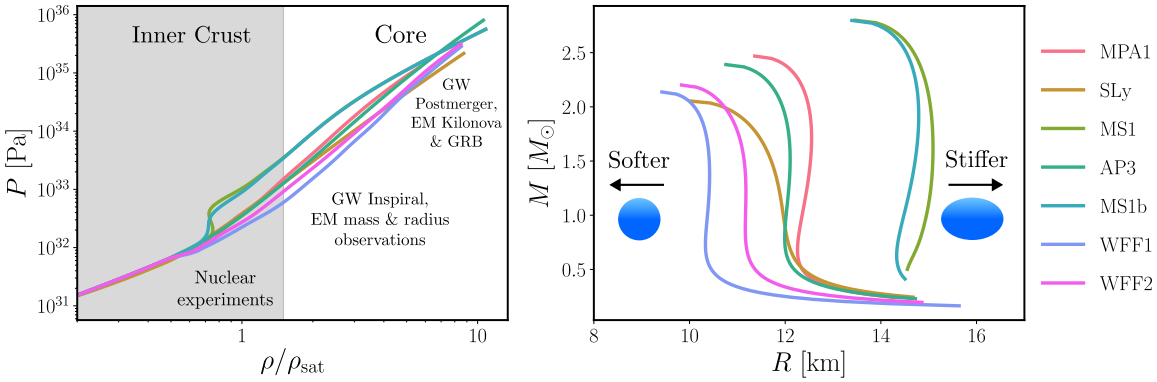

Figure 2.2: Various EOS *Left panel*: EOS as a function of pressure P and density ρ in terms of the nuclear saturation density $\rho_{\rm sat} = 2.7{\times}10^{17}$ kg m^{-3}. The density region of the inner crust (grey shaded), and the core (unshaded) are shown alongside different sources of EOS information. *Right panel*: The corresponding mass M, radius R relationship of the EOSs, with the softer and stiffer regions labelled alongside a visual physical representation of the tidal deformation of the NS.

maximum mass of $\sim 2.5M_\odot$ to 95% confidence.

(b) *X-ray pulse profiling with NICER:* The NICER experiment allows measurements of both the mass and radius of pulsars with X-ray pulse profiling [128]. Pulse profiling exploits the fact that the X-ray emission from NSs is not thermally uniform across the surface [129–132], and folds in light bending caused by GR to make mass and radius measurements. This approach is model dependent, with the grey and green regions in Fig. 2.3 depicting constraints with two different modelling techniques [3, 4]. These differences arise from the dimensionality of the pulse profile modelling, which must take into account various geometrical parameters to describe the hot spots positioning on the NS crust, temperature variations, the magnetic field and rotational axis.

2. Nuclear physics experiments

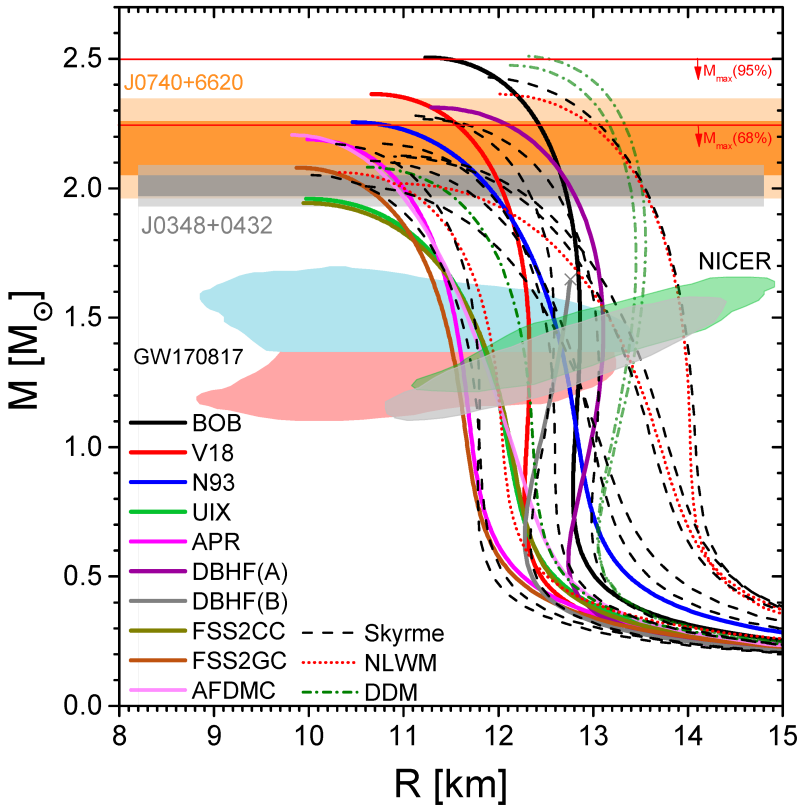

Figure 2.3: Mass radius curves of various EOS alongside observational constraints, including from pulsars PSR J0740+ 6620 [1] and PSR J0348+ 0432 [2], NICER's analysis of PSR J0030+ 0451 [3, 4], and GW170817 [5]. Different linestyles correspond to different categories of EOS. This figure was taken from [6].

(a) *Measurement of neutron skin thickness:* Typically, neutrons and protons occupy the same space within nuclei, however in neutron rich elements the neutrons extend further out to form a "neutron skin". The thickness of the neutron skin can provide a direct measure of the slope of the symmetry energy, which quantifies the energy difference between symmetric nuclear matter and asymmetric nuclear matter as a function of density. Mapping the relationship between the symmetry energy and density for neutron rich matter provides a direct NS EOS constraint, unlike mass-radius measurements. The PREX-2 [133] and CREX [134] experiments use parity-violating asymmetry in polarised electron scattering [135, 136] to measure the neutron skin thickness of ^{208}Pb nuclei and ^{48}Ca respectively, probing the EOS near nuclear saturation density.

3. BNS mergers

(a) *GW170817:* A landmark multimessenger event, GW170817 was a BNS merger which allowed observational constraints of the NS EOS though mass and tidal deformability measurements of the component NSs [137–153]. These constraints are shown in Fig. 2.3 where the blue and red shaded regions correspond to the more massive and less massive components respectively. The kilonova from BNS mergers, including from GW170817, also allows additional constraints due to the close link between luminosity and total mass [148, 154, 155]. Though there has been a further BNS merger detected, GW190425 [156] and several NSBHs [157–159], none of these yielded measurable tides or detectable electromagnetic counterparts.

These sources of data combined lead to critical information on the NS EOS. How-

ever, we observe from Fig. 2.3 that though results from NICER and GW170817 show general agreement, there is still a large uncertainty in both results, and a significant number of EOS models that satisfy both results. To further complicate issues, results from PREX-2 which favour a stiffer EOS, are at weak contention with NICER and GW170817 which both tend towards a softer EOS [160].

2.3 Tidal responses

The EOS is constrained through the effect of the tidal response of the NSs on one another, which alters the dynamics of the system and imprints on the GW phase. Here we introduce the various parameters that characterise the tidal response and are used within GW astronomy.

After years of studying physics, it becomes a common joke among students that nearly everything can be approximated as a harmonic oscillator - and BNS systems are no exception. In addition to the dominant energy losses from GWs due to the motion of the binary, a BNS system can be approximated as a driving tidal field, dampened by the loss of energy due to GWs, which enhances the rate at which the orbit shrinks compared to a system without tidal interactions [161–163]. This approach allows us to divide the inspiral into regions depending on the tidal forcing frequency (i.e. orbital frequency $\omega_{\rm orb}$) relative to the internal oscillation frequency $\omega_{2,A}$ [164] of the A-th NS as depicted in Fig. 2.4. At large separations where the tidal field is negligible, the system can be considered as *point particles*, which is equivalent to a BBH system with no matter effects coming into play. However as the NSs move closer, they begin to tidally deform one another. Initially this deformation can be treated as static *adiabatic tides* [165, 166] when $\omega_{\rm orb} \ll \omega_{2,A}$, however this approximation breaks down as the

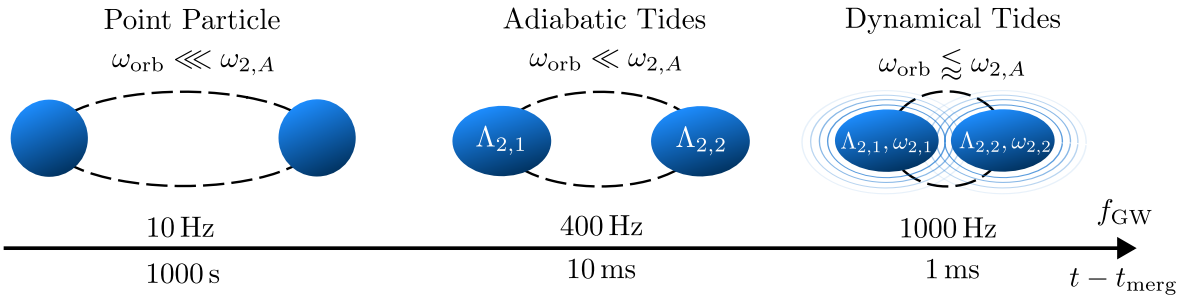

Figure 2.4: Schematic showing tidal sectors within a BNS inspiral with respect to their GW frequency $f_{\rm GW} = 2f_{\rm orb}$ or equivalently time to merger $t - t_{\rm merg}$. The dominant quadrupolar parameters which describe each sector $\Lambda_{2,A}, \omega_{2,A}$ are labelled for the A-th NS. Deformation is intended to be shown as increasing, and approach to resonance is shown with concentric lines around each NS.

system approaches resonance $\omega_{\rm orb} \lessapprox \omega_{2,A}$ and time dependency must be taken into account, giving rise to *dynamical tides* [167–170].

2.3.1 Static tides & tidal deformability

At frequencies far below the NSs internal oscillation frequencies $\omega_{2,A}$ the tidal field varies slowly, and the tidal response can be approximated as time independent and therefore quasi-static. This leads to adiabatic tides, which describes the tidal response of the system in the early inspiral.

Given that the tides are considered independent of time, the perturbed tidal field and the induced quadrupole moment can be considered as linearly proportional. This tidal field can be decomposed into an *electric* component $\mathcal{E}_L$ (even parity or polar) and *magnetic* component (odd parity) $\mathcal{M}_L$, which induces a mass multipole moment $\mathcal{Q}_L$ and a current multipole moment $\mathcal{S}_L$ respectively with multipolar index $L = i_1 i_2 ... i_\ell$ such that all components are tensors of rank ℓ. In the adiabatic limit these components

are related to their induced quadrupole moments through

$$\mathcal{Q}_L = \lambda_\ell \mathcal{E}_L \,, \tag{2.6}$$

$$\mathcal{S}_L = \sigma_\ell \mathcal{M}_L \,, \tag{2.7}$$

where we have defined the electric tidal deformability λ_ℓ and the magnetic tidal deformability σ_ℓ. In the case of BHs $\lambda_\ell = \sigma_\ell = 0$ [171, 172]. These are related to the *electric Love number* k_ℓ and *magnetic Love number* j_ℓ through

$$k_\ell = \frac{(2\ell-1)!!}{2}\lambda_\ell \,, \tag{2.8}$$

$$j_\ell = 4(2\ell-1)!!\sigma_\ell \,. \tag{2.9}$$

Love numbers [173] are a dimensionless parameter that measures the degree of static deformation of an object in response to an external tidal potential. Love numbers are not unique to GW astronomy and have been extensively used in the Newtonian case for planetary bodies. In the context of GW detection, it is useful to define tidal deformabilities as dimensionless

$$\Lambda_\ell = \frac{2}{(2\ell-1)!!} k_\ell \left(\frac{R}{M}\right)^{2\ell+1} , \tag{2.10}$$

$$\Sigma_\ell = \frac{1}{4(2\ell-1)!!} j_\ell \left(\frac{R}{M}\right)^{2\ell+1} . \tag{2.11}$$

From hereon in when referring to the tidal deformability, it should be assumed it is dimensionless unless stated otherwise, and referring to the dominant [174–176] $\ell = 2$ mode.

The electric tidal deformability [177] corresponds to the amount of physical defor-

mation of the NS induced by the static tidal field and is analogous to Newtonian tides. The magnetic tidal deformability is related to the motion of mass and "twisting" deformations and has no Newtonian analoge - it is purely a GR effect [171, 172]. Therefore, it is only at relativistic speeds or high spins that gravito-magnetic contributions become significant, and they are still generally dominated by gravito-electric effects [178]. Thus commonly in the literature and from this point forwards we will refer to electric tidal deformability simply as tidal deformability unless otherwise stated.

Larger values for tidal deformability physically correspond to higher deformation of the NS, and indicate a stiffer EOS. Conversely, lower tidal deformability indicates a softer EOS. This is visualised in Fig. 6.1. Therefore, measurement of tidal deformability for a given mass can lead directly to an EOS constraint.

The tidal deformability is obtained through calculation of the (relativistic) tidal Love number [165, 166]. This involves perturbing the metric (Eq. (2.1)) and the stress energy tensor (Eq. (2.2)) both internally and externally to the NS and solving the perturbed EFE

$$\delta G_{\mu\nu} = 8\pi \delta T_{\mu\nu} \,. \tag{2.12}$$

Boundary conditions are then enforced to ensure there exists no unphysical singularities at the centre of the NS, and there is continuity between the internal and external solutions. The tidal deformability is computed by matching the interior to the exterior g_{tt} solution in the star's local asymptotic rest frame in mass-centered Cartesian coordinates [179]

$$\frac{1 - g_{tt}}{2} = -\frac{M}{r} - 3\frac{\mathcal{Q}_{ij}}{2r^3}\left(n^i n^j - \frac{1}{3}\delta^{ij}\right) + \frac{\mathcal{E}_{ij}}{2} x^i x^j + \dots \,, \tag{2.13}$$

where $n^i = x^i/r$ denotes a unit vector. Observing that Eq. (2.13) describes both the

tidal field and induced quadrupole moment, we can follow Eq. (2.6) to extract the tidal deformability.

2.3.2 Dynamical tides

As the BNS system approaches merger and the orbital timescales inevitably approach that of the internal oscillation modes, the static assumption breaks down and time dependency must be taken into account. Therefore, we must now describe a more complex system, making the description more cumbersome, but consequently richer in physics which we can use to our advantage. The oscillation modes of a NS can be disentangled into quasi-normal modes described by spherical harmonic indices (n, ℓ, m) where each mode has an oscillation frequency $\omega_{n\ell m}$. The lowest coupling to the gravitational field (and therefore the strongest) is the quadrupolar $\ell = 2$ mode. The angular m mode is degenerate for non-rotating stars as a consequence rotation symmetry, and thus can be discarded. Oscillation modes of interest for GW detection can be categorised in the following families:

- *f-mode*: The *fundamental mode*, or f-mode is the standing waves upon the NS with $n = 0$, with no radial nodes within. This is the simplest form of oscillation, where the NS is oscillating simultaneously as a whole at its characteristic f-mode frequency $f_\ell = \omega_\ell/2\pi$. The $\ell = 2$ f_2-mode frequency is approximately proportional to the square root of the density within the NS, and has a value $f_2 \sim$1 kHz [174]. The restoring force is a combination of pressure gradient and gravity on the fluid elements.

- *p-modes*: The *pressure modes* are the overtones ($n \geq 1$) of the f-mode, and are driven by a restoring force of pressure gradients, and determined though the speed

of sound within the NS. The p-mode frequencies lie above the f-mode frequency at ∼few kHz.

- *g-modes*: The *gravity modes* are also overtones ($n \geq 1$) driven by buoyancy of the gravitational force"flattening out" perturbations in the density profile. The g-mode frequencies are lower than that of the f-mode at ~ 100 Hz. However, the g-mode couples weakly to the tidal field and thus has a negligible effect for GW detection [174].

- *r-modes*: The *Rossby modes* arise when the NS is rotating, with a restoring Coriolis force. The r-mode frequency is directly proportional (though not equivalent) to the angular frequency of the NS, meaning that it can lie at $\sim$ few 100 Hz. Again the r-mode couples weakly to the tidal field [180], and though detection GWs from isolated spinning NSs have been attempted, no detection has been found to date [181].

The mode with the strongest coupling to the tidal field is the $\ell = 2$ f_2-mode [164, 174, 175]. In the context of GW analysis it is also useful to define the dimensionless angular f-mode frequency $\Omega_\ell = m_A \omega_\ell$ for the A-th NS in a binary. The f-mode frequency is calculated similarly to the Love number, in the sense that the NS is perturbed alongside the metric using the TOV equations with appropriate boundary conditions. However, here the perturbation does not originate from an external tidal field but internal fluid oscillation. The frequency can be obtained through an eigenvalue problem, where f_2 corresponds to the real part of the complex eigenvalue, and the imaginary part corresponds to the dampening time.

For a typical BNS system, the f_2-mode frequency is too large for the resonance to

take place within the inspiral[2] [180]. However, as the orbital frequency approaches ω_2 a cumulative effect from the f_2-mode is present [165, 167, 169, 182], which accumulates to accelerate the dynamics by up to several orbits over the course of the inspiral (see Sec. 4.3.1). This is not to be confused with the f_2-mode peak in the postmerger GW signal [183–190], which corresponds to the resonance with the f_2-mode of the remnant. Independent measurement of the f_2-mode frequencies of the pre-merger components alongside measurement of the postmerger f_2-mode peak does however allow probing of the EOS of hot matter [183, 191]. We will explore this in more detail in Ch. 4.

2.4 Quasi-universal relations

Rather conveniently, there exists a set of (quasi-)*universal relations* (URs), which relate a series of NS properties to one another quasi-independently of EOS. Here we touch upon the URs utilised within this thesis, though a full account of available URs can be found in Ref. [192].

- $\Lambda_2 - \Lambda_3$: Higher-order multipole Love numbers and therefore tidal deformabilites can be related to each other [193], in particular the octopolar $\ell = 3$ (and also the hexadecapolar $\ell = 4$). This UR is shown in Fig. 2.5 and is EOS independent to $\lessapprox$10%. We will later utilise this UR in Ch. 4.

- $\Lambda_2 - \omega_2$: The tidal deformability can also be related to the f-mode frequency, known as f-Love relations [194–202]. Again this has been computed for $\Lambda_\ell - \omega_\ell$ for $2 \leq \ell \leq 4$. When considering the quadrupole UR depicted in Fig. 2.5, this UR is EOS independent to $\lessapprox$0.1%, where it only exceeds this at $\Lambda_2 > 10000$.

[2]We consider only dynamical tides for non-spinning systems, though if the NS is spinning anti-aligned to the orbital angular momentum, the f_2-mode frequency is shifted to lower frequencies in the inertial frame. Therefore with spin the system can reach f_2-mode resonance in the inspiral [180].

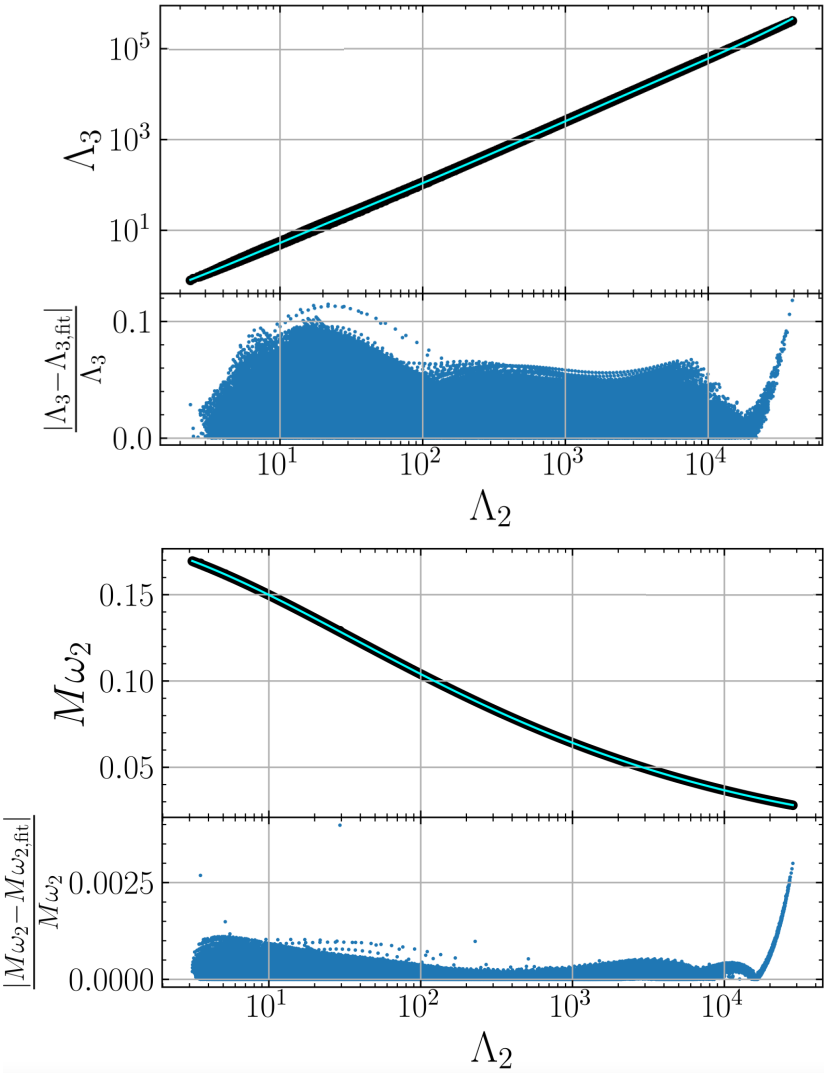

Figure 2.5: URs $\Lambda_2 - \Lambda_3$ (top) and $\Lambda_2 - \omega_2$ (bottom). The URs are shown (upper panels) with the raw data (black dots) and the fit (blue line), alongside the relative error (lower panels). This figure was adapted from Ref. [7].

- $\Lambda_a - \Lambda_s$: The *binary Love relations* [192, 193] describe the tidal deformability as a system rather than as individual NSs. This UR relates an asymmetric and symmetric combination of the individual NSs tidal deformabilities

$$\Lambda_a = \frac{1}{2}(\Lambda_{2,2} - \Lambda_{2,1}), \tag{2.14}$$

$$\Lambda_s = \frac{1}{2}(\Lambda_{2,1} + \Lambda_{2,2}). \tag{2.15}$$

  The binary Love relations are specific for a given mass ratio q, where the error increases as the masses become more unequal. The binary Love URs are particularly useful for GW parameter estimation [203] in which individual tidal defomabilities are hard to disentangle from the overall effects of tides on the dynamics. The binary Love URs are depicted in Fig. 2.6 is EOS independent to $\mathcal{O}(10)\%$. We will explore this further in Ch. 6.

URs allow the dimensionality of GW data analysis to be greatly reduced. If we consider multipoles $2 \leq \ell \leq 4$ for $\Lambda_\ell, \Sigma_\ell, \omega_\ell$ of each NS in a binary, it allows reduction from 18 parameters to up to a single Λ_s parameter, where all other parameters can be inferred with URs [204]. However, a large number of assumptions are taken into account when calculating URs, which must be considered. These assumptions include lack of a magnetic field [205], a barotropic EOS [206], pressure isotropy [207], GR [208–218] and slow rotation [219–221]. Therefore, by providing independent measurements of the NS tidal deformabilities and f-mode frequencies, and comparing to predicted values form URs, phenomena such as deviations from GR and exotic EOS models can be experimentally probed [222].

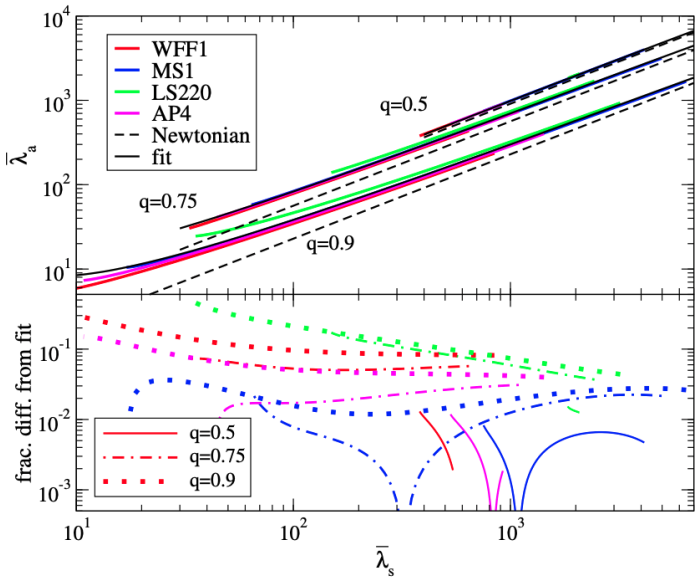

Figure 2.6: Binary Love UR presented in [8] for a selection of EOS at mass ratios $q \in \{0.5, 0.75, 0.9\}$ where Yagi & Yunes use the convention $q = m_2/m_1 \leq 1$ and notation $\bar{\lambda}_a \equiv \Lambda_a$ and $\bar{\lambda}_s \equiv \Lambda_s$. *Top*: The URs (black solid lines) with the EOS (coloured lines) and the Newtonian result. *Bottom*: The error on the UR fit for the EOS and mass ratios considered. This figure was taken from [8].

Chapter 3

Modelling binary neutron star gravitational waveforms

In this chapter, we combine Ch. 1 on gravitational waves and Ch. 2 on neutron stars together to quantify the effect of matter on gravitational waveforms and the various waveform modelling techniques currently utilised in data analysis. In Sec. 3.1 we introduce the general effect of matter and the phenomenology of binary neutron star waveforms, before listing the input parameters for the waveforms in Sec. 3.2. We then discuss the various families of binary neutron star waveform models in Sec. 3.3. We finish by introducing numerical relativity in 3.4.

This chapter is a review of the current state of binary neutron star waveform modelling and contains no original material.

3.1 Introduction

We have described how the detector responds to a gravitational wave event, working forwards from the source to the resulting change in proper length at the detector.

In practice, we work backwards from a given signal to the source parameters to make conclusions on the astrophysical origins of the event. This requires accurate waveform models, which capture the resulting strain from a source given the properties of the binary. Before we explore the details of various waveform modelling techniques, let us consider the general phenomenology of BNS waveforms, to visualise what we aim to capture. We have discussed that due to the matter content of BNS systems as opposed to BBH systems, tidal forces are exerted upon each NS to dissipate more energy, thus enhancing GW emission and accelerating the merger linked through $f_{\rm GW} = 2f_{\rm orb}$. Though thinking of this evolution in the time domain is intuitive (and indeed there are prominent time domain models), it is often more practical to think in the frequency domain. This is due to the likelihood evaluation (Eq. (1.46)) within parameter estimation requiring a noise weighted inner product (Eq. (1.41)) which natively is in the frequency domain. Therefore generating waveforms directly in the frequency domain bypasses the need to convert from the time domain which can add unnecessary computational cost. We visualise a frequency domain waveform in Fig. 3.1, which shows the real h_+ part of the waveform (Eq. (1.32)), as well as the amplitude A and phase ψ (Eq. (1.33)). This depicts a sequence of equal mass systems, with increasing tidal deformability $\Lambda_{2,1} = \Lambda_{2,2} = \Lambda$, where $\Lambda = 0$ is equivalent to the waveform of a BBH system. The point at which the amplitude drops off is the merger frequency $f_{\rm merg}$. Physically, after the merger frequency there lies a complex postmerger depending on the composition and fate of the remnant (i.e. prompt collapse, hypermassive NS, magnetar) with a plethora of physical phenomena such as turbulence, neutrino emission, thermal effects [223] and possible phase transitions. However, currently detectors are not sufficiently sensitive to the postmerger regime. Therefore the postmerger is typically modelled separately to the inspiral and merger, therefore there is no model

analogous to the BBH inspiral-merger-ringdown models for BNS mergers which include a full inspiral-merger-postmerger. Isolated postmerger models include non-parametric models for which the postmerger is analysed separately [224, 225], phenomenological postmerger models that can be attached to a chosen inspiral model for joint analysis [190, 226–228], and NR fitted models [188, 229].

Current detectors are sensitive at frequencies associated with the inspiral portion of the dynamics, with the NS merger frequency lying outside detector sensitivities at $\mathcal{O}(1000)$Hz (see Fig. 4.1 in Ch. 4). During the inspiral, it is evident from Fig. 3.1 that it is primarily the phase that is affected by the presence of matter, therefore BNS waveform modelling is focused on modelling the phase.

3.2 Parameterisations

In order to dive into the current waveform models, we first list the key parameters intrinsic to a BNS waveform:

- *Component masses*: Though a binary can be adequately described with component masses m_i for components $i = \{1, 2\}$, there are also various other parameterisations which are commonly used within waveform modelling and analysis. One such parameterisation is total mass $M = m_1 + m_2$ and mass ratio $q = m_1/m_2$ (we use the convention $q \geq 1$). Alternatively the symmetric mass ratio $\eta = q/(1+q^2)$ can also be used in conjunction with M to quantify the component masses. Another mass parameterisation is the *chirp mass* $\mathcal{M}_c$

$$\mathcal{M}_c = \eta^{3/5} M \tag{3.1}$$

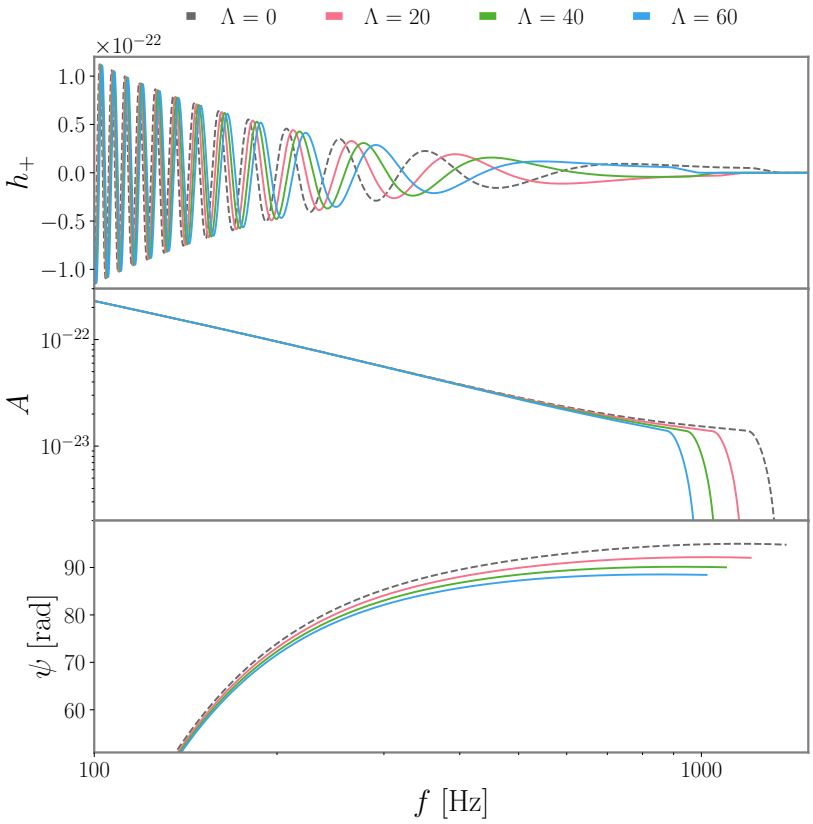

Figure 3.1: An example of a frequency domain waveform of a BNS system with $m_1 = m_2 = 5$, varying $\Lambda_{2,1} = \Lambda_{2,2} = \Lambda$. These unphysical large masses are chosen to clearly illustrate the dephasing, and thus do not represent a physical BNS system. *Top*: The real h_+ part of the waveform. *Middle*: The amplitude A of the waveform. *Bottom*: The phase ψ of the waveform. This example uses waveform model IMRPhenomPv2_NRTidalv2 [9] implemented with LAL [10].

which is derived from the leading order energy loss of the system due to GW emission and dominates the orbital evolution and thus GW frequency. This is a useful quantity as it is the mass parameter most accurately measured in GW data analysis. One important caveat to all mass measurements is that as observers, we are in the detector frame and therefore measure redshifted mass. The detector frame component mass m_i^D is connected to the source frame component mass m_i^S through

$$m^D = m^S(1+z) \tag{3.2}$$

where redshift z is a function of the distance to the source and the cosmology (i.e. the Hubble constant). This relationship similarly holds for the total mass and chirp mass.

- *Spins*: Compact objects may also have spin, where each component has spin vector $\vec{S}_i$ which is combined with orbital angular momentum $\vec{L}$ to give the total angular momentum $\vec{J}$

$$\vec{J} = \vec{L} + \vec{S}_1 + \vec{S}_2 \tag{3.3}$$

In data analysis the spin is weighted by the component mass to give the dimensionless spin

$$\vec{\chi}_i = \frac{\vec{S}_i}{m_i^2} \tag{3.4}$$

The case where $\chi_{i,z} \neq 0, \chi_{i,x} = \chi_{i,y} = 0$ (where z denotes the direction perpendicular to the orbital plane, or equivalently the orbital (total) angular momentum) is an *aligned* spin system, where $\vec{S}_i$ for both NSs is aligned (or anti-aligned) with the orbital angular momentum $\vec{L}$. As a result, the total angular momentum $\vec{J}$ is also aligned (or anti-aligned) with $\vec{L}$. The generic case where the spins are mis-

aligned with $\vec{L}$ is a *precessing* system, and results in $\vec{L}$ precessing about $\vec{J}$. To fully capture precession, 6 spins parameters are required. In comparison, aligned spin systems require only 2 components, $\chi_{1,z}, \chi_{2,z}$. Throughout this thesis we will only consider aligned spin systems, and therefore remove the z-component from the notation such that the spin parameters are given simply as χ_1, χ_2 unless otherwise stated.

- *Tides*: Without the use of URs and when only considering adiabatic quadrupolar tides, we have discussed that we can describe the tidal deformations in terms of Λ_A, Λ_B, or equivalently as symmetric and antisymmetric terms Λ_a, Λ_s (Eqs. (2.14), (2.15)). In the following section we will define and explore another parameterisation of tides used within waveform modelling: $\tilde{\Lambda}, \delta\tilde{\Lambda}$.

- *Eccentricity*: When considering CBCs in Sec. 1.2.1 we considered a circular binary. However binaries may also have non-negligible orbital eccentricity, which is also an indication that the binary was formed dynamically. Given the long inspiral time of BNSs, it is assumed for the vast majority of systems that $e = 0$ (i.e. a circular orbit) by the time they enter the detection band, as GWs radiate away eccentricity [230]. Therefore we assume quasi-circular binaries thorughout this thesis. However, we note that exploring and subset of dynamically formed BNS systems will require eccentricity built into future BNS models.

3.3 Binary neutron star waveform model families

Due to their low masses, BNS systems take a longer time to inspiral than a nominal BBH system, which makes waveform generation computationally challenging. Particularly in parameter estimation, stochastic samplers can require up to $\mathcal{O}(10^9)$ model

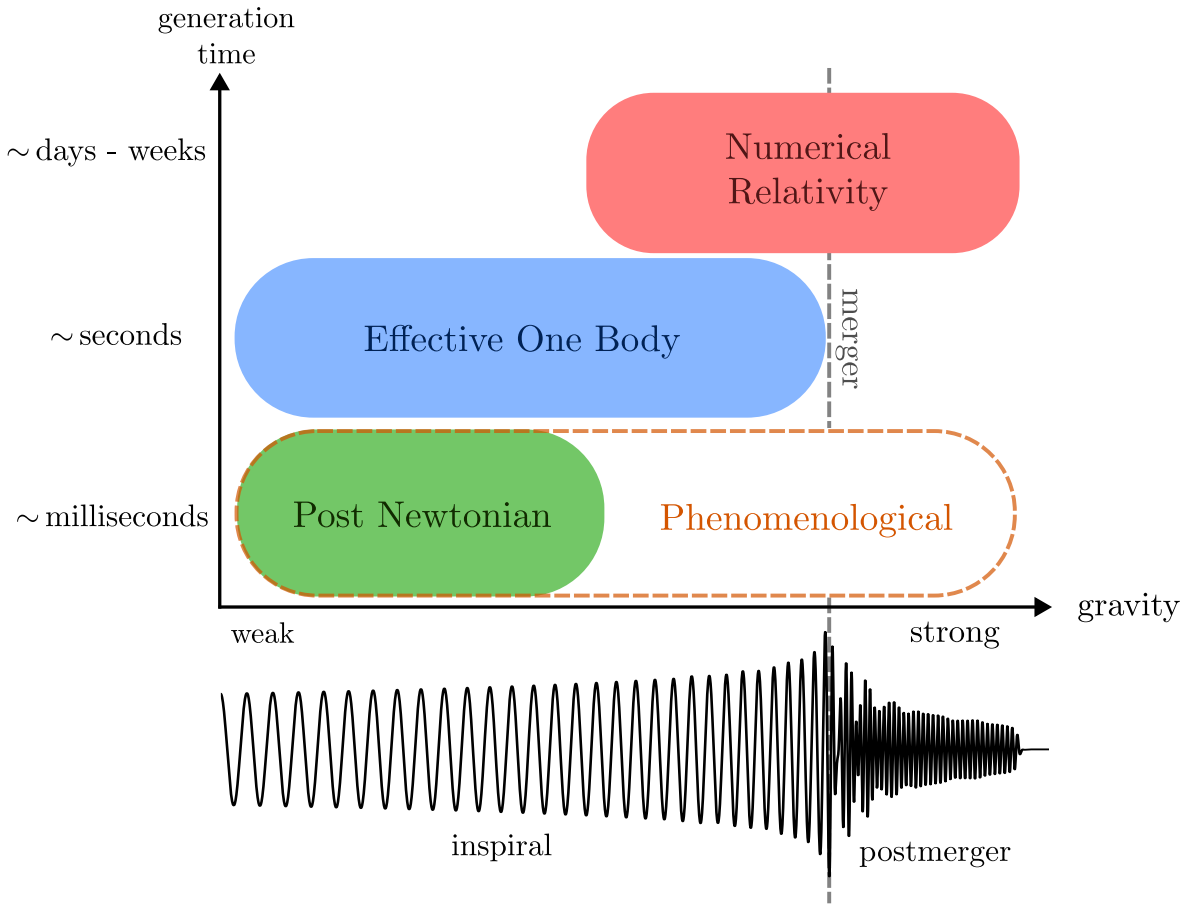

Figure 3.2: Simple schematic to show the broad families of BNS waveform modelling techniques with their viable regions of gravity and generation time. The real part of the strain of an example waveform (EOB-NR hybrid constructed from BAM 0002 [11] for the CoRe database [12] using TEOBResumS [13]) is shown to add context below, with the inspiral, merger, and postmerger labelled.

evaluations to accurately recover the source parameters. Given a realistic waveform generation time $\sim \mathcal{O}(1\text{s})$, this translates to a sampling time of 30 years! Therefore, we must also require efficiency from waveform models, without sacrificing accuracy. The main families of currently used BNS waveforms are shown in Fig. 3.2, where generation time is compared to the regime of gravity for which they are valid. Generally speaking, the stronger the gravity, the more costly the generation time. *Post-Newtonian* (PN) waveforms [231] are expansions of the EFEs in the weak-field, slow-motion limit. Therefore, PN waveforms are analytic expressions which can be evaluated quickly. However, due to the approximations of PN theory, these waveforms do not remain accurate close to merger [232–238]. The *Effective-one-body* (EOB) formalism [13, 167, 169, 239–248] extends this, by remapping the two body problem of a binary to a single particle moving in an effective spacetime. By including re-summed PN expressions and numerical relativity (NR) information, it stays accurate up to near merger. However, EOB requires iteratively solving the equations of motion, which for long BNS signals, slows the waveform generation. In the regime of merger and postmerger, currently the only way to produce fully accurate results is through numerically solving the EFEs with NR. Given the complexity of this problem with the addition of relativistic magnetohydrodynamics, this process can take weeks and extreme computing power. Linked to these families are phenomenological models, which aim to incorporate information from other modelling techniques and NR whilst speeding up the waveform generation considerably.

In this section we will discuss these modelling families[1] and touch on the specific

[1] We do not discuss *surrogate modelling* [249–256], where a large library of waveforms is interpolated across at time nodes as a function of the waveform parameters. In BBH waveform modelling this is typically done with NR waveforms, though this is not possible due for BNS waveforms due to a lack of NR simulations. However there is a BNS surrogate model [257] which is fitted to EOB model SEOBNRv4T [167, 169, 243].

BNS models utilised within this thesis.

3.3.1 Post-Newtonian waveforms

As there exists no analytical solution to the EFEs for binary systems, it is advantageous to derive an approximate analytical formalism. In the weak gravity, slow moving limit ($v \ll c$) this is achieved through PN theory [231], which expands the equations of motion beyond Newtonian order in powers of (v/c). Recalling $c = 1$, and using a Keplerian orbit

$$v = \sqrt{\frac{M}{r}} = (\pi M f)^{1/3}\,, \tag{3.5}$$

where $f \equiv f_{\rm GW}$. The accuracy of the PN approximant generally scales with the power of expansion[2], with each term in increasing complexity. The order of expansion is denoted as n PN, corresponding to $v^{2n} = (M/r)^n$ for $2n \in \mathbb{Z}_{\geq 0}$. The binding energy E of the system and GW flux $\mathcal{F}$ can be expressed in terms of v and using conservation of energy

$$\mathcal{F}(v) = -\frac{dE(v)}{dt}\,. \tag{3.6}$$

Under the assumption that the inspiral is adiabatic ($\dot{f}_{\rm orb}/f_{\rm orb}^2 \ll 1$), one can derive differential equations to lead us to the time domain orbital phase Φ

$$\frac{d\Phi(t)}{dt} = \frac{v^3}{M}\,, \tag{3.7}$$

$$\frac{dv}{dt} = -\mathcal{F}(v)\frac{dv}{dE(v)}\,. \tag{3.8}$$

There are multiple distinct families of post-Newtonian (PN) models available based on the expression of Eq. (3.8). We focus in particular on the TaylorF2 model, which

[2]Though not exclusively, see Sec. 5.4.2 for details.

expresses the frequency domain GW phase ψ through the stationary phase approximation (SPA) [163, 258–261]. Following this calculation through in detail leads to a GW phase $\psi(f) \equiv \psi$ (neglecting spin)[3] of the form

$$\psi_{\rm TF2} = 2\pi f t_c - \phi_c - \frac{\pi}{4} + \psi_{\rm BBH}^{\rm 0PN\to 4.5PN} + \psi_{\rm AT}^{\rm 6PN\to 7.5PN} + \psi_{\rm DT}^{\rm 8PN\to 10PN}, \tag{3.9}$$

where the the PN orders X PN $\to$ Y PN denote the PN order that the effect enters the signal X, and the highest available PN expression Y, the coalescence time t_c and phase ϕ_c are gauge degrees of freedom, and the phase is split into point particle BBH contribution $\psi_{\rm BBH}$ complete to 4.5PN [266–274], adiabatic tidal contribution $\psi_{\rm AT}$ complete up to 7.5PN [275–277] and dynamical tidal contribution $\psi_{\rm DT}$ up to 10PN [278]. The leading order mass dependence within $\psi_{\rm BBH}$ is $(\eta^{3/5}M)^{5/3}$ which gives rise to the chirp mass $\mathcal{M}_c$ (Eq. (3.1)). This is the dominant contribution to the phase evolution of a CBC and the most accurately measured mass parameter for low mass systems. The leading order adiabatic tidal contributions dependent on $(\Lambda_2^{\rm A}, \Lambda_2^{\rm B})$ enter the GW phase at 5PN [279][4], indicating why at large separation a BNS system may be approximated as a BBH. If we consider only the leading order 5PN and next-to-leading order 6PN contributions [233, 280]

$$\psi_{\rm AT}^{\rm 5PN\to 6PN} = -\frac{39}{9}\tilde{\Lambda}v^{10} + v^{12}\left(\frac{6595}{364}\delta\tilde{\Lambda} - \frac{3115}{64}\tilde{\Lambda}\right) \tag{3.10}$$

where we have defined the joint tidal deformability $\tilde{\Lambda}$ in the same spirit as $\mathcal{M}_c$, the leading order tidal contribution. Therefore this is the most accurately measured tidal

[3]The inclusion of spin adds in up to 3.5PN currently known BBH spin orbit terms [262], up to 3PN spin-spin terms [263], and also tidal spin terms [236, 247, 264, 265] which we will discuss in Sec. 5.4.4.

[4]Terms from 6.5N onwards also depend on the octopolar tidal deformabilities $(\Lambda_3^{\rm A}, \Lambda_3^{\rm B})$

parameter

$$\tilde{\Lambda} = \frac{8}{13}\Bigg[(1+7\eta-31\eta^2)(\Lambda_1+\Lambda_2) + \sqrt{1-4\eta}(1+9\eta-11\eta^2)(\Lambda_1-\Lambda_2)\Bigg], \tag{3.11}$$

with the 6PN next-to-leading order contribution governed by a combination $\tilde{\Lambda}$ and

$$\delta\tilde{\Lambda} = \frac{1}{2}\Bigg[\sqrt{1-4\eta}\left(1-\frac{13272}{1319}\eta-\frac{8944}{1319}\eta^2\right)(\Lambda_1+\Lambda_2) + \left(1-\frac{15910}{1319}\eta-\frac{32850}{1319}\eta^2+\frac{3380}{1319}\eta^3\right)(\Lambda_1-\Lambda_2)\Bigg]. \tag{3.12}$$

Therefore, it is convenient in data analysis to use $(\tilde{\Lambda}, \delta\tilde{\Lambda})$ when sampling and measuring tides from a GW signal. Also note here that disentangling (Λ_1, Λ_2) requires accurate measurements of $(\eta, \tilde{\Lambda}, \delta\tilde{\Lambda})$.

The dynamical tides used within this thesis are implemented with model FMTIDAL [278], which adds the Newtonian[5] tidal excitation of the f-mode linearly into the phase. In this prescription dynamical tides enter the phase at 8PN. In generic terms

$$\psi_{\rm DT}^{\rm 8PN\to 10PN} = \Big[g_1(m_1, m_2, \Lambda_{2,1}, \Lambda_{2,2}, \Omega_{2,1}, \Omega_{2,2})v^{16} \tag{3.13}$$

$$+ g_2(m_1, m_2, \Lambda_{3,1}, \Lambda_{3,2}, \Omega_{3,1}, \Omega_{3,2})v^{20}\Big] \tag{3.14}$$

where the full form of functions g_1, g_2 can be found in Ref. [278].

[5]Relativistic effects from redshift and frame dragging nearly cancel in the case of f-mode excitations [167], hence this approximation is used.

3.3.2 Effective-one-body theory

The breakdown of PN theory in the strong field gave rise to an alternative approach, aiming to remain accurate up to merger. EOB theory entails mapping the two body problem to a test particle in an effective spacetime. This mapping imposes the relation between the energies of the real and effective systems

$$\frac{E_{\rm eff}}{\mu} = \frac{(E_{\rm real})^2 - m_1^2 - m_2^2}{2m_1 m_2}\,. \tag{3.15}$$

This results in a semi-analytical approach that solves for the system dynamics over time. EOB theory incorporates PN information which is commonly re-summed into a rational Padé form such that it remains stable close to merger. There are two currently used EOB models which contain tides, TEOBResumS [13, 246, 248] and SEOBNRv4T [167, 169, 243]. Though both families follow the same guiding principles, they are quite different in their formulation. We will specifically utilise TEOBResumS within this thesis, and focus on its implementation moving forwards. There are three main ingredients within the EOB formalism:

1. *Hamiltonian*: The conservative dynamics of a circular, non-spinning system is described by the EOB Hamiltonian

$$\hat{H}_{\rm EOB} = \frac{1}{\eta}\sqrt{1 + 2\eta(\hat{H}_{\rm eff} - 1)}\,, \tag{3.16}$$

with

$$\hat{H}_{\rm eff} = \sqrt{p_{r*}^2 + A(r)\left(1 + \frac{p_\varphi^2}{r^2} + 2\eta(4-3\eta)\frac{p_{r*}^4}{r^2}\right)}\,, \tag{3.17}$$

where r is the radial coordinate, φ is the orbital phase, $p_{r*} = \sqrt{A(r)/B(r)}p_r$ is the

momentum for the tortoise radial coordinate p_r, p_φ is the angular momentum, and $A(r), B(r)$ are EOB potentials which includes re-summed PN information and may also include NR calibration. For example, the A potential in BBH case my be re-summed as a series of $u \equiv 1/r$ as

$$\begin{aligned} A_{\rm BBH} &= 1 - 2u + 2\eta u^3 + \eta a_4 u^4 + \eta a_5 u^5 + \eta a_5 u^6 + \mathcal{O}(u^7) \\ &= \frac{1 - n_1 u}{1 + d_1 u + d_2 u^2 + d_3 u^3 + d_4 u^4 + d_5 u^5} + \mathcal{O}(u^7) \end{aligned} \tag{3.18}$$

where here the PN series of coefficients[6] a_i is re-summed with a (1, 5) Padé approximant of coefficients n_i, d_i. The adiabatic[7] tidal interactions enter the EOB potential [248, 280, 282–284] as

$$A = A_{\rm BBH} + A_T \,, \tag{3.19}$$

which we will discuss in detail in Ch. 5.

2. *Radiation reaction*: The above Hamiltonian results in Hamiltons equations

$$\frac{d\varphi}{dt} = \omega_{\rm orb} = \frac{\partial \hat{H}_{\rm EOB}}{\partial p_\varphi} \tag{3.20}$$

$$\frac{dr}{dt} = \left(\frac{A}{B}\right)^{1/2} \frac{\partial \hat{H}_{\rm EOB}}{\partial p_{r_*}} \tag{3.21}$$

$$\frac{dp_\varphi}{dt} = \hat{\mathcal{F}}_\varphi \,, \tag{3.22}$$

$$\frac{dp_{r_*}}{dt} = -\left(\frac{A}{B}\right)^{1/2} \frac{\hat{H}_{\rm EOB}}{\partial r} \,, \tag{3.23}$$

[6] This is not solely PN as the coefficient a_6 is a pseudo-PN fitted to NR.

[7] Though we do not utilise the dynamical tides prescription of TEOBResumS, dynamical tides can be included through a mapping of the static Love number to a frequency enhanced effective Love number [241, 281].

where the energy and angular momentum losses to GWs are taken into account through the radiation reaction [285–288] force $\hat{\mathcal{F}}_\varphi$. The radiation reaction is expressed as a re-summation of the waveform multipolar modes $h_{\ell m}$.

3. *Multipolar waveform modes*: The final piece is the waveform modes [289–291] as these are the output of interest. The BBH waveform multipoles $h_{\ell m}^{\rm BBH}$ are factorised by Newtonian terms and include re-summed tail terms and amplitude corrections. The tides are incorporated linearly

$$h_{\ell m} = h_{\ell m}^{\rm BBH} + h_{\ell m}^{\rm tides} \tag{3.24}$$

where $h_{\ell m}^{\rm tides}$ contains tidal amplitude corrections.

We will expand on the inclusion of tides within TEOBResumS in Ch. 5, and in particular on the information from *gravitational self-force* (GSF), the effect of a body's gravitational field on it motion. The EOB framework has been shown to replicate the two body dynamics [239], and retains accuracy to merger[8]. However iteratively evolving the equations of motion is time consuming, and defines EOB models as native in the time domain. This means that for use in data analysis a transformation to the frequency domain is required [292], which adds extra computational cost.

3.3.3 Phenomenological models

Phenomenological modelling includes information from PN, EOB and NR in the aim to create a model which remains accurate in the strong gravity regime whilst significantly cutting down the waveform evaluation time. This is achieved by fitting piece-

[8]Whilst the BBH version of TEOBResumS contains a merger-ringdown, the BNS version halts at merger and contains no postmerger or ringdown.

wise closed-form ansatzes describing the amplitude and phase of spherical harmonic modes, to a large library of pre-generated waveforms. Therefore phenomenological models do not generate the dynamics of the system, but directly model the resulting waveform. Phenomenological models are also commonly devised in the frequency domain (though not exclusively [293]), which is particularly efficient for data analysis. Due to these strengths, phenomenological models have been utilised in all GW detections to date [294]. Here we briefly introduce the BBH family PhenomX [295, 296] and BNS family NRTidal [9, 297, 298].

PhenomX [295, 296, 299, 300]

The current state of the art BBH phenomenological models are the PhenomX family. This family encompasses IMRPhenomXAS [295] (the base model with $\ell = 2, |m| = 2$ spherical harmonic mode with aligned spin), IMRPhenomXP [296] (builds in precession), IMRPhenomXHM [299] (builds in higher order multipoles), IMRPhenomXPHM [296] (builds in precession and higher order multipoles) and IMRPhenomXO4a [300] (includes NR fitted precession angles and mode asymmetry). We focus in particular on PhenomXAS, as we do not consider spin precession or higher order modes. PhenomXAS is split into regions of inspiral, merger-ringdown, and an intermediate region to smoothly join them together. Each region is fitted a discrete *collocation points*, where the number of collocation points is equal to the number of phenomenological parameters. We will utilise the inspiral, which is fitted to waveforms generated with EOB model SEOBNR and test mass waveforms, utilising ansatzes expressed as an expansion of frequency f

$$\psi_{\rm ins}^{\rm PhenomXAS}(\vec{\theta}, f) = \psi_{\rm TF2}^{\rm BBH}(\vec{\theta}, f) + \frac{1}{\eta}\left(a_0(\vec{\theta}) + \sum_{i=1}^{3} \frac{3}{2+i} a_i(\vec{\theta})(Mf)^{(2+i)/3}\right), \tag{3.25}$$

$$A_{\rm ins}^{\rm PhenomXAS}(\vec{\theta}, f) = A_{\rm PN}^{\rm BBH}(\vec{\theta}, f) + \sum_{i=1}^{3} b_i(\vec{\theta})(\pi f)^{(6+i)/3}\,. \tag{3.26}$$

where $\psi_{\rm TF2}^{\rm BBH}$ is the phase given by the BBH TaylorF2 phase, $A_{\rm PN}^{\rm BBH}$ is the PN BBH amplitude and a_i, b_i are phenomenological parameters given as a function of source parameters $\vec{\theta} \in \{\eta, \chi_1, \chi_2\}$. Each phenomenological parameter is fitted across the parameter space by building a hierarchical fit from 1D to 3D at each collocation point. We will expand on hierarchical fitting in Ch. 5, where we utilise it in the construction of model PhenomGSF.

NRTidal [9, 297, 298]

The NRTidal family provides a phenomenological approach to modelling the effect of matter on the waveform. We focus in particular on NRTidalv2 [9], which builds on the original NRTidal model by including higher order PN information, provides an amplitude correction, and includes tidal spin PN terms [236, 247]. NRTidalv2 isolates tidal effects on the amplitude and phase of the waveform is added linearly to the BBH equivalent

$$A_{\rm BNS} = A_{\rm BBH} + A_{\rm NRTidal} \tag{3.27}$$

$$\psi_{\rm BNS} = \psi_{\rm BBH} + \psi_{\rm NRTidal} \tag{3.28}$$

where $A_{\rm BBH}, \psi_{\rm BBH}$ are the amplitude and phase of any chosen BBH model. NRTidalv2 is fitted to 3 NR equal mass BNS waveforms. NRTidalv2 is not fitted at discrete frequency nodes, but directly to the full frequency[9] phenomenology up to the NR merger frequency, in a 1D fit. Within the fit, the leading order Newtonian prefactor is

[9] There is also an equivalent time domain fit [9].

factored out such that

$$\psi_{\text{NRTidalv2}}(f) = -\frac{117}{256\eta}\tilde{\Lambda}x^{5/2}\frac{1 + n_1 x + n_{3/2}x^{3/2} + n_2 x^2 + n_{5/2}x^{5/2} + n_3 x^3}{1 + d_1 x + d_{3/2}x^{3/2} + d_2 x^2} \tag{3.29}$$

where n_i, d_i are phenomenological coefficients which fitted to the NR waveforms whilst requiring consistency with PN. Note that the only dependence on the mass ratio is within the leading order Newtonian term, and there are no corrections containing unequal masses[10].

3.4 Numerical relativity

The most rigorous route of calculating waveforms is to fully solve EFEs across spacetime. This, however, involves solving all 10 non-linear coupled equations over time and cannot be analytically solved. Numerical methods must therefore be employed, which is extremely computationally prohibitive. This process of numerically solving EFEs is known as NR [301], and in the strong field regime where the binary approaches relativistic speeds and we cannot assume linearised gravity, it is the only available method for fully obtaining the binary evolution. Simulating matter only further complicates this process as the EFEs must be solved simultaneously with the equations of general relativistic magneto-hydrodynamics [302, 303]. Therefore BNS simulations are limited in quantity and generally short, only solving for the late inspiral and merger stages [12, 235, 304–307]. There are also many degrees of freedom that impact BNS simulations, including but not limited to masses [308–312], EOSs [305, 313], spins [11, 314–326], eccentricity [327–332], magnetic effects [333–341], neutrino trans-

[10]Recently the development of NRTidalv3 has allowed the extension to unequal masses due to new availability of unequal mass NR waveforms [298].

port [145, 342–353], electromagnetic counterparts [354, 355] and ejecta [356–359]. The GWs are extracted from NR simulations in terms of the Newman-Penrose scalar [360] ψ_4. The Newman-Penrose scalar for the (2,2) mode is related to gravitational-wave strain $h_{22}(t)$ via

$$\psi_{4,22}(t) = \frac{d^2 h_{22}(t)}{dt^2}. \tag{3.30}$$

Due to the process of performing the NR on a grid, this extraction takes place at a fixed radius. However, GWs are defined at future null infinity, therefore the Newman-Penrose scalar must be also extrapolated to infinity [361].

Since NR is the only available method for directly solving the EFEs, it is often used as the benchmark to which waveform models are built upon and validated against. However NR itself holds intrinsic errors which must be taken into account, which arise from the initial data [362], from the discrete grid [363, 364], and finite radius extrapolation [364–367].

Chapter 4

Prospects for measuring dynamical tides in third generation gravitational-waveform detectors

Declaration

This chapter is a reformatted version of Ref. [368], *Prospects for Measuring Dynamical Tides in Third Generation Gravitational-Waveform detectors* published in *Phys. Rev. D* 105.123032. where N. Williams is first author. The concept of assessing the detectability of dynamical tides in 3G detectors was proposed by P. Schmidt and builds upon the presentation of the FMTIDAL model presented in Ref. [278] by P. Schmidt and T. Hinderer. This work is also closely linked to work presented by G. Pratten, P. Schmidt and T. Hinderer in Ref. [369] which provided the first f-mode constraints on GW170817. The code for FMTIDAL was provided by P. Schmidt, and routine codes for mismatches and construction of KDEs was provided by G. Pratten. All analysis for this work was completed by N. Williams, with the exception of the astrophysical rates which were calculated by G. Pratten. Parameter estimation was completed by N.

Williams, with code provided by P. Schmidt and G. Pratten for which FMTIDAL was coded up within BILBY. The discussion, interpretation and original writing was a joint contribution from N. Williams, P. Schmidt and G. Pratten. All figures were created by N. Williams.

4.1 Introduction

The detection of GWs from BNS mergers [5, 156] has opened up a new avenue to study the microscopic physics of NSs from their macroscopic properties. This inference is enabled by the imprint of tidal effects on the GW signal, which allows for the extraction of information about the as-of-yet unknown nuclear EOS of NSs [165, 234] as discussed in Ch. 2. The discovery of the BNS inspiral GW170817 allowed to place the first constraints on the nuclear EOS of NSs favouring a soft to medium-soft EOS with a median pressure at twice the nuclear saturation density [137]. In addition, complimentary constraints on the NS EOS have been obtained from the NICER observation of PSR J0740+6620 [84, 85], and the neutron skin thickness of the lead isotope ^{208}Pb(R^{208}_{skin}) as measured by the PREX-2 experiment [370].

Improvements in the sensitivity of the currently operating network of ground-based GW detectors Advanced LIGO [39], Virgo [41] and KAGRA [371] will allow for observation of many more BNS signals [372] in the coming years. However, the third generation (3G) of GW detectors is particularly promising not only for the detection of all BNS out to a redshift of $z = 3$ [373, 374] but especially for precision measurements of the EOS from GW observations [375].

The measurement of the NS EOS from BNS observations is made possible by the

characteristic imprint left in the GW signal due to interaction of the star with its companion's gravitational field [165, 171, 275, 279, 376, 377] as discussed in Ch. 3, which leads to the excitation of various fluid oscillation modes introduced in Sec. 2.3. Here, we consider only the GW signature of the f-modes with $n = 0$ radial nodes. The ℓ-th multipolar oscillation mode is characterised by two parameters: The tidal deformability λ_ℓ and the angular mode frequency ω_ℓ. In the regime where ω_ℓ is much smaller than the orbital frequency of the binary motion, the dominant tidal effects are adiabatic f-modes, which depend purely on λ_ℓ and are known to 7.5 PN order [275, 378]. The observation of GW170817 allowed for the first measurement of the tidal deformability [5, 87, 137]. In the late inspiral at GW frequencies $\gtrsim$ 800 Hz, finite-ω_ℓ dynamical tidal effects, become important, further enhancing the GW emission. The first constraints on the f-mode frequency of the companions of GW170817 were presented in [369].

Assuming GR and a hadronic composition of the NS, the tidal deformability and f-mode frequency can be related through URs [202] as introduced in Sec. 2.4. By directly measuring both dynamical and adiabatic tides, the assumptions behind these URs use can be tested, most prominently as a platform to test GR and exotic matter models. Furthermore, the f-mode frequency is commonly contextualised as a property of the postmerger if a NS is formed [183, 194, 379], however, measuring it also during the inspiral would allow for consistency tests between the inspiral and remnant properties and to search for possible phase transitions during the merger[1].

Current GW detectors are not sufficiently sensitive at frequencies above $\sim$ 800Hz where dynamical tides become more prominent, and hence the measurements of the

[1]The extraction of the f-mode frequency in the postmerger is not covered here but we note that several physical effects that are assumed as negligable in the insiral, should be taken into account in the postmerger calculation. This includes finite temperature effects, magnetic fields and neutrino transport.

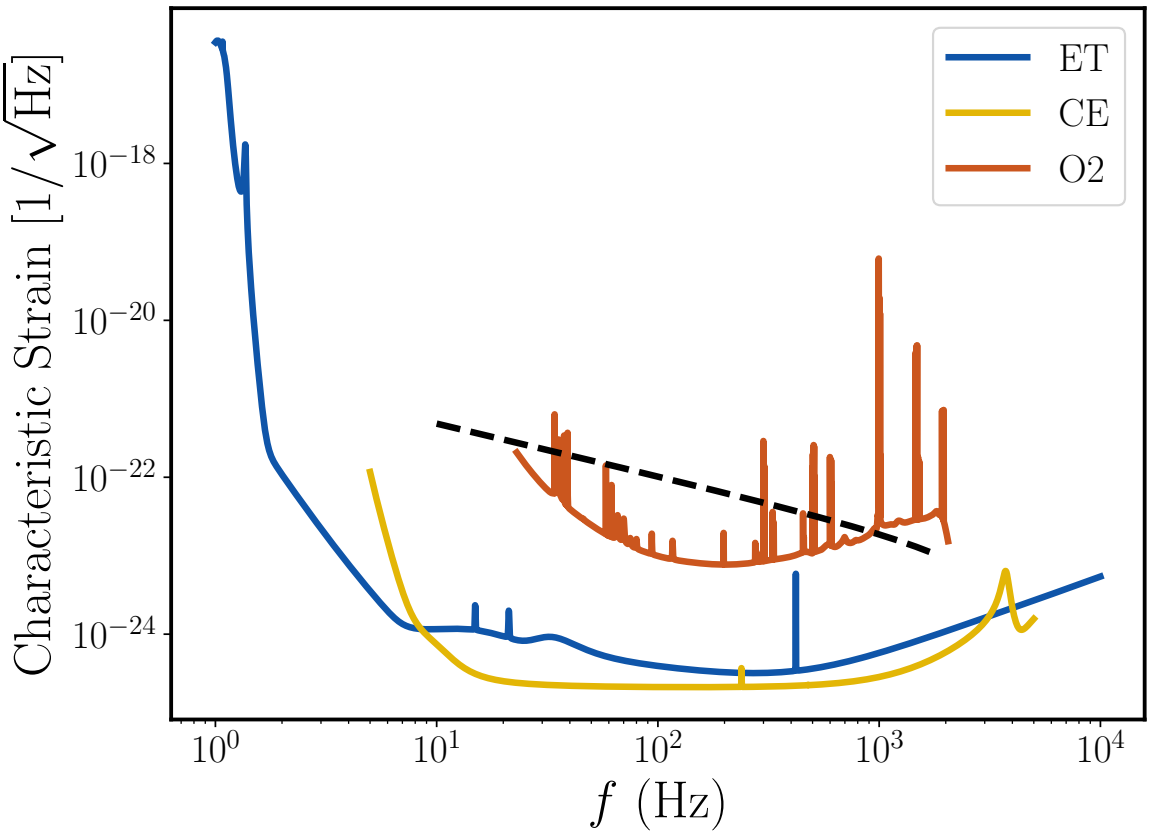

Figure 4.1: Sensitivity curves for ET (blue) and CE (yellow) [14] and the one for LIGO-Hanford at time of the observation of GW170817 [15] during the second observing run (O2) for comparison. The inspiral waveform for a GW170817-like binary starting at 10Hz is shown by the black dashed line. The regime above $\sim$ 800Hz will be easily accessible for the 3G detectors.

f-mode frequency is difficult. However, 3G detectors such as the Einstein Telescope (ET) [380] and Cosmic Explorer (CE) [374] will have a much improved sensitivity in the high-frequency regime as illustrated in Fig. 4.1, and therefore the complete BNS signal through merger will be detectable for many of the anticipated 10^4 detections per year [110], allowing us to also measure such higher-order tidal effects.

In this chapter we investigate the prospect for distinguishing dynamical tides in inspiralling BNS in 3G detectors. To do this, we calculate the SNRs required to

distinguish between adiabatic and dynamical tides, and apply this to a fiducial BNS population to determine the proportion of events from which we can expect to measure dynamical tides. Furthermore, we perform full Bayesian inference on a GW170817-like binary to study how well the f-mode frequency can be measured.

The chapter is organised as follows: In Sec. 4.2 we introduce the methodology including the waveform model we employ (Sec. 4.2.1), the distinguishability criterion (Sec 4.2.2), and provide a short summary of the Bayesian inference in Sec. 4.2.3. In Sec. 4.3 we present our results, first the distinguishability SNRs required to differentiate dynamical tides in Sec. 4.3.1 and then applied to realistic population of BNS Sec. 4.3.2; in Sec. 4.3.3 we perform full Bayesian inference a GW170817-like event. Finally, we conclude in Sec. 4.4.

4.2 Methodology

4.2.1 Waveform model

To simulate the BNS, we model the frequency-domain GW phase $\psi(f)$ of their signals as the post-Newtonian point-particle inspiral phase at 3.5PN order (see [87, 295] and Refs. therein for details) augmented with quadrupolar ($\ell = 2$) adiabatic tidal effects up to 7.5PN order [275, 280], the 6PN octopolar ($\ell = 3$) adiabatic contribution [182], and the quadrupolar as well as octopolar dynamical tides contributions of Ref. [278]. For consistency with the dynamical tides prescription we only consider non-spinning NSs.[2] The inclusion of spin will in practice affect the measurability of resonant tidal effects [168, 170, 180, 381, 405–408]. For spins which are (anti-)aligned with the

[2]We note that recent work in the EOB framework has started to include the effect of the NS spin on the f-mode frequency and the associated GW phase [170, 381]

orbital angular momentum, the f-mode frequency is shifted upwards (downwards) [409] and thus results in less (more) dephasing in the signal [170] but we caution that rather high NS spins are needed to have a noticeable effect on the tidal phase [381, 407]. We do not include any tidal corrections in the PN amplitude. Hence, the BNS signal is schematically given as

$$\tilde{h}_{\rm BNS}(f) = A_{\rm BBH}(f) e^{i(\psi_{\rm BBH}(f)+\psi_{\rm AT}(f)+\psi_{\rm DT}(f))}, \tag{4.1}$$

where $A_{\rm BBH}$ is the pure point-particle amplitude without tidal corrections, $\psi_{\rm BBH}$ the point particle contribution to the GW phase, $\psi_{\rm AT}$ the adiabatic, and $\psi_{\rm DT}$ the dynamical phase all in the frequency domain.

The leading-order adiabatic tidal effects enters the GW phase at 5PN order (Eq. (3.9)) and are entirely characterised by the binary tidal deformability $\tilde{\Lambda}$ [165, 234](Eq. (3.11)). The quadrupolar adiabatic tidal terms depend on the individual dimensionless tidal deformability of the A-th NS, $\Lambda_{2,A}$, and the octopolar term on $\Lambda_{3,A}$ (Eq. (2.10)). The dynamical tidal terms additionally depend on the stars' dimensionless angular f-mode frequencies $\Omega_{2,A}$ and $\Omega_{3,A}$. We consider these terms and neglect the quadrupole-monopole contribution [264] which arises from self-deformation due to spin, as we only consider nonspinning NSs.

For the majority of analyses we choose a waveform starting frequency of $f_{\rm min} = 10$ Hz unless stated otherwise, and truncate the waveforms at a maximum frequency $f_{\rm max}$ either given by the (Newtonian) contact frequency [382, 383] or the frequency of the innermost stable circular orbit (ISCO) whichever one is smaller.

4.2.2 Distinguishability Criterion

The agreement between two waveforms h_1 and h_2 is measured in terms of the match $\mathcal{M}(h_1, h_2)$ given by Eq. (1.40). The noise-weighted inner product of a GW h with itself is the *optimal* SNR

$$\rho_{\rm opt}(h) = \sqrt{\langle h, h\rangle}. \tag{4.2}$$

We will use the PSDs of [14] for the ET-D and CE sensitivities in our analysis. We place ET at the current Virgo site and CE at the current Hanford site of Advanced LIGO.

Two waveforms h_1 and h_2 are considered *indistinguishable* in a given detector if

$$\mathcal{MM}(h_1, h_2) < \frac{D}{2\rho^2}, \tag{4.3}$$

where ρ is the *measured* SNR, D denotes the number of measurable intrinsic binary parameters [384, 385] and mismatch $\mathcal{MM}$ is given in Eq. (1.42). Conversely, two signals can be distinguished if the measured SNR is larger than the necessary *distinguishability* SNR defined as

$$\rho_{\rm dist} = \sqrt{\frac{D}{2\mathcal{MM}}}. \tag{4.4}$$

We will use the distinguishability SNR in Sec. 4.3.1 to determine where in the BNS parameter space dynamical tides will be, in principle, measurable in 3G detectors.

4.2.3 Bayesian inference

While the distinguishability criterion is a sufficient condition to gauge for which binaries dynamical tides may be significant, it does not allow us to determine to what degree the f-mode frequencies $\Omega_{\ell,A}$ can be constrained in future BNS obser-

vations. Therefore, we perform full Bayesian inference on a 3G detector networks for a GW170817-like BNS merger.

For the BNS systems that we will consider in Sec. 4.3.3, $\vec{\theta}$ consists of the intrinsic parameters of the binary, i.e. the component masses m_A, the quadrupolar tidal deformabilities $\Lambda_{2,A}$ and the quadrupolar f_2-mode frequencies $\Omega_{2,A}$ (all octopolar contributions are omitted) with $A = 1, 2$, and extrinsic parameters, i.e. the sky location, inclination, distance, polarisation, coalescence time and phase.

For a detector network the joint likelihood is given by the product of the individual detector likelihoods from Eq. (1.44),

$$p(d|\vec{\theta}) = \prod_{i=1}^{N} p(d_i|\vec{\theta}), \tag{4.5}$$

where N is the number of detectors in the network.

One-dimensional and two-dimensional PDFs are obtained by marginalising over the other parameters. We utilise the Bilby inference library [66, 386] in conjunction with the nested sampler dynesty [65] using slice sampling to sample the parameter space and estimate the posterior density. We inject simulated signals into zero noise, which is broadly equivalent to the results obtained by averaging the PSD over many noise realisations. However, we do not neglect noise entirely as it still enters the likelihood calculation through the PSD.

4.3 Results

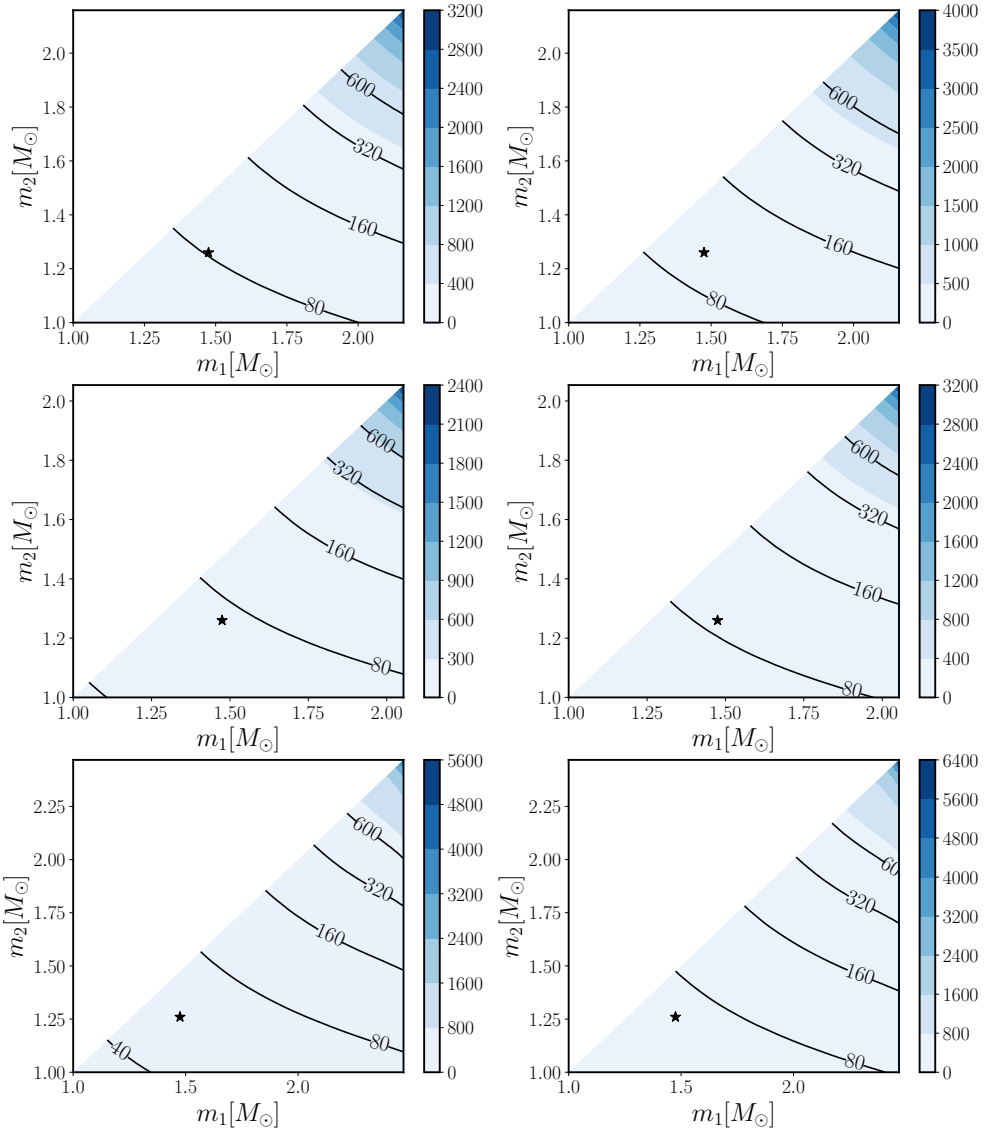

Figure 4.2: Contour plots for the minimal SNR required to distinguish between adiabatic and dynamical tides as a function of component mass m_1, m_2 for ET (left column) and CE (right column). We show results for three different EOS: APR4 (top row), SLy (middle row) and MPA1 (bottom row). The black star represents a GW170817-like event.

4.3.1 Distinguishability SNR for BNS

Despite their high relative PN order, dynamical tides are expected to be distinguishable from adiabatic tides in the late inspiral of BNS if the SNR is large enough. Here, we perform a first assessment of the SNR required to separate adiabatic and dynamical tides in 3G detectors for a range of NS masses. Considering only nonspinning BNS with tides up to octopolar order, we compute the distinguishability SNR $\rho_{\rm DT}$ following Eq. (4.4) with $D = 6$, where the six intrinsic parameters are $m_A, \Lambda_{2,A}, \Omega_{2,A}$[3] and the match $\mathcal{M}$ between a waveform containing only adiabatic tides, $h_{\rm AT}$, and one that includes both adiabatic and dynamic tides, $h_{\rm DT}$, for the same parameters for ET and CE with $f_{\rm min} = 10$ Hz. Both waveforms $h_{\rm AT}$ and $h_{\rm DT}$ include quadrupolar and octopolar adiabatic tidal terms; $h_{\rm DT}$ additionally includes the quadrupolar and octopolar dynamical tidal terms.

We consider three hadronic EOS representative of soft to medium-soft EOS consistent with GW170817 [137]: APR4 [116], SLy [387–389] and MPA1 [390] and use the UR of Ref. [202] to evaluate the quadrupolar f_2-mode and octopolar f_3-mode frequencies. In reality the EOS is unlikely to adhere to any specific model listed here, but lie somewhere in the parameter space that they cover. We choose a minimum NS mass of $1\,M_\odot$ up to the maximum mass allowed by each EOS. Figure 4.2 shows the distinguishability SNR for dynamical tides for ET (left column) and CE (right column) for APR4 (top row), SLy (middle row) and MPA1 (bottom row). In all panels we indicate a GW170817-like binary with mass ratio $q_\star = 1.17$ and source-frame total mass $M_\star^{\rm src} = 2.735\,M_\odot$ with a star.

[3] We do not include the $\ell = 3$ tidal parameters in D as these are even more difficult to measure but their neglect in waveform models may induce a bias in the $\ell = 2$ tidal parameters and hence they are included in our inspiral model.

The dependence of $\rho_{\rm DT}$ on the total mass M and EOS is a consequence of their effect on $\psi_{\rm DT}$. Figure 4.3 shows the dynamical tides part of the phase for 10% changes in either the total mass or mass ratio q for a GW170817-like system. It is evident that $\psi_{\rm DT}$ is maximised for low total masses. Consequently, we see that for heavy BNS systems the dynamical tides are suppressed and therefore more difficult to measure. Variation in EOS shows that for a given pair of (M, q), stiffer EOS (e.g. MPA1) produce the largest contribution to the dynamical tidal phase for the EOS considered here. Physically, this corresponds to between a quarter and half an orbit dephasing at the contact frequency solely due to dynamical tides for our softest and stiffest EOS in the case of GW170817. These observations explain the distribution of $\rho_{\rm DT}$ in Fig. 4.2: At regions where $\psi_{\rm DT}$ is maximised, i.e. lighter NSs, a lower $\rho_{\rm DT}$ is required to disentangle adiabatic and dynamical tides. The SNRs required to see a noticeable impact of dynamical tides on the tidal phase reach up to 6400 in ET for the MPA1 EOS, which admits the largest NS mass of the EOS considered here. However, when quantifying these SNRs, the overall increased sensitivity of 3G detectors must be taken into account as illustrated below.

Considering a GW170817-like event as a typical event, we measure $\rho_{\rm DT} = 84$, 74, 56 (102, 89, 67) for APR4, SLy and MPA1 respectively in ET (CE). For comparison, the measured SNR of GW170817 in the LIGO-Virgo network was ~ 32 [5]. For ET and CE the optimal SNRs for a GW170817-like binary would be 1031 and 2935 respectively for this event. In this scenario, any EOS considered here would lead to results that exceed the minimum distinguishability SNR $\rho_{\rm DT}$ by at least a factor of 10. It is also important to note that these results consider only one detector, while for any coincident event the network SNR is the quadrature sum of the individual detector SNRs.

When comparing the two 3G detectors, we consistently find that CE requires larger values of $\rho_{\rm DT}$. It may seem counterintuitive to require a higher distinguishability

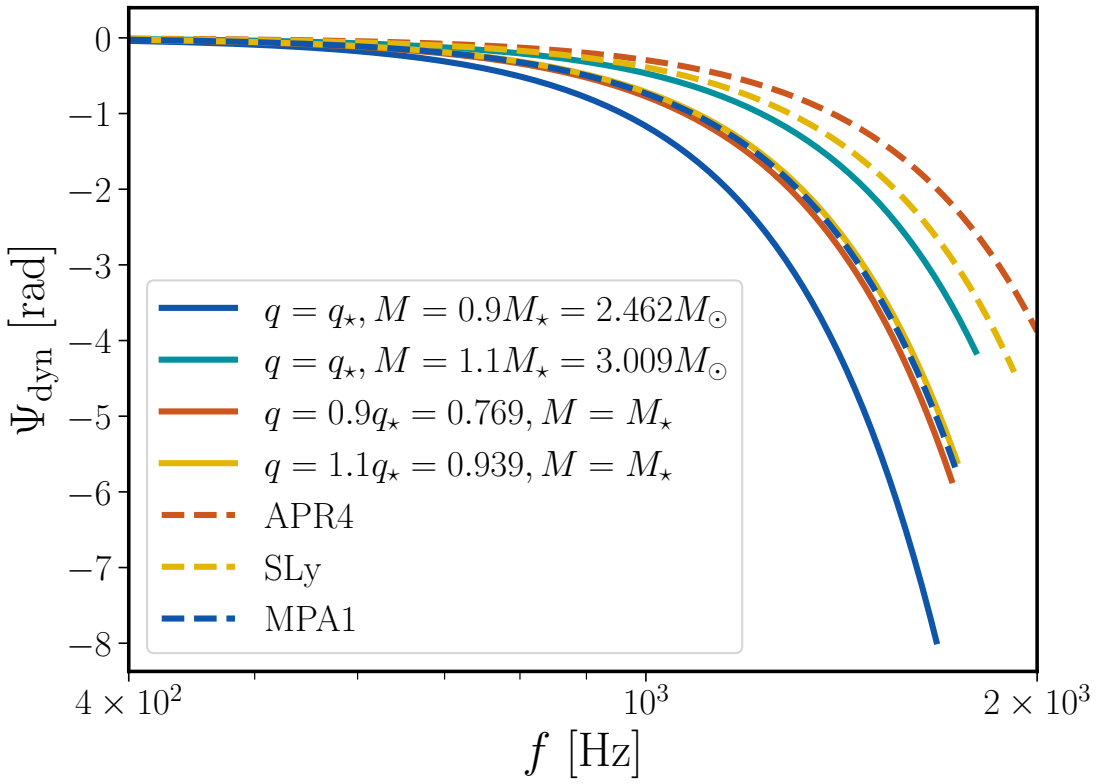

Figure 4.3: GW phase contribution from dynamical tides, $\psi_{\rm dyn}$, as a function of GW frequency for a variation of total mass and/or mass ratio (solid lines) and EOS (dashed lines). We either vary the total mass M or the mass ratio q by 10% from a GW170817-like binary with $q_\star = 0.854$, and $M_\star = 2.735M_\odot$ and EOS MPA1. We also vary the EOS for a GW170817-like binary showing the tidal phase for APR4 (orange), SLy (yellow) and MPA1 (blue).

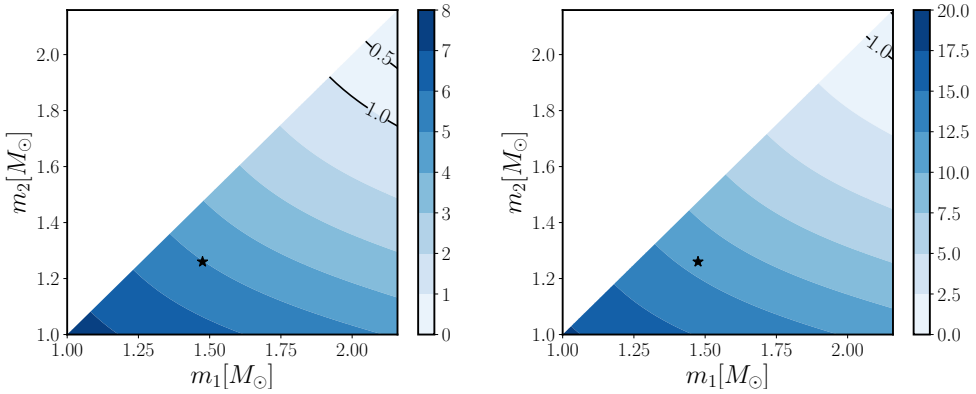

Figure 4.4: Contour plots for $\rho_{\rm opt}/\rho_{\rm DT}$ for an optimally orientated source at 100Mpc with EOS APR4, as a function of component mass m_1, m_2 for ET (left) and CE (right). The black star represents a GW170817-like event. Dynamical tides are distinguishable when $\rho_{\rm opt}/\rho_{\rm DT} > 1$.

SNR for a more sensitive detector at first glance, however, the higher optimal SNR (Eq. (4.2)) of a signal detected by CE must be remembered comparatively. Therefore, to meaningfully compare the two 3G detectors, it is necessary to also take the optimal SNR into account. We demonstrate a comparison between detectors in Fig. 4.4, where we mirror Fig. 4.2 but show the ratio $\rho_{\rm opt}/\rho_{\rm DT}$ assuming the BNS are at a luminosity distance of 100 Mpc. This ratio can be interpreted as the fraction of the optimal SNR that is required to distinguish between adiabatic and dynamical tides. It follows that for $\rho_{\rm opt}/\rho_{\rm DT} > 1$, it is possible to distinguish dynamical tides in this signal for the chosen luminosity distance. Therefore despite the higher $\rho_{\rm DT}$ in CE relative to ET, the required fraction of the optimal SNR is much lower, and hence dynamical tides are more easily detectable. For example, in the case of a GW170817-like system at 100 Mpc $\rho_{\rm DT} = \rho_{\rm opt}/5$ for ET and $\rho_{\rm DT} = \rho_{\rm opt}/11$ for CE.

We also explored the distinguishability of octopolar ($\ell = 3$) dynamical tides from quadrupolar dynamical tides, which, as expected, requires even higher SNRs. As reference, for a GW170817-like binary the SNRs required to discriminate the two would be

1258, 1050, 684 (1545, 1278, 822) for APR4, SLy and MPA1 respectively in ET (CE). Comparing this to the optimal SNRs of 1031 (ET) and 2935 (CE), it is evident that for the softer EOS (as preferred by GW170817) ET is unlikely to be able to disentangle octopolar from quadrupolar dynamical tides, whereas CE would be able due to its increased sensitivity.

4.3.2 Population study

We now consider a realistic population of BNS to which we apply the distinguishability methodology for our choices of EOS. We assume that the EOS is universal, i.e. it is the same for all NSs.

Following the NS population model outlined in Ref. [391], we sample NS masses from the formation channel corresponding to the second-born NS of the binary system, referred to as "slow" NSs due to their effectively zero spin. Ref. [391] assumes here that the first and second-born mass distributions are independent. This population takes the form of a double Gaussian in which the probability of a NS with mass m is given by

$$p(m) = \xi_s \mathcal{N}(\mu_1, \sigma_1) + (1 - \xi_s)\mathcal{N}(\mu_2, \sigma_2), \tag{4.6}$$

where $\mathcal{N}(\mu_i, \sigma_i)$ are normalised Gaussians with mean μ_i and standard deviation σ_i, and ξ_s is the fraction of binaries in the low mass peak. The values for $\xi_s, \mu_1, \sigma_1, \mu_2, \sigma_2$ are taken from Tab. 1 of Ref. [391]. Here the low mass peak corresponds to radio-visible NS, and the high mass peak is informed by GW190425 as originating from a fast merging population.

Although the BNS redshift horizon of 3G detectors is predicted to reach up to $z \sim 3$ [373, 374], we recall from Sec. 4.2.2 that high SNRs are required to distinguish higher

order tidal effects, and we therefore introduce a redshift cut-off of $z = 0.5$ (equivalent to a luminosity distance $D_L \sim 3000$ Mpc assuming a Planck15 [392] cosmology) for our population study. We also impose a minimum SNR of $\rho_{\rm opt} > 8$ for each detector. Considering a GW170817-like event placed at $z = 3$, the measured SNR would be ~ 5 (6) for ET (CE), which would not be detectable and demonstrates our choice for the distance cut. We distribute the BNS in redshift following the Madau-Dickinson star formation rate (SFR) [393], as at low redshift regardless of the time delay distribution chosen between birth and merger, merger rates broadly follow the SFR. We specifically adopt the distribution described in Ref. [394], in which the probability distribution of redshift z is given by

$$p(z) = \frac{dV_c}{dz}\frac{1}{1+z}\zeta(z), \tag{4.7}$$

where V_c is the comoving volume and $\zeta(z)$ is the SFR

$$\zeta(z) = 0.015\frac{(1+z)^{2.7}}{1+[(1+z)/2.9]^{5.6}}M_\odot \mathrm{yr}^{-1}\mathrm{Mpc}^{-3}. \tag{4.8}$$

Current GW observations constrain the local merger rate for BNS to be $\sim 10 - 1700\,\mathrm{Gpc}^{-3}\,\mathrm{yr}^{-1}$ [294]. Following Ref. [395], we estimate the detection rate of BNS up to $z \sim 0.5$ for a single CE detector to be $\sim \mathcal{O}(\text{few} \times 10^4)\,\mathrm{yr}^{-1}$, which is consistent with the estimated detection rate for BNS mergers in 3G detectors [110]. We therefore generate ten (random) realisations of 10^4 binaries, where the gpstime of each binary is chosen randomly from the uniform interval $[1703721618, 1735257618]$, to place a conservative bound on the observability of dynamical tides from a population of BNS.

Extrinsic parameters are randomly drawn from uniform distributions to reflect an isotropic distribution, where declination δ is sampled in cosine, inclination ι in sine, and right ascension α and polarisation angle Ψ are sampled between 0 and π. The

	$\rho_{\rm opt} \geq \rho_{\rm AT}$		$\rho_{\rm opt} \geq \rho_{\rm DT}$	
	ET	CE	ET	CE
APR4	404.1	1018.4	14.9	43.0
SLy	558.1	1309.8	22.3	68.6
MPA1	1150.5	2392.6	46.8	149.7

Table 4.1: The average number of events detected by ET and CE where adiabatic tides are distinguishable $\rho_{\rm opt} \geq \rho_{\rm AT}$, and the subset of these for which also dynamical tides are distinguishable $\rho_{\rm opt} \geq \rho_{\rm DT}$ from 10 realisations of 10^4 BNS for different EOS.

optimal SNR $\rho_{\rm opt}$ is then calculated as in Eq. (4.2), however, due to varying extrinsic parameters there now also exists a geometric factor folded in via the detector response.

Table 4.1 shows the number of events for which tidal information is recovered when averaged over our ten realisations, i.e. all binaries satisfying $\rho_{\rm opt} \geq \rho_{\rm AT}$, where $\rho_{\rm AT}$ is the distinguishability SNR Eq. (4.3) for adiabatic tides. No tidal information would be recovered in cases that do not satisfy this, making them indistinguishable from BBH events, and the only evidence for a BNS would be from the component masses. We also list the subset of events that have detectable dynamical tides, i.e. where ($\rho_{\rm opt} \geq \rho_{\rm DT}$). Considering the stiff EOS MPA1, tidal information is measurable in 11.5% (23.9%) of binaries, and for 4.2% (6.7%) of those also dynamical tides can be recovered in ET (CE). This fraction decreases for softer EOS such as APR4, reducing to 4.0% (10.2%) of events with measurable tides, and 3.7% (4.2%) of those have distinguishable dynamical tides. Figure 4.5 shows the average number of BNS as a function of $\rho_{\rm opt}/\rho_{\rm AT}$ for the soft APR4 EOS. For events with $\rho_{\rm opt}/\rho_{\rm AT} < 1$, no tidal information is measurable. For all EOS considered here, the vast majority of events would not be distinguishable from BBH events. However, taking into account that the predicted BNS detection rates for a

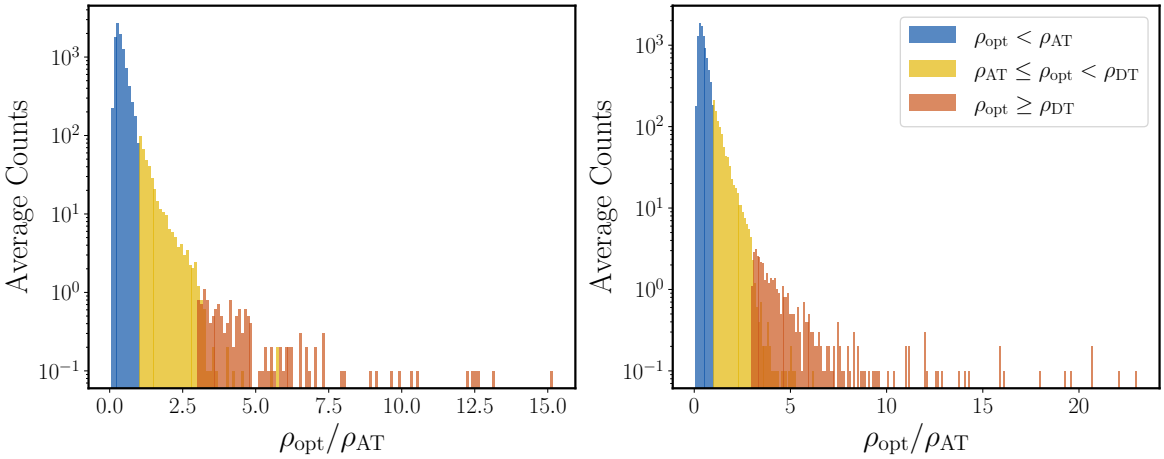

Figure 4.5: Histograms of the average number of BNS events as a function of the SNR divided by the distinguishability SNR for adiabatic tides for ET (left) and CE (right) for APR4. All events with $\rho_{\rm opt}/\rho_{\rm AT} < 1$ (blue) are indistinguishable from BBH signals; for events with $\rho_{\rm AT} \leq \rho_{\rm opt} < \rho_{\rm DT}$ (yellow) the adiabatic contribution to the phase can be distinguished; for events that satisfy $\rho_{\rm opt} \geq \rho_{\rm DT}$ (orange) both adiabatic and dynamical contributions to the phase are distinguishable.

network of 3G detectors is on the order of $\sim 10^3 - 10^5$ binaries per year, we still expect a substantial number of binaries to have dynamical tidal contributions depending on the true EOS and detector network. From Table 4.1, we expect $\sim \mathcal{O}(\text{few} \times 10^3)$ binaries per year with distinguishable adiabatic tides and $\sim \mathcal{O}(50)$ binaries per year with distinguishable dynamical tides with a single CE detector.

4.3.3 Parameter estimation

Whilst the distinguishability criterion Eq. (4.3) is a useful measure to estimate for which events dynamical tides may be significant, it does not inform on the accuracy to which the f_2-mode frequency can be constrained from a GW observation. Thus, we perform full Bayesian inference on a GW170817-like BNS signal in an ET-CE 3G detector network to determine the posterior probability densities of the tidal parameters

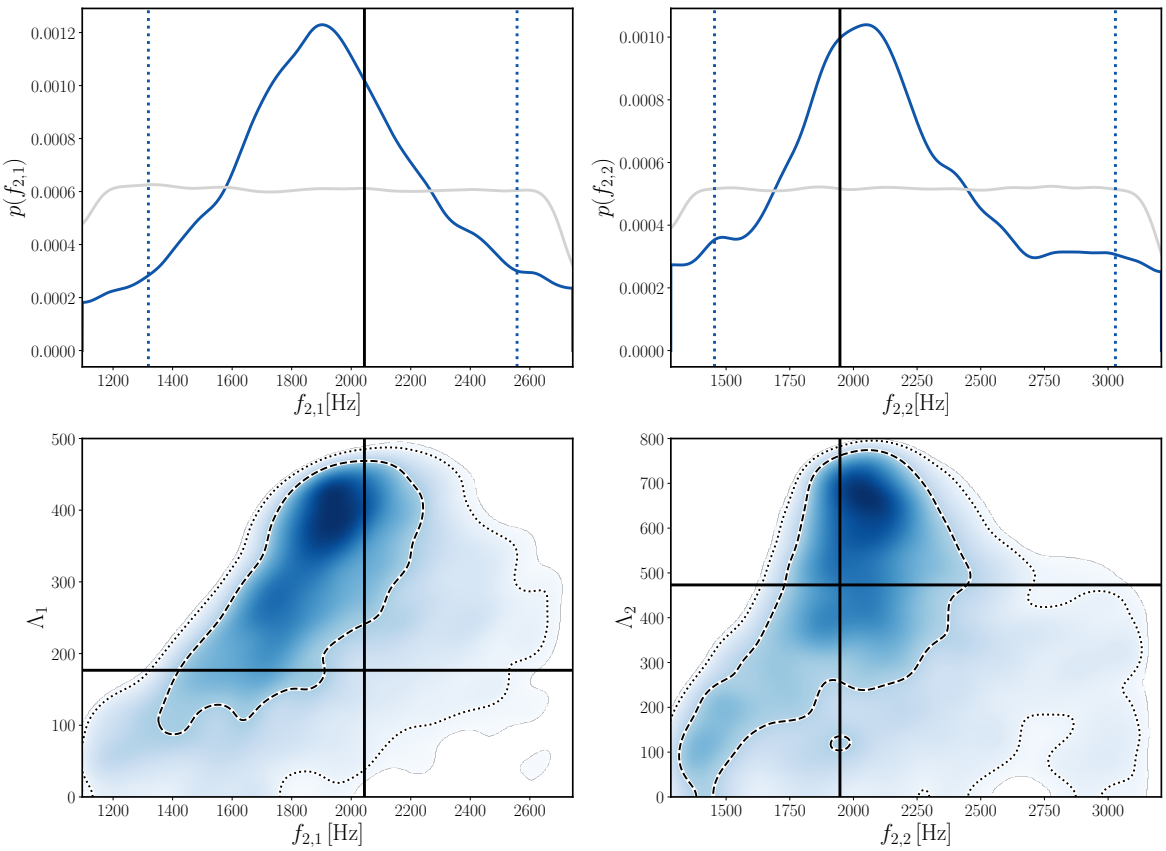

Figure 4.6: Posterior distributions for tidal parameters. Top: 1D posterior of the quadrupolar f-mode frequencies $f_{2,A}$ for the primary (left) and the secondary (right). Bottom: Joint 2D posteriors of $f_{2,A}$ and the tidal deformability $\Lambda_{2,A} \equiv \Lambda_A$. The injected values (black solid lines) are shown alongside 50% (dashed lines), 90% (dotted lines) credible intervals/contours and priors (grey lines).

and, in particular, the accuracy to which the f_2-mode frequency can be measured during the inspiral. Here, we only consider quadrupolar adiabatic and dynamical tides to limit dimensionality. We use the same waveform model for our simulated GW signal and to infer the parameters as detailed in Sec. 4.2.1.

We opt for a full Bayesian analyses over a Fisher matrix estimate despite the high SNR of the overall signal, as the dynamical effects only contribute to a small fraction of SNR and thus correlations may not be accurately captured.

Consistent with GW170817 we choose source-frame component masses of the primary $m_1 = 1.475\,M_\odot$ and the secondary $m_2 = 1.26\,M_\odot$, and the soft APR4 EOS for the simulated signal. The extrinsic parameters are as follows: The inclination between the orbital angular momentum and the line-of-sight $\iota = 0.1$ rad, right ascension $\alpha = 2.554$ rad, declination $\delta = -0.41$ rad, luminosity distance $D_L = 40$Mpc. We set the phase ϕ, polarisation angle Ψ and GPS time to zero.

To reduce the computational cost of the sampling, we assume that the sky location (α, δ), distance d_L and polarisation Ψ are known. This assumption is justified by the detection of an electromagnetic counterpart to pin the sky location and distance, which, for a nonspinning system, trivially gives a measurement of the polarisation.[4] We integrate the likelihood from a GW frequency $f_{\rm min} = 20$ Hz up to the Schwarzschild ISCO frequency of 1593 Hz. We note that for the chosen parameters, the BNS contact frequency is estimated to be 1843 Hz, which is significantly higher than the point at which we truncate the analysis and hence it is safe to assume that the two stars are still well separated and that the f_2-mode frequency of each NS is a well defined quantity. While the choice of the lower frequency cutoff reduces the signal length and hence the accumulated SNR, (adiabatic) tidal contributions to the phase only become prominent at GW frequencies $\gtrsim 400$ Hz [165] and dynamical tides become relevant at even higher frequencies [278]. We therefore expect the impact of this choice to be small for the measurement of the f_2-mode frequency. Our simulated signal has an ET-CE network SNR of 2360 which per the results of Sec. 4.2.2 easily satisfies the distinguishability criterion for a GW170817-like binary and hence we expect that some information about the f_2-mode frequency can be recovered from such an observation.

We obtain posterior probability distributions of the source parameters using the

[4] We note that electromagnetic counterparts are expected to be observable up to distances of ~ 200 Mpc for the next generation of telescopes [396].

Nested Sampling algorithm DYNESTY [65], as implemented in BILBY [66], with random slice sampling and 2000 live points. The simulated GW signal is injected into zero noise to avoid any noise-induced biases in the results. For our fiducial analysis we sample in chirp mass $\mathcal{M}_c$ and the inverse mass ratio $1/q$ and adopt the following uniform priors: $\mathcal{M}_c^{\rm det} \in [1.19666, 1.19675] M_\odot$, $1/q \in [0.825, 0.875]$, $\Lambda_{2,A} \in [0, 1000]$, $\Omega_{2,A} \in [0.05, 0.125]$, phase $\phi \in [0, 2\pi]$ and geocentric time $[-0.1, 0.1]$ around the injected value.

Figure 4.6 shows the 1D and 2D posteriors of the tidal parameters. The complete results are shown in Fig. A.1 in Appendix A.1. At 90% confidence we find the median f-mode frequencies of the stars to be $f_{2,1} = 1916^{+641}_{-598}$ Hz, and $f_{2,1} = 2103^{+926}_{-649}$ Hz, compared to the injected values of $f_{2,1} = 2044$ Hz and $f_{2,2} = 1947$ Hz. While the recovered median values are in good agreement with the injected values, the 90% credible intervals are wider than 1000 Hz despite the large SNR. From the 2D posteriors it becomes evident that there is a noticeable correlation between the f_2-mode frequency and Λ_2. As an attempt to break this correlation, we repeat the inference but choose a different mass prior. This choice is motivated by examination of the quadrupolar contribution of the dynamical phase, which is dependent on various combinations of component masses and tidal parameters. Noting the dependence of the dimensionless tidal deformability on the mass, by improving the component mass measurement we expect to improve constraints on the tidal parameters, leading to an improvement in the measurement of $\Omega_{2,A}$. To do so, we first determine the component mass posteriors from a low-frequency analysis from $10 - 20$ Hz entirely without tides and use the resulting mass posterior distributions as prior for the subsequent tidal analysis. For this restricted analysis, the SNR is 1582, and we sample again in $\mathcal{M}_c$ and q, keeping the $\mathcal{M}_c$ prior as before, however widening the mass ratio uniform prior to $1/q \in [0.5, 1]$. We also

restrict the allowed range for the component masses to be $m_A \in [1,3]M_\odot$. Everything else remains unchanged relative to our fiducial analysis. Once the mass posteriors are determined from the restricted analysis, we proceed with the tidal analysis from 20Hz as before but now sample directly in the component masses. The mean and variance are $\mu_1 = 1.4465, \sigma_1 = 0.0320$ and $\mu_2 = 1.3078, \sigma_2 = 0.0285$, respectively.

Figure 4.7 shows the resulting 1D posteriors of $f_{2,A}$ in comparison to the results with the uniform mass prior. With the Gaussian mass priors we find the f_2-mode frequencies at 90% confidence to be $f_{2,1} = 1959^{+649}_{-517}$ Hz, and $f_{2,2} = 2154^{+935}_{-684}$ Hz. When considering the primary mass, the Gaussian mass prior results show improvement in the posterior around the injected value and in turn a reduction in the 90% interval. However, in the case of the secondary mass, no improvement is evident. This is unsurprising, as tidal deformation is enhanced for smaller masses, and thus the regime in which we can gain the most improvement is for the larger primary mass. The complete results for the analysis with the Gaussian mass prior and the non-tidal $10-20$ Hz run are shown in Figs. A.2 and A.3 in Appendix A.1.

While the individual tidal parameters $\Lambda_{2,A}$ yield only broad posterior distributions (see e.g. Fig. A.1 in Appendix A.1), the binary tidal deformability $\tilde{\Lambda}$ [234] is well constrained to $\tilde{\Lambda} = 294^{+14}_{-13}$ for the fiducial run at the 90% credible interval, which is in excellent agreement with the injected value as shown in the left panel of Fig. 4.8. Similarly, we find that the quadrupolar dynamical phasing coefficient given by

$$c_2^{\rm DT} := -\frac{1}{X_1 X_2}\left[\frac{\Lambda_{2,1}}{\Omega_{2,1}^2}X_1^6(155-147X_1) + \frac{\Lambda_{2,2}}{\Omega_{2,2}^2}X_2^6(155-147X_2)\right], \tag{4.9}$$

where $X_A = m_A/M$, is found to be $c_2^{\rm DT} = -4.3^{+0.7}_{-0.7} \times 10^5$ at 90% confidence, which is

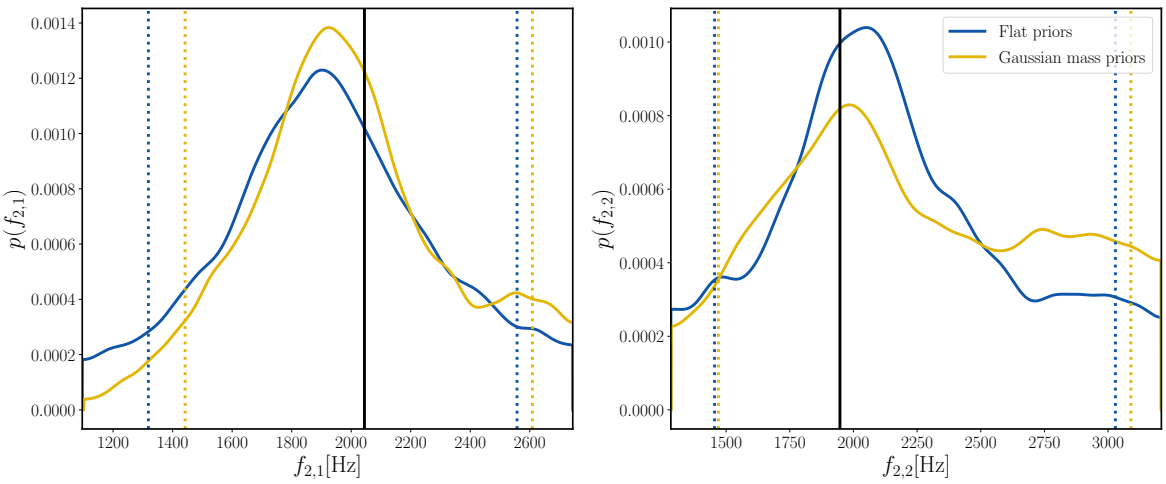

Figure 4.7: One-dimensional posterior distributions of the quadrupolar f-mode frequency for the primary (left) and secondary (right) NS for a GW170817-like binary in an ET-CE detector network. Flat priors (blue) and Gaussian component mass priors (yellow) are shown alongside the injected values (black solid lines) and the 90% credible intervals (dotted lines).

in excellent agreement with the injected value $c_2^{\rm DT} = -4.3 \times 10^5$. For comparison, the prior range is $c_2^{\rm DT} \in [-4.3 \times 10^6, 0]$ as shown in the right panel of Fig. 4.8. We find that $c_2^{\rm DT} = 0$ (adiabatic limit) is excluded at $> 99\%$ confidence, showing a coherent measurement of dynamically driven dephasing within the signal.

4.4 Conclusions

The next generation of ground-based GW detectors will have unprecedented sensitivities between $\sim$ 10 Hz and a few kHz. The improved sensitivity at frequencies $\simeq$ 400 Hz is particularly enticing as it will allow to place formidable constraints on the as-of-yet unknown EOS of NSs by measuring tidal effects in inspiralling NS binaries. Beyond the leading-order adiabatic tidal effects, dynamical tides can become important at higher frequencies and may be measurable in 3G detectors [369]. This would allow

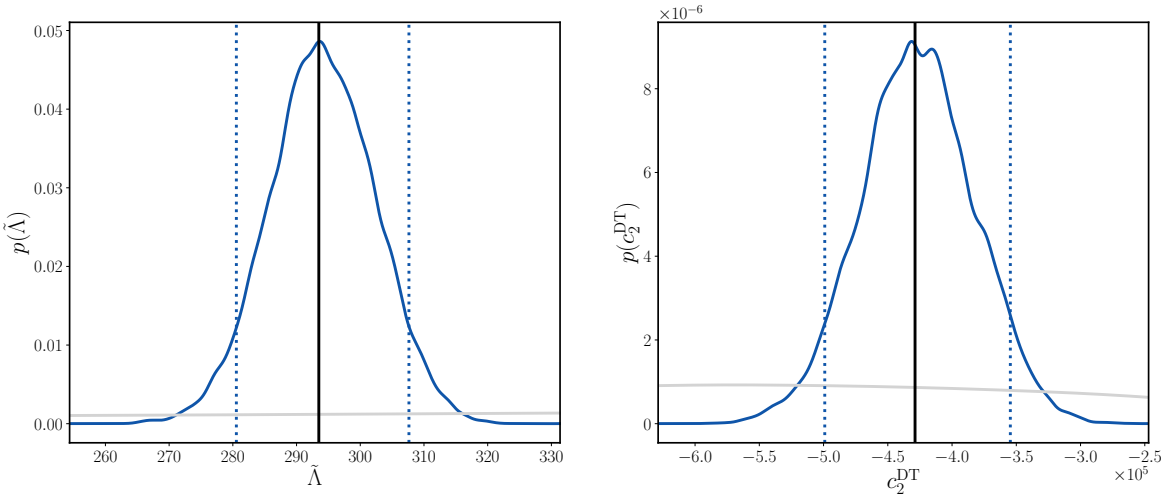

Figure 4.8: *Left*: One-dimensional posterior distribution for $\tilde{\Lambda}$ for the fiducial run, showing the 90% credible intervals (dotted lines), injected value (solid black line) and prior (solid grey line) with prior range $\tilde{\Lambda} \in [0, 1025]$. *Right*: One-dimensional posterior distribution for c_2^{DT} for the fiducial run, showing the 90% credible intervals (dotted lines), injected value (solid black line) and part of the prior (solid grey line) with the full prior range spanning $c_2^{\mathrm{DT}} \in [-4.3 \times 10^6, 0]$.

to independently verify EOS-independent relations [192, 202, 397] and search for phase transitions between the inspiral and post-merger regime [398] and therefore provide a means to study potentially new physics.

In this chapter, we have investigated the detectability of dynamical tides from inspiralling BNS in 3G detectors. First, using the conservative distinguishability criterion [385] we determined the SNRs required to disentangle dynamical from leading order adiabatic tides. We found that for loud enough signals, dynamical tides are indeed distinguishable but that the required SNR depends on the NS EOS, component masses and detector: binaries with a stiff EOS and low total mass present the best candidates for measuring dynamical tides. For a GW170817-like signal we found that irrespective of the EOS and the specific detector network, the distinguishability criterion is always fulfilled since the optimal SNR would be SNR 1031 (2935) for ET (CE) and the highest required SNR to distinguish dynamical tides is 84 and 102 respectively.

We then applied this methodology to a population of BNS: We simulated 10,000 BNS inspiral signals with masses drawn from a double-peaked mass distribution consistent with the galactic double NS *and* recycled pulsar distribution and three different EOS up to a redshift of $z = 0.5$. We found that for the vast majority of signals no tidal information is recovered, and therefore they cannot be discerned from BBHs unless an electromagnetic counterpart is detected simultaneously [399]. In the case of the soft APR4 EOS tidal information can be obtained in only 4.0% (10.2%) of cases, for 3.7% (4.2%) dynamical tides can be measured in addition to adiabatic effects. However, given the BNS detection rates expected for 3G instruments of $10^3 - 10^5$ per year, for a significant number of BNS detections dynamical tides will be distinguishable.

To understand whether simple distinguishability maps into a measurement of the f-mode frequencies of the two stars during the inspiral, we performed full Bayesian

inference on a GW170817-like signal in a CE-ET detector network. While we found that the f-mode frequencies of the individual stars are only constrained to within a few hundred Hz, the leading-order PN phasing coefficient for dynamical tides $c_2^{\rm DT}$ is measured to $\mathcal{O}(30\%)$ and purely adiabatic tides (i.e. $c_2^{\rm DT} = 0$) is excluded at $> 99\%$ confidence. Fisher estimates promise tighter bounds on the f-mode frequencies, but we observe large correlations between the star's tidal deformability $\Lambda_{2,A}$ and its f_2-mode frequency, which are neglected in Fisher estimates for low SNR effects. Similarly, the individual $\Lambda_{2,A}$ are poorly constrained, but the binary tidal deformability parameter $\tilde{\Lambda}$ is measured to within $\sim 5\%$ at the 90% CI. Preliminary studies suggest that similar to $\tilde{\Lambda}$, $c_2^{\rm DT}$ might be a preferred sampling parameter and we leave further investigations to future work. We leave a more comprehensive investigation across the BNS parameter space to future work.

The results presented here assume perfect knowledge of the waveform describing a BNS inspiral in GR as well as the correctness of quasi-URs for tidal parameters. In addition, we assume perfect calibration knowledge when performing parameter estimation. All three assumptions are simplifications and hence pose a caveat to our analyses. Recent work suggests that systematic waveform errors will have the largest impact on astrophysical inference of the nuclear EOS while detector calibration errors still play a crucial but subdominant role [400–402]. A future avenue we will explore is understanding how dynamical tidal information can be incorporated into the joint inference of the astrophysical population and the EOS [403], especially in the presence of correlated parameters [404] and waveform systematics [401]. Another caveat to our analysis is the neglect of spin. In addition, the inclusion of spin precession in the point-particle sector is known to break mass – spin degeneracies, which results in a more accurate mass measurement [410–413] and therefore may improve the measurement of tidal parameters.

We leave the extension to spinning NSs for future work.

Chapter 5

A phenomenological model of gravitational self-force enhanced tides in inspiralling binary neutron stars

Declaration

This chapter is a reformatted version of Ref. [414], *Phenomenological model of gravitational self-force enhanced tides in inspiralling binary neutron stars* accepted for publication in *Phys. Rev. D.* where N. Williams is first author. The concept of creating a phenomenological model fitted to tides within TEOBResumS was posited by P. Schmidt and G. Pratten and builds its methodology from IMRPhenomXAS presented in Ref. [295] by G. Pratten and collaborators. Tutorials and example code for the building of phenomenological models was provided by G. Pratten. Development of ideas for the methodology of the fitting process was a joint effort between N. Williams, P. Schmidt and G. Pratten. Generation of the calibration dataset was done by N. Williams. The fitting process and the PhenomGSF model was coded

by N. Williams. All model validation was completed by N. Williams, with code for mismatch routines, KDE generation and fixed Fourier integration provided by G. Pratten. TEOBResumS-NR hybrid waveforms were coded and generated by N. Williams, with hybridisation code adapted from G. Pratten. Parameter estimation was ran by N. Williams. All figures were created by N. Williams.

5.1 Introduction

Detections of GWs from BNS hold the potential to probe nuclear matter at densities which cannot easily be achieved under laboratory conditions, and shed light on the currently unknown NS EOS [165, 234]. The observation of the inspiralling BNS GW170817 [5, 138] provided the first constraints on the EOS obtained from GWs. Complementary EOS constraints for nuclear matter can be obtained from X-ray observations of pulsars [84, 85] or the measurement of the thickness of the neutron skin in laboratory experiments [133, 415]. Notable differences in inferred constraints on the NS radius between different astrophysical and laboratory-based measurements [370], however, highlight the crucial role of more observations, e.g. from GWs and NICER to resolve the tension.

Matter leaves characteristic imprints on the GW signal, making the signal distinct from that of a BBH. The most prominent GW signature arises from the excitation of a NS's fundamental oscillation modes or f-modes, which, at leading order, is characterised by the quadrupolar tidal deformability λ_2 [165]. Its measurement in GW observations allows us to constrain the EOS [137]. However, in order to do so, waveform models that accurately capture the relevant physics are needed. Current state-of-the-

art tidal waveform models are obtained either within PN theory [165, 275, 276, 278, 280, 416–419], the EOB framework [13, 167, 169, 170, 242, 243, 248, 275, 282, 283], or by utilising a phenomenological approach [9, 246, 297, 298, 420]. One particular advantage of phenomenological waveform models is their computational efficiency, which is highly desirable when performing Bayesian inference which often requires $\sim 10^6 - 10^9$ model evaluations to accurately sample the posterior distributions. The computational efficiency of phenomenological models is achieved by directly describing the waveform as piecewise closed-form expressions in the frequency domain by fitting ansatzes for the amplitude and phase to hybrid waveforms, which combine state-of-the-art analytical knowledge with NR waveforms. This approach has been successfully applied to obtain fast waveform models for BBHs [295, 296, 299, 300, 421–423], NSBHs [424, 425] and BNSs [9, 298]. Alternative approaches to decreasing the waveform generation cost include the SPA [395], reduced-order modelling [250] and post-adiabatic expansion [426]. Parameter estimation itself can also be sped up by techniques such as relative binning [427–431], multi-banding [432, 433] and reduced-order quadratures [434–437].

Current BNS waveform models do not only differ in their computational speed but also in their physics content. In particular, the phenomenological models of the NRTidal series [9, 297, 298] are calibrated to a limited range of BNS simulations. While this allows for the incorporation of non-perturbative information, it also comes with some caveats: firstly, the NR data are themselves limited in their physics content due to the complexity of matter simulations. Secondly, different tidal effects that arise in the strong-field regime such as higher-order multipoles or other oscillation modes including pressure (p-) and gravity (g-) modes, are difficult to separate in NR simulations and hence when modelled phenomenlogically are entangled in the parameterisation. Thirdly, NR simulations make specific assumptions on the nuclear EOS

such a hadronic composition. Finally, to reduce the dimensionality of the parameter space, tidal models also often invoke quasi-EOS independent URs [192] between different tidal parameters. While this dimensional reduction may be desirable, any such assumptions will limit the applicability of the model and exclude them from being used for exploring e.g. the possibility of the presence of exotic matter such as hyperons or deconfined quarks or boson stars [438].

In this chapter we present PhenomGSF, a new phenomenological tidal phase model in the frequency-domain based on the tidal EOB model TEOBResumS [13], which can readily be added to *any* BBH baseline to provide a complete BNS model. We restrict our model to the dominant tidal effects associated with the quadrupolar gravitoelectric static Love number k_2 including tidal contributions informed by GSF, and only model the phase of the $\ell = |m| = 2$ mode. PhenomGSF is calibrated to both equal and unequal mass systems and freely fits the component tidal deformabilities without assuming URs, hardonic matter or specific parameterisations of the EOS.

The chapter is organised as follows: Section 5.2 details some preliminaries, the used conventions and parameterisations. In Sec. 5.3 we specify the input waveforms used to build the model, the parameter space of the model and detail the construction of TEOBResumS-NR hybrid waveforms. Then, in Sec. 5.4 we detail the hierarchical phenomenological fitting procedure and give details of the model construction. In Sec. 5.5 we validate our model against the input waveforms, a set of independent waveforms as well as a selection of NR-hybrid waveforms. We then perform Bayesian inference with PhenomGSF on model injections, a hybrid waveform and reanalyse the data of GW170817. We then conclude with a discussion in Sec. 5.6. The complete PhenomGSF fit can be found in App. A.2, while the full parameter estimation results

for GW170817 are shown in App. A.3.

5.2 Preliminaries

PhenomGSF models the tidal phase of the $\ell = |m| = 2$ spin-weighted spherical harmonic modes (Eq. (1.35)) of the GW signal of nonspinning NS inspirals. As we will be only utilising the quadrupolar $\ell = 2$ tidal deformability $\Lambda_{2,A}$ from this point forwards, for simplicity we use convention $\Lambda_{2,A} \equiv \Lambda_A$ for the Ath star. We utilise the orbital plane reflection symmetry of aligned spin systems (Eq. (1.39)) to map between the $(m = 2)$-mode and $(m = -2)$-mode.

Each mode can be further decomposed into an amplitude $A_{\ell m}(f, \vec{\theta})$ and a phase $\psi_{\ell m}(f, \vec{\theta})$ (Eq. (1.38)). The presence of tides predominantly affects the phase, although there are small amplitude corrections [235], which we do not take into account here, yielding

$$\tilde{h}_{22}(f, \vec{\theta}) = A_{22}^{\rm BBH}(f, \vec{\theta}) e^{-i\psi_{22}(f,\vec{\theta})}, \tag{5.1}$$

where $\psi_{\ell m}$ denotes the complete Fourier phase given by the point particle phase plus the tidal phase

$$\psi_{\ell m} = \psi_{\ell m}^{\rm BBH} + \psi_{\ell m}^{\rm PhenomGSF} + \psi_{\ell m}^{\rm SS}, \tag{5.2}$$

where $\psi_{\ell m}^{\rm SS}$ denotes the tidal self-spin PN corrections [236, 247] described in more detail in Sec. 5.4.4.

5.3 Input waveforms

5.3.1 TEOBResumS waveforms

The EOB framework provides a map from the general relativistic two-body problem to the motion of a test particle in a deformed effective spacetime as introduced in Sec. 3.3.2. The EOB formalism allows one to calculate the full orbital dynamics and the complete waveform through merger. The EOB Hamiltonian describes the conservative dynamics with dissipative effects entering through the radiation reaction force in the equations of motion. Here we provide an overview of how tidal effects enter the TEOBResumS [13], with a particular focus on the GSF-resummed tidal potentials in the Hamiltonian introduced in [284] and extended in [246, 248]. We emphasise that no NR information is included in the tidal sector. Tidal contributions also enter the radiation reaction force within the waveform multipoles as PN corrections to the amplitude (see [242] for more details). The EOB tidal model outlined here sets the baseline for the tidal content included in the PhenomGSF calibration dataset.

Tidal forces enter the Hamiltonian through a modification of the EOB radial potential

$$A(u) = A_0(u) + A_T(u), \tag{5.3}$$

where $u = 1/r$ is the Newtonian potential, $A_0(u)$ denotes the point-particle potential, and $A_T(u)$ encodes the tidal interactions [171]

$$\begin{aligned} A_T(u) = \sum_{\ell} \Big[& A_A^{(\ell+)\mathrm{LO}}(u)\hat{A}^{(\ell+)}(u) \\ & + A^{(\ell-)\mathrm{LO}}(u)\hat{A}^{(\ell-)}(u)\Big] + (A \leftrightarrow B), \end{aligned} \tag{5.4}$$

where A, B label the stars, $(+)$ denotes the gravitoelectric sector, $(-)$ the gravitomagnetic sector, and $\hat{A}$ denotes terms beyond leading-order (LO).

The gravitoelectric tidal coefficients broadly relate to mass multipole moments induced in a star by an external gravitoelectric tidal field and the gravitomagnetic tidal coefficients to the current multipoles moments induced in a star by an external gravitomagnetic field [171]. The gravitomagnetic tides are therefore typically associated to frame-dragging effects which in turn excite inertial modes in the NS [180, 405, 439], including those that are associated to the Coriolis effect. As we predominantly focus on non-spinning binaries, we choose not to implement the gravitomagnetic terms at this time. The following therefore pertains only to the gravitoelectric tides. Likewise, we restrict ourselves to the dominant $\ell = 2$ quadrupole and disregard all higher multipole moments unless otherwise stated.

Under the above restrictions, the Newtonian tidal potential can be written as

$$A^{\mathrm{LO}}(u) = -\kappa_A u^6, \tag{5.5}$$

where κ_A denotes the electric tidal coupling constant, which can be expressed in terms of the dimensionless tidal love number $k_A^{(\ell)}$ as

$$\kappa_A = 2k_A^{(2)} \frac{X_B}{X_A} \left(\frac{X_A}{\mathcal{C}_A}\right)^5, \tag{5.6}$$

$$= 3X_B X_A^4 \Lambda_A, \tag{5.7}$$

where $\mathcal{C}_A = m_A/R_A$ denotes the compactness parameter, and the dimensionless tidal

deformability is related to the Love number via

$$\Lambda_A = \frac{2}{3} k_A^{(2)} \mathcal{C}_A^{-5}. \tag{5.8}$$

The EOB radial potential subsequently simplifies to

$$A_T = -[\kappa_A u^6 \hat{A}_A(u) + \kappa_B u^6 \hat{A}_B(u)]. \tag{5.9}$$

Following [248, 284], the terms beyond LO admit a series expansion in terms of the expansion parameter $X_A = m_A/M \ll 1$, informed by results at first-order GSF

$$\hat{A}_A(u) = \hat{A}^{0\mathrm{GSF}} + X_A \hat{A}^{1\mathrm{GSF}} + X_A^2 \hat{A}^{2\mathrm{GSF}}. \tag{5.10}$$

While GSF is typically considered within the context of systems with large mass ratios [440], computed GSF terms have been demonstrated to provide insights into higher-order tidal PN information currently available [283]. In addition to this, resummed GSF information gives rise to a pole in the GSF potential at the light-ring, which can be utilised to enhance attractiveness of the tidal potential in the last few orbits [284]. This additional attraction improves agreement with NR simulations, which predict stronger tidal potential compared to the those provided by PN and EOB [246, 248, 284]. The 0GSF potential is given by [284]

$$\hat{A}^{0\mathrm{GSF}}(u) = 1 + \frac{3u^2}{1 - r_{\mathrm{LR}} u}, \tag{5.11}$$

where r_{LR} denotes the EOB light-ring.

The 1GSF potential is expressed in terms of the light-ring singularity together with

a fit against strong-field GSF information [248]

$$\hat{A}^{\rm 1GSF} = \frac{5u}{2(1-3u)^{7/2}}(1-a_1u)(1-a_2u)\frac{1+n_1u}{1+d_2u^2} \tag{5.12}$$

with coefficients

$$\begin{aligned} a_1 &= 8.53352 \quad a_2 = 3.04309 \\ n_1 &= 0.84006 \quad d_2 = 17.7324. \end{aligned} \tag{5.13}$$

In contrast, the 2GSF potential only incorporates partial knowledge of the second-order GSF result [283]

$$X_A^2 \hat{A}_A^{\rm 2GSF}(u) = \frac{337}{28} X_A^2 u^2 \left(1 + \mathcal{O}(u)\right), \tag{5.14}$$

such that near the light-ring, the quadrupolar electric tidal potential must blow up as [284]

$$\frac{c_2 X_A^2}{(1-r_{\rm LR}u)^p}, \qquad p \geq 4. \tag{5.15}$$

The 2GSF tidal potentials can therefore be written as

$$\hat{A}^{\rm 2GSF} = \frac{337}{28}\frac{u^2}{(1-r_{\rm LR}u)^p}, \tag{5.16}$$

where the value of p depends on as-of-yet-unknown 2GSF information. It was argued in [284] that $p \geq 4$ together with a further argument that $p \leq 6$. Following [246, 248], the unknown exponent is taken to be $p = 4$, though both coefficients may generically have mass ratio and EOS dependence.

We choose to not include dynamical tidal effects within PhenomGSF, which would further increase the dimensionality of the parameter space, corresponding to each stars fundamental mode frequency ω_2, unless we use URs to relate the values of ω_2 to Λ_2. We note that due to the modularity of our model, it is in principle straight forward to incorporate the PN dynamical tides using the fmtidal model [278].

As TEOBResumS is natively defined in the time-domain, we need to transform the model to frequency-domain in order to calibrate PhenomGSF. We use the numerical SPA implemented in TEOBResumS [292]

$$\frac{d^2\psi(f)}{d\omega} = \frac{1}{\omega}\frac{d\psi(t)}{d\omega},$$

where $\omega = 2\pi f = \dot{\psi}(t)$. We use the SPA over a full Fourier transform due to small dephasing that was arising from spectral leakage and tapering in the BBH limit. We independently verified that the SPA agrees with the Fourier transform on a sub-radian scale over the parameter space under consideration.

5.3.2 Parameter space

PhenomGSF is calibrated across the parameter space $q \in [1, 3]$ and $\Lambda_{1,2} \in [0, 5000]$ using 8446 TEOBResumS waveforms. The total mass M scales out of the tidal phase when we consider the phase as a function of geometric frequency Mf. This allows us to reduce the problem to a 3-dimensional parameter space governed by a single mass parameter, taken to be either q or η.

For sampling the mass ratio, we choose a log-uniform spacing in order to have higher resolution near the equal-mass limit $q = 1$. Due to the hierarchical fitting process employed later on and explained in Sec. 5.4, a subset of 446 of these waveforms

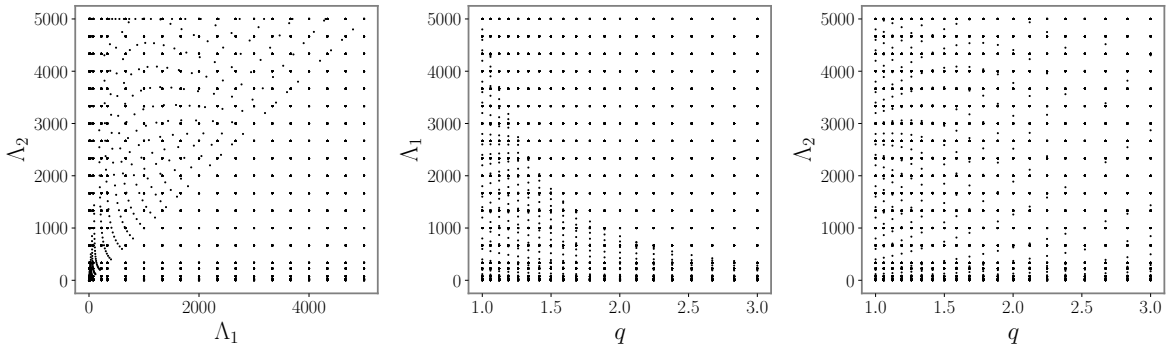

Figure 5.1: Visualisation of the parameter space covered by the TEOBResumS waveforms used in the calibration of PhenomGSF.

was specifically generated such that $\delta\tilde{\Lambda} = 0$. Within this subset, $\tilde{\Lambda}$ is uniformly sampled between the limits defined by a given q for $\Lambda_{1,2} \in [0, 5000]$. An additional layer of log-uniform spaced waveforms with $\tilde{\Lambda} \in [0, 200]$ is also added in order to accurately capture the approach to the BH limit, i.e. $\tilde{\Lambda} = 0$. The remaining 8000 waveforms are sampled uniformly directly in $\Lambda_{1,2}$, including another log-uniform layer inserted between $\Lambda_{1,2} = 0$ and the first uniformly chosen point. A visualisation of the calibration region is shown in Fig. 5.1.

An important point to note is that we do not assume hadronic physics, i.e. we do not enforce for $q \neq 1$, $\Lambda_2 > \Lambda_1$, and for $q = 1$, $\Lambda_2 = \Lambda_1$ when sampling the training space. This is done deliberately to ensure that the model is well-behaved without imposing such limiting assumptions and that no pathologies occur.

This is a particular strength of PhenomGSF, as it allows for more flexibility and separates it from models that are informed by NR data that assume a hadronic EOS. Consequently, this also allows the consideration of objects such as boson stars and quark stars and other exotic models which are not comprised of hadronic matter.

When generating the TEOBResumS waveforms, we choose a sampling rate of 16384 Hz and a starting frequency of 10 Hz below the equivalent of $0.0005Mf$ in Hz

for a given total mass M to allow for a buffer between the start of the waveform and the fitting regime. We stop the EOB evolution at an orbital separation of $r = 4M$. We also explicitly turn off gravitomagnetic tides, dynamical tides, the use of URs, and set the octupolar and hexadecapolar tidal deformabilities to 10^{-8}, the lowest possible value we found.

5.3.3 TEOBResumS-NR hybrids

For the model validation of PhenomGSF we perform comparisons against a set of six TEOBResumS-NR hybrid waveforms. The NR waveforms are taken from the CoRe database [12, 307, 441] and were produced with the BAM code (see Refs. in [12] for details), which we hybridise with TEOBResumS waveforms using identical settings to those used for the calibration of PhenomGSF and generated from 30 Hz. Details of the six aligned-spin NR waveforms used in this paper are given in Tab. 5.1. The choice of these simulations is motivated by simulation length requirements and minimal residual eccentricity.

Our $(\ell, m) = (2, 2)$ hybrids are generated as follows: We take the Newman-Penrose scalar $\psi_{4,22}$ at the largest fixed extraction radius available r_0 for the simulation and extrapolate it to infinity via [443, 444]

$$\psi^{\infty}_{4,22}(t, r_0) = \left(1 - \frac{2M_{\rm ADM}}{r_A}\right) \times \left[\psi^{r_0}_{4,22}(t, r_0) - \frac{2}{r_A}\int_0^t \psi^{r_0}_{4,22}(t', r_0)dt'\right], \tag{5.17}$$

where $r_A = r_0[1 + M_{\rm ADM}/(2r_0)]^2$ and $M_{\rm ADM}$ is the ADM mass of the system [445] obtained from the CoRE metadata.

We implement double time-integration via the fixed frequency integration (FFI) to

CoRE ID	EOS	$M_{\rm ADM}\,[M_\odot]$	q	Λ_1	Λ_2	χ_{1z}	χ_{2z}	e	$f_{\rm NR}$ [Hz]	Ref.
BAM 0001	2B	3.05	1.0	126.7	126.7	0.0	0.0	7.0×10^{-3}	454.5	[246]
BAM 0120	SLy	3.05	1.0	346.1	346.1	0.0	0.0	1.5×10^{-2}	424.4	[442]
BAM 0127	SLy	3.07	1.5	93.1	1367.9	0.0	0.0	8.0×10^{-3}	426.3	[442]
BAM 0124	SLy	2.76	1.5	191.0	2313.7	0.0	0.0	1.2×10^{-2}	407.8	[442]
BAM 0104	SLy	2.99	1.0	388.2	388.2	0.19	0.19	7.4×10^{-4}	453.1	[297]
BAM 0066	MS1b	2.94	1.0	1531.5	1531.5	0.18	0.18	1.9×10^{-3}	427.2	[297]
BAM 0095	SLy	2.7	1.0	390.1	390.1	0.0	0.0	4.0×10^{-4}	453.3	[297]

Table 5.1: Summary of the parameters of the aligned-spin NR waveforms from the CoRe database used to create the TEOBResumS-NR hybrids. The columns denote the CoRE ID number, the EOS [16] used for the simulations, the Arnowitt–Deser–Misner (ADM) mass $M_{\rm ADM}$, mass ratio q, tidal deformabilities Λ_1, Λ_2, component spins χ_1, χ_2, the residual eccentricity e, the NR starting frequency $f_{\rm NR}$, and relevant references. All quantities are taken from the CoRE metadata.

convert to strain (Eq. (3.30)), where the waveform is windowed such that it smoothly tapers to zero below $t = 200M$ to remove any residual non-physical "junk radiation" at the start of the NR waveform due to imperfect initial data. This process eliminates artefacts which would otherwise impact the analysis. We also taper to zero at an arbitrary time just after merger for each waveform to avoid edge effects in the FFI. The waveform is then zero-padded to reduce any spectral leakage. We implement the FFI following Ref. [446] choosing the NR starting frequency $f_{\rm NR}$ given in Tab. 5.1 as the fixed-frequency to perform the integration.

The NR waveforms are then hybridised with TEOBResumS waveforms, where all settings are the same as those detailed in Sec. 5.3 for the TEOBResumS generation with the exception of using the time-domain rather than the SPA implementation. The TEOBResumS waveforms are initialised with the same intrinsic parameters as the NR

simulations. We note here that we used the non-eccentric version of TEOBResumS, however, the NR waveforms have non-negligible eccentricity as shown in Tab. 5.1, which constitutes a source of error in the hybridisation procedure.

For the hybridisation between the NR and TEOBResumS waveforms, we first ensure that the amplitudes of both waveforms peak at $t = 0$, and then choose a Planck window $\sigma(t)$ [447] across a time interval $[t_1, t_2]$ to smoothly join the two waveforms such that

$$\sigma(t) = \begin{cases} 0 & \text{if } t < t_1, \\ \frac{1}{1+e^z}, z = \frac{1}{t} - \frac{1}{1-t} & \text{if } t_1 \leq t \leq t_2, \\ 1 & \text{if } t > t_2, \end{cases} \tag{5.18}$$

where we find that $t_1 = 1200M$ (with the exception of BAM 0095, where $t_1 = 1000M$) after the start of the NR waveform and a window length of $1000M$ are sufficient. Across this window a time domain alignment is performed by minimising

$$\min \left[\int_{t_1}^{t_2} \left| \psi^{\text{TEOB}}(t) - \psi^{\text{NR}}(t + t_0) - 2\psi_0 \right|^2 dt \right], \tag{5.19}$$

and a visual inspection to check for the continuity of amplitude, phase and phase derivative is done as shown in Fig. 5.2.

5.4 Tidal phase model

5.4.1 Phenomenological modelling

A key motivation for building phenomenological waveform models is that they can yield closed-form frequency-domain expressions, making them extremely computation-

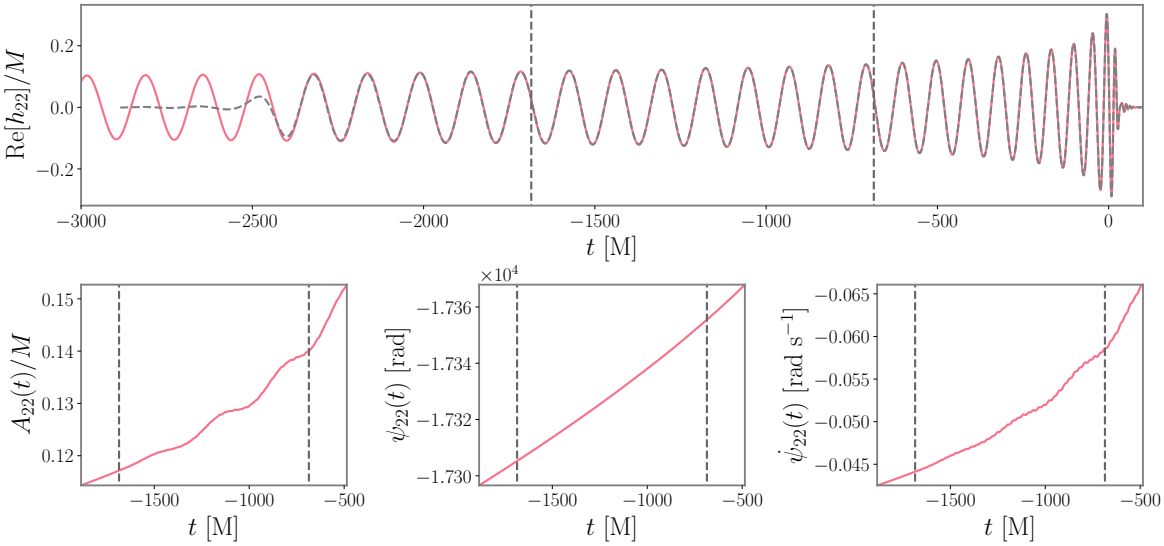

Figure 5.2: TEOBResumS-NR hybrid example for BAM_0001. *Top panel*: Real part of h_{22} showing the NR data (dashed grey), the aligned TEOBResumS waveform (pink) and hybridisation region marked by the two dashed vertical lines. *Bottom panel*: Close ups of the hybridisation region for the resulting hybrid waveform for the amplitude (left), the phase (middle), and the first time derivative of the phase (right).

ally efficient for GW data analysis whilst retaining a high level of accuracy. As a result, phenomenological models have become a very popular choice in many aspects of gravitational-wave data analysis, including matched-filter searches, e.g. [448–453], and Bayesian inference, e.g. [29, 36, 157–159, 454–457]. We note that an alternative phenomenological model of TEOBResumS using a different approach was developed in Ref. [242].

In PhenomGSF, we follow the framework previously described for the BBH waveform model IMRPhenomXAS [295]. We will first briefly outline the main elements in the construction of a phenomenological phase model before presenting the detailed fits in the remainder of this section.

We recall that the goal is to build a closed-form expression of the tidal phase of binary NSs in the frequency domain. The first step is to choose an appropriate mathematical ansatz for the tidal phase for each section of the different stages of the binary evolution. As we are only considering the inspiral phase here with a known PN expansion, a natural choice is a parameterised continuation of the finite-order PN series, schematically given by

$$\psi_T(\vec{\theta}, Mf) = \psi_T^{\rm PN}(\vec{\theta}, Mf) + \sum_i a_i(\vec{\theta})(Mf)^i, \tag{5.20}$$

where $\vec{\theta}$ denotes the model parameters and Mf is the dimensionless GW frequency.

Note that the powers of the frequency are for illustrative purposes only. In the latest generation of phenomenological models, the phenomenological coefficients $a_i(\vec{\theta})$ are not directly calibrated due to numerical instabilities and poor numerical conditioning [295]. Instead, the phenomenological coefficients are reconstructed by solving a linear system of equations expressed in terms of a finite number of collocation points that are placed

at prescribed frequency nodes, $\{Mf_j\}$.

In order for this to be a deterministic system, the number of constraints, e.g. boundaries, *and* collocation points must equal the total number of free parameters. At each collocation point, a fit is constructed such that

$$\lambda_j(\vec{\theta}) \equiv \psi_T(\vec{\theta}, Mf_j). \tag{5.21}$$

The resulting linear system of equations can then be solved for the phenomenological coefficients using standard matrix methods, e.g. via an lower-upper decomposition.

5.4.2 Tidal residual fit

For the PN baseline, we use TaylorF2 for computational efficiency with quadrupolar adiabatic tidal contributions up to 7.5PN [275, 276, 283]. We add five pseudo-PN coefficients a^i that are calibrated to the TEOBResumS dataset

$$\psi_{\ell m}^{\text{PhenomGSF}} = \psi_T^{7.5\text{PN}} + \sum_{i=1}^{5} a^i \left(\eta, \tilde{\Lambda}.\delta\tilde{\Lambda}\right) (Mf)^{(10+i)/3}. \tag{5.22}$$

Instead of directly fitting the phase, we fit the residual between TEOBResumS and TaylorF2,

$$r \equiv \psi_T^{\text{TEOB}} - \psi_T^{7.5\text{PN}} - 2\pi Mft_0 + \phi_0, \tag{5.23}$$

where $\{t_0, \phi_0\}$ are two gauge degrees of freedom corresponding to an overall time and phase shift and are determined by minimising the residuals over a frequency interval

$$\min \left[\int_{0.0005M}^{0.001M} |r|^2 dMf \right]. \tag{5.24}$$

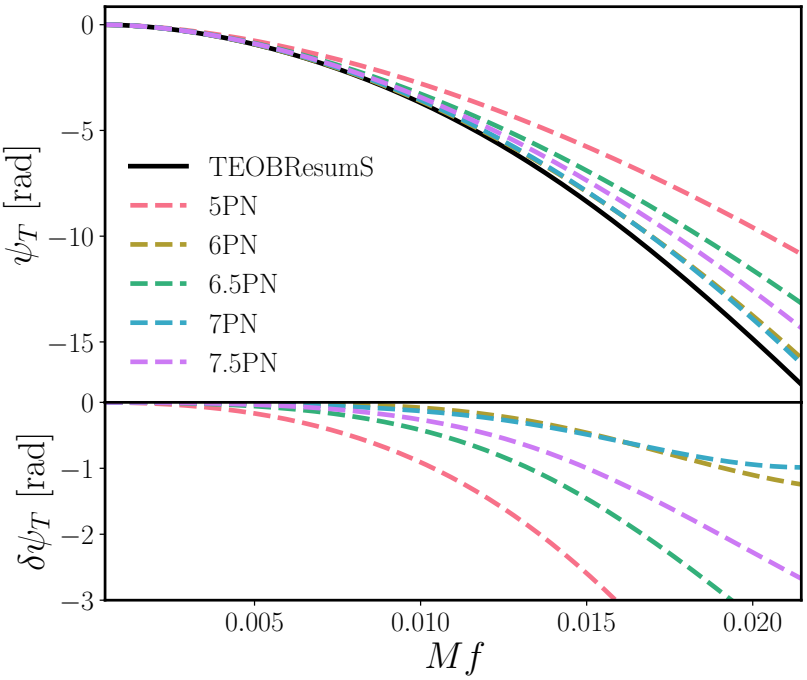

Figure 5.3: *Top*: Tidal phase ψ_T as a function of frequency for a binary with parameters $\{q = 1, \Lambda_1 = \Lambda_2 = 600\}$. We show the TEOBResumS data (solid black) alongside several TaylorF2 approximants of different PN orders (dashed lines) aligned as per Eq. (5.24). *Bottom*: Phase difference $\delta\psi_T = \psi_T^{\rm TEOB} - \psi_T^{\rm xPN}$ between between TEOBResumS and each Taylor approximant.

A choice that must be made is the PN baseline for the phenomenological model. It is well known that the PN expansion is slowly converging, and higher-order PN terms do not necessarily lead to smaller residuals. In fact, successively higher-order PN terms often lead to partial cancellations. Whilst the 6PN and 7PN terms yield a smaller residual relative to TEOBResumS, they also display a turning point at high frequencies for large tidal deformabilities. This introduces additional complexity into the function which can be difficult to accurately fit, often requiring more phenomenological coefficients in the PhenomGSF ansatz. Therefore, we adopt a 7.5PN baseline as it is the highest-order PN series and yields a monotonic residual across the parameter space, see Fig. 5.3.

We choose collocation points at Gauss-Chebyshev nodes to reduce fitting errors in comparison to equidistant nodes [295], in which the i^{th} node is placed at

$$f_i = f_{\min} + \frac{f_{\max} - f_{\min}}{2}\left(1 + \cos\left[\frac{i\pi}{n}\right]\right), \tag{5.25}$$

where $[f_{\min}, f_{\max}]$ is the frequency range over which the nodes are placed and n is the number of collocation points. We find that five phenomenological coefficients provides an optimal balance between goodness-of-fit and the subsequent computational efficiency of the model. An example of this procedure is shown in Fig 5.4.

A practical consideration is that the choice of termination frequency dictates the frequency spacing of the collocation points, and the concomitant structure of each phenomenological fit. A choice of a constant termination frequency would correspond to each collocation point lying at the same geometric frequency at every point in the parameter space. This leads to problems for binaries with extremely large and extremely small tidal deformabilities, with the relevant morphological features being

poorly captured. For example, a termination frequency that is too high can result in information beyond the frequency of the minimum energy circular orbit (MECO) $f_{\rm MECO}$ being included, where the PN expansion has formally broken down.

To resolve this, one may try to adopt a parameter dependent termination frequency, though this often results in a more complex structure to the global fit of the collocation values. One such example is the NR informed contact frequency $Mf_{\rm contact}$ [12], though we find that this leads to a number of subtle issues. First, $Mf_{\rm contact}$ spans a large dynamical range across the parameter space, introducing significant substructure to the fits. Second, we find issues in constructing a fit across the parameter space related to how the frequency smoothly transitions to the black-hole limit and exotic equations-of-state that are outside the calibration regime of $Mf_{\rm contact}$, especially when $\Lambda_2 > \Lambda_1$.

Overall, we find that the best compromise is the non-spinning hybrid minimum energy circular orbit (MECO) frequency, $Mf_{\rm MECO}$, introduced in [458]. This spans a comparatively small range of frequencies that are well-behaved and simplify the resulting phenomenological fits. In practice, we use the phenomenological fit for $Mf_{\rm MECO}$ provided in Ref. [295],

$$Mf_{\rm MECO}(\eta) = \frac{a_0 + a_1\eta + a_2\eta^2 + a_3\eta^3}{1 + b\,\eta}, \tag{5.26}$$

with coefficients

$$\begin{aligned} a_0 &= 0.018744, & a_1 &= 0.007790, \\ a_2 &= 0.003940, & a_3 &= -0.000067, \\ b &= -0.104233. \end{aligned}$$

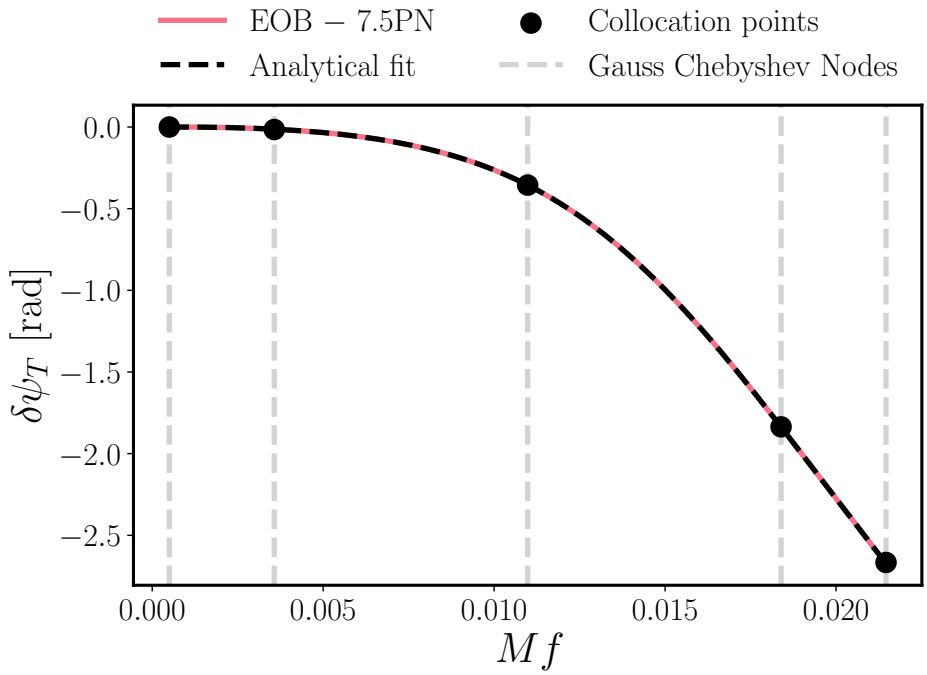

Figure 5.4: Example of a tidal residual $\{q = 1, \Lambda_{1,2} = 600\}$ as a function of frequency (pink solid line) with the corresponding analytical fit from a 5^{th} order polynomial (black dashed line). The Gauss-Chebyshev nodes (grey dashed line) are shown alongside their corresponding collocation points (black circles).

The TEOBResumS waveforms are then generated over the frequency interval $[Mf_{\min}, Mf_{\max}] = [0.0005M, Mf_{\text{MECO}}]$. For a $2M_\odot$ binary, the lower frequency limit corresponds to 50Hz, which is significantly below the GW frequency ($\sim$ 400Hz) where tidal effects introduce a measurable phase difference relative to the BBH case [165]. As we do not recalibrate the point-particle sector, we find no practical benefit in going to lower starting-frequencies.

5.4.3 Parameter space fits

While we sample the binary parameter space in $\{q, \Lambda_1, \Lambda_2\}$ to build our training dataset, we transform to $\{\eta, \tilde{\Lambda}, \delta\tilde{\Lambda}\}$ to construct the PhenomGSF model. At each col-

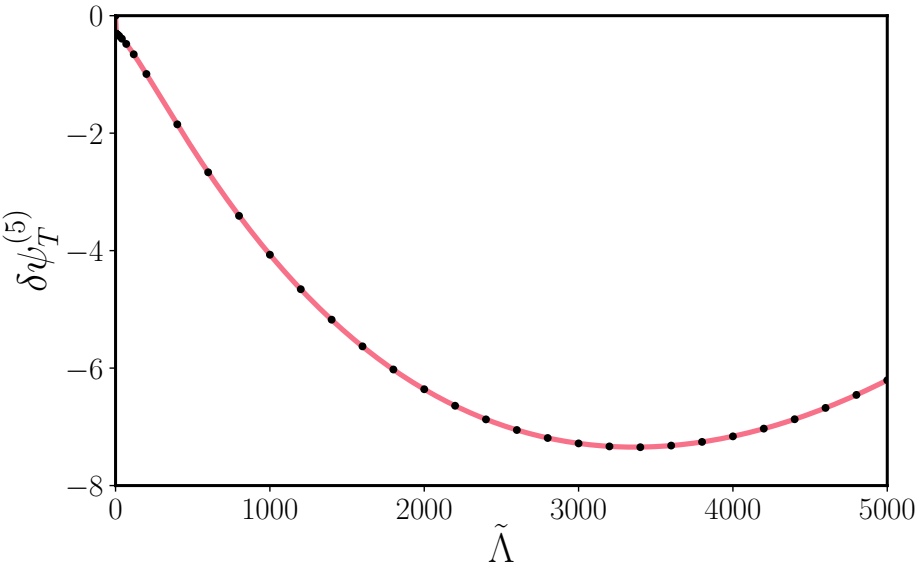

Figure 5.5: 1D fit for equal mass ($\eta = 0.25$) systems with $\delta\tilde{\Lambda} = 0$ across $\tilde{\Lambda}$ at the 5^{th} colocation point. The values of the dephasing at this colocation point are shown (black dots), as well as the final Pade fit (pink solid line).

location point, we construct a fit for the value of the collocation point. This provides a map from $\{\eta, \tilde{\Lambda}, \delta\tilde{\Lambda}\}$ to the value of residual at the collocation node. We explored further reducing the parameter space to $\{\eta, \tilde{\Lambda}\}$, but this resulted in a significant degradation of the accuracy. As such, in this section we only discuss the full 3D fit. Due to the high dimensionality, we adopt a hierarchical approach in which the parameter space fits are constructed dimension-by-dimension [295, 459]. In practice, the starting point is a 1D fit across a well-defined subspace. From this, we can construct the 2D fit by expanding the 1D basis in terms of the second dimension. The complete 3D information is then incorporated by re-expanding the 2D basis in terms of the final dimension. All fits are computed using Mathematica's `NonlinearModelFit` package.

1D Fit

The 1D fit is taken to correspond to the equal mass, $\eta = 0.25$, and equal tidal deformability, i.e. $\delta\tilde{\Lambda} = 0$, subspace. In Fig. 5.5, we show the dephasing at the fifth collocation point as a function of $\tilde{\Lambda}$. This collocation point corresponds to $Mf_{\rm MECO}$. We note that there is a notable change in the slope of the fit as $\tilde{\Lambda} \to 0$ corresponding to the transition from a binary NS to a BBH, which is related to the minimum tidal deformability enforced in TEOBResumS. In practice, we find that such features do not cause significant issues in the fitting procedure and we have verified that the model extrapolates sufficiently smoothly to the BBH limit.

We fit polynomial ansatzes against the data up to various orders I

$$F(\eta = 0.25, \tilde{\Lambda}, \delta\tilde{\Lambda} = 0) = \sum_{i=0}^{I} a_i \tilde{\Lambda}^i, \tag{5.27}$$

where a best fit is defined for the lowest Bayesian Information Criterion (BIC), which attempts to avoid overfitting by adding a penalty for the number of parameters in a given model, e.g. see discussion in [459]. After selecting the best fit, we construct a Padé approximant at a given order, which helps to effectively resum the information,

$$\sum_{i=0}^{I} a_i \tilde{\Lambda}^i \to \frac{\sum_{j=0}^{J} b_j \tilde{\Lambda}^j}{1 + \sum_{k=1}^{K} c_k \tilde{\Lambda}^k}, \tag{5.28}$$

where $J, K \leq I$. A benefit of using Padé approximants is that they are more robust when extrapolating outside the calibration region than standard Taylor expanded results [460].

As before, we construct a range of Padé approximants with differing orders and use NonlinearModelFit to infer the BIC. The residuals and BIC are used to determine

the functional form of the final 1D fit.

2D Fit

To obtain the $\{\eta, \tilde{\Lambda}\}$ fit, we expand Eq. (5.28) about η keeping $\delta\tilde{\Lambda} = 0$. The hierarchical process involves inserting a polynomial of order M into the 1D fit via

$$a_l \to a_l \sum_{m=0}^{M} b_{lm}\eta^m. \tag{5.29}$$

We only apply this insertion to the numerator of the 1D fit Eq. (5.28) to avoid singularities. To asses the fit quality we found that in the 2D case, the penalty introduced in the BIC is not sufficient to avoid over-fitting. We introduce 3 sets of randomly generated data in the subparameter space $\{\eta, \tilde{\Lambda}, \delta\tilde{\Lambda} = 0\}$ and evaluate the goodness of fit between the independent data and the proposed ansätze. To measure the goodness-of-fit, we use an R^2 criterion

$$R^2 = 1 - \frac{\sum_i (r_i - \hat{r}_i)^2}{\sum_i (r_i - \bar{r}_i)^2}, \tag{5.30}$$

where r_i is the residual fit value, $\hat{r}_i$ is the true value, and $\bar{r}_i$ is the mean. We impose a condition of $1 - R^2 \leq 10^{-3}$, with fits exceeding this tolerance being discarded. Due to the increasing complexity of the higher-order fits, we evaluate the BIC for each fit with the highest-scoring, and therefore lowest contributing factor, being removed. This process is iterated until 1-R^2 decreases by at least an order of magnitude. This helps eliminate parameters in the fit that are not contributing and slowing the computation time down. An example of a 2D fit is shown in Fig. 5.6.

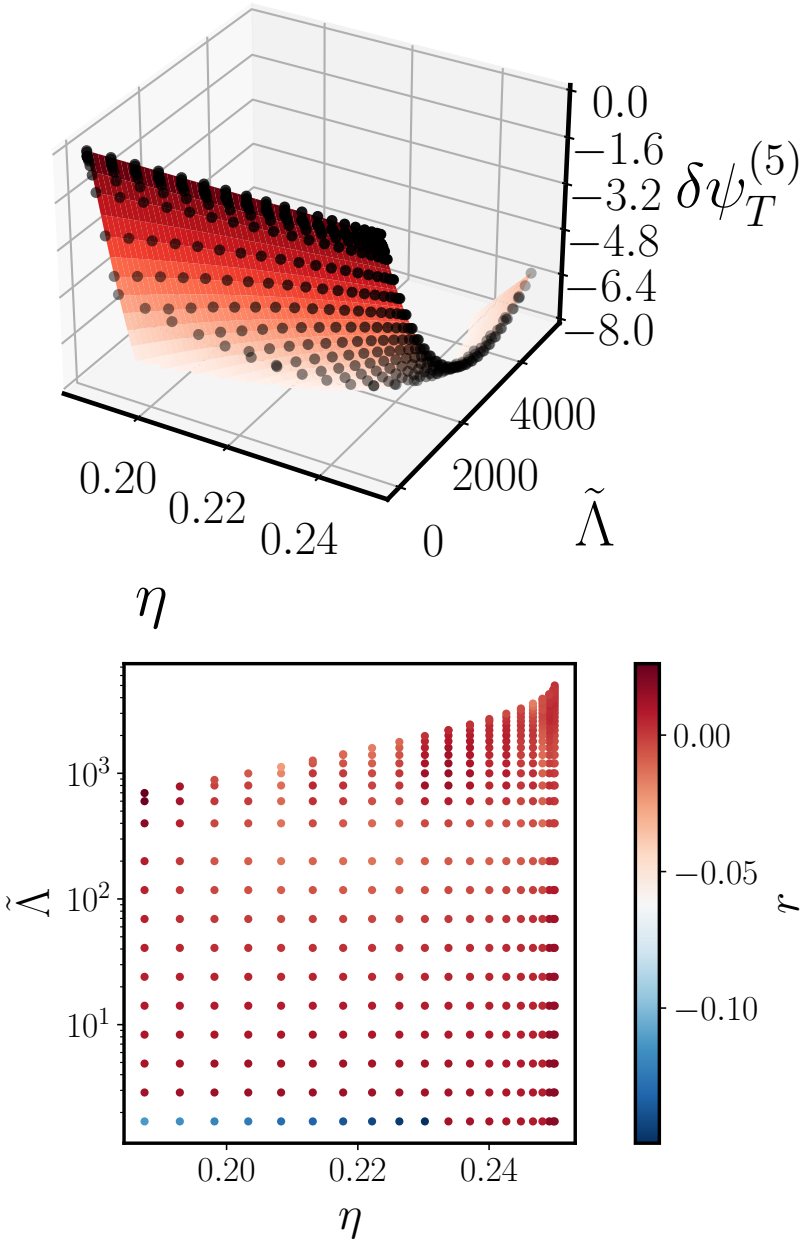

Figure 5.6: *Above*: 2D fit across $\{\eta, \tilde{\Lambda}\}$ for $\delta\tilde{\Lambda} = 0$ at the 5^{th} collocation point. The values of the dephasing at this collocation point are shown (black dots), as well as the final 2D fit (red surface). *Below*: Residuals between the 2D fit and the values of dephasing $r = \delta\psi_T^{(5),\text{fit}} - \delta\psi_T^{(5),\text{true}}$.

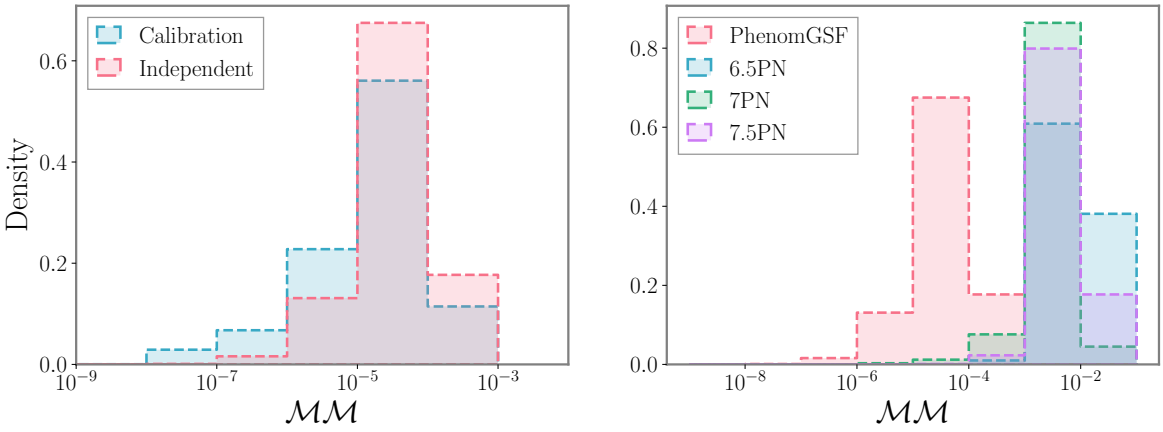

Figure 5.7: Mismatches between TEOBResumS and several other tidal models. *Left panel*: Mismatches of PhenomGSF against the calibration data (blue) as well as randomly selected binaries within the calibration region but not seen in the fitting (pink). *Right panel*: Mismatches of PhenomGSF data (pink), and TaylorF2 6.5PN (blue), 7PN (green) and 7.5PN (purple) and against TEOBResumS.

3D Fit

This process is then repeated for the full 3D fit, with all input data, covering the full $\eta, \tilde{\Lambda}, \delta\tilde{\Lambda}$ space as detailed in Sec. 5.3. Once again a polynomial of order N is inserted in the numerator

$$a_l b_{lm} \to a_l b_{lm} \sum_{n=1}^{N} c_{lmn} \delta\tilde{\Lambda}^n. \tag{5.31}$$

Note here that by definition $\delta\tilde{\Lambda} = 0$ recovers the 2D case. Once again the same R^2 criterion as in the 2D fit is implemented alongside the iterative cutting of c_{lmn}. At this point a full parameter space fit is achieved, full expressions for the 3D fits at each collocation point is given in Appendix A.2.

5.4.4 Inclusion of spin

Whilst PhenomGSF is only calibrated to nonspinning data, spin-effects, such as the spin-spin and self-spin tidal terms, can be incorporated into the phase using the PN expressions directly

$$\psi_{\rm T} = \psi_{\rm BBH} + \psi_{\rm PhenomGSF} + \psi_{\rm SS}. \tag{5.32}$$

Contributions associated to the mass-monopole and spin-dipole are already incorporated in the point-particle phase. We use the PN baseline from Ref. [295], which includes all point-particle spin information up to 3.5PN [461, 462]. We subsequently incorporate the equation-of-state dependent quadrupole and octupole terms, which are related to the mass and spin moments via $M_2^{(A,B)} = -C_{\rm Q}^A M_{A,B}^3 \chi_{A,B}^2$ and $S_3^{(A,B)} = -C_{\rm Oct}^{A,B} M_{A,B}^4 \chi_{A,B}^3$ respectively. Here $C_{\rm Q}$ and $C_{\rm Oct}$ parameterize the quadrupolar and octupolar deformations of the stars induced by their spin, e.g. [9, 13, 171, 247, 264, 461–464]. For NSs or other exotic compact objects, $C_X \neq 1$ and need to be calculated assuming a given equation-of-state. The self-spin terms can be schematically written as [9]

$$\psi_{\rm SS} = \frac{3x^{5/2}}{128\nu}\left(\psi^A_{\rm SS,2PN}x^2 + \psi^A_{\rm SS,3PN}x^3 + \psi^A_{\rm SS,3.5PN}x^{7/2}\right), \tag{5.33}$$

where $x = (2\pi/f)^{2/3}$ and the individual coefficients can be found in [9], ensuring that contributions from the BH multipoles are explicitly removed to avoid double-counting their effect, which is already contained in the point-particle phase.

This extends the model to include partial aligned-spin information, though we note that these contribution are not calibrated within the PhenomGSF model and therefore not informed by TEOBResumS. This is similar to how spin information is incorpo-

rated in other models, e.g. [9, 298]. Should we wish to reduce the number of free parameters in the model, we can impose URs that relate $C_{\rm Q}^A$ and $C_{\rm Oct}^A$ to the tidal deformability Λ_A, e.g. [465]. This is the strategy we employ by default, though the model also allows us to treat $C_{\rm Q}^A$ and $C_{\rm Oct}^A$ as free EOS-dependent parameters to be constrained by the data.

Model validation including spin is considered in Sec. 5.5 to check for consistency. We note that when including the 3.5PN spin-spin term, we do make use of URs, which are required to calculate the compactness of each NS [192]. Extending this to generic compact objects, such as boson stars, is left to future work. Nonetheless, this is a comparatively small contribution to the phase and as we do not impose URs between the mass and tidal deformability, we do not expect this to have a significant impact. If desired, the spin-spin contributions in PhenomGSF can be disabled, given the modularity and flexibility of the framework.

5.5 Model validation

To assess the accuracy of PhenomGSF we perform several mismatch comparisons as well as full Bayesian parameter estimation.

5.5.1 Mismatch comparisons

To assess how similar two waveforms are, we compute the mismatch $\mathcal{MM}$ via Eq. (1.42). To compute mismatches, we first need to construct complete waveforms h_1, h_2. We choose the TEOBResumS BBH phase, the TEOBResumS BNS amplitude and vary the choice of tidal phase. Therefore, in all mismatches shown the only difference is the tidal phase allowing for a direct comparison. The left panel of Fig. 5.7

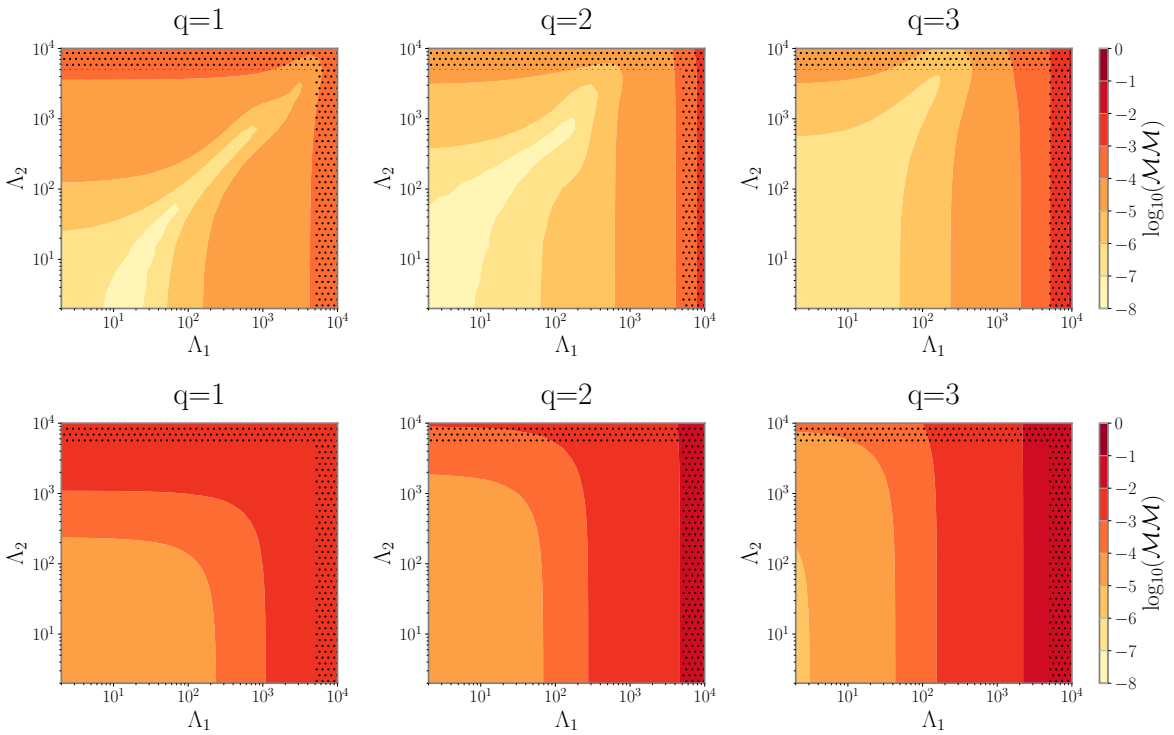

Figure 5.8: Mismatches across the parameter space over $Mf = [0.0005, Mf_{\rm MECO}]$ at $q = 1$, $q = 2$ and $q = 3$. The dotted areas denote regions of parameter space outside the calibration range of the model. *Top row*: Mismatches between TEOBResumS and PhenomGSF. *Bottom row*: Mismatches between TEOBResumS and TaylorF2 at 7.5PN.

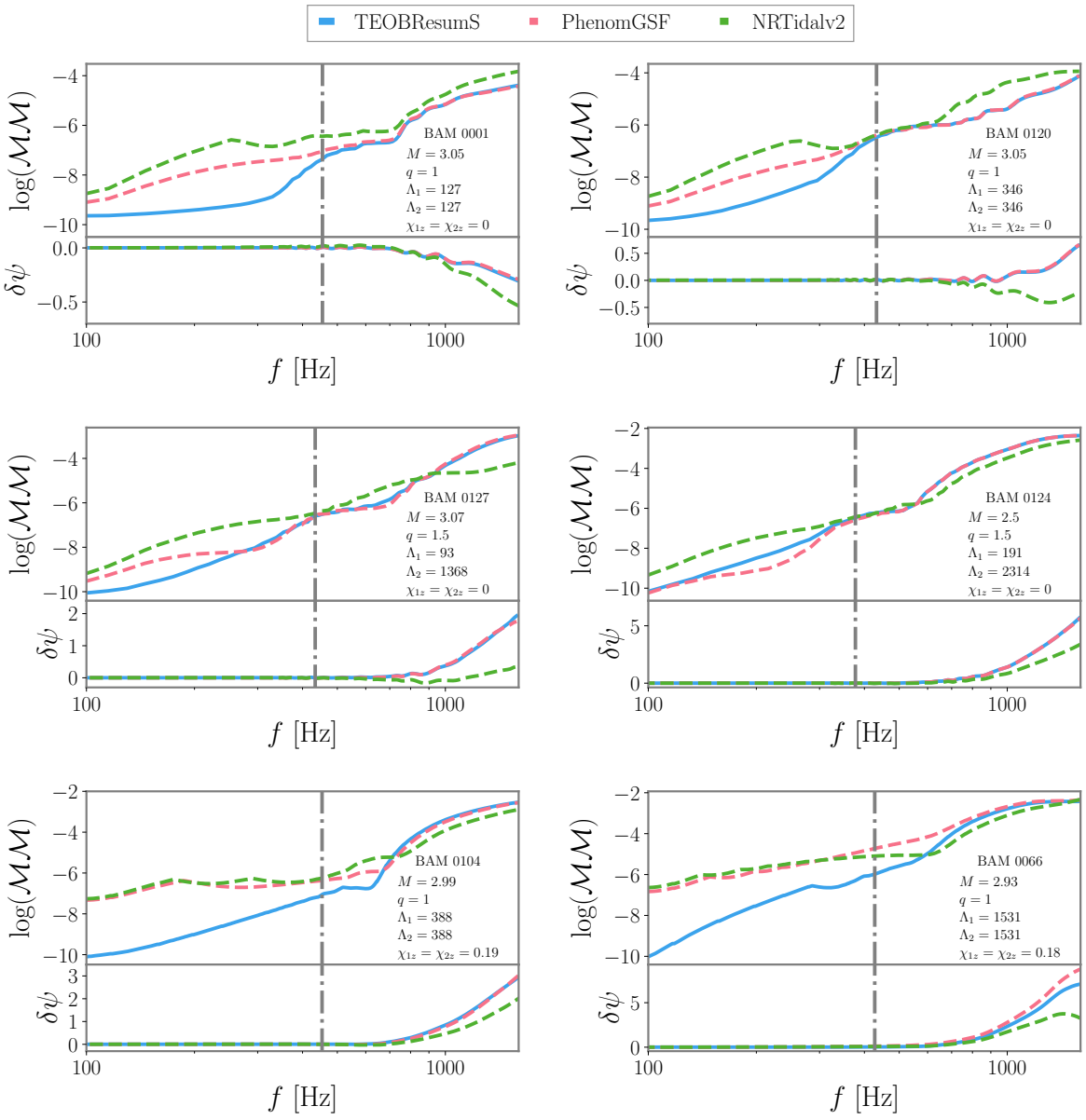

Figure 5.9: Comparisons for TEOBResumS-NR hybrid waveforms against TEOBResumS (blue solid) , PhenomGSF (orange dashed) and NRTidalv2 (green dashed). Both PhenomGSF and NRTidalv2 use a BBH baseline of TEOBResumS for clear comparison. In each plot the upper panel shows log mismatches computed from 40 Hz to a maximum frequency f; the lower panel shows the dephasing between the NR hybrid and one of the tidal approximants, i.e. $\delta\psi = \psi_{NR} - \psi_X$ where X is one of the approximants. The NR starting frequency is marked by the grey dot-dashed line. *Top row*: Equal-mass nonspinning systems. *Middle row*: Unequal mass nonspinning systems. *Bottom row*: Equal-mass spinning systems. The details of the NR simulations are given in Tab. 5.1.

shows histograms of the mismatches between TEOBResumS and PhenomGSF for the 8446 waveforms used in the model calibration, and 1000 independent waveforms that lie within the model's calibration range but were not used in the fitting. The mismatches in both data sets are $\mathcal{MM} \leq 10^{-3}$, with a median mismatch of $\sim 2 \times 10^{-5}$ for the calibration dataset and $\sim 3 \times 10^{-5}$ for the independent dataset, which quantifies the average modelling error. We also see excellent agreement between the two distributions, with a tail towards lower mismatches, demonstrating that the PhenomGSF model is robust and not overfitted. The improvement of PhenomGSF over TaylorF2 at different PN orders is shown in the right panel of Fig. 5.7. Here we find that the agreement between PhenomGSF and TEOBResumS is on average ~ 3 orders of magnitude better than with any of the considered PN approximants.

In Fig. 5.8 we show how the mismatches of TEOBResumS against PhenomGSF (top row) and TaylorF2 with 7.5PN tides (bottom row) vary as a function of $\{\Lambda_1, \Lambda_2\}$ for $q = \{1, 2, 3\}$. Here, we also include waveforms outside the calibration region of PhenomGSF to test for the robustness of the model under extrapolation to $\Lambda_{1,2} \leq 10000$ (dotted regions). We find that the PhenomGSF mismatches degrade for more unequal-mass systems, although they remain $< 10^{-3}$ throughout the calibration range. We note that in the equal-mass limit the mismatches are not fully symmetric in the $\Lambda_1 - \Lambda_2$ plane, even though the input data is symmetric under the interchange $1 \leftrightarrow 2$. This is due to the fact that in the fitting procedure, we did not enforce this symmetry in the equal-mass limit. Nonetheless, the mismatches in this regime are negligible and of the order $\sim \mathcal{O}(10^{-7})$. The asymmetry observed for unequal masses is as expected. In contrast, tidal TaylorF2 performs significantly worse even for moderate parameters, exceeding mismatches of 10^{-3} for $\Lambda_{1,2} \gtrsim 1000$ at $q = 1$, and $\Lambda_1 \gtrsim 100$ for $q = 3$. We observe better agreement within the regions nominally consistent with hadronic EOSs:

For example, for equal masses $\Lambda_1 = \Lambda_2$ gives the lowest mismatches, and for unequal mass ratios the lowest mismatches are found for $\Lambda_2 > \Lambda_1$.

Outside the calibration region, PhenomGSF achieves mismatches $< 10^{-3}$ for equal-mass binaries; for $q = 3$, mismatches remain below 10^{-3} for $\Lambda_2 < 10000$ provided that $\Lambda_1 < 5000$ but start to degrade significantly for larger values of Λ_1. We note, however, that this requires the radius of the primary NS to be ~ 2.6 times larger than that of the secondary.

Finally, we quantify the model's accuracy by also computing mismatches against a selection of TEOBResumS-NR hybrid waveforms as detailed in Sec. 5.3.3. In Fig. 5.9 we show comparisons against TEOBResumS, PhenomGSF and NRTidalv2, where both PhenomGSF and NRTidalv2 use a BBH baseline of TEOBResumS with no tides. We note that the NRTidalv2 model is the only tidal phase model in this comparison that is calibrated to NR simulations. Hence, we expect this model to have better agreement with the hybrids close to merger. At low frequencies, however, we expect PhenomGSF to yield dephasing results similar to those of TEOBResumS by construction. The top two panels of Fig. 5.9 are for equal-mass nonspinning systems, the middle two for unequal mass nonspinning systems, and the bottom two are for equal-mass systems with aligned spins. For each panel, the top figure shows the mismatch where $f_{\rm min} = 40$ Hz to varying $f_{\rm max}$ up to a maximum of $f_{\rm max} = f_{\rm MECO}$, while the bottom shows the phase difference as a function of GW frequency.

As anticipated, PhenomGSF tracks the phase of TEOBResumS to a very high degree. The only notable phase difference between PhenomGSF and TEOBResumS is seen for BAM 0066. In all cases, except for the equal-mass nonspinning hybrids, NRTidalv2 gives the smallest dephasing for the NR portion of the hybrid waveforms. The observed oscillations in the dephasing are due to non-negligible residual eccentric-

ities in the NR initial data (see Tab. 5.1). For the mismatches we find that for all comparisons the PhenomGSF results consistently approach those of TEOBResumS around or after the NR starting frequency indicated by the vertical line. The mismatches seemingly disagree at lower frequencies, however, we note that this difference is $\sim \mathcal{O}(10^{-10})$ for the nonspinning cases and $\sim \mathcal{O}(10^{-7})$ for the spinning cases. Surprisingly, for the equal mass non-spinning cases (top row) we find that PhenomGSF performs better than NRTidalv2 across the entire frequency range. For the unequal mass cases, PhenomGSF obtains lower mismatches in the low-frequency region, however, in the high frequency regime NRTidalv2 performs better. For the spinning comparisons we find that PhenomGSF and NRTidalv2 are comparable for low frequencies, while TEOBResumS is by far the most faithful. When including the NR region, all three models are comparable with NRTidalv2 being slightly better than the other two models.

5.5.2 Parameter estimation

To further validate PhenomGSF we carry out full Bayesian inference on simulated nonspinning and aligned-spin PhenomXAS_PhenomGSF signals (injections), a TEOBResumS-NR hybrid waveform, and GW170817 data [466].

For our analyses, we consider the following model parameters:

$$\boldsymbol{\theta} = \{\mathcal{M}_c, q, \chi_1, \chi_2, \tilde{\Lambda}, \delta\tilde{\Lambda}, \alpha, \delta, \iota, \psi, \phi, t_c\}\,,$$

where $\mathcal{M}_c = (m_1 m_2)^{3/5}/M^{1/5}$ denotes the chirp mass, q the mass ratio, χ_1 and χ_2 the two spin magnitudes for the aligned-spin runs, α and δ the right ascension and declination of the binary in the sky, ψ the polarisation angle, ϕ and t_c the phase and

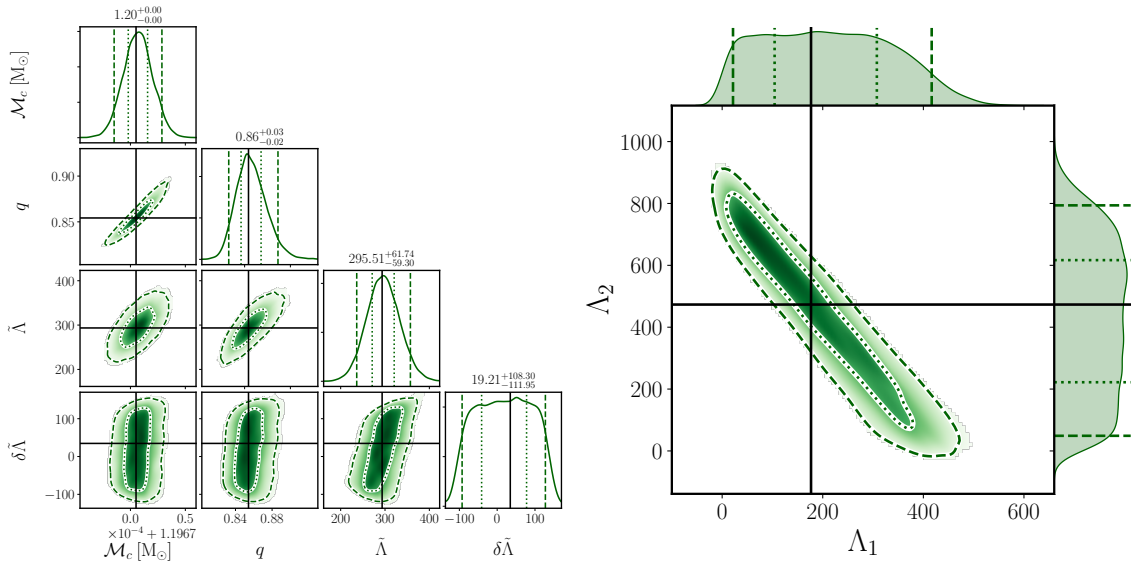

Figure 5.10: 1D and 2D posteriors for a nonspinning GW170817-like injection with IMPPHENOMXAS_PHENOMGSF. *Left panel*: Posteriors of the intrinsic parameters with their 50% (dotted) and 90% confidence intervals (dashed). The injected values are indicated by solid black lines. *Right panel*: Posteriors for the individual tidal deformabilites with their 50% (dotted) and 90% confidence intervals (dashed).

time of coalescence respectively, and ι the inclination of the total angular momentum w.r.t. to the line-of-sight. The luminosity distance D_L and phase ϕ are marginalised over in the likelihood evaluation and reconstructed in post-processing. All runs were performed with BILBY [66] in conjunction with the nested sampler DYNESTY [65] with slice sampling. For all analyses we used 2000 live points, 20 slices and 50 autocorrelation lengths with 32 CPU cores. Although we sample in $\mathcal{M}_c$ and q, we select priors that are uniform in component masses, whilst $\tilde{\Lambda}$ and $\delta\tilde{\Lambda}$ are sampled directly from uniform priors. The priors for each analysis are given in Tabs. 6.1 and 5.3. Additionally, we constraint the individual tidal deformabilities $\Lambda_{1,2}$ to be between 0 and 5000.

Parameter	Injected Value	Prior	Nonspinning	Aligned-Spin
$\mathcal{M}_c[M_\odot]$	1.20	$\mathrm{U}_{(m_1,m_2)}[\mathcal{M}_{\rm min}, \mathcal{M}_{\rm max}]$	$1.20\ \pm^{2.17\times10^{-5}}_{2.17\times10^{-5}}$	$1.20\ \pm^{4.34\times10^{-5}}_{3.20\times10^{-5}}$
q	0.86	$\mathrm{U}_{(m_1,m_2)}$[0.125, 1.0]	$0.86\pm^{0.03}_{0.02}$	$0.89\pm^{0.10}_{0.13}$
$\tilde{\Lambda}$	293.5	U[0, 5000]	$296\pm^{62}_{59}$	$290\pm^{61}_{60}$
$\delta\tilde{\Lambda}$	34.7	U[-5000, 5000]	$19\pm^{108}_{112}$	$10\pm^{112}_{103}$
χ_1	NA/0.01	NA/U[0, 0.05]	NA	$0.01\pm^{0.02}_{0.01}$
χ_2	NA/0.01	NA/U[0, 0.05]	NA	$0.01\pm^{0.02}_{0.01}$
α	2.55	U[0, 2π]	$2.55\pm^{0.01}_{0.01}$	$2.55\pm^{0.01}_{0.01}$
δ [rad]	-0.40	Sine	$-0.41\pm^{0.01}_{0.01}$	$-0.41\pm^{0.01}_{0.01}$
D_L [Mpc]	40	U[0, 2π]	$35\pm^{5}_{8}$	$35\pm^{5}_{8}$
ι [rad]	0.1	Sine	$0.52\pm^{0.35}_{0.37}$	$0.52\pm^{0.35}_{0.38}$
ϕ [rad]	0	U[0, 2π]	$3.16\pm^{2.79}_{2.86}$	$3.16\pm^{2.79}_{2.86}$
ψ [rad]	0	U[0, π]	$1.63\pm^{1.37}_{1.45}$	$1.66\pm^{1.34}_{1.47}$
t_c [s]	0	U[-0.005, 0.005]	$t_c\pm^{1.8\times10^{-4}}_{1.7\times10^{-4}}$	$t_c\pm^{1.8\times10^{-4}}_{1.8\times10^{-4}}$

Table 5.2: Injected parameters for a nonspinning and aligned spin GW170817-like system with the corresponding prior ranges and recovered values. Here $\mathrm{U}_{(m_1,m_2)}$ denotes that the prior is conditional on the detector-frame component masses and we set $\mathcal{M}_{\rm min} = \mathcal{M}_{c,\rm inj} - 10^{-3}$ and $\mathcal{M}_{\rm max} = \mathcal{M}_{c,\rm inj} + 10^{-3}$. The recovered values denote the median and 90% credible interval. NA indicates that a parameter was not applicable to the nonspinning analysis.

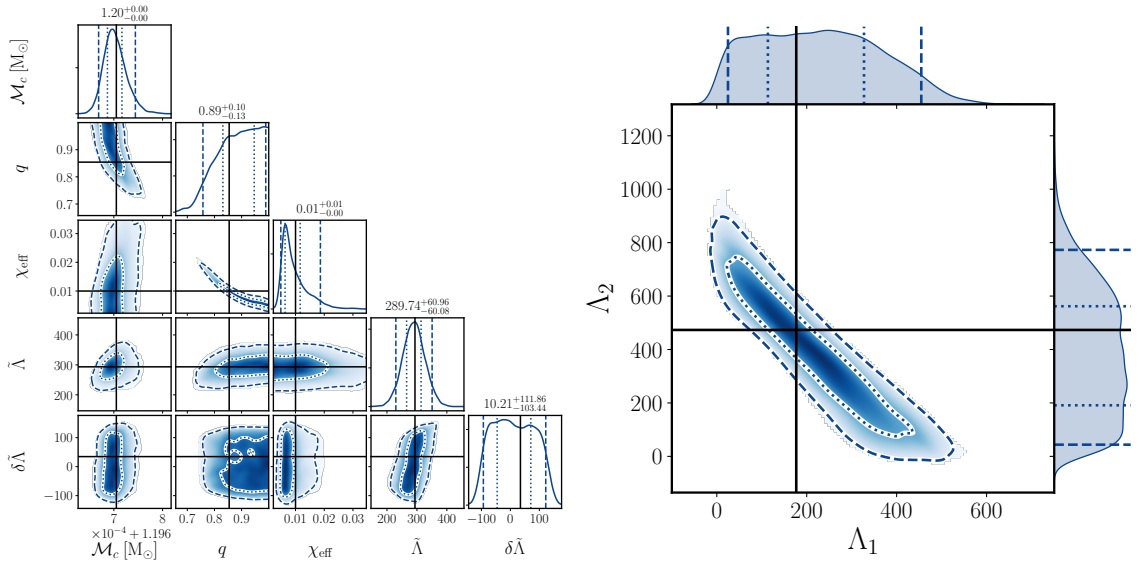

Figure 5.11: 1D and 2D posteriors for an aligned-spin GW170817-like IMPPHENOMXAS_PHENOMGSF injection. *Left panel*: Posteriors of the intrinsic parameters with their 50% (dotted) and 90% confidence intervals (dashed). The injected values are indicated by solid black lines. *Right panel*: Posteriors for the individual tidal deformabilites with their 50% (dotted) and 90% confidence intervals (dashed).

c

Zero-noise injections

We first perform two zero-noise injections with IMRPhenomXAS_PhenomGSF into a three-detector network consisting of LIGO-Hanford, LIGO-Livingston [39] and Virgo [41] (HLV) with the sensitivity of the fourth observing run (O4) [467] and recover with the same model. We note that zero-noise is representative of the results when averaging over many different noise realisations. The frequency-dependence of the sensitivity is taken into account through the PSD. The injected parameters are similar to those of GW170817 (see Tab. 6.1 for details). For the EOS we choose the relatively soft APR4 [116] one, which is compatible with the EOS-constraints obtained from GW170817 [137, 468]. We perform two analyses: one with zero NS spin and another one with aligned-spins of magnitudes $\chi_1 = \chi_2 = 0.01$. We integrate the likelihood from a minimum frequency $f_{\rm min} = 23$ Hz to $f_{\rm max} = 2048$ Hz, which corresponds to the Nyquist frequency of our sampling rate. Although PhenomGSF is only calibrated from a minimum frequency of 37 Hz for such a GW170817-like system, we have confirmed that extrapolating to lower frequencies is robust due to the nature of our ansatz. Both configurations have a network SNR of ~ 97.

A selection of 1D and 2D posterior distributions for the nonspinning injection is shown in Fig. 5.10. We find that for all parameters the injected values lies confidently within the 90% credible interval. As expected, $\tilde{\Lambda}$ is recovered with better accuracy than $\delta\tilde{\Lambda}$ as it is the leading-order tidal contribution to the GW phase, while $\delta\tilde{\Lambda}$ is subdominant. We also observe the expected linear correlation between the chirp mass and $\tilde{\Lambda}$. Mapping the binary tidal parameters to the individual tidal deformabilities, we observe the known correlation between the two and recover the injected values at the 50% credible level as can be seen in the right panel of Fig. 5.10. The median values and

90% credible intervals for all parameters are given in the fourth column of Tab. 6.1.

In Fig. 5.11 we show a similar selection of 1D and 2D posteriors for the aligned-spin analysis, but now also including the effective spin $\chi_{\rm eff}$ [421]. We find that the chirp mass and tidal parameters are recovered equally accurately as in the nonspinning case, but we now observe the known non-linear correlation between the mass ratio and the effective spin [469, 470], pushing the mass ratio posterior towards more equal masses for low spin magnitudes. The tidal parameters are, however, still recovered well. The median values and 90% credible intervals for all parameters are given in the fifth column of Tab. 6.1.

	TEOBResumS-NR hybrid			**GW170817**	
Parameter	Injected Value	Prior	Recovered	Prior	Inferred
$\mathcal{M}_c[M_\odot]$	1.18	$U_{(m_1,m_2)}$[1.1,1.3]	$1.18\pm^{3.28\times10^{-5}}_{5.74\times10^{-5}}$	$U_{(m_1,m_2)}$[1.197,1.198]	$1.1976\pm^{1.25\times10^{-4}}_{1.07\times10^{-4}}$
q	1.0	$U_{(m_1,m_2)}$[0.125, 1]	$0.94\pm^{0.05}_{0.08}$	$U_{(m_1,m_2)}$[0.125, 1]	$0.86\pm^{0.13}_{0.16}$
$\tilde{\Lambda}$	390	U[0,5000]	$371\pm^{104}_{115}$	U[0,5000]	$410\pm^{516}_{237}$
$\delta\tilde{\Lambda}$	0	U[-5000,5000]	$-1\pm^{152}_{133}$	U[-5000,5000]	$18\pm^{207}_{205}$
χ_1	0	NA	NA	U[0,0.05]	$0.007\pm^{0.02}_{0.01}$
χ_2	0	NA	NA	U[0,0.05]	$0.007\pm^{0.02}_{0.01}$
α [rad]	2.55	U[0, 2π]	$2.55\pm^{0.01}_{0.01}$	U[0, 2π]	$3.42\pm^{0.03}_{0.03}$
δ [rad]	-0.41	Cosine	$-0.41\pm^{0.02}_{0.02}$	Cosine	$-0.40\pm^{0.06}_{0.06}$
D_L [Mpc]	40	U[10,100]	$36\pm^{5}_{8}$	U[10,100]	$37\pm^{8}_{16}$
ι [rad]	0.1	Sine	$2.64\pm^{0.36}_{0.35}$	Sine	$2.53\pm^{0.44}_{0.51}$
ϕ [rad]	0	U[0, 2π]	$2.96\pm^{2.96}_{2.67}$	U[0, 2π]	$3.17\pm^{2.81}_{2.93}$
ψ [rad]	0	U[0, π]	$1.63\pm^{1.37}_{1.48}$	U[0, π]	$1.53\pm^{1.49}_{1.44}$
t_c [s]	1187008882.4	U[t_c - 0.1, t_c + 0.1]	$t_c\pm^{3.9\times10^{-4}}_{4.3\times10^{-4}}$	U[t_c - 0.1, t_c + 0.1]	$t_c\pm^{1.1\times10^{-3}}_{0.9\times10^{-3}}$

Table 5.3: Injected parameters for the TEOBResumS-NR hybrid with the corresponding priors and 1D posterior medians with their 90% credible intervals, and priors as well as the median inferred parameter values with their 90% credible intervals for the GW event GW170817. Here, $U_{(m_1,m_2)}$ denotes uniform priors in component masses, and $t_c = 1187008882.4$ s is the GPS time of GW170817. NA indicates that a parameter was not applicable to the nonspinning analysis.

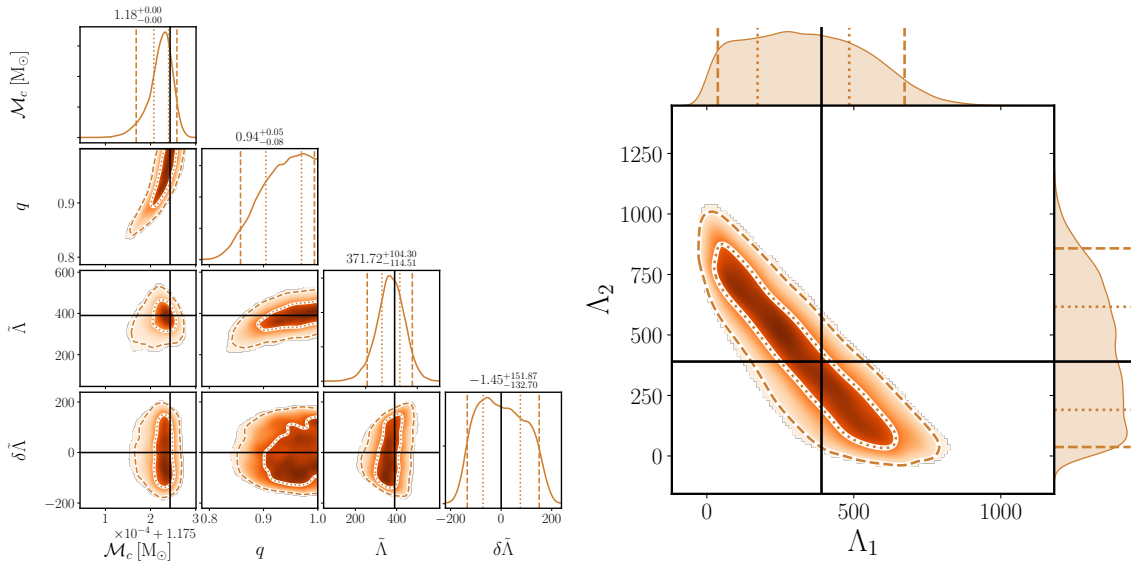

Figure 5.12: 1D and 2D posteriors for the TEOBResumS-NR hybrid injection with BAM 0095 analysed with IMPPhenomXAS_PhenomGSF. *Left panel*: Posteriors of the intrinsic parameters with their 50% (dotted) and 90% confidence intervals (dashed). The injected values are indicated by solid black lines. We note that the injected mass ratio is $q = 1$ and hence overlaps with the plot axis. *Right panel*: Posteriors for the individual tidal deformabilites with their 50% (dotted) and 90% confidence intervals (dashed).

TEOBResumS-NR hybrid injection

Next, we perform a TEOBResumS-NR hybrid zero-noise injection into the same HLV network and recover again with IMPPhenomXAS_PhenomGSF. For this analysis we use the BAM 0095 simulations. Details on the hybrid generation are given in Sec. 5.3.3. The hybrid starting frequency is $f_{\rm min} = 30$ Hz, while the NR starting frequency is $f_{\rm NR} = 433$ Hz. To perform the analysis, we convert the hybrid into the LIGO-Virgo-KAGRA-NR format [471] and use the tools provided by the LIGO Algorithms Library [10]. Starting at $f_{\rm min} = 33$ Hz, we obtain a network SNR of ~ 51 with the O4 design sensitivity, where the extrinsic parameters are the same as for the previous injections. We note that as this is a nonspinning injection, we set the spins to

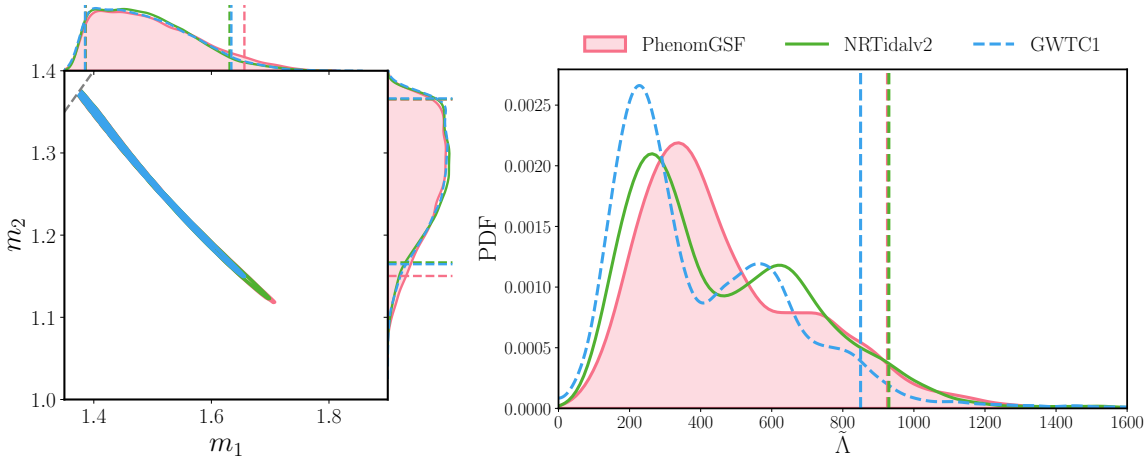

Figure 5.13: Selection of 1D and 2D posterior distributions for GW170817 for IMRPhenomXAS_PhenomGSF (pink, solid), IMRPhenomXAS_NRTidalv2 (green, solid) and IMRPhenomPv2_NRTidalv2 (blue, dashed) from GWTC-1. *Left panel*: Joint 2D component mass posteriors with their 1D 90% credible intervals (vertical dashed lines) and 90% credible region, respectively. The grey dashed line indicates the equal-mass limit. *Right panel*: 1D posteriors for the binary tidal deformability $\tilde{\Lambda}$ with their respective 95$^{\text{th}}$ percentiles (vertical dashed lines).

zero in the recovery. The injected values, prior choices and recovered values are given in Tab. 5.3.

In Fig. 5.12 we show the obtained 1D and 2D posterior distributions for the chirp mass, mass ratio and tidal deformability parameters. We find that despite the differences in the BBH baseline and the lack of NR calibration of PhenomGSF, all injected values are recovered accurately and contained within either the 90% or even the 50% credible interval, indicating that modelling systematics due to the BBH baseline and the lack of NR calibration are subdominant in this region of the parameter space.

GW170817

Finally, we analyse the data of GW170817 with PhenomGSF again using IMRPhenomXAS as the BBH baseline model. We follow previous analyses [138, 472]

and employ a low-spin prior. Details for all priors are given in the fifth column of Tab. 5.3. We analyse 128 s of data around the trigger time with a sampling rate of 4096 Hz. For the likelihood integration we choose a minimum frequency $f_{\rm min} = 23$ Hz consistent with the analyses presented in GWTC-1, and a maximum frequency $f_{\rm max} = f_{\rm Nyquist} = 2048$Hz.

The inferred posterior distributions for the masses and tidal deformability are shown in Fig. 5.13; the results for all other parameters are shown in Fig. A.4 in App. A.3. For comparison, we also show the posteriors obtained with the waveform model IMRPhenomPv2_NRTidal from the GWTC-1 analysis [472, 473] as well as posteriors from an analysis identical to ours but with the model IMRPhenomXAS_NRTidalv2. The GWTC-1 analysis used flat priors in $\Lambda_{2,A}$, hence our posteriors for $\tilde{\Lambda}$ has been reweighted to a flat $\tilde{\Lambda}$-prior as used in our setup.

Overall, we observe a very high degree of consistency between the three results. The component mass posteriors show excellent agreement between all three models, with a slightly higher 90% upper bound for PhenomGSF. Similarly for the tides, where we also find a slightly higher value of $\tilde{\Lambda}$ with PhenomGSF than what was found in GWTC-1. This is also consistent with the analysis using TEOBResumS presented in Ref. [474]. Notably, however, it also appears that the secondary peak in the $\tilde{\Lambda}$ posterior is reduced in comparison to the other models, suggesting that this feature is likely inherent to this generation of NRTidal approximants or the previously used BBH baselines. We note that both of these observations are also in agreement with the recent analysis of GW170817 with NRTidalv3 presented in Fig. 16 of Ref. [298].

5.6 Discussion

We presented PhenomGSF, a new phenomenological tidal phase model for inspiralling unequal mass BNS systems valid for mass ratios between 1 and 3 and dimensionless NS tidal deformabilities up to 5000. PhenomGSF is a closed-form phenomenological fit to the tidal phase of the effective-one-body model TEOBResumS, which includes GSF-informed tides. The fit is constructed by employing a hierarchical procedure using the collocation point method to a large suite of TEOBResumS waveforms.

PhenomGSF is fully modular and can readily be added to any frequency-domain BBH baseline model, such as the state-of-the-art IMRPhenomX waveform family.

We note that we did not include EOB-calibrated spin effects in PhenomGSF, instead relying on standard PN spin-tidal expressions. Whilst we could have assumed an EOS or imposed URs, this is not explicitly required.

We assessed the accuracy and performance of PhenomGSF extensively by comparing it against independent TEOBResumS waveforms, obtaining mismatches $\mathcal{MM} \leq 10^{-3}$ across the parameter space the model was calibrated against. For $q \sim 1$ we find that the model extrapolates well and retains its accuracy for tidal deformabilities up to 10000. We also computed frequency-dependent mismatches against a suite of TEOBResumS-NR hybrid waveforms, finding that PhenomGSF tracks the accuracy of TEOBResumS as expected.

Finally, we performed full Bayesian inference on a suite of mock signals and the GW event GW170817. Parameter estimation on IMRPhenomXAS_PhenomGSF injections into zero-noise show consistent recovery of the injected parameters. We then analyse a TEOBResumS-NR hybrid injection and find that neither the lack NR

calibration of PhenomGSF nor the difference in the underlying BBH baseline lead to any significant systematic differences. A more systematic Bayesian study across a wider parameter space is left for future work. Lastly, we independently analysed the data of GW170817 with IMRPhenomXAS_PhenomGSF. Our results are consistent with previous analysis, but we obtain a slightly higher upper limit for $\tilde{\Lambda}$ than for example with NRTidal and NRTidalv2. We also found that the secondary peak in $\tilde{\Lambda}$ is less pronounced for PhenomGSF consistent with the TEOBResumS results of GWTC-1. The computational efficiency is comparable to that of the NRTidal approximants.

We have demonstrated that PhenomGSF is a robust, highly accurate, modular and computationally efficient model of quadrupolar gravitoelectric tides. Moreover, it is flexible in that it allows for the addition of PN spin terms and the use of non-hadronic EOS, making it an ideal candidate for exploring exotic matter. Nevertheless, there are several avenues for further improving the model which we leave for future work, including:

1. A full treatment of NS spin effects, extending the 3-dimensional phenomenological fit presented here to higher dimensions to incorporate aligned-spin and precessing binaries.

2. The incorporation of dynamical tidal effects, such as adding the PN model of f-mode dynamical tides fmtidal [278], as their neglect is known to introduce biases in the inferred EOS [369, 401].

3. Extension to higher-order multipoles beyond the $(2, 2)$-mode. This is of particular importance for unequal-mass and precessing systems, where more power is radiated in subdominant harmonics, and could play an important role in constraining the geometry of the merger and breaking the distance-inclination degeneracy.

4. Modelling tidal corrections to the amplitude, e.g. [9].

There are also numerous other avenues for extending the model that are being pursued. For example, there are higher-order tidal moments such at the octopolar and hexadecapolar terms [248]. The NS excites a spectrum of fluid modes beyond just the f-modes that need to be modelled, e.g. see [405, 408, 475, 476]. Including the effects of orbital eccentricity could also be important [477, 478], though this may be of less astrophysical significance [479].

Finally, we note that although we did not include precession effects in the analysis presented here, it is straightforward to follow the framework outlined in [480] to construct an approximate precessing BNS model by augmenting the BBH baseline [9, 297, 298, 481]. A notable benefit is that precession can help break the mass-spin degeneracy, leading to tighter constraints on the component masses [412, 413].

Though the analytical framework of PhenomGSF makes it inherently computationally efficient, the code is currently employed within Python as a proof of principle. The BBH baseline PhenomXAS is generated with LAL [60] in C, thus there is a current mix in coding languages when generating the full waveform, which hinders the overall waveform generation cost. Consequently, regarding timing, PhenomGSF is not currently directly comparable to the waveform models within LAL, which are fully native in C. Therefore, we leave timing tests to future work, after PhenomGSF has been incorporated into LAL and optimised. In the current form, for a $1.4M_{\odot}$+$1.4M_{\odot}$ fiducial BNS system of $\Lambda_1 = \Lambda_2 = 500$, the current generation time of the tidal phase correction is 3×10^{-2}s on a 2 GHz quad-core Intel core i5 CPU.

Chapter 6

Investigating the impact of universal relations for gravitational-wave parameter estimation of binary neutron stars with extreme equations of state

Declaration

This chapter is a review of ongoing exploratory research performed by N. Williams. The concept of investigating the use of universal relations in parameter estimation with extreme equations of state was posited by N. Williams, and builds upon the work presented in Ch. 5 as an application of the PhenomGSF model. The details of the project were formulated collaboratively between N. Williams, P. Schmidt and G. Pratten. All parameter estimation runs were performed by N. Williams. Interpretation of the results was discussed between N. Williams, P. Schmidt and G. Pratten. All figures were created by N. Williams.

6.1 Introduction

A primary motivation for observing GWs from BNS inspirals is to gain insights into ultra-dense nuclear matter [165, 234]. Encoded within the GW signal are tidal effects from the deformation of the NSs, which can be used to infer the NS EOS [280]. Currently, constraints on the EOS from GW observations remain weak, largely because GW170817 is the only event to date with measured tidal effects [36, 137, 138]. However, with improved detector sensitivity in upcoming observing runs [482, 483] the number of BNS events from which we can infer matter effects is expected to increase [110, 368, 484], leading to a more precise EOS measurement [485].

Matter effects are predominantly captured within the GW signal through the ($\ell = 2$) tidal deformability of each NS $\Lambda_{1,2}$ [165], which must be included within BNS waveform models to make accurate measurements. These tidal parameters can be treated separately within parameter estimation, or connected to one another through URs [8, 192, 193, 222, 465].

URs provide a convenient EOS quasi-independent mapping between stellar observables, as introduced in Sec. 2.4. Utilising URs within waveform modelling and parameter estimation can therefore drastically reduce the dimensionality and computational cost when inferring tidal effects, removing degeneracies and potentially resulting in more accurate tidal posteriors [203]. This mapping also adds implicit information *a priori* that the NSs must obey the same EOS. This technique was introduced in Ref [203] through binary Love URs [8], relating Λ_s and Λ_a (Eqs. (2.15) and (2.14)), and utilised for parameter estimation of GW170817 [137]. The framework reduced the 90% credible interval for the $\Lambda_1 - \Lambda_2$ 2D posterior by a factor of ~ 3 when using URs as opposed to EOS independent sampling.

However, the use of URs introduces certain assumptions. Firstly, due to their quasi-EOS independent nature, a subset of EOS models exhibit significant deviation from URs [438, 486–489]. Additionally, it may not be advantageous to restrict ourselves to the assumption that all NS obey the same EOS, or indeed that both objects are both NSs and not exotic compact bodies. Therefore, assuming URs within parameter estimation may have the potential to bias results of tidal parameters, and in turn the EOS, if one or both of the bodies follow an extreme EOS. These extreme EOS may reflect non-hadronic models with exotic matter such as deconfined quarks [488, 489], strange matter [486] or boson stars [490].

In Ref. [203], the authors conducted such an investigation through simulated BNS signals and recovery of tidal parameters with Bayesian parameter estimation. The authors found that by marginalising over the error from URs, and thus restricting the measurement uncertainty to a *minimum* of 10%, no biases were observed. However this work holds certain caveats. Firstly, the EOSs injected were included in the UR fittings used within the parameter estimation. Secondly, the waveform model IMRPhenomD_NRTidal [297, 491, 492] was used in this study, which is calibrated to NR simulations of equal mass BNS systems with parameterised EOS. Therefore, this model does not account for extreme EOS models, or unequal mass systems beyond the leading order PN term [234]. In the case of equal mass systems, assuming that equal masses translates to components of equal tidal deformability, lead to a trivial result of $\Lambda_a = 0$. Therefore, when assessing the applicability of binary Love URs it is of interest to consider unequal mass systems where $\Lambda_a \neq 0$.

These caveats potentially restrict their results to be inherently restricted to the input EOSs, creating a bias where the conclusions are predisposed to reflect the initial EOS assumptions. This risks self-reinforcement, limiting the potential for probing

extreme EOS which were not included in the UR fitting or waveform model. These limitations are reflection of the available models at the time, however with a variety of new extreme EOSs and development of EOS independent waveform models, these limitations can be addressed.

Here, we present an extension to this work, to assess whether biases are observed in parameter estimation when:

1. Injecting simulated signals with extreme EOSs introduced in Ref. [438], which violate URs, and were not included in the binary Love fitting.

2. Modelling the tidal sector of the injected signals with the waveform model PHENOMGSF [414] introduced in Ch. 5, which assumes no parameterised EOS or URs and is calibrated to unequal mass systems[1].

This chapter is organised as follows: In Sec. 6.2 we outline our methodology, detailing our choices of EOSs in Sec. 6.2.1, summarising the parameter estimation runs in Sec. 6.2.2 and defining quantities to describe our results in Sec. 6.2.3. In Sec. 6.3 we then present current working results and discuss their implications in Sec. 6.4.

6.2 Methodology

6.2.1 Equations of state

We simulate the BNS signals with two astrophysically motivated EOSs which have been demonstrated to violate URs [438]. Though these EOSs were constructed to violate the $\Lambda - f_2$ UR [202], they additionally violate the $\Lambda_s - \Lambda_a$ UR [8], which we

[1]We note that recently the updated NRTIDALV3 [298] was made available which is calibrated to unequal mass systems, this model is still fitted to parameterised EOSs from which URs are fitted upon.

will utilise in this work. Ref. [438] extended on the findings that URs break down for EOSs that present strong first-order phase transitions [487, 493], demonstrating that *any* EOS that is characterised by a significantly non-vertical mass-radius slope, results in violation of URs. We therefore adopt two EOSs with extreme negative and positive slope in the mass-radius curve, which we label EOS$^-$ [438] and EOS$^+$ [494] respectively, and are shown in Fig. 6.1. Note that for a $1.4M_\odot$ NS, both EOSs give a radius of 13 km, consistent with constraints from GW170817 [137].

EOS$^-$ and EOS$^+$ are constructed such that the maximum allowed mass is at least $2M_\odot$ to comply with observational constraints on massive pulsars [1, 2, 495, 496], and that the EOS remains causal and thermodynamically stable. The EOSs are constructed as piecewise polytropes [16] above $0.5\rho_{\rm sat}$ with 3 and 5 segments for EOS$^-$ and EOS$^+$ respectively. The negative slope EOS$^-$ is constructed through stiffening of the EOS at intermediate densities $\sim$few$\times\rho_{\rm sat}$, and likewise the positive slope EOS$^+$ is constructed through the softening of the EOS at intermediate densities. Phenomenologically, stiffening refers to a steep gradient in the $P(\rho)$ relationship and softening to a shallow gradient. At the first fiducial density for EOS$^-$, a lower limit on the pressure is set by the two-body potential of Argonne AV8 [497]. Likewise, lower limits on pressure are set for the first two fiducial densities for EOS$^+$. At densities below $0.5\rho_{\rm sat}$ both EOSs are modelled with EOS SFHo [498], a soft EOS based on relativistic mean-field interactions [499].

6.2.2 Parameter estimation

We consider a set of simulated BNS signals in a three-detector network consisting of LIGO-Hanford, LIGO-Livingston and Virgo operating at the A+ low limit design sensitivity [482] for the projected O5 observing run [500].

		EOS$^-$		**EOS$^+$**	
q	M	Λ_1	Λ_2	Λ_1	Λ_2
1.05	2.05	3339.7	4501.5	2938.0	3707.6
1.1	2.1	2501.3	4501.5	2326.2	3707.6
1.2	2.2	1443.9	4501.5	1475.5	3707.6
	3.1	122.5	452.6	216.9	594.6
	4.1	10.5	64.7	41.1	132.8
1.6	2.6	203.8	4501.5	326.7	3707.6
	3.1	49.9	1465.7	111.2	1493.9
	3.6	10.5	537.4	41.1	675.4
2.0	3.0	33.8	4501.5	86.0	3707.6
	3.2	20.3	3191.3	59.8	2833.4
	3.4	10.5	2291.5	41.1	2164.6

Table 6.1: Injected values for simulated BNS signals of mass ratio q, total mass M, and tidal deformabilities Λ_1, Λ_2 for each EOS.

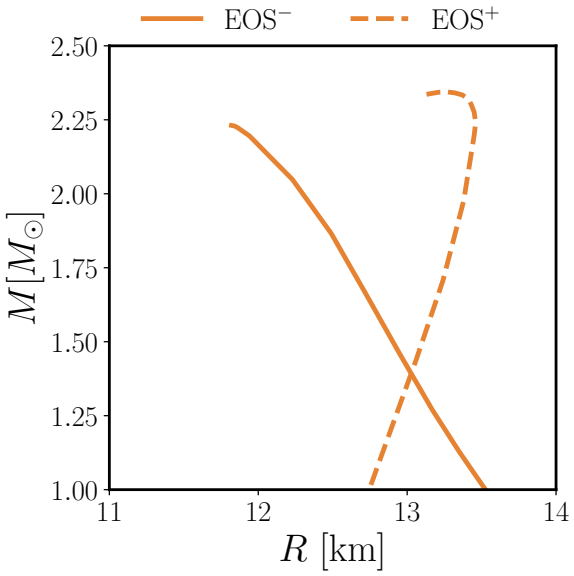

Figure 6.1: The mass-radius curves of the extreme EOSs used in this study. The negative sloping EOS$^-$ is shown (solid line) alongside the positive sloping EOS$^+$ (dashed line).

We model the BNS signals using the frequency-domain inspiral model IMRPhenomXAS_PhenomGSF [295, 414] as presented in Ch. 5 which captures the quadrupolar ($\ell = 2$) adiabatic tidal effects. PhenomGSF is particularly suited to studies that explore extreme EOS and exotic matter, as the model is constructed such that it does not assume any parameterised EOS or URs. This is achieved by treating the tidal parameters fully independently, and is valid across $q \in [1, 3], \Lambda_{1,2} \in [0, 5000]$. Moreover, as a phenomenological model, PhenomGSF provides fast waveform generation, which is particularly advantageous for low-mass binary systems like those considered in this study, where the signal duration can extend up to 512 seconds in A+ sensitivity. We assume that the neutron stars are non-spinning with negligible eccentricity, and generate the waveforms between $f_{\rm min} = 20$Hz and the frequency at $f_{\rm max} = 2048$Hz which corresponds to the Nyquist frequency of the used sampling rate, noting that waveform amplitude tapers to zero at $f_{\rm MECO}$.

We incorporate the assumption of URs into our analyses by using the binary Love UR within the sampling of the tidal parameters, as introduced in Ref. [203]. Here sampling is carried out in the symmetric combination Λ_s (Eq. (2.15)) and is mapped to the anti-symmetric Λ_a (Eq. (2.14)) through UR

$$\Lambda_a = \Lambda_a(\Lambda_s, q; \vec{b}) + \mathcal{N}(\mu(\Lambda_s, q), \sigma(\Lambda_s, q)) \,, \tag{6.1}$$

where $\mathcal{N}(\mu, \sigma)$ is a normal distribution with mean μ and standard deviation σ, and $\vec{b}$ are parameters fitted across a number of EOSs. The functional form of $\Lambda_a(\Lambda_s, q; \vec{b})$ and fitted parameters $\vec{b}$ can be found in Ref. [203]. We emphasise that the EOSs used in this injection study are not included in this dataset. The normal distribution here aims to marginalise over error from EOS independence, limiting the measurement uncertainty to a minimum of 10% to minimise bias.

We perform parameter estimation through Bayesian inference using Bilby [66] in conjunction with the nested sampler Dynesty [65] with slice sampling. Within the sampling we use 2000 live points, 20 slices and 50 autocorrelation lengths with 32 CPU cores. For all analyses we assume an electromagnetic counterpart, and we are interested here in the effect on "golden" events and not on the population as a whole (though we will consider the bias and error on the population solely to gain an understanding of the average impact). Therefore we fix the sky location to right ascension $\alpha = 1.27\,\text{rad}$, declination $\delta = -0.41\,\text{rad}$, inclination $\iota = 0.1\,\text{rad}$ and fix the distance for each events such that they all have a network SNR of 50. This leaves us with the following model parameters to sample over: $\boldsymbol{\theta}^{\text{indep}} = \{\mathcal{M}_c, q, \tilde{\Lambda}, \delta\tilde{\Lambda}, \psi, \phi, t_c\}$ for the independent sampling and $\boldsymbol{\theta}^{\text{BL}} = \{\mathcal{M}_c, q, \Lambda_s, \psi, \phi, t_c\}$ for the binary Love sampling.

In Tab 6.1 we list the intrinsic properties of the injected BNS signals where we

explore various mass ratios q and total mass M for both EOS$^-$ and EOS$^+$. For mass ratios $q = \{1.2, 1.6, 2.0\}$, we choose binaries at 3 uniformly spaced total masses that span between the lowest and highest possible total masses allowed by both EOS given a minimum NS mass of $1M_\odot$. We additionally inject binaries at the low total mass limit for mass ratios $q = \{1.05, 1.1\}$ to investigate near the equal mass limit where total allowed mass is lowest and in turn largest tides. For each injected binary we recover the inferred source parameter posterior distributions twice: once with independent sampling in $(\tilde{\Lambda}, \delta\tilde{\Lambda})$ and once in Λ_s utilising the binary Love UR to infer Λ_a. Both of these parameterisations can be converted into Λ_1, Λ_2.

We perform one additional set of runs, where we take the $q = 1.1$ binary and rerun the parameter estimation, changing from the A+ detector network to a single CE [374], to investigate how these results may change with the higher sensitivities of the 3G era. This set of runs has an SNR of 597, roughly an order of magnitude louder than the corresponding A+ analyses.

We show the deviation from the binary Love URs of these injected binaries in Fig. 6.2. EOS$^-$(triangles) tends towards an asymmetric contribution higher than the UR, whilst EOS$^+$(squares) tends towards a lower asymmetric contribution. Overall, the magnitude of deviation from URs is greater in EOS$^-$. We observe here that deviation from the URs tends to increase as the symmetric tidal contribution increases, though it is heavily influenced by mass ratio. The deviation is largest for the lowest mass binaries of mass ratio $q = 1.2$ for EOS$^-$ and $q = 1.6$ for EOS$^+$. This suggests that a balance must be struck: while lower total mass, and consequently stronger tidal effects, are achievable at mass ratios closer to equal-mass, this diminishes the magnitude of the asymmetric contribution.

We use mass priors within the sampling that are uniform in component masses

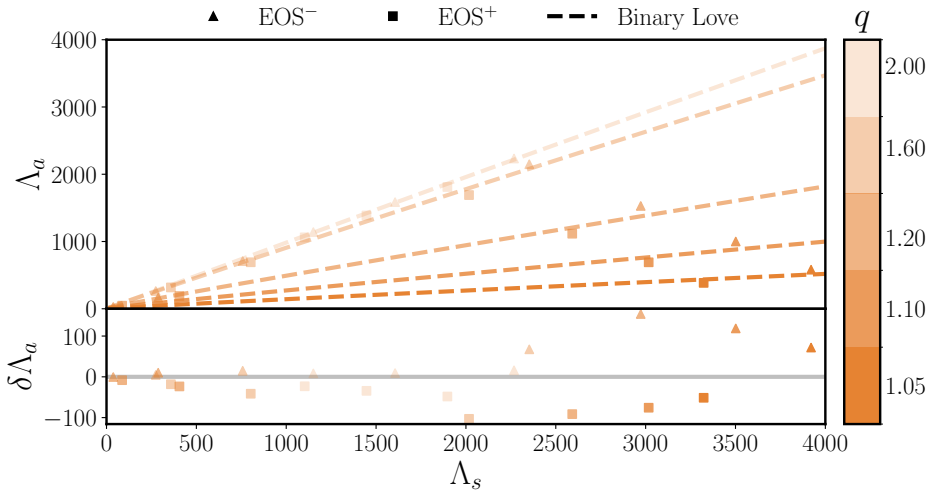

Figure 6.2: Values of injected Λ_s and Λ_a for EOS$^-$ (circles) and EOS$^+$ (squares) for each binary with a range of mass ratios q. *Top panel*: Values of injected Λ_a alongside the binary Love relation (dashed lines) for each mass ratio. *Bottom panel*: The residual $\delta\Lambda_a = \Lambda_a^{\rm inj} - \Lambda_a^{\rm BL}$ between the injected $\Lambda_a^{\rm inj}$ and the prediction through the binary Love UR $\Lambda_a^{\rm BL}$.

m_1, m_2 but sample in mass ratio $1/q \in [0.125, 1]$ and detector frame chirp mass $\mathcal{M}_c \in [\mathcal{M}_{c,inj} - 0.001, \mathcal{M}_{c,inj} + 0.001]M_\odot$ where $\mathcal{M}_{c,inj}$ is the injected detector frame chirp mass. We apply constraints to the individual component masses such that they are within $m_{1,2} \in [0.5, 5]M_\odot$. We also sample uniformly in polarisation angle $\Psi \in [0, \pi]$, phase $\phi \in [0, 2\pi]$ and coalescence time $t_c \in [t_c - 0.1, t_c - 0.1]$s, where the injected coalescence time is $t_c = 1187008882.4$s. In the independent tidal parameter sampling, priors uniform in $\tilde{\Lambda} \in [0, 5000]$ and $\delta\tilde{\Lambda} \in [-5000, 5000]$ are used. In the binary Love sampling, priors are uniform $\Lambda_s \in [0, 5000]$, with the error drawn uniformly from a normal distribution as in Eq. (6.1). We apply constraints such that $\Lambda_a \in [0, 5000]$. In the case of both independent sampling and UR sampling we additionally apply constraints such that $\Lambda_{1,2} \in [0, 5000]$.

6.2.3 Bias quantification

To assess the degree of bias and accuracy between the recovered results, we use the following quantities.

We define the bias on a parameter x as the posterior quantile between the minimum value in the distribution and the median

$$Q^x(p) := \frac{1}{2} - \int_{x^{\min}}^{x^{\text{inj}}} p(x|d) \in [-0.5, 0.5] \tag{6.2}$$

where $Q > 0$ implies positive bias and $Q < 0$ implies negative bias. We also define the *percentage error* Γ^x to assess the relative width of the obtained posterior on parameter x

$$\Gamma^x \equiv \frac{\sigma^x_{90\%}}{x_{\text{inj}}} \tag{6.3}$$

where $\sigma^x_{90\%}$ is the 90% credible interval of parameter x, and x_{inj} is the injected value. This percentage error fraction can be trivially translated to a percentage through scaling by 100%.

To quantify the favour of a model h over noise n, it often instructive to compute the Bayes factor

$$\mathcal{B} \equiv \mathcal{B}^h = \frac{\mathcal{Z}^h}{\mathcal{Z}^n} \tag{6.4}$$

where $\mathcal{Z}$ is the evidence (Eq. (1.45)). Here we are interested in comparing the Bayes factors obtained when independently sampling $\mathcal{B}^{\text{indep}}$ and the Bayes factors obtained when using URs $\mathcal{B}^{\text{UR}}$.

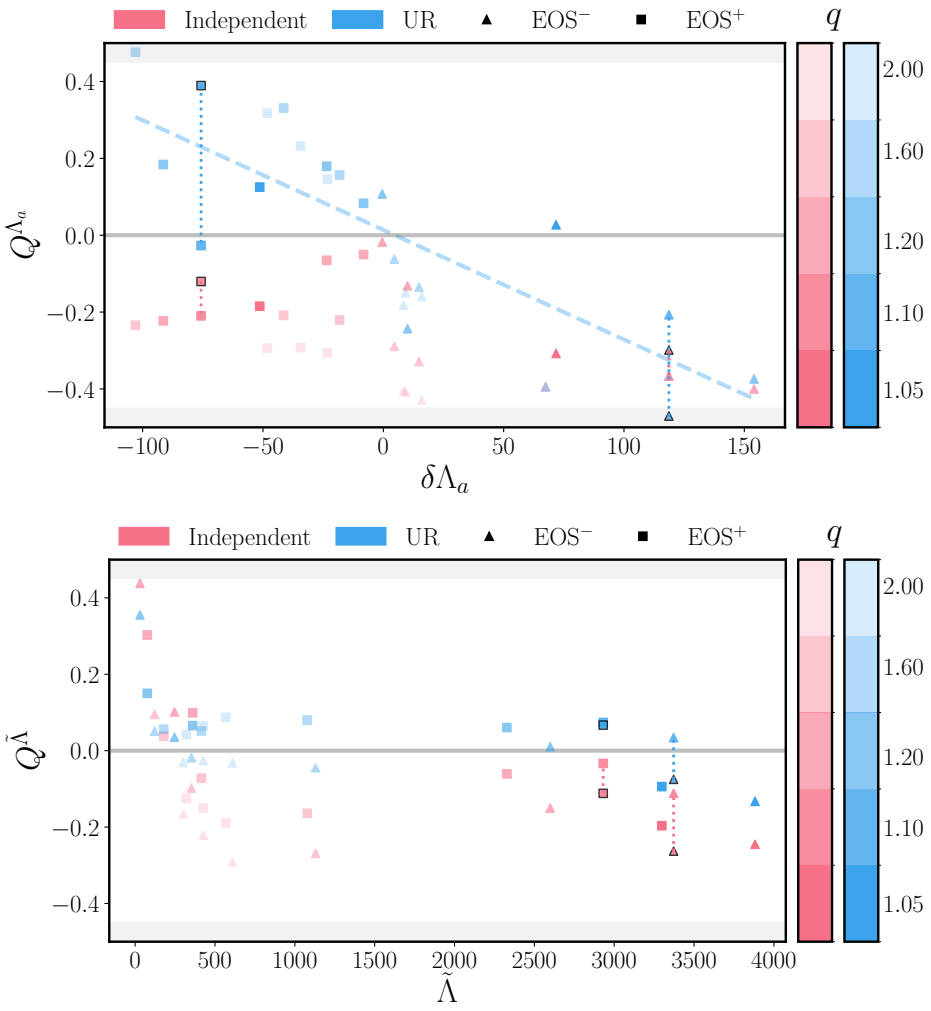

Figure 6.3: Biases obtained from posteriors against injected values. Injected signals with EOS$^-$ (triangles) and EOS$^+$ (squares) are shown for independent sampling (pink), and UR sampling (blue), with the opacity corresponding to the mass ratio q. We additionally display the region for which the true value lies outside the 90% credible interval (shaded grey). The results from the 3G run are shown with black outlines, joined to the corresponding original A+ sample (dotted lines). *Top*: Q^{Λ_a} against the injected deviation from URs of the injected binary $\delta\Lambda_a$. The fitted linear relationship between $\delta\Lambda_a$ and Q^{Λ_a} is shown (blue dashed line). *Bottom*: Bias $Q^{\tilde{\Lambda}}$ of recovered against injected joint tidal deformability $\tilde{\Lambda}$.

6.3 Results

We first examine the bias of the recovered posteriors from parameter estimation, where we consider the tidal parameter $\delta\Lambda_a$ as the parameter directly inferred by the UR, and $\tilde{\Lambda}$ as the tidal parameter which is typically best measured in analyses. These biases are shown in Figure 6.3 for posteriors recovered with independent sampling and UR sampling for the injected EOS$^-$ and EOS$^+$. The shaded regions crucially describes the region where the posterior is sufficiently biased such that the true injected value is excluded to 90% confidence. When sampling using URs, there is a weak correlation between the direction of deviation from URs to the direction of the bias, which we have visualised with a linear fit (dashed blue line)[2] with a slope of -0.00285 and a χ^2 value of -1.72. In contrast, the independent sampling shows consistent negative bias of $\delta\Lambda_a$. We attribute this to the poor recovery of $\delta\tilde{\Lambda}$, with a posterior which resembles the prior. In both sampling cases the bias appears to have little dependence on mass ratio. These results are unsurprising, it follows that deviation from the UR of the injected value would lead to a biased posterior distribution, skewed towards the assumed UR. In turn it is also expected that the independent sampling is independent of UR deviation. We show the medians and 90% intervals of the overall bias distributions in Tab. 6.2. This reflects that although the UR sampling produces less bias on average, it yields larger variation in bias. This is evidenced in the event sampled with UR with $\Lambda_a \approx -100$, which presents a Λ_a posterior biased such that the true value is not contained within the 90% credible interval. Furthermore, the sample with 3G detector CE shows an increase of bias when using UR sampling, and a decrease in bias when using the independent sampling. In both EOS cases for CE, the bias in Λ_a using UR sampling surpasses the

[2]We also fitted this relationship with a 2nd degree polynomial, however linear fitting corresponded to the best goodness-of-fit.

	Independent		UR	
X	Q^X	$\Gamma^X[\%]$	Q^X	$\Gamma^X[\%]$
Λ_a	$0.29\pm^{0.12}_{0.24}$	$174\pm^{524}_{63}$	$0.06\pm^{0.42}_{0.28}$	$66\pm^{205}_{42}$
$\tilde{\Lambda}$	$0.05\pm^{0.10}_{0.13}$	$48\pm^{143}_{39}$	$-0.12\pm^{0.41}_{0.15}$	$47\pm^{139}_{39}$
$\delta\tilde{\Lambda}$	$-0.29\pm^{0.24}_{0.13}$	$286\pm^{1302}_{875}$	$0.05\pm^{0.33}_{0.47}$	$80\pm^{42}_{235}$

Table 6.2: Values of the medians and 90% confidence intervals of bias Q^X and percentage error Γ^X for parameter $X \in \{\Lambda_a, \tilde{\Lambda}, \delta\tilde{\Lambda}$ across overall population of A+ sensitivity detections when recovered with independent sampling and UR sampling.

previously higher bias using independent sampling for A+. The increase in bias for the UR sampling is substantial, with one event in particular biased such that the true value is excluded to 90% confidence.

Considering the bias in $\tilde{\Lambda}$, we observe that near the BBH limit of $\tilde{\Lambda} = 0$ both sampling methods show extreme positive bias. This is to be expected as the credible interval is calculated as a symmetric quantile, and near the limit of $\tilde{\Lambda} = 0$ a more careful treatment should use a one-sided confidence interal. However beyond the BBH limit the posteriors of $\tilde{\Lambda}$ obtained through both sampling techniques appear independent of the magnitude of the tides. On average, independent sampling shows more bias in $\tilde{\Lambda}$ than UR sampling as quantified in Tab. 6.2. In the binary with the additional 3G detector analysis, the biases obtained with CE tend towards increasingly negative values for both sampling methods than obtained with A+ sensitivity, where only one case reduces the magnitude of the bias, which corresponds to the UR sampling.

Though bias is a useful quantity, we are also interested in the width of the posteriors, as it provides insight into the error on the measurement. Therefore, we next consider the percentage error on the recovered distributions for Λ_a and $\tilde{\Lambda}$ in Fig. 6.4. We

observe for both Λ_a and $\tilde{\Lambda}$ that the magnitude of Λ_a or $\tilde{\Lambda}$ anti-correlates with the percentage error. The percentage error when using UR sampling is consistently lower than percentage error when independently sampling across all events for Λ_a which is reflected in the average percentage error in Tab. 6.2. We also observe that the variation in percentage error for Λ_a is large, and in the case of independent sampling, every binary has a percentage error $\Gamma^{\Lambda_a} > 100\%$. In contrast, the variation in percentage error for $\Gamma^{\tilde{\Lambda}}$ is much smaller, and the error for the majority of both sampling techniques $\Gamma^{\tilde{\Lambda}} < 100\%$. The binary with the additional 3G run shows that percentage error in reduced for both techniques, though more dramatically for the UR sampling, with an improvement of almost an order of magnitude in all cases.

To gain a sense of bias in conjunction with error, we show plots comparing the two quantities in Fig 6.5. Firstly considering Λ_a, we observe that the magnitude of the bias increases as the percentage error decreases, and independent of the direction of the bias for UR sampling. We also note that although the UR sampling ranges spans comparable magnitudes of bias as the independent sampling, the percentage error using UR sampling is constantly lower. An important observation here is that when considering the binary in 3G sensitivity, in the case of independent sampling both the magnitude of bias and percentage error decrease marginally. Decrease in percentage error is to be expected, as posterior width scales with SNR. However, when using UR sampling the percentage error decreases, but the bias vastly increases. This indicates a heavily biased posterior with deceptively high accuracy. This is to be expected, as statistical errors scale as $\propto 1/\mathrm{SNR}^2$, where systematic errors are SNR independent [385]. These results reflect the increased impact of waveform systematics when looking forwards to the 3G era.

Next considering $\tilde{\Lambda}$, the sampling techniques show comparable values of percentage

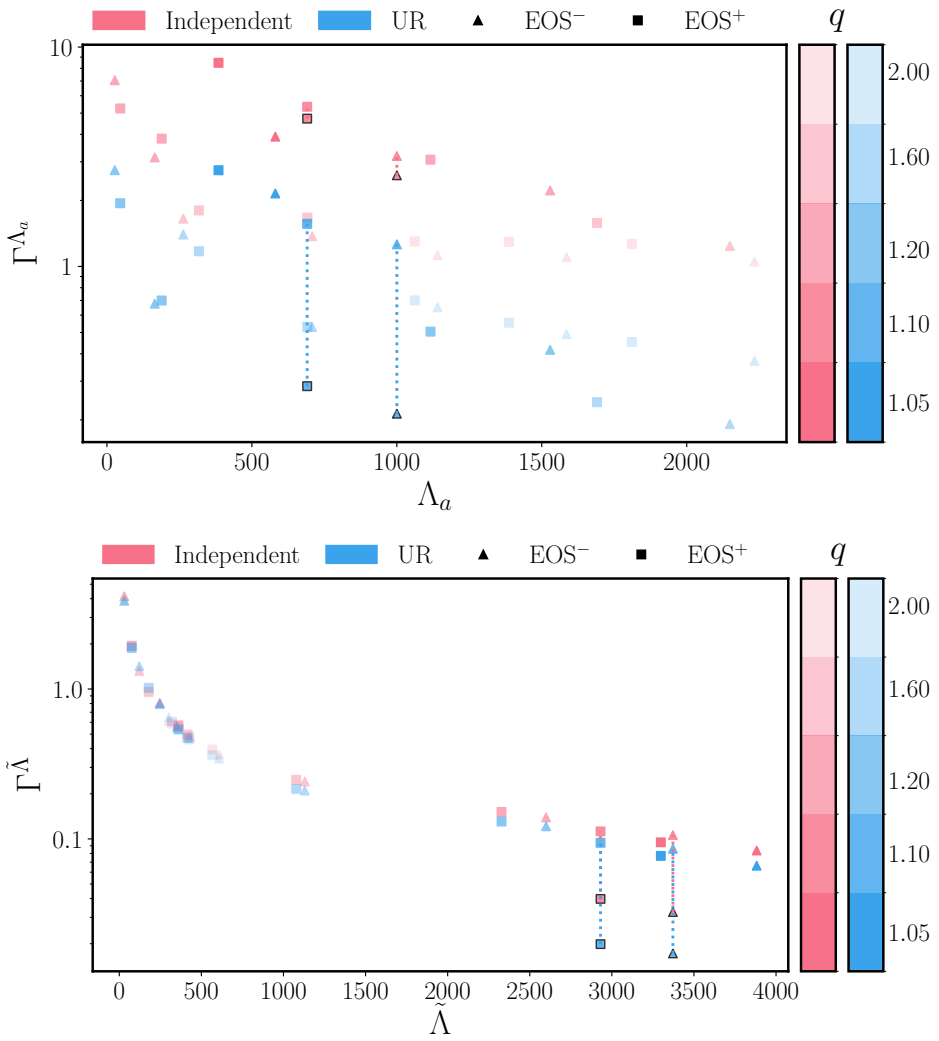

Figure 6.4: Percentage error of recovered posteriors against the injected values. Injected signals with EOS$^-$ (triangles) and EOS$^+$ (squares) are shown for independent sampling (pink), and UR sampling (blue), with the opacity corresponding to the mass ratio q. The results from the 3G run are shown with black outlines, joined to the corresponding original A+ sample (dotted lines). *Top*: Percentage error Γ^{Λ_a} against injected Λ_a. *Bottom*: Percentage error $\Gamma^{\tilde{\Lambda}}$ against injected $\tilde{\Lambda}$.

error with the UR sampling displaying less average bias. In contrast to the bias in Λ_a, the direction of bias in $\tilde{\Lambda}$ is correlated with the error. Positive bias is associated with a higher percentage error, while negative bias is linked to a lower percentage error. When increasing detector sensitivity, we observe that the percentage error decreases for both EOS and sampling techniques, and the bias on $\tilde{\Lambda}$ is pulled increasingly negative indicating under-measurement.

The ratio of Bayes factors between independent sampling and UR sampling $\mathcal{B}^{\text{indep}}/\mathcal{B}^{\text{UR}}$ are shown in Fig. 6.6. We found these results statistically insignificant, with variations $\mathcal{O}(10^{-3})$ from unity. Therefore we do not consider this a meaningful metric in this study.

6.4 Discussion

URs hold the potential to introduce a priori information and produce more accurate tidal constraints by eliminating tidal degeneracies. Here, we investigated if these assumptions pose the potential to bias tidal parameters if the EOS is of an extreme nature. We preformed an injection study of two extreme EOSs to assess if we can expect biases in O5 and beyond. In particular we focus on biases in the anti-symmetric tidal deformability Λ_a and the joint tidal deformability $\tilde{\Lambda}$. Regarding Λ_a, we find that larger biases are present typically when sampling independently as opposed to sampling with URs. We attribute this larger bias to the poor measurement of the higher order tidal deformability $\delta\tilde{\Lambda}$ as shown in Tab. 6.2, where independent sampling recovers $\delta\tilde{\Lambda}$ on average with $\sim$3 times larger error than with UR sampling. However, though the biases on Λ_a are on average lower when using URs, the larger variation in bias results in a small population of events exhibiting extreme bias. The magnitude of bias is linked

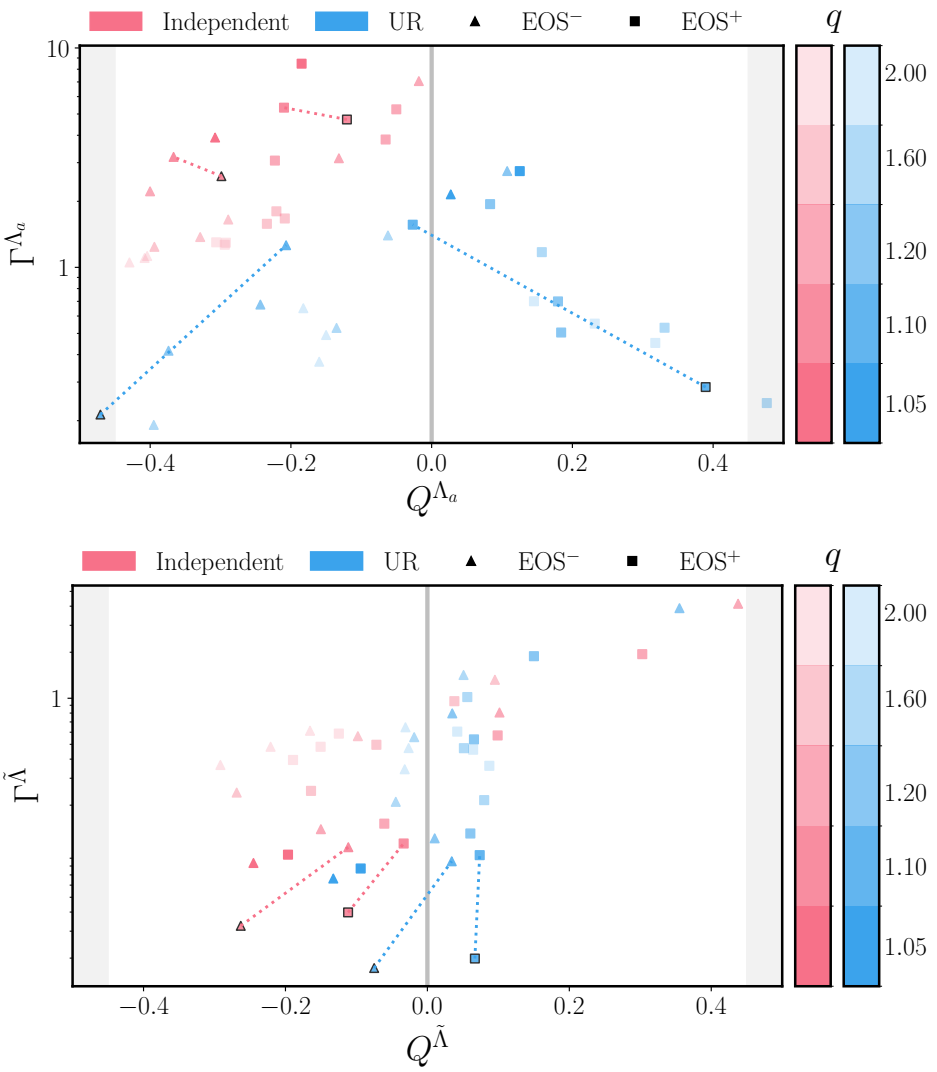

Figure 6.5: Percentage error on the recovered posteriors against the bias. Injected signals with EOS$^-$ (triangles) and EOS$^+$ (squares) are shown for independent sampling (pink), and UR sampling (blue), with the opacity corresponding to the mass ratio q. The results from the 3G run are shown with black outlines, joined to the corresponding original A+ sample (dotted lines). We additionally display the region for which the true value lies outside the 95% credible interval (shaded grey). *Top*:Percentage error Γ^{Λ_a} against the bias Q^{Λ_a}. *Bottom*: Percentage error $\Gamma^{\tilde{\Lambda}}$ against bias $Q^{\tilde{\Lambda}}$.

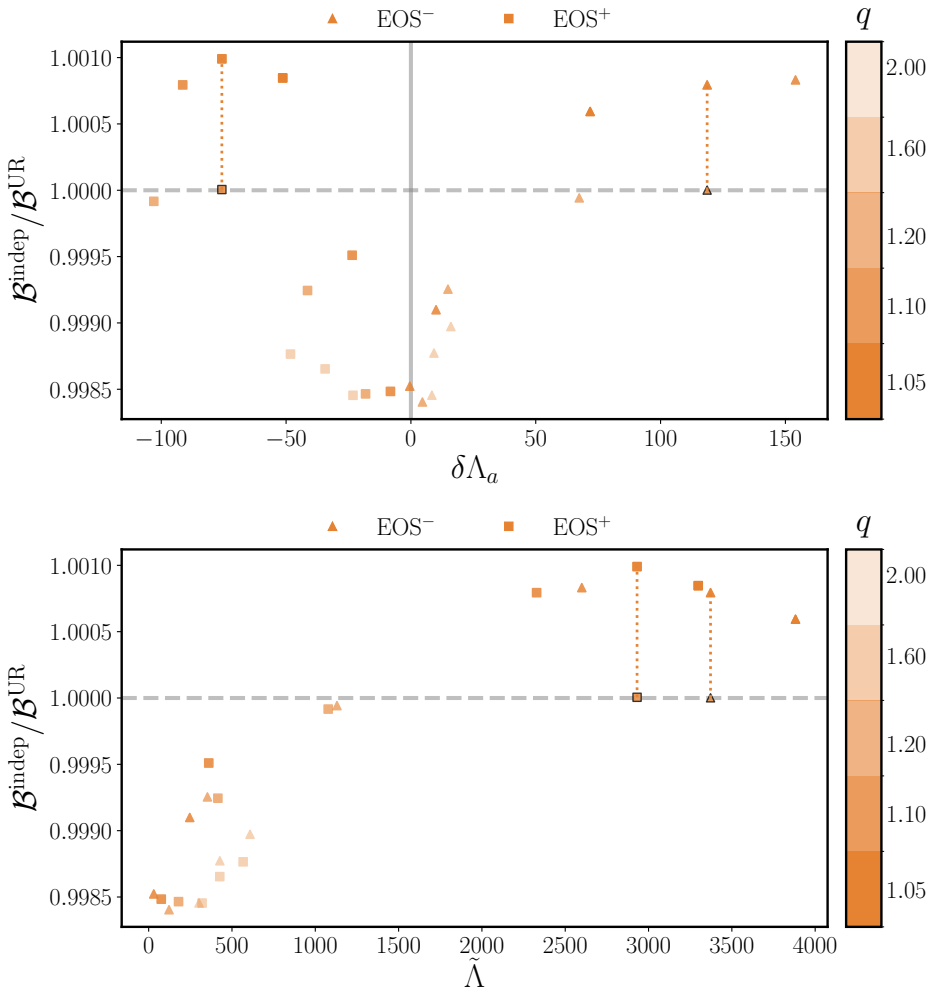

Figure 6.6: Ratio of Bayes factors from independent sampling $\mathcal{B}^{\rm indep}$ and UR sampling $\mathcal{B}^{\rm UR}$. Injected signals with EOS$^-$ (triangles) and EOS$^+$ (squares) are shown, with the opacity corresponding to the mass ratio q. The results from the 3G run are shown with black outlines, joined to the corresponding original A+ sample (dotted line). The boundary of equal Bayes factors $\mathcal{B}^{\rm indep}/\mathcal{B}^{\rm UR} = 1$ (dashed grey line). *Top*: Bayes ratio against the deviation from URs of the injected binary $\delta\Lambda_a$. UR $\delta\Lambda_a = 0$ (solid grey line) is additionally shown. *Bottom*: Bayes ratio against injected joint tidal deformability $\tilde{\Lambda}$.

to the deviation from URs. However, with no prior knowledge of the deviation from URs of the compact object's EOS, a considerable uncertainty is introduced regarding

the extent and direction of the potential bias. The bias from independent sampling in contrast is consistently negative, regardless of EOS. Though typically larger, this is a more uniform and predictable bias.

However, significant bias in Λ_a does not necessarily map to a significant bias in $\tilde{\Lambda}$, where UR sampling consistently yields lower bias than for independent sampling with comparable uncertainties.

Therefore, for O5 sensitivities we anticipate that using URs will generally yield less biased $\tilde{\Lambda}$, even with extreme EOS. In comparison, using independent sampling largely under-measures $\tilde{\Lambda}$, indicating a softer EOS than injected. This effect is not fully understood, and we leave to future work. However, care should be taken when considering the anti-symmetric tidal deformability Λ_a. In this study measured values of Λ_a with percentage errors $\Gamma^{\Lambda_a} \lessapprox 30\%$ have the potential to show significant bias for extreme EOSs. This effect is exacerbated in 3G detectors, where the increased SNR leads to less uncertainty. However, the presence of underlying bias from URs is amplified, potentially excluding the true value from the posterior distribution entirely. To assess the full extent of this effect, a 3G injection study should be carried out, which we leave for future work. However, it should be noted that the number of GW detections from BNS mergers is anticipated to increase. Thus in conjunction with complementary EOS information from experimental efforts such as nuclear physics and astrophysical observations, it is logical to expect that EOS information will be improved, and URs refined.

This work can be expanded on by propagating the information from parameter estimation runs to a constraint on the NS EOS, to compare to EOS^- and EOS^+, given a BNS population. We hypothesise that although URs within the sampling may give a better EOS constraint for an A+ detector network, the constraint for 3G would be

more stringent but systematically biased. Verifying this we leave to future work.

An important caveat to this work is that we assume perfect knowledge of the BNS waveform in General Relativity, alongside perfect calibration within parameter estimation. Additionally, we have not included dynamical tidal effects within the 3G analysis presented here, which will be important at expected detector sensitivities [368] as discussed in Ch. 4. Therefore extending this to 3G should formally include f-mode effects such as with the FMTIDAL [278] model. Additionally, this would allow exploration into the breaking of the $\Lambda - f$-mode UR in the inspiral, which may further amplify biases.

Chapter 7

Conclusions

Tidal measurements from GWs emitted by BNS inspirals offer a unique opportunity to study ultra-dense matter. Thus far, only GW170817 has yielded measurable tides and consequently GW derived information on the NS EOS. However with constant improvements in detector sensitivity, both the rate and SNR of BNS detections are estimated to substantially increase. These prospects hold exciting scientific potential, but rely on advancement of GW tidal waveform models to match these instrumentation advancements. This thesis assessed future prospects, contributed to the advancements of waveform modelling, and investigated the impact of assumptions within analyses.

Third generation detectors project increase in sensitivities, particularly at high frequencies. This corresponds late inspiral and merger of BNS systems, where the tidal interactions become dynamical. Dynamical tides encode information on the NSs fundamental f_2-mode frequencies, which is dependent on the NS EOS. Measuring the f_2-mode frequency offers more stringent EOS constraints, the testing of URs, and probing phase transitions in the merger. In Ch. 4 we studied the prospect of measuring dynamical tides with 3G detectors. We evaluated the SNRs required for dynamical

effects to be entangled from the leading order adiabatic tidal effects. We then applied this to a semi-realistic population of events and found that a small number of events will provide detectable dynamical tides. To translate this into a measurement we performed parameter estimation on a GW170817-like mock signal. Though we observed large corporations between the measured tidal deformability Λ_2 and the f_2-mode frequency, we found that measurement with leading order dynamical tide PN parameter $c_2^{\rm DT}$ provided improved accuracy.

Measurements such as these rely on waveform models that are (i) sufficiently accurate to enable precise measurements with minimal biases (ii) computationally efficient to ensure that parameter estimation can be performed within practical timescales, and (iii) flexible enough to accommodate a wide range of nuclear matter theories, allowing for the testing of exotic EOS models. In Ch. 5 we developed PhenomGSF, a phenomenological tidal phase model designed to replicate the tidal physics contained with EOB model TEOBResumS with a fraction of the generation cost. PhenomGSF is constructed in a modular fashion such that it can be added to any BBH waveform model, inheriting the point particle baseline physics. Moreover PhenomGSF treats the tidal parameters as independent quantities, therefore making no assumption of parameterised EOS or URs, and lends itself to the testing of exotic matter EOS models. We showed that PhenomGSF is faithful to TEOBResumS, performing a range of model validation and new parameter estimation results for GW170817, which predict consistent results with GWTC-1, with slightly higher tides.

We then sought to apply PhenomGSF in Ch. 6 to assess the impact of utilising URs in parameter estimation for extreme EOSs. Convenient URs between tidal parameters serve to reduce dimensionality and degeneracy, with the aim of providing more stringent tidal constraints. Using the UR and EOS independent nature of PhenomGSF we

performed parameter estimation, both assuming URs and independently sampling, on a set of mock signals which adopted extreme EOSs. We found that for O5, sampling with URs can increase accuracy and decrease bias on the joint tidal deformability, even if the true EOS is of extreme nature. However, significant biases may be present in the anti-symmetric tidal contribution, which may be intensified for future detectors.

The work within this thesis has contributed to the field of GWS from BNS mergers - however the future of this research area holds many challenges. There is a variety of physical effects that are currently not considered within BNS waveform models - this not only limits the physics that can be extracted, but potentially biases the recovered constraints. The authors of Ref. [401] for example, found that exclusion of dynamical tides within the phase modelling results in large biases in the measured adiabatic tides and recovered EOS. Waveform systematics such as these must be minimised by including the relevant physics and studying the impact of their inclusion. Matter effects that will need to be considered in future modelling include oscillation modes other than the f-mode as discussed in Sec. 2.3.2 [168, 175, 180, 405, 501–503] as well as nonlinear mode coupling between the p- and g-modes [501, 504–509], tidal dissipation effects[1], magnetic fields [514, 515], and effects of the NS crust [516–519]. In particular, BNS waveform models assume circular orbits, since the vast majority of BNS systems circularise before they enter the detection band. However, this assumption may not hold for BNS systems formed from dynamical formation channels, where a small number is estimated to have non-negligible eccentricity (in the 3G era it is predicted that 4% of BNS systems will have eccentricity ≈ 0.01 when entering the detection band [230]). Eccentricity has a significant impact on the tidal response of the system [520–523], where highly eccentric systems can induce f-mode resonance at the close passage of the peri-

[1]There has been recent development in this area [510] [100, 511, 512], with the first dissipation constraints on GW170817 [513].

helion [477]. Postmerger modelling will also require improvement, with current models giving typical mismatches $\sim 10\%$ when compared to NR simulations [188, 190, 224–229], largely due to NR uncertainty. Therefore tangentially, improvements in BNS NR simulations for both inspiral and postmerger will be imperative moving forwards to both improve and validate waveform models.

Appendix A

Appendix

A.1 Complete parameter estimation results

Here we show the full 1- and 2D posterior distributions for all parameter estimation analyses presented in Sec. 4.3.3, reformatted from Ref. [368]. Due to fixing most of the extrinsic parameters, we show all intrinsic parameters as well as the angle between the total angular momentum and the line-of-sight, ι. The dashed vertical lines in the marginalised 1D distributions indicate the 90% credible interval. All mass parameters are shown in the source frame. The posteriors for the fiducial run are shown in Fig. A.1, whilst posteriors for the results containing Gaussian mass priors are shown in Fig. A.2 and the corresponding 10-20 Hz results to inform the Gaussian mass priors are shown in Fig. A.3. The injection parameters for all runs are as follows: $\mathcal{M} = 1.186 M_\odot$, $M = 2.735 M_\odot$, $m_1 = 1.475 M_\odot$, $m_2 = 1.26 M_\odot$, $q = 0.854$, $\Lambda_{2,1} = 176.7$, $\Lambda_{2,2} = 473.2$, $f_{2,1} = 2044\,\mathrm{Hz}$, $f_{2,2} = 1947\,\mathrm{Hz}$, $\iota = 0.1\,\mathrm{rad}$.

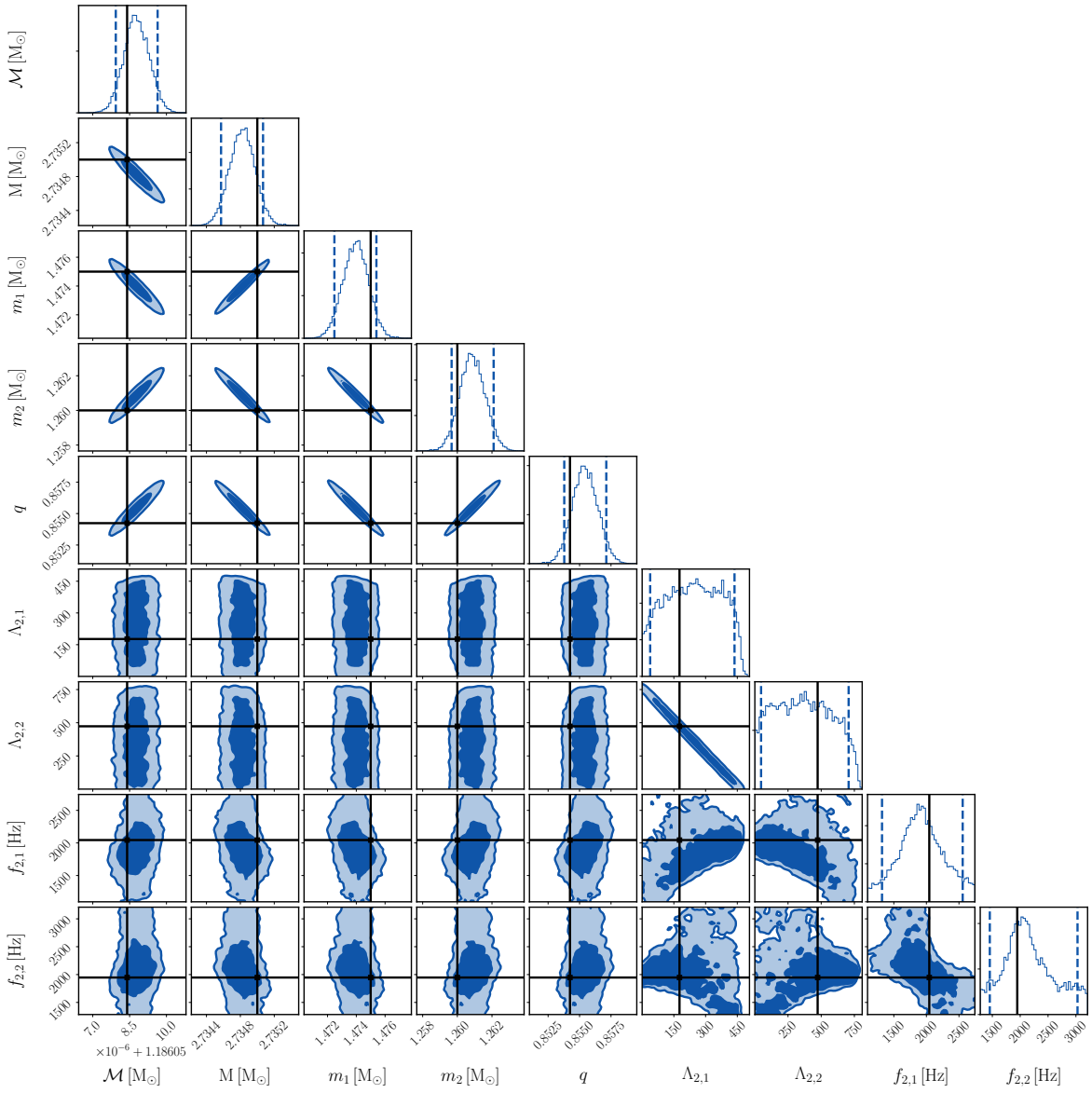

Figure A.1: Corner plot showing the posterior distributions for all parameters of the fiducial analysis. The injected values (black lines) are shown alongside 50% and 90% contours for 2D posteriors, and 90% confidence interval (blue dashed lines) for 1D posteriors.

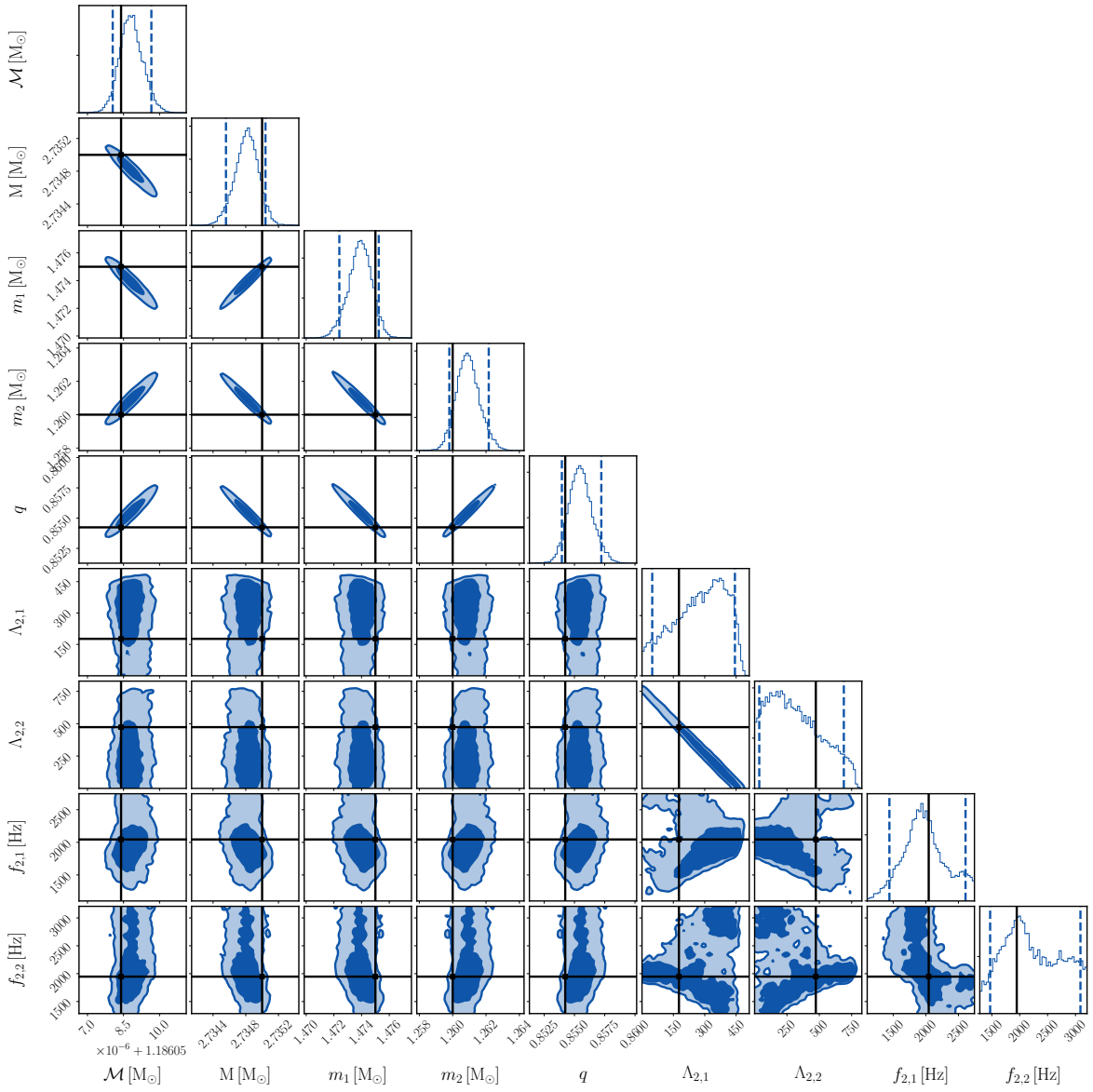

Figure A.2: Corner plot showing the posterior distributions for all parameters of the analysis with the Gaussian mass prior. The injected values (black lines) are shown alongside 50% and 90% contours for 2D posteriors, and 90% confidence interval (blue dashed lines) for 1D posteriors.

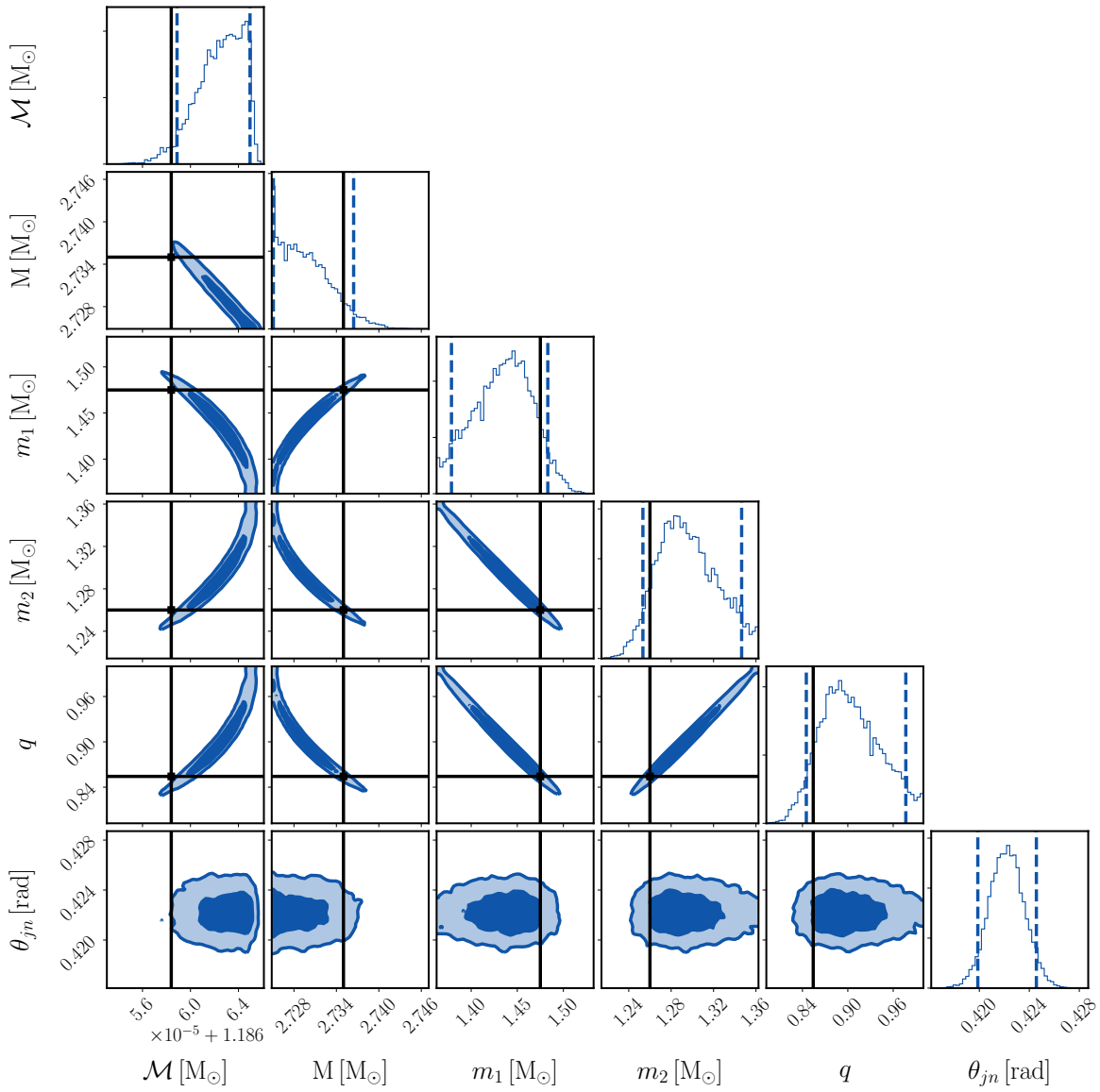

Figure A.3: Corner plot showing the posterior distributions for all parameters from the 10-20 Hz non-tidal run which informed the Gaussian prior run. The injected values (black lines) are shown alongside 50% and 90% contours for 2D posteriors, and 90% confidence interval (blue dashed lines) for 1D posteriors. $\theta_{jn} \equiv \iota$ was not constrained correctly in this run, and the true value is not contained within the posterior.

A.2 Parameter space fits

The full phenomenological fits of the five collocation points $\lambda^{(i)}$ needed to evaluate PhenomGSF are given below, reformatted from Ref. [414]. The phenomenological coefficients are listed in Tab. A.1.

$$\begin{aligned}\lambda^{(1)}(\eta,\tilde{\Lambda},\delta\tilde{\Lambda}) =& \frac{1}{1+a_1^{(1)}\tilde{\Lambda}+a_2^{(1)}\tilde{\Lambda}^2+a_3^{(1)}\tilde{\Lambda}^3+a_4^{(1)}\tilde{\Lambda}^4}\Big[\\ & b_1^{(1)}(1+d_{11}^{(1)}\delta\tilde{\Lambda}+d_{12}^{(1)}\delta\Lambda^2)\eta\tilde{\Lambda}\\ & -b_2^{(1)}(c_{11}^{(1)}(1+d_{21}^{(1)}\delta\tilde{\Lambda}-d_{22}^{(1)}\delta\tilde{\Lambda}^2)-c_{12}^{(1)}(1-d_{31}^{(1)}\delta\tilde{\Lambda}+d_{32}^{(1)}\delta\tilde{\Lambda}^2)\eta)\tilde{\Lambda}^4\\ & +b_3^{(1)}(c_{21}^{(1)}(1+d_{41}^{(1)}\delta\tilde{\Lambda}+d_{42}^{(1)}\delta\tilde{\Lambda}^2)+c_{22}^{(1)}(1+d_{51}^{(1)}\delta\tilde{\Lambda}+d_{52}^{(1)}\delta\tilde{\Lambda}^2)\eta)\tilde{\Lambda}^5\Big]\end{aligned} \tag{A.1}$$

$$\begin{aligned}\lambda^{(2)}(\eta,\tilde{\Lambda},\delta\tilde{\Lambda}) =& \frac{1}{1+a_1^{(2)}\tilde{\Lambda}+a_2^{(2)}\tilde{\Lambda}^2+a_3^{(2)}\tilde{\Lambda}^3}\Big[b_1^{(2)}(c_{11}^{(2)}(1+d_{11}^{(2)}\delta\tilde{\Lambda})\\ & +c_{12}^{(2)}(1+d_{21}^{(2)}\delta\tilde{\Lambda})\eta)\tilde{\Lambda}+b_2^{(2)}(c_{21}^{(2)}(1+d_{31}^{(2)}\delta\tilde{\Lambda})+c_{22}^{(2)}(1+d_{41}^{(2)}\delta\tilde{\Lambda})\eta)\tilde{\Lambda}^2\\ & +b_3^{(2)}(c_{31}^{(2)}(1+d_{51}^{(2)}\delta\tilde{\Lambda})+c_{32}^{(2)}(1+d_{61}^{(2)}\delta\tilde{\Lambda})\eta)\tilde{\Lambda}^3+b_4^{(2)}(1+d_{71}^{(2)}\delta\tilde{\Lambda})\tilde{\Lambda}^4\Big]\end{aligned} \tag{A.2}$$

$$\begin{aligned}\lambda^{(3)}(\eta,\tilde{\Lambda},\delta\tilde{\Lambda}) =& \frac{1}{1+a_1^{(3)}\tilde{\Lambda}+a_2^{(3)}\tilde{\Lambda}^2+a_3^{(3)}\tilde{\Lambda}^3}\Big[b_1^{(3)}(c_{11}^{(3)}(1+d_{11}^{(3)}\delta\tilde{\Lambda})\eta\\ & +c_{12}^{(3)}(1+d_{21}^{(3)}\delta\tilde{\Lambda})\eta^2)\tilde{\Lambda}\\ & +b_2^{(3)}(c_{21}^{(3)}(1+d_{31}^{(3)}\delta\tilde{\Lambda})+c_{22}^{(3)}(1+d_{41}^{(3)}\delta\tilde{\Lambda})\eta+c_{23}^{(3)}\eta^3)\tilde{\Lambda}^2\\ & +b_3^{(3)}(c_{31}^{(3)}-c_{32}^{(3)}\eta)\tilde{\Lambda}^3\Big]\end{aligned} \tag{A.3}$$

$$\begin{aligned}\lambda^{(4)}(\eta,\tilde{\Lambda},\delta\tilde{\Lambda}) =& \frac{1}{1+a_1^{(4)}\tilde{\Lambda}+a_2^{(4)}\tilde{\Lambda}^2+a_3^{(4)}\tilde{\Lambda}^3+a_4^{(4)}\tilde{\Lambda}^4}\Big[b_1^{(4)}(1+d_{11}^{(4)}\delta\tilde{\Lambda})\eta^2\tilde{\Lambda} \\ &+ b_2^{(4)}(c_{21}^{(4)}(1+d_{21}^{(4)}\delta\tilde{\Lambda})+c_{22}^{(4)}(1+d_{31}^{(4)}\delta\tilde{\Lambda})\eta)\tilde{\Lambda}^2 \\ &+ b_3^{(4)}(c_{31}^{(4)}(1+d_{41}^{(4)}\delta\tilde{\Lambda})+c_{32}^{(4)}(1+d_{51}^{(4)}\delta\tilde{\Lambda})\eta+c_{33}^{(4)}\eta^2)\tilde{\Lambda}^3 \\ &+ b_4^{(4)}\eta\tilde{\Lambda}^4\Big]\end{aligned} \tag{A.4}$$

$$\begin{aligned}\lambda^{(5)}(\eta,\tilde{\Lambda},\delta\tilde{\Lambda}) =& \frac{1}{1+a_1^{(5)}\tilde{\Lambda}+a_2^{(5)}\tilde{\Lambda}^2+a_3^{(5)}\tilde{\Lambda}^3}\Big[b_1^{(5)}\eta^2\tilde{\Lambda}+b_2^{(5)}(c_{11}^{(5)}(1+d_{11}^{(5)}\delta\tilde{\Lambda}) \\ &+ c_{12}^{(5)}(1+d_{12}^{(5)}\delta\tilde{\Lambda})\eta)\tilde{\Lambda}^2+b_3^{(5)}(c_{21}^{(5)}+c_{22}^{(5)}(1+d_{21}^{(5)}\delta\tilde{\Lambda})\eta+c_{23}^{(5)}\eta^2)\tilde{\Lambda}^3 \\ &+ b_4^{(5)}\eta^2\tilde{\Lambda}^4+b_5^{(5)}\tilde{\Lambda}^5\Big]\end{aligned} \tag{A.5}$$

$x^{(1)}$	Value	$x^{(2)}$	Value	$x^{(3)}$	Value	$x^{(4)}$	Value	$x^{(5)}$	Value
$a_1^{(1)}$	704.35868	$a_1^{(2)}$	29.78722	$a_1^{(3)}$	3.93783e13	$a_1^{(4)}$	6.11502e13	$a_1^{(5)}$	1.65802e12
$a_2^{(1)}$	0.61592	$a_2^{(2)}$	0.00029	$a_2^{(3)}$	1.57134e10	$a_2^{(4)}$	1.59883e11	$a_2^{(5)}$	1.03757e10
$a_3^{(1)}$	0.00037	$a_3^{(2)}$	4.42273e−6	$a_3^{(3)}$	4.06194e5	$a_3^{(4)}$	1.50039e7	$a_3^{(5)}$	2.06815e6
$a_4^{(1)}$	9.36183e−8	$b_1^{(2)}$	−0.20692	$b_1^{(3)}$	−3.07059e12	$a_4^{(4)}$	−407.21516	$b_1^{(5)}$	−7.50478e12
$b_1^{(1)}$	−0.06132	$b_2^{(2)}$	−0.00013	$b_2^{(3)}$	−1.37322	$b_1^{(4)}$	−2.01764e14	$b_2^{(5)}$	−5.45113e9
$b_2^{(1)}$	−3.15315e−10	$b_3^{(2)}$	−6.05658e−7	$b_3^{(3)}$	−1.68496e7	$b_2^{(4)}$	−1.09596e11	$b_3^{(5)}$	−5.61410e7
$b_3^{(1)}$	5.46894e−14	$b_4^{(2)}$	7.15217e−11	$c_{11}^{(3)}$	−3.94830	$b_3^{(4)}$	−6.39775e8	$b_4^{(5)}$	7.04369e4
$c_{11}^{(1)}$	4.10522	$c_{11}^{(2)}$	−1.78228	$c_{12}^{(3)}$	31.60021	$b_4^{(4)}$	2.10833e5	$b_5^{(5)}$	0.36838
$c_{12}^{(1)}$	−12.80678	$c_{12}^{(2)}$	11.01742	$c_{21}^{(3)}$	10.06460	$c_{21}^{(4)}$	3.93019	$c_{11}^{(5)}$	2.96697
$c_{21}^{(1)}$	4.38039	$c_{21}^{(2)}$	16.30702	$c_{22}^{(3)}$	−63.87040	$c_{22}^{(4)}$	−11.63559	$c_{12}^{(5)}$	−7.84667
$c_{22}^{(1)}$	−13.84189	$c_{22}^{(2)}$	−61.74570	$c_{23}^{(3)}$	110.41652	$c_{31}^{(4)}$	7.32205	$c_{21}^{(5)}$	7.56107
$d_{11}^{(1)}$	−0.01033	$c_{31}^{(2)}$	1.92755	$c_{31}^{(3)}$	3.08006	$c_{32}^{(4)}$	−42.95971	$c_{22}^{(5)}$	−43.79735
$d_{12}^{(1)}$	6.81023e−6	$c_{32}^{(2)}$	−3.65176	$c_{32}^{(3)}$	−8.31909	$c_{33}^{(4)}$	70.66872	$c_{23}^{(5)}$	70.23612
$d_{21}^{(1)}$	−0.00122	$d_{11}^{(2)}$	0.02351	$d_{11}^{(3)}$	0.04560	$d_{11}^{(4)}$	−0.02398	$d_{11}^{(5)}$	−0.03780
$d_{22}^{(1)}$	−8.60463e−7	$d_{21}^{(2)}$	0.01609	$d_{21}^{(3)}$	0.02267	$d_{21}^{(4)}$	−0.01840	$d_{12}^{(5)}$	−0.05580
$d_{31}^{(1)}$	−0.00154	$d_{31}^{(2)}$	−0.00046	$d_{31}^{(3)}$	−0.00144	$d_{31}^{(4)}$	−0.02534	$d_{21}^{(5)}$	4.36021
$d_{32}^{(1)}$	−1.09916e−6	$d_{41}^{(2)}$	−0.00008	$d_{41}^{(3)}$	−0.00088	$d_{41}^{(4)}$	0.00017		
$d_{41}^{(1)}$	−0.00072	$d_{51}^{(2)}$	−0.00024			$d_{51}^{(4)}$	0.00013		
$d_{42}^{(1)}$	−5.84154e−7	$d_{61}^{(2)}$	−0.00095						
$d_{51}^{(1)}$	−0.00086	$d_{71}^{(2)}$	0.00012						
$d_{52}^{(1)}$	−7.22994e−7								

Table A.1: Values of the phenomenological coefficients of the parameter space fits, where x is a placeholder variable.

A.3 GW170817 posteriors

We present the full set of posteriors for the low-spin analysis of GW170817 in Fig. A.4, reformatted from Ref. [414]. Information on priors and recovered values can be found in Tab. 5.3.

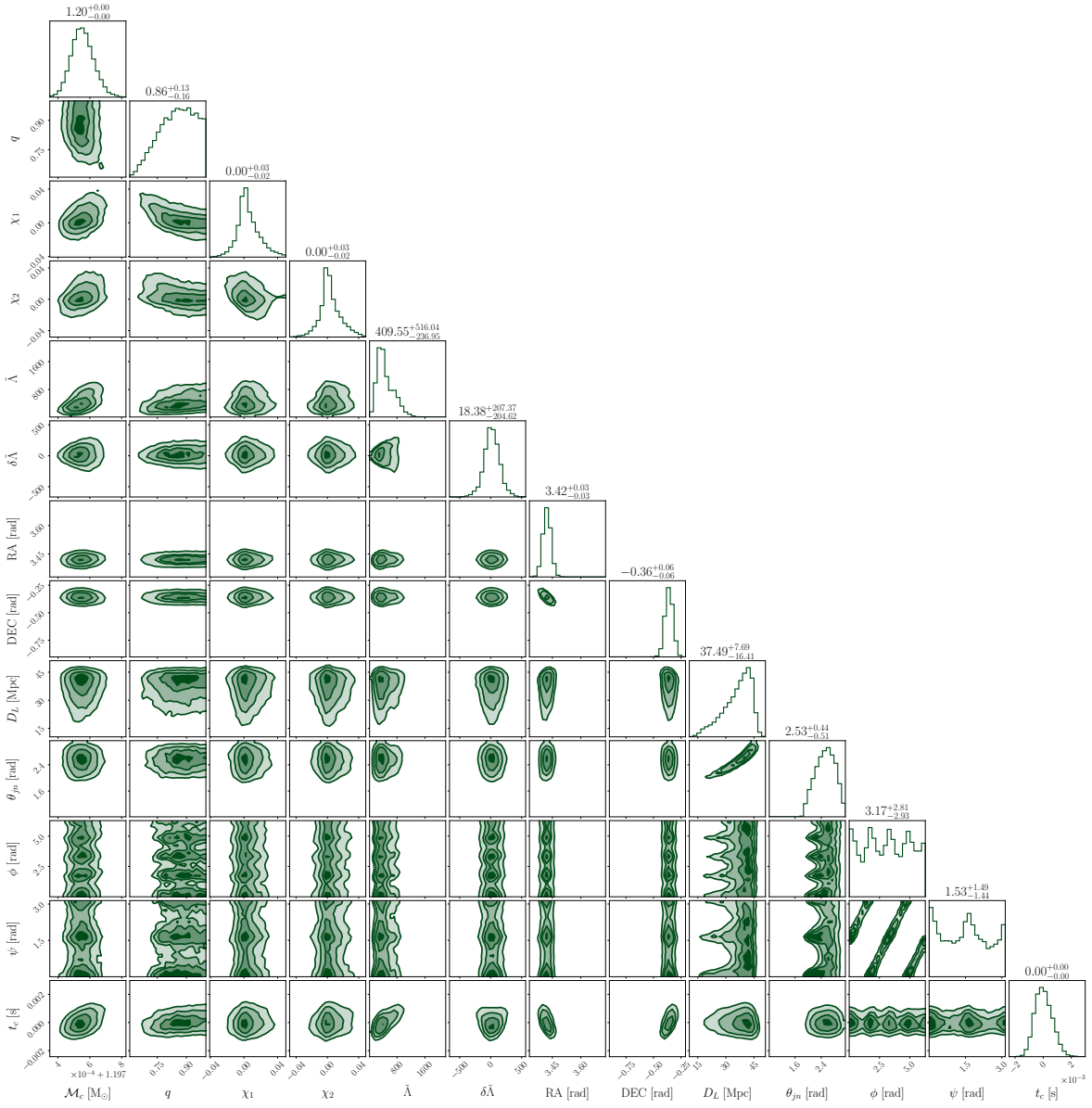

Figure A.4: 1D and 2D posteriors of all parameters obtained for GW170817 with IMRPhenomXAS_PhenomGSF. The geocentric time is shown with an offset of the true injected $t_c = 1187008882.4$s for better visualisation.

Bibliography

[1] H. T. Cromartie et al. (NANOGrav), Nature Astron. **4**, 72 (2019), arXiv:1904.06759 [astro-ph.HE].

[2] J. Antoniadis et al., Science **340**, 6131 (2013), arXiv:1304.6875 [astro-ph.HE].

[3] M. C. Miller et al., Astrophys. J. Lett. **887**, L24 (2019), arXiv:1912.05705 [astro-ph.HE].

[4] T. E. Riley et al., Astrophys. J. Lett. **887**, L21 (2019), arXiv:1912.05702 [astro-ph.HE].

[5] B. P. Abbott et al. (LIGO Scientific, Virgo), Phys. Rev. Lett. **119**, 161101 (2017), arXiv:1710.05832 [gr-qc].

[6] G. F. Burgio, H.-J. Schulze, I. Vidaña, and J.-B. Wei, Symmetry **13**, 400 (2021).

[7] B. K. Pradhan, A. Vijaykumar, and D. Chatterjee, Phys. Rev. D **107**, 023010 (2023), arXiv:2210.09425 [astro-ph.HE].

[8] K. Yagi and N. Yunes, Class. Quant. Grav. **33**, 13LT01 (2016), arXiv:1512.02639 [gr-qc].

[9] T. Dietrich, A. Samajdar, S. Khan, N. K. Johnson-McDaniel, R. Dudi, and W. Tichy, Phys. Rev. D **100**, 044003 (2019), arXiv:1905.06011 [gr-qc].

[10] LIGO Scientific Collaboration, Virgo Collaboration, and KAGRA Collaboration, LVK Algorithm Library - LALSuite, Free software (GPL) (2018).

[11] S. Bernuzzi, A. Nagar, S. Balmelli, T. Dietrich, and M. Ujevic, Phys. Rev. Lett. **112**, 201101 (2014), arXiv:1402.6244 [gr-qc].

[12] A. Gonzalez et al., Class. Quant. Grav. **40**, 085011 (2023), arXiv:2210.16366 [gr-qc].

[13] A. Nagar, S. Bernuzzi, W. Del Pozzo, G. Riemenschneider, S. Akcay, G. Carullo, P. Fleig, S. Babak, K. W. Tsang, M. Colleoni, et al., Phys. Rev. D **98**, 104052 (2018).

[14] M. Evans, J. Harms, and S. Vitale, Exploring the Sensitivity of Next Generation Gravitational Wave Detectors, https://dcc.ligo.org/LIGO-P1600143/public (2016).

[15] R. Abbott et al., Power Spectral Densities (PSD) release for GWTC-1, https://dcc.ligo.org/LIGO-P1900011/public (2018).

[16] J. S. Read, B. D. Lackey, B. J. Owen, and J. L. Friedman, Phys. Rev. D **79**, 124032 (2009), arXiv:0812.2163 [astro-ph].

[17] A. Einstein, Annalen Phys. **49**, 769 (1916).

[18] B. F. Schutz, *A FIRST COURSE IN GENERAL RELATIVITY* (Cambridge Univ. Pr., Cambridge, UK, 1985).

[19] M. Maggiore, *Gravitational Waves. Vol. 1: Theory and Experiments* (Oxford University Press, 2007).

[20] C. W. Misner, K. S. Thorne, and J. A. Wheeler, *Gravitation* (W. H. Freeman, San Francisco, 1973).

[21] S. M. Carroll, *Spacetime and Geometry: An Introduction to General Relativity* (Cambridge University Press, 2019).

[22] W. Rindler, *Relativity: Special, general, and cosmological* (2006).

[23] J. V. Narlikar, *An Introduction to Relativity* (Cambridge University Press, 2010).

[24] R. M. Wald, *General Relativity* (Chicago Univ. Pr., Chicago, USA, 1984).

[25] A. Einstein, Sitzungsber. Preuss. Akad. Wiss. Berlin (Math. Phys.) **1918**, 154 (1918).

[26] J. A. Wheeler and K. Ford, *Geons, black holes, and quantum foam: A life in physics* (1998).

[27] C. Cutler and K. S. Thorne, in *16th International Conference on General Relativity and Gravitation (GR16)* (2013) pp. 72–111, arXiv:gr-qc/0204090.

[28] B. S. Sathyaprakash and B. F. Schutz, Living Rev. Rel. **12**, 2 (2009), arXiv:0903.0338 [gr-qc].

[29] R. Abbott et al. (KAGRA, VIRGO, LIGO Scientific), Phys. Rev. X **13**, 041039 (2023), arXiv:2111.03606 [gr-qc].

[30] R. Abbott et al. (LIGO Scientific, Virgo, KAGRA), Astrophys. J. **913**, L27 (2021), arXiv:2012.12926 [astro-ph.HE].

[31] R. Abbott et al. (LIGO Scientific, KAGRA, VIRGO), Astrophys. J. **932**, 133 (2022), arXiv:2112.10990 [gr-qc].

[32] G. Agazie et al. (NANOGrav), Astrophys. J. Lett. **951**, L9 (2023), arXiv:2306.16217 [astro-ph.HE].

[33] G. Agazie et al. (NANOGrav), Astrophys. J. Lett. **951**, L8 (2023), arXiv:2306.16213 [astro-ph.HE].

[34] J. Antoniadis et al. (EPTA), Astron. Astrophys. **678**, A48 (2023), arXiv:2306.16224 [astro-ph.HE].

[35] H. Xu et al., Res. Astron. Astrophys. **23**, 075024 (2023), arXiv:2306.16216 [astro-ph.HE].

[36] B. P. Abbott et al. (LIGO Scientific, Virgo), Phys. Rev. Lett. **119**, 161101 (2017), arXiv:1710.05832 [gr-qc].

[37] B. P. Abbott et al. (LIGO Scientific, Virgo), Phys. Rev. Lett. **116**, 061102 (2016), arXiv:1602.03837 [gr-qc].

[38] B. P. Abbott et al. (LIGO Scientific), Rept. Prog. Phys. **72**, 076901 (2009), arXiv:0711.3041 [gr-qc].

[39] J. Aasi et al. (LIGO Scientific), Class. Quant. Grav. **32**, 074001 (2015), arXiv:1411.4547 [gr-qc].

[40] A. Giazotto, Nucl. Instrum. Meth. A **289**, 518 (1990).

[41] F. Acernese et al. (VIRGO), Class. Quant. Grav. **32**, 024001 (2015), arXiv:1408.3978 [gr-qc].

[42] K. Somiya (KAGRA), Class. Quant. Grav. **29**, 124007 (2012), arXiv:1111.7185 [gr-qc].

[43] N. Mio (LCGT), Prog. Theor. Phys. Suppl. **151**, 221 (2003).

[44] Y. Aso, Y. Michimura, K. Somiya, M. Ando, O. Miyakawa, T. Sekiguchi, D. Tatsumi, and H. Yamamoto (KAGRA), Phys. Rev. D **88**, 043007 (2013), arXiv:1306.6747 [gr-qc].

[45] A. A. Michelson and E. W. Morley, Am. J. Sci. **34**, 333 (1887).

[46] B. P. Abbott et al., Phys. Rev. D **93**, 112004 (2016), [Addendum: Phys.Rev.D 97, 059901 (2018)], arXiv:1604.00439 [astro-ph.IM].

[47] B. P. Abbott et al. (LIGO Scientific, Virgo), Class. Quant. Grav. **37**, 055002 (2020), arXiv:1908.11170 [gr-qc].

[48] J. D. Romano and N. J. Cornish, Living Rev. Rel. **20**, 2 (2017), arXiv:1608.06889 [gr-qc].

[49] J. N. Goldberg, A. J. MacFarlane, E. T. Newman, F. Rohrlich, and E. C. G. Sudarshan, J. Math. Phys. **8**, 2155 (1967).

[50] D. Brown, S. Fairhurst, B. Krishnan, R. A. Mercer, R. K. Kopparapu, L. Santamaria, and J. T. Whelan, (2007), arXiv:0709.0093 [gr-qc].

[51] J. J. Sakurai and J. Napolitano, *Modern Quantum Mechanics*, Quantum physics, quantum information and quantum computation (Cambridge University Press, 2020).

[52] C. Mills and S. Fairhurst, Phys. Rev. D **103**, 024042 (2021), arXiv:2007.04313 [gr-qc].

[53] P. Schmidt, M. Hannam, S. Husa, and P. Ajith, Phys. Rev. D **84**, 024046 (2011), arXiv:1012.2879 [gr-qc].

[54] M. Boyle, R. Owen, and H. P. Pfeiffer, Phys. Rev. D **84**, 124011 (2011), arXiv:1110.2965 [gr-qc].

[55] R. O'Shaughnessy, J. Healy, L. London, Z. Meeks, and D. Shoemaker, Phys. Rev. D **85**, 084003 (2012), [Erratum: Phys.Rev.D 87, 069901 (2013)], arXiv:1201.2113 [gr-qc].

[56] L. Pekowsky, R. O'Shaughnessy, J. Healy, and D. Shoemaker, Phys. Rev. D **88**, 024040 (2013), arXiv:1304.3176 [gr-qc].

[57] M. Boyle, L. E. Kidder, S. Ossokine, and H. P. Pfeiffer, (2014), arXiv:1409.4431 [gr-qc].

[58] S. Fairhurst, R. Green, C. Hoy, M. Hannam, and A. Muir, Phys. Rev. D **102**, 024055 (2020), arXiv:1908.05707 [gr-qc].

[59] E. Thrane and C. Talbot, Publ. Astron. Soc. Austral. **36**, e010 (2019), [Erratum: Publ.Astron.Soc.Austral. 37, e036 (2020)], arXiv:1809.02293 [astro-ph.IM].

[60] J. Veitch et al., Phys. Rev. D **91**, 042003 (2015), arXiv:1409.7215 [gr-qc].

[61] T. Bayes, Rev., Phil. Trans. Roy. Soc. Lond. **53**, 370 (1764).

[62] N. Metropolis, A. W. Rosenbluth, M. N. Rosenbluth, A. H. Teller, and E. Teller, J. Chem. Phys. **21**, 1087 (1953).

[63] W. K. Hastings, Biometrika **57**, 97 (1970).

[64] J. Skilling, Bayesian Analysis **1**, 833 (2006).

[65] J. S. Speagle, Mon. Not. R. Astron. Soc. **493**, 3132 (2020), arXiv:1904.02180 [astro-ph.IM].

[66] G. Ashton et al., Astrophys. J. Suppl. **241**, 27 (2019), arXiv:1811.02042 [astro-ph.IM].

[67] N. K. Glendenning, *Compact stars: Nuclear physics, particle physics, and general relativity* (1997).

[68] J. M. Lattimer, Ann. Rev. Nucl. Part. Sci. **71**, 433 (2021).

[69] M. Oertel, M. Hempel, T. Klähn, and S. Typel, Rev. Mod. Phys. **89**, 015007 (2017), arXiv:1610.03361 [astro-ph.HE].

[70] F. Özel and P. Freire, Ann. Rev. Astron. Astrophys. **54**, 401 (2016), arXiv:1603.02698 [astro-ph.HE].

[71] J. M. Lattimer and M. Prakash, Science **304**, 536 (2004), arXiv:astro-ph/0405262.

[72] P. Russotto et al., Phys. Rev. C **94**, 034608 (2016), arXiv:1608.04332 [nucl-ex].

[73] A. Le Fèvre, Y. Leifels, W. Reisdorf, J. Aichelin, and C. Hartnack, Nucl. Phys. A **945**, 112 (2016), arXiv:1501.05246 [nucl-ex].

[74] P. Danielewicz, R. Lacey, and W. G. Lynch, Science **298**, 1592 (2002), arXiv:nucl-th/0208016.

[75] M. B. Tsang, W. G. Lynch, P. Danielewicz, and C. Y. Tsang, Phys. Lett. B **795**, 533 (2019), arXiv:1906.02180 [nucl-ex].

[76] J. C. Collins and M. J. Perry, Phys. Rev. Lett. **34**, 1353 (1975).

[77] E. Annala, T. Gorda, A. Kurkela, J. Nättilä, and A. Vuorinen, Nature Phys. **16**, 907 (2020), arXiv:1903.09121 [astro-ph.HE].

[78] H. J. Schulze, A. Polls, A. Ramos, and I. Vidana, Phys. Rev. C **73**, 058801 (2006).

[79] K. Chatziioannou and S. Han, Phys. Rev. D **101**, 044019 (2020), arXiv:1911.07091 [gr-qc].

[80] A. Hewish, S. J. Bell, J. D. H. Pilkington, P. F. Scott, and R. A. Collins, Nature **217**, 709 (1968).

[81] J. H. Taylor, Rev. Mod. Phys. **66**, 711 (1994).

[82] J. W. T. Hessels, S. M. Ransom, I. H. Stairs, P. C. C. Freire, V. M. Kaspi, and F. Camilo, Science **311**, 1901 (2006), arXiv:astro-ph/0601337.

[83] J. M. Lattimer, Ann. Rev. Nucl. Part. Sci. **62**, 485 (2012), arXiv:1305.3510 [nucl-th].

[84] G. Raaijmakers, S. K. Greif, K. Hebeler, T. Hinderer, S. Nissanke, A. Schwenk, T. E. Riley, A. L. Watts, J. M. Lattimer, and W. C. G. Ho, Astrophys. J. Lett. **918**, L29 (2021), arXiv:2105.06981 [astro-ph.HE].

[85] M. C. Miller et al., Astrophys. J. Lett. **918**, L28 (2021), arXiv:2105.06979 [astro-ph.HE].

[86] L. Baiotti, Prog. Part. Nucl. Phys. **109**, 103714 (2019), arXiv:1907.08534 [astro-ph.HE].

[87] B. P. Abbott et al. (LIGO Scientific, Virgo), Phys. Rev. **X9**, 011001 (2019), arXiv:1805.11579 [gr-qc].

[88] M. Soares-Santos et al. (DES, Dark Energy Camera GW-EM), Astrophys. J. Lett. **848**, L16 (2017), arXiv:1710.05459 [astro-ph.HE].

[89] B. P. Abbott et al. (LIGO Scientific, Virgo, Fermi GBM, INTEGRAL, IceCube, AstroSat Cadmium Zinc Telluride Imager Team, IPN, Insight-Hxmt, ANTARES, Swift, AGILE Team, 1M2H Team, Dark Energy Camera GW-EM, DES, DLT40, GRAWITA, Fermi-LAT, ATCA, ASKAP, Las Cumbres Observatory Group, OzGrav, DWF (Deeper Wider Faster Program), AST3, CAASTRO, VINROUGE, MASTER, J-GEM, GROWTH, JAGWAR, CaltechNRAO, TTU-NRAO, NuSTAR, Pan-STARRS, MAXI Team, TZAC Consortium, KU, Nordic Optical Telescope, ePESSTO, GROND, Texas Tech University, SALT Group, TOROS, BOOTES, MWA, CALET, IKI-GW Follow-up, H.E.S.S., LOFAR, LWA, HAWC, Pierre Auger, ALMA, Euro VLBI Team, Pi of Sky, Chandra Team at McGill University, DFN, ATLAS Telescopes, High Time Resolution Universe Survey, RIMAS, RATIR, SKA South Africa/MeerKAT), Astrophys. J. Lett. **848**, L12 (2017), arXiv:1710.05833 [astro-ph.HE].

[90] B. P. Abbott et al. (LIGO Scientific, Virgo, Fermi-GBM, INTEGRAL), Astrophys. J. Lett. **848**, L13 (2017), arXiv:1710.05834 [astro-ph.HE].

[91] G. Hallinan et al., Science **358**, 1579 (2017), arXiv:1710.05435 [astro-ph.HE].

[92] K. D. Alexander et al., Astrophys. J. Lett. **863**, L18 (2018), arXiv:1805.02870 [astro-ph.HE].

[93] R. Margutti et al., Astrophys. J. Lett. **856**, L18 (2018), arXiv:1801.03531 [astro-ph.HE].

[94] G. Ghirlanda et al., Science **363**, 968 (2019), arXiv:1808.00469 [astro-ph.HE].

[95] E. Troja et al., Nature **551**, 71 (2017), arXiv:1710.05433 [astro-ph.HE].

[96] P. D'Avanzo et al., Astron. Astrophys. **613**, L1 (2018), arXiv:1801.06164 [astro-ph.HE].

[97] B. P. Abbott et al. (LIGO Scientific, Virgo, 1M2H, Dark Energy Camera GW-E, DES, DLT40, Las Cumbres Observatory, VINROUGE, MASTER), Nature **551**, 85 (2017), arXiv:1710.05835 [astro-ph.CO].

[98] S. Dhawan, M. Bulla, A. Goobar, A. S. Carracedo, and C. N. Setzer 10.3847/1538-4357/ab5799 (2019), arXiv:1909.13810 [astro-ph.HE].

[99] B. P. Abbott et al. (LIGO Scientific, Virgo, VIRGO), Astrophys. J. **909**, 218 (2021), arXiv:1908.06060 [astro-ph.CO].

[100] C. S. Kochanek, Astrophys. J. **398**, 234 (1992).

[101] M. W. Coughlin, T. Dietrich, J. Heinzel, N. Khetan, S. Antier, M. Bulla, N. Christensen, D. A. Coulter, and R. J. Foley, Phys. Rev. Res. **2**, 022006 (2020), arXiv:1908.00889 [astro-ph.HE].

[102] T. Dietrich, M. W. Coughlin, P. T. H. Pang, M. Bulla, J. Heinzel, L. Issa, I. Tews, and S. Antier, Science **370**, 1450 (2020), arXiv:2002.11355 [astro-ph.HE].

[103] P. S. Cowperthwaite et al., Astrophys. J. Lett. **848**, L17 (2017), arXiv:1710.05840 [astro-ph.HE].

[104] S. J. Smartt et al., Nature **551**, 75 (2017), arXiv:1710.05841 [astro-ph.HE].

[105] M. M. Kasliwal et al., Science **358**, 1559 (2017), arXiv:1710.05436 [astro-ph.HE].

[106] D. Kasen, B. Metzger, J. Barnes, E. Quataert, and E. Ramirez-Ruiz, Nature **551**, 80 (2017), arXiv:1710.05463 [astro-ph.HE].

[107] P. Kumar and B. Zhang, Phys. Rept. **561**, 1 (2014), arXiv:1410.0679 [astro-ph.HE].

[108] R. Fernández and B. D. Metzger, Ann. Rev. Nucl. Part. Sci. **66**, 23 (2016), arXiv:1512.05435 [astro-ph.HE].

[109] M. Shibata and K. Hotokezaka, Ann. Rev. Nucl. Part. Sci. **69**, 41 (2019), arXiv:1908.02350 [astro-ph.HE].

[110] V. Baibhav, E. Berti, D. Gerosa, M. Mapelli, N. Giacobbo, Y. Bouffanais, and U. N. Di Carlo, Phys. Rev. D **100**, 064060 (2019), arXiv:1906.04197 [gr-qc].

[111] C. G. Bernal, C. Frajuca, H. D. Hirsch, B. Minari, N. S. Magalhaes, and L. B. Selbach, Front. Astron. Space Sci. **11**, 1390597 (2024).

[112] J. R. Oppenheimer and G. M. Volkoff, Phys. Rev. **55**, 374 (1939).

[113] H. Müther, M. Prakash, and T. L. Ainsworth, Phys. Lett. B **199**, 469 (1987).

[114] F. Douchin and P. Haensel, Astron. Astrophys. **380**, 151 (2001), arXiv:astro-ph/0111092.

[115] H. Mueller and B. D. Serot, Nucl. Phys. A **606**, 508 (1996), arXiv:nucl-th/9603037.

[116] A. Akmal, V. R. Pandharipande, and D. G. Ravenhall, Phys. Rev. **C58**, 1804 (1998), arXiv:nucl-th/9804027 [nucl-th].

[117] R. B. Wiringa, V. Fiks, and A. Fabrocini, Phys. Rev. C **38**, 1010 (1988).

[118] S. Banik, M. Hempel, and D. Bandyopadhyay, Astrophys. J. Suppl. **214**, 22 (2014), arXiv:1404.6173 [astro-ph.HE].

[119] D. Chatterjee and I. Vidaña, Eur. Phys. J. A **52**, 29 (2016), arXiv:1510.06306 [nucl-th].

[120] M. Alford, M. Braby, M. W. Paris, and S. Reddy, Astrophys. J. **629**, 969 (2005), arXiv:nucl-th/0411016.

[121] D. B. Kaplan and A. E. Nelson, Nucl. Phys. A **479**, 273c (1988).

[122] R. Knorren, M. Prakash, and P. J. Ellis, Phys. Rev. C **52**, 3470 (1995), arXiv:nucl-th/9506016.

[123] P. Char and S. Banik, Phys. Rev. C **90**, 015801 (2014), arXiv:1406.4961 [astro-ph.HE].

[124] G. Panotopoulos and I. Lopes, Phys. Rev. D **96**, 083004 (2017), arXiv:1709.06312 [hep-ph].

[125] P. Routaray, S. R. Mohanty, H. C. Das, S. Ghosh, P. J. Kalita, V. Parmar, and B. Kumar, JCAP **10**, 073, arXiv:2304.05100 [nucl-th].

[126] H.-M. Liu, J.-B. Wei, Z.-H. Li, G. F. Burgio, and H. J. Schulze, Phys. Dark Univ. **42**, 101338 (2023), arXiv:2307.11313 [nucl-th].

[127] B. D. Lackey, M. Nayyar, and B. J. Owen, Phys. Rev. D **73**, 024021 (2006), arXiv:astro-ph/0507312.

[128] A. L. Watts et al., Rev. Mod. Phys. **88**, 021001 (2016), arXiv:1602.01081 [astro-ph.HE].

[129] P. A. Sturrock, Astrophys. J. **164**, 529 (1971).

[130] M. A. Ruderman and P. G. Sutherland, Astrophys. J. **196**, 51 (1975).

[131] Y.-S. Tsai, Rev. Mod. Phys. **46**, 815 (1974), [Erratum: Rev.Mod.Phys. 49, 421–423 (1977)].

[132] G. Greenstein and G. J. Hartke, ApJ **271**, 283 (1983).

[133] D. Adhikari et al. (PREX), Phys. Rev. Lett. **126**, 172502 (2021), arXiv:2102.10767 [nucl-ex].

[134] D. Adhikari et al. (CREX), Phys. Rev. Lett. **129**, 042501 (2022), arXiv:2205.11593 [nucl-ex].

[135] T. W. Donnelly, J. Dubach, and I. Sick, Nucl. Phys. A **503**, 589 (1989).

[136] C. J. Horowitz, (2000), arXiv:nucl-th/0010010.

[137] B. P. Abbott et al. (LIGO Scientific, Virgo), Phys. Rev. Lett. **121**, 161101 (2018), arXiv:1805.11581 [gr-qc].

[138] B. P. Abbott et al. (LIGO Scientific, Virgo), Phys. Rev. X **9**, 011001 (2019), arXiv:1805.11579 [gr-qc].

[139] A. Bauswein, O. Just, H.-T. Janka, and N. Stergioulas, Astrophys. J. Lett. **850**, L34 (2017), arXiv:1710.06843 [astro-ph.HE].

[140] E. Annala, T. Gorda, A. Kurkela, and A. Vuorinen, Phys. Rev. Lett. **120**, 172703 (2018), arXiv:1711.02644 [astro-ph.HE].

[141] E. R. Most, L. R. Weih, L. Rezzolla, and J. Schaffner-Bielich, Phys. Rev. Lett. **120**, 261103 (2018), arXiv:1803.00549 [gr-qc].

[142] M. Ruiz, S. L. Shapiro, and A. Tsokaros, Phys. Rev. D **97**, 021501 (2018), arXiv:1711.00473 [astro-ph.HE].

[143] B. Margalit and B. D. Metzger, Astrophys. J. Lett. **850**, L19 (2017), arXiv:1710.05938 [astro-ph.HE].

[144] L. Rezzolla, E. R. Most, and L. R. Weih, Astrophys. J. Lett. **852**, L25 (2018), arXiv:1711.00314 [astro-ph.HE].

[145] M. Shibata, S. Fujibayashi, K. Hotokezaka, K. Kiuchi, K. Kyutoku, Y. Sekiguchi, and M. Tanaka, Phys. Rev. D **96**, 123012 (2017), arXiv:1710.07579 [astro-ph.HE].

[146] B. P. Abbott et al. (LIGO Scientific, Virgo), Phys. Rev. Lett. **121**, 161101 (2018), arXiv:1805.11581 [gr-qc].

[147] S. De, D. Finstad, J. M. Lattimer, D. A. Brown, E. Berger, and C. M. Biwer, Phys. Rev. Lett. **121**, 091102 (2018), [Erratum: Phys.Rev.Lett. 121, 259902 (2018)], arXiv:1804.08583 [astro-ph.HE].

[148] D. Radice, A. Perego, F. Zappa, and S. Bernuzzi, Astrophys. J. Lett. **852**, L29 (2018), arXiv:1711.03647 [astro-ph.HE].

[149] M. W. Coughlin et al., Mon. Not. Roy. Astron. Soc. **480**, 3871 (2018), arXiv:1805.09371 [astro-ph.HE].

[150] M. W. Coughlin, T. Dietrich, B. Margalit, and B. D. Metzger, Mon. Not. Roy. Astron. Soc. **489**, L91 (2019), arXiv:1812.04803 [astro-ph.HE].

[151] L. Dai, T. Venumadhav, and B. Zackay, (2018), arXiv:1806.08793 [gr-qc].

[152] D. Radice and L. Dai, Eur. Phys. J. A **55**, 50 (2019), arXiv:1810.12917 [astro-ph.HE].

[153] C. D. Capano, I. Tews, S. M. Brown, B. Margalit, S. De, S. Kumar, D. A. Brown, B. Krishnan, and S. Reddy, Nature Astron. **4**, 625 (2020), arXiv:1908.10352 [astro-ph.HE].

[154] D. Radice, A. Perego, K. Hotokezaka, S. A. Fromm, S. Bernuzzi, and L. F. Roberts, Astrophys. J. **869**, 130 (2018), arXiv:1809.11161 [astro-ph.HE].

[155] D. Radice, S. Bernuzzi, and A. Perego, Ann. Rev. Nucl. Part. Sci. **70**, 95 (2020), arXiv:2002.03863 [astro-ph.HE].

[156] B. P. Abbott et al. (LIGO Scientific, Virgo), Astrophys. J. Lett. **892**, L3 (2020), arXiv:2001.01761 [astro-ph.HE].

[157] R. Abbott et al. (LIGO Scientific, Virgo), Astrophys. J. Lett. **896**, L44 (2020), arXiv:2006.12611 [astro-ph.HE].

[158] R. Abbott et al. (LIGO Scientific, KAGRA, VIRGO), Astrophys. J. Lett. **915**, L5 (2021), arXiv:2106.15163 [astro-ph.HE].

[159] A. G. Abac et al. (LIGO Scientific, VIRGO, KAGRA), (2024), arXiv:2404.04248 [astro-ph.HE].

[160] R. Essick, P. Landry, A. Schwenk, and I. Tews, Phys. Rev. C **104**, 065804 (2021), arXiv:2107.05528 [nucl-th].

[161] P. C. Peters and J. Mathews, Phys. Rev. **131**, 435 (1963).

[162] P. C. Peters, Phys. Rev. **136**, B1224 (1964).

[163] L. Blanchet, Living Rev. Rel. **27**, 4 (2024).

[164] K. D. Kokkotas and B. G. Schmidt, Living Rev. Rel. **2**, 2 (1999), arXiv:gr-qc/9909058.

[165] E. E. Flanagan and T. Hinderer, Phys. Rev. D **77**, 021502 (2008), arXiv:0709.1915 [astro-ph].

[166] T. Hinderer, Astrophys. J. **677**, 1216 (2008), [Erratum: Astrophys.J. 697, 964 (2009)], arXiv:0711.2420 [astro-ph].

[167] J. Steinhoff, T. Hinderer, A. Buonanno, and A. Taracchini, Phys. Rev. D **94**, 104028 (2016), arXiv:1608.01907 [gr-qc].

[168] D. Lai and Y. Wu, Phys. Rev. D **74**, 024007 (2006), arXiv:astro-ph/0604163.

[169] T. Hinderer et al., Phys. Rev. Lett. **116**, 181101 (2016), arXiv:1602.00599 [gr-qc].

[170] J. Steinhoff, T. Hinderer, T. Dietrich, and F. Foucart, Phys. Rev. Res. **3**, 033129 (2021), arXiv:2103.06100 [gr-qc].

[171] T. Damour and A. Nagar, Phys. Rev. D **80**, 084035 (2009), arXiv:0906.0096 [gr-qc].

[172] T. Binnington and E. Poisson, Phys. Rev. D **80**, 084018 (2009), arXiv:0906.1366 [gr-qc].

[173] A. Love, Proc. R. Soc. Lond. A **82**, 10.1098/rspa.1909.0008 (1909).

[174] K. D. Kokkotas and G. Schaefer, Mon. Not. Roy. Astron. Soc. **275**, 301 (1995), arXiv:gr-qc/9502034.

[175] D. Lai, Mon. Not. Roy. Astron. Soc. **270**, 611 (1994), arXiv:astro-ph/9404062.

[176] M. Shibata, Phys. Rev. D **48**, 663 (1993).

[177] P. Pani, L. Gualtieri, T. Abdelsalhin, and X. Jiménez-Forteza, Phys. Rev. D **98**, 124023 (2018), arXiv:1810.01094 [gr-qc].

[178] P. K. Gupta, J. Steinhoff, and T. Hinderer, Phys. Rev. D **108**, 124040 (2023), arXiv:2302.11274 [gr-qc].

[179] K. S. Thorne, Phys. Rev. D **58**, 124031 (1998), arXiv:gr-qc/9706057.

[180] W. C. G. Ho and D. Lai, Mon. Not. Roy. Astron. Soc. **308**, 153 (1999), arXiv:astro-ph/9812116.

[181] K. Riles, Living Rev. Rel. **26**, 3 (2023), arXiv:2206.06447 [astro-ph.HE].

[182] T. Hinderer, B. D. Lackey, R. N. Lang, and J. S. Read, Phys. Rev. D **81**, 123016 (2010), arXiv:0911.3535 [astro-ph.HE].

[183] A. Bauswein and H. T. Janka, Phys. Rev. Lett. **108**, 011101 (2012), arXiv:1106.1616 [astro-ph.SR].

[184] J. Clark, A. Bauswein, L. Cadonati, H. T. Janka, C. Pankow, and N. Stergioulas, Phys. Rev. D **90**, 062004 (2014), arXiv:1406.5444 [astro-ph.HE].

[185] K. Takami, L. Rezzolla, and L. Baiotti, Phys. Rev. Lett. **113**, 091104 (2014), arXiv:1403.5672 [gr-qc].

[186] S. Bernuzzi, T. Dietrich, and A. Nagar, Phys. Rev. Lett. **115**, 091101 (2015), arXiv:1504.01764 [gr-qc].

[187] A. Bauswein and N. Stergioulas, Phys. Rev. D **91**, 124056 (2015), arXiv:1502.03176 [astro-ph.SR].

[188] J. A. Clark, A. Bauswein, N. Stergioulas, and D. Shoemaker, Class. Quant. Grav. **33**, 085003 (2016), arXiv:1509.08522 [astro-ph.HE].

[189] L. Rezzolla and K. Takami, Phys. Rev. D **93**, 124051 (2016), arXiv:1604.00246 [gr-qc].

[190] K. W. Tsang, T. Dietrich, and C. Van Den Broeck, Phys. Rev. D **100**, 044047 (2019), arXiv:1907.02424 [gr-qc].

[191] D. Radice, S. Bernuzzi, W. Del Pozzo, L. F. Roberts, and C. D. Ott, Astrophys. J. Lett. **842**, L10 (2017), arXiv:1612.06429 [astro-ph.HE].

[192] K. Yagi and N. Yunes, Class. Quant. Grav. **34**, 015006 (2017), arXiv:1608.06187 [gr-qc].

[193] K. Yagi, Phys. Rev. D **89**, 043011 (2014), [Erratum: Phys.Rev.D 96, 129904 (2017), Erratum: Phys.Rev.D 97, 129901 (2018)], arXiv:1311.0872 [gr-qc].

[194] N. Andersson and K. D. Kokkotas, Mon. Not. Roy. Astron. Soc. **299**, 1059 (1998), arXiv:gr-qc/9711088.

[195] O. Benhar, V. Ferrari, and L. Gualtieri, Phys. Rev. D **70**, 124015 (2004), arXiv:astro-ph/0407529.

[196] L. K. Tsui and P. T. Leung, Mon. Not. Roy. Astron. Soc. **357**, 1029 (2005), arXiv:gr-qc/0412024.

[197] N. Andersson and K. D. Kokkotas, Phys. Rev. Lett. **77**, 4134 (1996), arXiv:gr-qc/9610035.

[198] O. Benhar, E. Berti, and V. Ferrari, Mon. Not. Roy. Astron. Soc. **310**, 797 (1999), arXiv:gr-qc/9901037.

[199] H. K. Lau, P. T. Leung, and L. M. Lin, Astrophys. J. **714**, 1234 (2010), arXiv:0911.0131 [gr-qc].

[200] C. Chirenti, G. H. de Souza, and W. Kastaun, Phys. Rev. D **91**, 044034 (2015), arXiv:1501.02970 [gr-qc].

[201] D. D. Doneva and K. D. Kokkotas, Phys. Rev. D **92**, 124004 (2015), arXiv:1507.06606 [astro-ph.SR].

[202] T. K. Chan, Y. H. Sham, P. T. Leung, and L. M. Lin, Phys. Rev. **D90**, 124023 (2014), arXiv:1408.3789 [gr-qc].

[203] K. Chatziioannou, C.-J. Haster, and A. Zimmerman, Phys. Rev. D **97**, 104036 (2018), arXiv:1804.03221 [gr-qc].

[204] B. Kumar and P. Landry, Phys. Rev. D **99**, 123026 (2019), arXiv:1902.04557 [gr-qc].

[205] B. Haskell, R. Ciolfi, F. Pannarale, and L. Rezzolla, Mon. Not. Roy. Astron. Soc. **438**, L71 (2014), arXiv:1309.3885 [astro-ph.SR].

[206] G. Martinon, A. Maselli, L. Gualtieri, and V. Ferrari, Phys. Rev. D **90**, 064026 (2014), arXiv:1406.7661 [gr-qc].

[207] K. Yagi and N. Yunes, Phys. Rev. D **91**, 123008 (2015), arXiv:1503.02726 [gr-qc].

[208] N. Yunes, D. Psaltis, F. Ozel, and A. Loeb, Phys. Rev. D **81**, 064020 (2010), arXiv:0912.2736 [gr-qc].

[209] Y. Ali-Haimoud and Y. Chen, Phys. Rev. D **84**, 124033 (2011), arXiv:1110.5329 [astro-ph.HE].

[210] K. Yagi, L. C. Stein, N. Yunes, and T. Tanaka, Phys. Rev. D **87**, 084058 (2013), [Erratum: Phys.Rev.D 93, 089909 (2016)], arXiv:1302.1918 [gr-qc].

[211] B. Kleihaus, J. Kunz, S. Mojica, and M. Zagermann, Phys. Rev. D **93**, 064077 (2016), arXiv:1601.05583 [gr-qc].

[212] B. Kleihaus, J. Kunz, and S. Mojica, Phys. Rev. D **90**, 061501 (2014), arXiv:1407.6884 [gr-qc].

[213] D. D. Doneva and S. S. Yazadjiev, JCAP **11**, 019, arXiv:1607.03299 [gr-qc].

[214] P. Pani and E. Berti, Phys. Rev. D **90**, 024025 (2014), arXiv:1405.4547 [gr-qc].

[215] D. D. Doneva, S. S. Yazadjiev, K. V. Staykov, and K. D. Kokkotas, Phys. Rev. D **90**, 104021 (2014), arXiv:1408.1641 [gr-qc].

[216] D. D. Doneva, S. S. Yazadjiev, and K. D. Kokkotas, Phys. Rev. D **92**, 064015 (2015), arXiv:1507.00378 [gr-qc].

[217] Y. H. Sham, L. M. Lin, and P. T. Leung, Astrophys. J. **781**, 66 (2014), arXiv:1312.1011 [gr-qc].

[218] K. V. Staykov, D. D. Doneva, S. S. Yazadjiev, and K. D. Kokkotas, Phys. Rev. D **92**, 043009 (2015), arXiv:1503.04711 [gr-qc].

[219] D. D. Doneva, S. S. Yazadjiev, N. Stergioulas, and K. D. Kokkotas, Astrophys. J. Lett. **781**, L6 (2013), arXiv:1310.7436 [gr-qc].

[220] G. Pappas and T. A. Apostolatos, Phys. Rev. Lett. **112**, 121101 (2014), arXiv:1311.5508 [gr-qc].

[221] S. Chakrabarti, T. Delsate, N. Gürlebeck, and J. Steinhoff, Phys. Rev. Lett. **112**, 201102 (2014), arXiv:1311.6509 [gr-qc].

[222] K. Yagi and N. Yunes, Phys. Rev. D **88**, 023009 (2013), arXiv:1303.1528 [gr-qc].

[223] M. G. Alford, L. Bovard, M. Hanauske, L. Rezzolla, and K. Schwenzer, Phys. Rev. Lett. **120**, 041101 (2018), arXiv:1707.09475 [gr-qc].

[224] K. Chatziioannou, J. A. Clark, A. Bauswein, M. Millhouse, T. B. Littenberg, and N. Cornish, Phys. Rev. D **96**, 124035 (2017), arXiv:1711.00040 [gr-qc].

[225] M. Wijngaarden, K. Chatziioannou, A. Bauswein, J. A. Clark, and N. J. Cornish, Phys. Rev. D **105**, 104019 (2022), arXiv:2202.09382 [gr-qc].

[226] M. Breschi, S. Bernuzzi, F. Zappa, M. Agathos, A. Perego, D. Radice, and A. Nagar, Phys. Rev. D **100**, 104029 (2019), arXiv:1908.11418 [gr-qc].

[227] T. Soultanis, A. Bauswein, and N. Stergioulas, Phys. Rev. D **105**, 043020 (2022), arXiv:2111.08353 [astro-ph.HE].

[228] M. Breschi, R. Gamba, S. Borhanian, G. Carullo, and S. Bernuzzi, (2022), arXiv:2205.09979 [gr-qc].

[229] P. J. Easter, P. D. Lasky, A. R. Casey, L. Rezzolla, and K. Takami, Phys. Rev. D **100**, 043005 (2019), arXiv:1811.11183 [gr-qc].

[230] I. Kowalska, T. Bulik, K. Belczynski, M. Dominik, and D. Gondek-Rosinska, Astron. Astrophys. **527**, A70 (2011), arXiv:1010.0511 [astro-ph.CO].

[231] L. Blanchet, Living Rev. Rel. **17**, 2 (2014), arXiv:1310.1528 [gr-qc].

[232] S. Bernuzzi, A. Nagar, M. Thierfelder, and B. Brugmann, Phys. Rev. D **86**, 044030 (2012), arXiv:1205.3403 [gr-qc].

[233] M. Favata, Phys. Rev. Lett. **112**, 101101 (2014), arXiv:1310.8288 [gr-qc].

[234] L. Wade, J. D. E. Creighton, E. Ochsner, B. D. Lackey, B. F. Farr, T. B. Littenberg, and V. Raymond, Phys. Rev. D **89**, 103012 (2014), arXiv:1402.5156 [gr-qc].

[235] K. Hotokezaka, K. Kyutoku, Y.-i. Sekiguchi, and M. Shibata, Phys. Rev. D **93**, 064082 (2016), arXiv:1603.01286 [gr-qc].

[236] T. Dietrich et al., Phys. Rev. D **99**, 024029 (2019), arXiv:1804.02235 [gr-qc].

[237] R. Dudi, F. Pannarale, T. Dietrich, M. Hannam, S. Bernuzzi, F. Ohme, and B. Brügmann, Phys. Rev. D **98**, 084061 (2018), arXiv:1808.09749 [gr-qc].

[238] A. Samajdar and T. Dietrich, Phys. Rev. D **98**, 124030 (2018), arXiv:1810.03936 [gr-qc].

[239] A. Buonanno and T. Damour, Phys. Rev. D **59**, 084006 (1999), arXiv:gr-qc/9811091.

[240] A. Buonanno and T. Damour, Phys. Rev. D **62**, 064015 (2000), arXiv:gr-qc/0001013.

[241] R. Gamba and S. Bernuzzi, Phys. Rev. D **107**, 044014 (2023), arXiv:2207.13106 [gr-qc].

[242] R. Gamba et al., (2023), arXiv:2307.15125 [gr-qc].

[243] A. Bohé et al., Phys. Rev. D **95**, 044028 (2017), arXiv:1611.03703 [gr-qc].

[244] L. Baiotti, T. Damour, B. Giacomazzo, A. Nagar, and L. Rezzolla, Phys. Rev. Lett. **105**, 261101 (2010), arXiv:1009.0521 [gr-qc].

[245] L. Baiotti, T. Damour, B. Giacomazzo, A. Nagar, and L. Rezzolla, Phys. Rev. D **84**, 024017 (2011), arXiv:1103.3874 [gr-qc].

[246] S. Bernuzzi, A. Nagar, T. Dietrich, and T. Damour, Phys. Rev. Lett. **114**, 161103 (2015), arXiv:1412.4553 [gr-qc].

[247] A. Nagar, F. Messina, P. Rettegno, D. Bini, T. Damour, A. Geralico, S. Akcay, and S. Bernuzzi, Phys. Rev. D **99**, 044007 (2019), arXiv:1812.07923 [gr-qc].

[248] S. Akcay, S. Bernuzzi, F. Messina, A. Nagar, N. Ortiz, and P. Rettegno, Phys. Rev. D **99**, 044051 (2019), arXiv:1812.02744 [gr-qc].

[249] S. E. Field, C. R. Galley, F. Herrmann, J. S. Hesthaven, E. Ochsner, and M. Tiglio, Phys. Rev. Lett. **106**, 221102 (2011), arXiv:1101.3765 [gr-qc].

[250] S. E. Field, C. R. Galley, J. S. Hesthaven, J. Kaye, and M. Tiglio, Phys. Rev. X **4**, 031006 (2014), arXiv:1308.3565 [gr-qc].

[251] M. Pürrer, Class. Quant. Grav. **31**, 195010 (2014), arXiv:1402.4146 [gr-qc].

[252] J. Blackman, S. E. Field, C. R. Galley, B. Szilágyi, M. A. Scheel, M. Tiglio, and D. A. Hemberger, Phys. Rev. Lett. **115**, 121102 (2015), arXiv:1502.07758 [gr-qc].

[253] C. R. Galley and P. Schmidt, (2016), arXiv:1611.07529 [gr-qc].

[254] V. Varma, S. E. Field, M. A. Scheel, J. Blackman, D. Gerosa, L. C. Stein, L. E. Kidder, and H. P. Pfeiffer, Phys. Rev. Research. **1**, 033015 (2019), arXiv:1905.09300 [gr-qc].

[255] B. D. Lackey, S. Bernuzzi, C. R. Galley, J. Meidam, and C. Van Den Broeck, Phys. Rev. D **95**, 104036 (2017), arXiv:1610.04742 [gr-qc].

[256] B. D. Lackey, K. Kyutoku, M. Shibata, P. R. Brady, and J. L. Friedman, Phys. Rev. D **89**, 043009 (2014), arXiv:1303.6298 [gr-qc].

[257] B. D. Lackey, M. Pürrer, A. Taracchini, and S. Marsat, Phys. Rev. D **100**, 024002 (2019), arXiv:1812.08643 [gr-qc].

[258] T. Damour, B. R. Iyer, and B. S. Sathyaprakash, Phys. Rev. D **57**, 885 (1998), arXiv:gr-qc/9708034.

[259] T. Damour, B. R. Iyer, and B. S. Sathyaprakash, Phys. Rev. D **62**, 084036 (2000), arXiv:gr-qc/0001023.

[260] T. Damour, B. R. Iyer, and B. S. Sathyaprakash, Phys. Rev. D **63**, 044023 (2001), [Erratum: Phys.Rev.D 72, 029902 (2005)], arXiv:gr-qc/0010009.

[261] A. Buonanno, B. Iyer, E. Ochsner, Y. Pan, and B. S. Sathyaprakash, Phys. Rev. D **80**, 084043 (2009), arXiv:0907.0700 [gr-qc].

[262] A. Bohé, S. Marsat, and L. Blanchet, Class. Quant. Grav. **30**, 135009 (2013), arXiv:1303.7412 [gr-qc].

[263] S. Balmelli and T. Damour, Phys. Rev. D **92**, 124022 (2015), arXiv:1509.08135 [gr-qc].

[264] E. Poisson, Phys. Rev. D **57**, 5287 (1998), arXiv:gr-qc/9709032.

[265] N. V. Krishnendu, K. G. Arun, and C. K. Mishra, Phys. Rev. Lett. **119**, 091101 (2017), arXiv:1701.06318 [gr-qc].

[266] T. Marchand, Q. Henry, F. Larrouturou, S. Marsat, G. Faye, and L. Blanchet, Class. Quant. Grav. **37**, 215006 (2020), arXiv:2003.13672 [gr-qc].

[267] T. Marchand, L. Blanchet, and G. Faye, Class. Quant. Grav. **33**, 244003 (2016), arXiv:1607.07601 [gr-qc].

[268] F. Larrouturou, Q. Henry, L. Blanchet, and G. Faye, Class. Quant. Grav. **39**, 115007 (2022), arXiv:2110.02240 [gr-qc].

[269] F. Larrouturou, L. Blanchet, Q. Henry, and G. Faye, Class. Quant. Grav. **39**, 115008 (2022), arXiv:2110.02243 [gr-qc].

[270] D. Trestini and L. Blanchet, Phys. Rev. D **107**, 104048 (2023), arXiv:2301.09395 [gr-qc].

[271] L. Blanchet, G. Faye, Q. Henry, F. Larrouturou, and D. Trestini, Phys. Rev. Lett. **131**, 121402 (2023), arXiv:2304.11185 [gr-qc].

[272] L. Blanchet, G. Faye, Q. Henry, F. Larrouturou, and D. Trestini, Phys. Rev. D **108**, 064041 (2023), arXiv:2304.11186 [gr-qc].

[273] K. G. Arun, B. R. Iyer, B. S. Sathyaprakash, and P. A. Sundararajan, Phys. Rev. D **71**, 084008 (2005), [Erratum: Phys.Rev.D 72, 069903 (2005)], arXiv:gr-qc/0411146.

[274] L. E. Kidder, Phys. Rev. D **52**, 821 (1995), arXiv:gr-qc/9506022.

[275] T. Damour, A. Nagar, and L. Villain, Phys. Rev. **D85**, 123007 (2012), arXiv:1203.4352 [gr-qc].

[276] Q. Henry, G. Faye, and L. Blanchet, Phys. Rev. D **102**, 044033 (2020), [Erratum: Phys.Rev.D 108, 089901 (2023)], arXiv:2005.13367 [gr-qc].

[277] T. Narikawa, Phys. Rev. D **108**, 063029 (2023), arXiv:2307.02033 [gr-qc].

[278] P. Schmidt and T. Hinderer, Phys. Rev. D **100**, 021501 (2019), arXiv:1905.00818 [gr-qc].

[279] J. Vines, É. Flanagan and T. Hinderer, Phys. Rev. D **83**, 084051 (2011).

[280] J. Vines, E. E. Flanagan, and T. Hinderer, Phys. Rev. D **83**, 084051 (2011), arXiv:1101.1673 [gr-qc].

[281] N. Andersson and P. Pnigouras, Mon. Not. Roy. Astron. Soc. **503**, 533 (2021), arXiv:1905.00012 [gr-qc].

[282] T. Damour and A. Nagar, Phys. Rev. D **81**, 084016 (2010), arXiv:0911.5041 [gr-qc].

[283] D. Bini, T. Damour, and G. Faye, Phys. Rev. D **85**, 124034 (2012), arXiv:1202.3565 [gr-qc].

[284] D. Bini and T. Damour, Phys. Rev. D **90**, 124037 (2014), arXiv:1409.6933 [gr-qc].

[285] T. Damour and A. Nagar, Phys. Rev. D **90**, 044018 (2014), arXiv:1406.6913 [gr-qc].

[286] A. Nagar and A. Shah, Phys. Rev. D **94**, 104017 (2016), arXiv:1606.00207 [gr-qc].

[287] F. Messina, A. Maldarella, and A. Nagar, Phys. Rev. D **97**, 084016 (2018), arXiv:1801.02366 [gr-qc].

[288] A. Nagar, F. Messina, C. Kavanagh, G. Lukes-Gerakopoulos, N. Warburton, S. Bernuzzi, and E. Harms, Phys. Rev. D **100**, 104056 (2019), arXiv:1907.12233 [gr-qc].

[289] Y. Pan, A. Buonanno, R. Fujita, E. Racine, and H. Tagoshi, Phys. Rev. D **83**, 064003 (2011), [Erratum: Phys.Rev.D 87, 109901 (2013)], arXiv:1006.0431 [gr-qc].

[290] T. Damour, B. R. Iyer, and A. Nagar, Phys. Rev. D **79**, 064004 (2009), arXiv:0811.2069 [gr-qc].

[291] T. Damour and A. Nagar, Phys. Rev. D **76**, 064028 (2007), arXiv:0705.2519 [gr-qc].

[292] R. Gamba, S. Bernuzzi, and A. Nagar, Phys. Rev. D **104**, 084058 (2021), arXiv:2012.00027 [gr-qc].

[293] H. Estellés, S. Husa, M. Colleoni, D. Keitel, M. Mateu-Lucena, C. García-Quirós, A. Ramos-Buades, and A. Borchers, Phys. Rev. D **105**, 084039 (2022), arXiv:2012.11923 [gr-qc].

[294] R. Abbott et al. (LIGO Scientific, VIRGO, KAGRA), (2021), arXiv:2111.03634 [astro-ph.HE].

[295] G. Pratten, S. Husa, C. Garcia-Quiros, M. Colleoni, A. Ramos-Buades, H. Estelles, and R. Jaume, Phys. Rev. D **102**, 064001 (2020), arXiv:2001.11412 [gr-qc].

[296] G. Pratten et al., Phys. Rev. D **103**, 104056 (2021), arXiv:2004.06503 [gr-qc].

[297] T. Dietrich, S. Bernuzzi, and W. Tichy, Phys. Rev. D **96**, 121501 (2017), arXiv:1706.02969 [gr-qc].

[298] A. Abac, T. Dietrich, A. Buonanno, J. Steinhoff, and M. Ujevic, Phys. Rev. D **109**, 024062 (2024), arXiv:2311.07456 [gr-qc].

[299] C. García-Quirós, M. Colleoni, S. Husa, H. Estellés, G. Pratten, A. Ramos-Buades, M. Mateu-Lucena, and R. Jaume, Phys. Rev. D **102**, 064002 (2020), arXiv:2001.10914 [gr-qc].

[300] J. E. Thompson, E. Hamilton, L. London, S. Ghosh, P. Kolitsidou, C. Hoy, and M. Hannam, Phys. Rev. D **109**, 063012 (2024), arXiv:2312.10025 [gr-qc].

[301] L. Rezzolla, Fundam. Theor. Phys. **177**, 391 (2014), arXiv:1303.6464 [gr-qc].

[302] L. Rezzolla and O. Zanotti, *Relativistic Hydrodynamics* (Oxford University Press, 2013).

[303] L. Baiotti and L. Rezzolla, Rept. Prog. Phys. **80**, 096901 (2017), arXiv:1607.03540 [gr-qc].

[304] K. Hotokezaka, K. Kyutoku, H. Okawa, and M. Shibata, Phys. Rev. D **91**, 064060 (2015), arXiv:1502.03457 [gr-qc].

[305] K. Kiuchi, K. Kawaguchi, K. Kyutoku, Y. Sekiguchi, and M. Shibata, Phys. Rev. D **101**, 084006 (2020), arXiv:1907.03790 [astro-ph.HE].

[306] F. Foucart et al., Phys. Rev. D **99**, 044008 (2019), arXiv:1812.06988 [gr-qc].

[307] T. Dietrich, D. Radice, S. Bernuzzi, F. Zappa, A. Perego, B. Brügmann, S. V. Chaurasia, R. Dudi, W. Tichy, and M. Ujevic, Class. Quant. Grav. **35**, 24LT01 (2018), arXiv:1806.01625 [gr-qc].

[308] F. Foucart, R. Haas, M. D. Duez, E. O'Connor, C. D. Ott, L. Roberts, L. E. Kidder, J. Lippuner, H. P. Pfeiffer, and M. A. Scheel, Phys. Rev. D **93**, 044019 (2016), arXiv:1510.06398 [astro-ph.HE].

[309] S. Bernuzzi, D. Radice, C. D. Ott, L. F. Roberts, P. Moesta, and F. Galeazzi, Phys. Rev. D **94**, 024023 (2016), arXiv:1512.06397 [gr-qc].

[310] T. Dietrich, M. Ujevic, W. Tichy, S. Bernuzzi, and B. Bruegmann, Phys. Rev. D **95**, 024029 (2017), arXiv:1607.06636 [gr-qc].

[311] L. Lehner, S. L. Liebling, C. Palenzuela, O. L. Caballero, E. O'Connor, M. Anderson, and D. Neilsen, Class. Quant. Grav. **33**, 184002 (2016), arXiv:1603.00501 [gr-qc].

[312] Y. Sekiguchi, K. Kiuchi, K. Kyutoku, M. Shibata, and K. Taniguchi, Phys. Rev. D **93**, 124046 (2016), arXiv:1603.01918 [astro-ph.HE].

[313] K. Hotokezaka, K. Kyutoku, H. Okawa, M. Shibata, and K. Kiuchi, Phys. Rev. D **83**, 124008 (2011), arXiv:1105.4370 [astro-ph.HE].

[314] S. Bernuzzi, T. Dietrich, W. Tichy, and B. Brügmann, Phys. Rev. D **89**, 104021 (2014), arXiv:1311.4443 [gr-qc].

[315] P. Tsatsin and P. Marronetti, Phys. Rev. D **88**, 064060 (2013), arXiv:1303.6692 [gr-qc].

[316] W. Kastaun, F. Galeazzi, D. Alic, L. Rezzolla, and J. A. Font, Phys. Rev. D **88**, 021501 (2013), arXiv:1301.7348 [gr-qc].

[317] T. Dietrich, S. Bernuzzi, M. Ujevic, and W. Tichy, Phys. Rev. D **95**, 044045 (2017), arXiv:1611.07367 [gr-qc].

[318] W. E. East, V. Paschalidis, F. Pretorius, and S. L. Shapiro, Phys. Rev. D **93**, 024011 (2016), arXiv:1511.01093 [astro-ph.HE].

[319] W. Kastaun, R. Ciolfi, A. Endrizzi, and B. Giacomazzo, Phys. Rev. D **96**, 043019 (2017), arXiv:1612.03671 [astro-ph.HE].

[320] N. Tacik et al., Phys. Rev. D **92**, 124012 (2015), [Erratum: Phys.Rev.D 94, 049903 (2016)], arXiv:1508.06986 [gr-qc].

[321] T. Dietrich, S. Bernuzzi, B. Brügmann, M. Ujevic, and W. Tichy, Phys. Rev. D **97**, 064002 (2018), arXiv:1712.02992 [gr-qc].

[322] W. E. East, V. Paschalidis, F. Pretorius, and A. Tsokaros, Phys. Rev. D **100**, 124042 (2019), arXiv:1906.05288 [astro-ph.HE].

[323] A. Tsokaros, M. Ruiz, V. Paschalidis, S. L. Shapiro, and K. Uryū, Phys. Rev. D **100**, 024061 (2019), arXiv:1906.00011 [gr-qc].

[324] E. R. Most, L. J. Papenfort, A. Tsokaros, and L. Rezzolla, Astrophys. J. **884**, 40 (2019), arXiv:1904.04220 [astro-ph.HE].

[325] M. Ruiz, A. Tsokaros, V. Paschalidis, and S. L. Shapiro, Phys. Rev. D **99**, 084032 (2019), arXiv:1902.08636 [astro-ph.HE].

[326] S. V. Chaurasia, T. Dietrich, M. Ujevic, K. Hendriks, R. Dudi, F. M. Fabbri, W. Tichy, and B. Brügmann, Phys. Rev. D **102**, 024087 (2020), arXiv:2003.11901 [gr-qc].

[327] R. Gold, S. Bernuzzi, M. Thierfelder, B. Brugmann, and F. Pretorius, Phys. Rev. D **86**, 121501 (2012), arXiv:1109.5128 [gr-qc].

[328] T. Dietrich, N. Moldenhauer, N. K. Johnson-McDaniel, S. Bernuzzi, C. M. Markakis, B. Brügmann, and W. Tichy, Phys. Rev. D **92**, 124007 (2015), arXiv:1507.07100 [gr-qc].

[329] W. E. East and F. Pretorius, Astrophys. J. Lett. **760**, L4 (2012), arXiv:1208.5279 [astro-ph.HE].

[330] W. E. East, V. Paschalidis, and F. Pretorius, Class. Quant. Grav. **33**, 244004 (2016), arXiv:1609.00725 [astro-ph.HE].

[331] D. Radice, F. Galeazzi, J. Lippuner, L. F. Roberts, C. D. Ott, and L. Rezzolla, Mon. Not. Roy. Astron. Soc. **460**, 3255 (2016), arXiv:1601.02426 [astro-ph.HE].

[332] L. J. Papenfort, R. Gold, and L. Rezzolla, Phys. Rev. D **98**, 104028 (2018), arXiv:1807.03795 [gr-qc].

[333] M. Anderson, E. W. Hirschmann, L. Lehner, S. L. Liebling, P. M. Motl, D. Neilsen, C. Palenzuela, and J. E. Tohline, Phys. Rev. Lett. **100**, 191101 (2008), arXiv:0801.4387 [gr-qc].

[334] B. Giacomazzo, L. Rezzolla, and L. Baiotti, Phys. Rev. D **83**, 044014 (2011), arXiv:1009.2468 [gr-qc].

[335] L. Rezzolla, B. Giacomazzo, L. Baiotti, J. Granot, C. Kouveliotou, and M. A. Aloy, Astrophys. J. Lett. **732**, L6 (2011), arXiv:1101.4298 [astro-ph.HE].

[336] C. Palenzuela, L. Lehner, M. Ponce, S. L. Liebling, M. Anderson, D. Neilsen, and P. Motl, Phys. Rev. Lett. **111**, 061105 (2013), arXiv:1301.7074 [gr-qc].

[337] K. Kiuchi, K. Kyutoku, Y. Sekiguchi, M. Shibata, and T. Wada, Phys. Rev. D **90**, 041502 (2014), arXiv:1407.2660 [astro-ph.HE].

[338] C. Palenzuela, S. L. Liebling, D. Neilsen, L. Lehner, O. L. Caballero, E. O'Connor, and M. Anderson, Phys. Rev. D **92**, 044045 (2015), arXiv:1505.01607 [gr-qc].

[339] R. Ciolfi, W. Kastaun, J. V. Kalinani, and B. Giacomazzo, Phys. Rev. D **100**, 023005 (2019), arXiv:1904.10222 [astro-ph.HE].

[340] R. Ciolfi, W. Kastaun, B. Giacomazzo, A. Endrizzi, D. M. Siegel, and R. Perna, Phys. Rev. D **95**, 063016 (2017), arXiv:1701.08738 [astro-ph.HE].

[341] K. Kiuchi, K. Kyutoku, Y. Sekiguchi, and M. Shibata, Phys. Rev. D **97**, 124039 (2018), arXiv:1710.01311 [astro-ph.HE].

[342] Y. Sekiguchi, K. Kiuchi, K. Kyutoku, and M. Shibata, Phys. Rev. Lett. **107**, 051102 (2011), arXiv:1105.2125 [gr-qc].

[343] F. Galeazzi, W. Kastaun, L. Rezzolla, and J. A. Font, Phys. Rev. D **88**, 064009 (2013), arXiv:1306.4953 [gr-qc].

[344] D. Neilsen, S. L. Liebling, M. Anderson, L. Lehner, E. O'Connor, and C. Palenzuela, Phys. Rev. D **89**, 104029 (2014), arXiv:1403.3680 [gr-qc].

[345] Y. Sekiguchi, K. Kiuchi, K. Kyutoku, and M. Shibata, Phys. Rev. D **91**, 064059 (2015), arXiv:1502.06660 [astro-ph.HE].

[346] F. Foucart, E. O'Connor, L. Roberts, L. E. Kidder, H. P. Pfeiffer, and M. A. Scheel, Phys. Rev. D **94**, 123016 (2016), arXiv:1607.07450 [astro-ph.HE].

[347] F. Foucart, Mon. Not. Roy. Astron. Soc. **475**, 4186 (2018), arXiv:1708.08452 [astro-ph.HE].

[348] M. Shibata and Y. Sekiguchi, Prog. Theor. Phys. **127**, 535 (2012), arXiv:1206.5911 [astro-ph.HE].

[349] F. Foucart, E. O'Connor, L. Roberts, M. D. Duez, R. Haas, L. E. Kidder, C. D. Ott, H. P. Pfeiffer, M. A. Scheel, and B. Szilagyi, Phys. Rev. D **91**, 124021 (2015), arXiv:1502.04146 [astro-ph.HE].

[350] D. Radice, Astrophys. J. Lett. **838**, L2 (2017), arXiv:1703.02046 [astro-ph.HE].

[351] M. Shibata, K. Kiuchi, and Y.-i. Sekiguchi, Phys. Rev. D **95**, 083005 (2017), arXiv:1703.10303 [astro-ph.HE].

[352] M. Shibata and K. Kiuchi, Phys. Rev. D **95**, 123003 (2017), arXiv:1705.06142 [astro-ph.HE].

[353] S. Fujibayashi, K. Kiuchi, N. Nishimura, Y. Sekiguchi, and M. Shibata, Astrophys. J. **860**, 64 (2018), arXiv:1711.02093 [astro-ph.HE].

[354] A. Perego, D. Radice, and S. Bernuzzi, Astrophys. J. Lett. **850**, L37 (2017), arXiv:1711.03982 [astro-ph.HE].

[355] K. Hotokezaka, P. Beniamini, and T. Piran, Int. J. Mod. Phys. D **27**, 1842005 (2018), arXiv:1801.01141 [astro-ph.HE].

[356] K. Hotokezaka, K. Kiuchi, K. Kyutoku, H. Okawa, Y.-i. Sekiguchi, M. Shibata, and K. Taniguchi, Phys. Rev. D **87**, 024001 (2013), arXiv:1212.0905 [astro-ph.HE].

[357] A. Bauswein, S. Goriely, and H. T. Janka, Astrophys. J. **773**, 78 (2013), arXiv:1302.6530 [astro-ph.SR].

[358] S. Fujibayashi, Y. Sekiguchi, K. Kiuchi, and M. Shibata, Astrophys. J. **846**, 114 (2017), arXiv:1703.10191 [astro-ph.HE].

[359] L. Bovard, D. Martin, F. Guercilena, A. Arcones, L. Rezzolla, and O. Korobkin, Phys. Rev. D **96**, 124005 (2017), arXiv:1709.09630 [gr-qc].

[360] E. Newman and R. Penrose, J. Math. Phys. **3**, 566 (1962).

[361] N. T. Bishop and L. Rezzolla, Living Rev. Rel. **19**, 2 (2016), arXiv:1606.02532 [gr-qc].

[362] W. Tichy, Rept. Prog. Phys. **80**, 026901 (2017), arXiv:1610.03805 [gr-qc].

[363] L. Baiotti, B. Giacomazzo, and L. Rezzolla, Class. Quant. Grav. **26**, 114005 (2009), arXiv:0901.4955 [gr-qc].

[364] S. Bernuzzi and T. Dietrich, Phys. Rev. D **94**, 064062 (2016), arXiv:1604.07999 [gr-qc].

[365] D. Radice, L. Rezzolla, and F. Galeazzi, Mon. Not. Roy. Astron. Soc. **437**, L46 (2014), arXiv:1306.6052 [gr-qc].

[366] S. Bernuzzi, M. Thierfelder, and B. Bruegmann, Phys. Rev. D **85**, 104030 (2012), arXiv:1109.3611 [gr-qc].

[367] K. Kiuchi, K. Kawaguchi, K. Kyutoku, Y. Sekiguchi, M. Shibata, and K. Taniguchi, Phys. Rev. D **96**, 084060 (2017), arXiv:1708.08926 [astro-ph.HE].

[368] N. Williams, G. Pratten, and P. Schmidt, Phys. Rev. D **105**, 123032 (2022), arXiv:2203.00623 [astro-ph.HE].

[369] G. Pratten, P. Schmidt, and T. Hinderer, Nature Commun. **11**, 2553 (2020), arXiv:1905.00817 [gr-qc].

[370] B. T. Reed, F. J. Fattoyev, C. J. Horowitz, and J. Piekarewicz, Phys. Rev. Lett. **126**, 172503 (2021), arXiv:2101.03193 [nucl-th].

[371] T. Akutsu et al. (KAGRA), PTEP **2021**, 05A101 (2021), arXiv:2005.05574 [physics.ins-det].

[372] B. P. Abbott et al. (KAGRA, LIGO Scientific, VIRGO), Living Rev. Rel. **21**, 3 (2018), arXiv:1304.0670 [gr-qc].

[373] M. Maggiore et al., JCAP **03**, 050, arXiv:1912.02622 [astro-ph.CO].

[374] D. Reitze et al., Bull. Am. Astron. Soc. **51**, 035 (2019), arXiv:1907.04833 [astro-ph.IM].

[375] C. Pacilio, A. Maselli, M. Fasano, and P. Pani, Phys. Rev. Lett. **128**, 101101 (2022), arXiv:2104.10035 [gr-qc].

[376] T. Damour, in *Lecture Notes in Physics, Berlin Springer Verlag*, Lecture Notes in Physics, Berlin Springer Verlag, Vol. 124 (1983) pp. 59–144.

[377] T. Damour, M. Soffel, and C.-m. Xu, Phys. Rev. D **45**, 1017 (1992).

[378] T. Narikawa, N. Uchikata, and T. Tanaka, Phys. Rev. D **104**, 084056 (2021), arXiv:2106.09193 [gr-qc].

[379] N. Stergioulas, A. Bauswein, K. Zagkouris, and H.-T. Janka, Mon. Not. Roy. Astron. Soc. **418**, 427 (2011), arXiv:1105.0368 [gr-qc].

[380] E. S. Committee, Design Report Update 2020 for the Einstein Telescope, https://apps.et-gw.eu/tds/ql/?c=15418 (2020).

[381] H.-J. Kuan and K. D. Kokkotas, (2022), arXiv:2205.01705 [gr-qc].

[382] M. Agathos, J. Meidam, W. Del Pozzo, T. G. F. Li, M. Tompitak, J. Veitch, S. Vitale, and C. Van Den Broeck, Phys. Rev. D **92**, 023012 (2015), arXiv:1503.05405 [gr-qc].

[383] A. Maselli, V. Cardoso, V. Ferrari, L. Gualtieri, and P. Pani, Phys. Rev. D **88**, 023007 (2013), arXiv:1304.2052 [gr-qc].

[384] K. Chatziioannou, A. Klein, N. Yunes, and N. Cornish, Phys. Rev. D **95**, 104004 (2017), arXiv:1703.03967 [gr-qc].

[385] L. Lindblom, B. J. Owen, and D. A. Brown, Phys. Rev. D **78**, 124020 (2008), arXiv:0809.3844 [gr-qc].

[386] I. M. Romero-Shaw et al., Mon. Not. Roy. Astron. Soc. **499**, 3295 (2020), arXiv:2006.00714 [astro-ph.IM].

[387] P.-G. Reinhard and H. Flocard, Nuclear Physics A **584**, 467 (1995).

[388] P. Danielewicz and J. Lee, Nucl. Phys. A **818**, 36 (2009), arXiv:0807.3743 [nucl-th].

[389] F. Gulminelli and A. R. Raduta, Phys. Rev. C **92**, 055803 (2015), arXiv:1504.04493 [nucl-th].

[390] H. Müther, M. Prakash, and T. Ainsworth, Physics Letters B **199**, 469 (1987).

[391] S. Galaudage, C. Adamcewicz, X.-J. Zhu, S. Stevenson, and E. Thrane, Astrophys. J. Lett. **909**, L19 (2021), arXiv:2011.01495 [astro-ph.HE].

[392] P. A. R. Ade et al. (Planck), Astron. Astrophys. **594**, A13 (2016), arXiv:1502.01589 [astro-ph.CO].

[393] P. Madau and M. Dickinson, Ann. Rev. Astron. Astrophys. **52**, 415 (2014), arXiv:1403.0007 [astro-ph.CO].

[394] M. Fishbach, D. E. Holz, and W. M. Farr, Astrophys. J. Lett. **863**, L41 (2018), arXiv:1805.10270 [astro-ph.HE].

[395] L. S. Finn and D. F. Chernoff, Phys. Rev. D **47**, 2198 (1993), arXiv:gr-qc/9301003.

[396] R. Margutti et al. (LSST), (2018), arXiv:1812.04051 [astro-ph.HE].

[397] D. A. Godzieba, R. Gamba, D. Radice, and S. Bernuzzi, Phys. Rev. D **103**, 063036 (2021), arXiv:2012.12151 [astro-ph.HE].

[398] L. R. Weih, M. Hanauske, and L. Rezzolla, Phys. Rev. Lett. **124**, 171103 (2020), arXiv:1912.09340 [gr-qc].

[399] T. Hinderer et al., Phys. Rev. D **100**, 063021 (2019), arXiv:1808.03836 [astro-ph.HE].

[400] K. Chatziioannou, Phys. Rev. D **105**, 084021 (2022), arXiv:2108.12368 [gr-qc].

[401] G. Pratten, P. Schmidt, and N. Williams, (2021), arXiv:2109.07566 [astro-ph.HE].

[402] R. Essick, Phys. Rev. D **105**, 082002 (2022), arXiv:2202.00823 [astro-ph.IM].

[403] J. Golomb and C. Talbot, Astrophys. J. **926**, 79 (2022), arXiv:2106.15745 [astro-ph.HE].

[404] S. Biscoveanu, C. Talbot, and S. Vitale, Mon. Not. Roy. Astron. Soc. **511**, 4350 (2022), arXiv:2111.13619 [astro-ph.HE].

[405] E. E. Flanagan and E. Racine, Phys. Rev. D **75**, 044001 (2007), arXiv:gr-qc/0601029.

[406] E. Poisson and J. Doucot, Phys. Rev. D **95**, 044023 (2017), arXiv:1612.04255 [gr-qc].

[407] S. Ma, H. Yu, and Y. Chen, Phys. Rev. D **101**, 123020 (2020), arXiv:2003.02373 [gr-qc].

[408] E. Poisson, Phys. Rev. D **101**, 104028 (2020), arXiv:2003.10427 [gr-qc].

[409] D. D. Doneva, E. Gaertig, K. D. Kokkotas, and C. Krüger, Phys. Rev. D **88**, 044052 (2013), arXiv:1305.7197 [astro-ph.SR].

[410] A. Vecchio, Phys. Rev. D **70**, 042001 (2004), arXiv:astro-ph/0304051.

[411] R. N. Lang and S. A. Hughes, Phys. Rev. D **74**, 122001 (2006), [Erratum: Phys.Rev.D 75, 089902 (2007), Erratum: Phys.Rev.D 77, 109901 (2008)], arXiv:gr-qc/0608062.

[412] K. Chatziioannou, N. Cornish, A. Klein, and N. Yunes, Astrophys. J. Lett. **798**, L17 (2015), arXiv:1402.3581 [gr-qc].

[413] G. Pratten, P. Schmidt, R. Buscicchio, and L. M. Thomas, Phys. Rev. Res. **2**, 043096 (2020), arXiv:2006.16153 [gr-qc].

[414] N. Williams, P. Schmidt, and G. Pratten, (2024), arXiv:2407.08538 [gr-qc].

[415] K. Chatziioannou, H. T. Cromartie, S. Gandolfi, I. Tews, D. Radice, A. W. Steiner, and A. L. Watts, (2024), arXiv:2407.11153 [nucl-th].

[416] T. Abdelsalhin, L. Gualtieri, and P. Pani, Phys. Rev. D **98**, 104046 (2018), arXiv:1805.01487 [gr-qc].

[417] B. Banihashemi and J. Vines, Phys. Rev. D **101**, 064003 (2020), arXiv:1805.07266 [gr-qc].

[418] P. Landry, (2018), arXiv:1805.01882 [gr-qc].

[419] Q. Henry, G. Faye, and L. Blanchet, Phys. Rev. D **101**, 064047 (2020), arXiv:1912.01920 [gr-qc].

[420] K. Kawaguchi, K. Kiuchi, K. Kyutoku, Y. Sekiguchi, M. Shibata, and K. Taniguchi, Phys. Rev. D **97**, 044044 (2018), arXiv:1802.06518 [gr-qc].

[421] P. Ajith et al., Phys. Rev. Lett. **106**, 241101 (2011), arXiv:0909.2867 [gr-qc].

[422] L. Santamaria et al., Phys. Rev. D **82**, 064016 (2010), arXiv:1005.3306 [gr-qc].

[423] M. Hannam, P. Schmidt, A. Bohé, L. Haegel, S. Husa, F. Ohme, G. Pratten, and M. Pürrer, Phys. Rev. Lett. **113**, 151101 (2014), arXiv:1308.3271 [gr-qc].

[424] J. E. Thompson, E. Fauchon-Jones, S. Khan, E. Nitoglia, F. Pannarale, T. Dietrich, and M. Hannam, Phys. Rev. D **101**, 124059 (2020), arXiv:2002.08383 [gr-qc].

[425] A. Matas et al., Phys. Rev. D **102**, 043023 (2020), arXiv:2004.10001 [gr-qc].

[426] A. Nagar and P. Rettegno, Phys. Rev. D **99**, 021501 (2019), arXiv:1805.03891 [gr-qc].

[427] N. J. Cornish, (2010), arXiv:1007.4820 [gr-qc].

[428] B. Zackay, L. Dai, and T. Venumadhav, (2018), arXiv:1806.08792 [astro-ph.IM].

[429] D. Finstad and D. A. Brown, Astrophys. J. Lett. **905**, L9 (2020), arXiv:2009.13759 [astro-ph.IM].

[430] N. J. Cornish, Phys. Rev. D **104**, 104054 (2021), arXiv:2109.02728 [gr-qc].

[431] N. Leslie, L. Dai, and G. Pratten, Phys. Rev. D **104**, 123030 (2021), arXiv:2109.09872 [astro-ph.IM].

[432] S. Vinciguerra, J. Veitch, and I. Mandel, Class. Quant. Grav. **34**, 115006 (2017), arXiv:1703.02062 [gr-qc].

[433] S. Morisaki, Phys. Rev. D **104**, 044062 (2021), arXiv:2104.07813 [gr-qc].

[434] H. Antil, S. E. Field, F. Herrmann, R. H. Nochetto, and M. Tiglio, J. Sci. Comput. **57**, 604 (2013), arXiv:1210.0577 [cs.NA].

[435] P. Canizares, S. E. Field, J. R. Gair, and M. Tiglio, Phys. Rev. D **87**, 124005 (2013), arXiv:1304.0462 [gr-qc].

[436] P. Canizares, S. E. Field, J. Gair, V. Raymond, R. Smith, and M. Tiglio, Phys. Rev. Lett. **114**, 071104 (2015), arXiv:1404.6284 [gr-qc].

[437] R. Smith, S. E. Field, K. Blackburn, C.-J. Haster, M. Pürrer, V. Raymond, and P. Schmidt, Phys. Rev. D **94**, 044031 (2016), arXiv:1604.08253 [gr-qc].

[438] C. A. Raithel and E. R. Most, Astrophys. J. Lett. **933**, L39 (2022), arXiv:2201.03594 [astro-ph.HE].

[439] J. Provost, G. Berthomieu, and A. Rocca, A&A **94**, 126 (1981).

[440] S. R. Dolan, P. Nolan, A. C. Ottewill, N. Warburton, and B. Wardell, Phys. Rev. D **91**, 023009 (2015), arXiv:1406.4890 [gr-qc].

[441] S. Bernuzzi et al., Core computational relativity (2024).

[442] T. Dietrich and T. Hinderer, Phys. Rev. D **95**, 124006 (2017), arXiv:1702.02053 [gr-qc].

[443] H. Nakano, Class. Quant. Grav. **32**, 177002 (2015), arXiv:1501.02890 [gr-qc].

[444] H. Nakano, J. Healy, C. O. Lousto, and Y. Zlochower, Phys. Rev. D **91**, 104022 (2015), arXiv:1503.00718 [gr-qc].

[445] R. L. Arnowitt, S. Deser, and C. W. Misner, Gen. Rel. Grav. **40**, 1997 (2008), arXiv:gr-qc/0405109.

[446] C. Reisswig and D. Pollney, Class. Quant. Grav. **28**, 195015 (2011), arXiv:1006.1632 [gr-qc].

[447] D. J. A. McKechan, C. Robinson, and B. S. Sathyaprakash, Class. Quant. Grav. **27**, 084020 (2010), arXiv:1003.2939 [gr-qc].

[448] I. Harry, S. Privitera, A. Bohé, and A. Buonanno, Phys. Rev. D **94**, 024012 (2016), arXiv:1603.02444 [gr-qc].

[449] T. Venumadhav, B. Zackay, J. Roulet, L. Dai, and M. Zaldarriaga, Phys. Rev. D **100**, 023011 (2019), arXiv:1902.10341 [astro-ph.IM].

[450] C. McIsaac, C. Hoy, and I. Harry, Phys. Rev. D **108**, 123016 (2023), arXiv:2303.17364 [gr-qc].

[451] S. Schmidt, B. Gadre, and S. Caudill, Phys. Rev. D **109**, 042005 (2024), arXiv:2302.00436 [gr-qc].

[452] D. Wadekar, T. Venumadhav, A. K. Mehta, J. Roulet, S. Olsen, J. Mushkin, B. Zackay, and M. Zaldarriaga, (2023), arXiv:2310.15233 [gr-qc].

[453] D. Wadekar, T. Venumadhav, J. Roulet, A. K. Mehta, B. Zackay, J. Mushkin, and M. Zaldarriaga, (2024), arXiv:2405.17400 [gr-qc].

[454] B. P. Abbott et al. (LIGO Scientific, Virgo), Phys. Rev. Lett. **116**, 241102 (2016), arXiv:1602.03840 [gr-qc].

[455] B. P. Abbott et al. (LIGO Scientific, Virgo), Phys. Rev. X **9**, 031040 (2019), arXiv:1811.12907 [astro-ph.HE].

[456] R. Abbott et al. (LIGO Scientific, Virgo), Phys. Rev. X **11**, 021053 (2021), arXiv:2010.14527 [gr-qc].

[457] R. Abbott et al. (LIGO Scientific, Virgo), Astrophys. J. Lett. **900**, L13 (2020), arXiv:2009.01190 [astro-ph.HE].

[458] M. Cabero, A. B. Nielsen, A. P. Lundgren, and C. D. Capano, Phys. Rev. D **95**, 064016 (2017), arXiv:1602.03134 [gr-qc].

[459] X. Jiménez-Forteza, D. Keitel, S. Husa, M. Hannam, S. Khan, and M. Pürrer, Phys. Rev. D **95**, 064024 (2017), arXiv:1611.00332 [gr-qc].

[460] L. N. Trefethen, *Approximation theory and approximation practice, extended edition* (SIAM, 2019).

[461] S. Marsat, Class. Quant. Grav. **32**, 085008 (2015), arXiv:1411.4118 [gr-qc].

[462] A. Bohé, G. Faye, S. Marsat, and E. K. Porter, Class. Quant. Grav. **32**, 195010 (2015), arXiv:1501.01529 [gr-qc].

[463] R. A. Porto, A. Ross, and I. Z. Rothstein, JCAP **03**, 009, arXiv:1007.1312 [gr-qc].

[464] M. Levi and J. Steinhoff, JCAP **12**, 003, arXiv:1408.5762 [gr-qc].

[465] K. Yagi and N. Yunes, Phys. Rept. **681**, 1 (2017), arXiv:1608.02582 [gr-qc].

[466] R. Abbott et al. (LIGO Scientific, Virgo), SoftwareX **13**, 100658 (2021), arXiv:1912.11716 [gr-qc].

[467] Noise curves used for Simulations in the update of the Observing Scenarios Paper , https://dcc.ligo.org/LIGO-T2000012/public (2022).

[468] B. P. Abbott et al. (LIGO Scientific, Virgo), Class. Quant. Grav. **37**, 045006 (2020), arXiv:1908.01012 [gr-qc].

[469] C. Cutler and E. E. Flanagan, Phys. Rev. D **49**, 2658 (1994), arXiv:gr-qc/9402014.

[470] E. Poisson and C. M. Will, Phys. Rev. D **52**, 848 (1995), arXiv:gr-qc/9502040.

[471] P. Schmidt, I. W. Harry, and H. P. Pfeiffer, (2017), arXiv:1703.01076 [gr-qc].

[472] B. P. Abbott et al. (LIGO Scientific Collaboration and Virgo Collaboration), Phys. Rev. X **9**, 031040 (2019), arXiv:1811.12907 [astro-ph.HE].

[473] LIGO Scientific Collaboration, Virgo Collaboration, Gravitational Wave Open Science Center, https://www.gw-openscience.org (2019).

[474] R. Gamba, M. Breschi, S. Bernuzzi, M. Agathos, and A. Nagar, Phys. Rev. D **103**, 124015 (2021), arXiv:2009.08467 [gr-qc].

[475] S. Ma, H. Yu, and Y. Chen, Phys. Rev. D **103**, 063020 (2021), arXiv:2010.03066 [gr-qc].

[476] W. C. G. Ho and N. Andersson, Phys. Rev. D **108**, 043003 (2023), arXiv:2307.10721 [astro-ph.HE].

[477] C. Chirenti, R. Gold, and M. C. Miller, Astrophys. J. **837**, 67 (2017), arXiv:1612.07097 [astro-ph.HE].

[478] P. Dutta Roy and P. Saini, (2024), arXiv:2403.02404 [astro-ph.HE].

[479] D. R. Lorimer, Living Rev. Rel. **11**, 8 (2008), arXiv:0811.0762 [astro-ph].

[480] P. Schmidt, F. Ohme, and M. Hannam, Phys. Rev. D **91**, 024043 (2015), arXiv:1408.1810 [gr-qc].

[481] M. Colleoni, F. A. R. Vidal, N. K. Johnson-McDaniel, T. Dietrich, M. Haney, and G. Pratten, (2023), arXiv:2311.15978 [gr-qc].

[482] B. P. Abbott et al. (KAGRA, LIGO Scientific, Virgo), Living Rev. Rel. **19**, 1 (2016), arXiv:1304.0670 [gr-qc].

[483] J. Miller, L. Barsotti, S. Vitale, P. Fritschel, M. Evans, and D. Sigg, Phys. Rev. D **91**, 062005 (2015), arXiv:1410.5882 [gr-qc].

[484] A. H. Nitz, M. Schäfer, and T. Dal Canton, Astrophys. J. Lett. **902**, L29 (2020), arXiv:2009.04439 [astro-ph.HE].

[485] R. Huxford, R. Kashyap, S. Borhanian, A. Dhani, I. Gupta, and B. S. Sathyaprakash, Phys. Rev. D **109**, 103035 (2024), arXiv:2307.05376 [gr-qc].

[486] D. Bandyopadhyay, S. A. Bhat, P. Char, and D. Chatterjee, Eur. Phys. J. A **54**, 26 (2018), arXiv:1712.01715 [astro-ph.HE].

[487] S. Han and A. W. Steiner, Phys. Rev. D **99**, 083014 (2019), arXiv:1810.10967 [nucl-th].

[488] S. Y. Lau, P. T. Leung, and L. M. Lin, Phys. Rev. D **95**, 101302 (2017), arXiv:1705.01710 [astro-ph.HE].

[489] E. Annala, C. Ecker, C. Hoyos, N. Jokela, D. Rodríguez Fernández, and A. Vuorinen, JHEP **12**, 078, arXiv:1711.06244 [astro-ph.HE].

[490] C. Adam, J. Castelo, A. García Martín-Caro, M. Huidobro, R. Vázquez, and A. Wereszczynski, Phys. Rev. D **106**, 123022 (2022), arXiv:2203.16558 [gr-qc].

[491] S. Husa, S. Khan, M. Hannam, M. Pürrer, F. Ohme, X. Jiménez Forteza, and A. Bohé, Phys. Rev. D **93**, 044006 (2016), arXiv:1508.07250 [gr-qc].

[492] S. Khan, S. Husa, M. Hannam, F. Ohme, M. Pürrer, X. Jiménez Forteza, and A. Bohé, Phys. Rev. D **93**, 044007 (2016), arXiv:1508.07253 [gr-qc].

[493] A. Bauswein, N.-U. F. Bastian, D. B. Blaschke, K. Chatziioannou, J. A. Clark, T. Fischer, and M. Oertel, Phys. Rev. Lett. **122**, 061102 (2019), arXiv:1809.01116 [astro-ph.HE].

[494] E. R. Most and C. A. Raithel, Phys. Rev. D **104**, 124012 (2021), arXiv:2107.06804 [astro-ph.HE].

[495] P. Demorest, T. Pennucci, S. Ransom, M. Roberts, and J. Hessels, Nature **467**, 1081 (2010), arXiv:1010.5788 [astro-ph.HE].

[496] E. Fonseca et al., Astrophys. J. **832**, 167 (2016), arXiv:1603.00545 [astro-ph.HE].

[497] S. Gandolfi, J. Carlson, S. Reddy, A. W. Steiner, and R. B. Wiringa, Eur. Phys. J. A **50**, 10 (2014), arXiv:1307.5815 [nucl-th].

[498] A. W. Steiner, M. Hempel, and T. Fischer, Astrophys. J. **774**, 17 (2013), arXiv:1207.2184 [astro-ph.SR].

[499] M. Hempel and J. Schaffner-Bielich, Nucl. Phys. A **837**, 210 (2010), arXiv:0911.4073 [nucl-th].

[500] Noise curves used for Simulations in the update of the Observing Scenarios Paper , https://dcc.ligo.org/LIGO-T2000012/public (2020).

[501] N. Andersson and W. C. G. Ho, Phys. Rev. D **97**, 023016 (2018), arXiv:1710.05950 [astro-ph.HE].

[502] H. Yu and N. N. Weinberg, Mon. Not. Roy. Astron. Soc. **464**, 2622 (2017), arXiv:1610.00745 [astro-ph.HE].

[503] W. Xu and D. Lai, Phys. Rev. D **96**, 083005 (2017), arXiv:1708.01839 [astro-ph.HE].

[504] Y. Zhou and F. Zhang, Astrophys. J. **849**, 114 (2017), arXiv:1801.09675 [astro-ph.HE].

[505] N. N. Weinberg, Astrophys. J. **819**, 109 (2016), arXiv:1509.06975 [astro-ph.SR].

[506] N. N. Weinberg, P. Arras, and J. Burkart, Astrophys. J. **769**, 121 (2013), arXiv:1302.2292 [astro-ph.SR].

[507] B. P. Abbott et al. (LIGO Scientific, Virgo), Phys. Rev. Lett. **122**, 061104 (2019), arXiv:1808.08676 [astro-ph.HE].

[508] T. Venumadhav, A. Zimmerman, and C. M. Hirata, Astrophys. J. **781**, 23 (2014), arXiv:1307.2890 [astro-ph.HE].

[509] A. Hegade K. R., J. L. Ripley, and N. Yunes, Phys. Rev. D **109**, 104064 (2024), arXiv:2403.03254 [gr-qc].

[510] A. Hegade K. R., J. L. Ripley, and N. Yunes, Phys. Rev. D **110**, 044041 (2024), arXiv:2407.02584 [gr-qc].

[511] L. Bildsten and C. Cutler, Astrophys. J. **400**, 175 (1992).

[512] J. L. Ripley, A. Hegade K. R., and N. Yunes, Phys. Rev. D **108**, 103037 (2023), arXiv:2306.15633 [gr-qc].

[513] J. L. Ripley, A. Hegade K. R., R. S. Chandramouli, and N. Yunes 10.1038/s41550-024-02323-7 (2023), arXiv:2312.11659 [gr-qc].

[514] R. Tang, W.-B. Han, X. Zhong, Y. Jiang, P. Shen, and Y. Wang, (2023), arXiv:2311.13157 [gr-qc].

[515] M. Lira, J. C. Degollado, C. Moreno, and D. Núñez, Gen. Rel. Grav. **54**, 146 (2022), arXiv:2201.02287 [gr-qc].

[516] D. Tsang, Astrophys. J. **777**, 103 (2013), arXiv:1307.3554 [astro-ph.HE].

[517] J. P. Pereira, M. Bejger, N. Andersson, and F. Gittins, Astrophys. J. **895**, 28 (2020), arXiv:2003.10781 [gr-qc].

[518] F. Gittins, N. Andersson, and J. P. Pereira, Phys. Rev. D **101**, 103025 (2020), arXiv:2003.05449 [astro-ph.HE].

[519] Z. Pan, Z. Lyu, B. Bonga, N. Ortiz, and H. Yang, Phys. Rev. Lett. **125**, 201102 (2020), arXiv:2003.03330 [astro-ph.HE].

[520] J. P. Bernaldez and S. Datta, Phys. Rev. D **108**, 124014 (2023), arXiv:2303.01398 [gr-qc].

[521] H. Yang, W. E. East, V. Paschalidis, F. Pretorius, and R. F. P. Mendes, Phys. Rev. D **98**, 044007 (2018), arXiv:1806.00158 [gr-qc].

[522] H. Yang, Phys. Rev. D **100**, 064023 (2019), arXiv:1904.11089 [gr-qc].

[523] J.-S. Wang and D. Lai, Phys. Rev. D **102**, 083005 (2020), arXiv:2009.08300 [astro-ph.HE].